Ph.D. Thesis

Structuring atoms with structured light: Optomechanical pattern dynamics and transport in cold atomic gases

Submitted in partial fulfilment of the requirements for the degree of
Doctor of Philosophy

Giuseppe Baio
Department of Physics

Supervisor: Dr. Gordon R. M. Robb
Second supervisors: Dr. Alison M. Yao, Prof. Gian-Luca Oppo

February 23, 2022

Contents

List of Figures

List of Publications/Conference contributions

Various results from the main areas of interest within this thesis have been published/submitted in the following list of works:

1. *Optomechanical transport of cold atoms induced by structured light*

   G. Baio, G. R. M. Robb, A. M. Yao, and G.-L. Oppo

   Published in Physical Review Research **2**, 023126 (2020).

2. *Multiple self-organized phases and spatial solitons in cold atoms mediated by optical feedback*

   G. Baio, G. R. M. Robb, A. M. Yao, G.-L. Oppo, and T. Ackemann

   Published in Physical Review Letters **126**, 203201 (2021).

3. *Rotating and spiralling spatial dissipative solitons of light and cold atoms*

   G. Baio, T. Ackemann, G.-L. Oppo, G. R. M. Robb, A. M. Yao

   Published in Physical Review A **105**, 023318 (2022).

4. *Spontaneous atomic crystallization via diffractive dephasing in optical cavities*

   A. Costa-Boquete, **G. Baio**, G. R. M. Robb, G.-L. Oppo, P. Griffin, T. Ackemann

   Published in Journal of Physics: Conference Series 1919 (1), 012014 (2021).

5. *Self-Organization in cold atoms mediated by diffractive coupling*

   T. Ackemann, G. Labeyrie, **G. Baio**, I. Krešic, J. G. M. Walker, A. Costa-Boquete, P. Griffin, W. J. Firth, R. Kaiser, G.-L. Oppo, G. R. M. Robb

   Published in Atoms 9 (3), 35 (2021).

Dissemination of the results to the following international conferences:

1. Central European Workhop on Quantum Optics 2018, Poster presentation (title: *Optomechanical self-structuring involving orbital angular momentum*) – Universitat de les Illes Balears, Palma de Mallorca, 21-25 May 2018.

2. Photon 2018, Poster presentation (title: *Optomechanical self-structuring instabilities involving orbital angular momentum*) – Aston University, Birmingham, 3-6 September 2018.

3. ColOpt winterschool 2019 (Young scientists workshop), Oral presentation (title: *Optomechanical transport of cold atoms induced by structured light*) – Herrsching am Ammersee, 4-8 March 2019.

4. Nonlinear Photonics 2020 (OSA Photonics congress), Oral presentation (title: *Rotational dynamics of Turing patterns and cavity solitons induced by optical angular momentum*) - 13-16 July, 2020.

5. Photon 2020 (IOP conference in Optics/Photonics), Oral presentation (title: *Rotation of self-organized patterns, bunched atoms, and cavity solitons induced by optical angular momentum*) - 1-4 September, 2020.

6. European Quantum Electronics Conference 2021 (World of Photonics congress), Oral presentations (titles: *Structural phase transitions in cold atoms mediated by optical feedback, Rotating and Spiralling Optomechanical Cavity Solitons*) - 21–25 June 2021.

Further publications with University of Strathclyde affiliation and related to previously established/external research activities:

1. *Bounds on the entanglement of two-qutrit systems from fixed marginals*

   G. Baio, D. Chruściński, P. Horodecki, A. Messina, and G. Sarbicki

   Published in Physical Review A **99**, 062312 (2019).

2. *A possible time-dependent generalization of the bipartite quantum marginal problem*

   G. Baio, D. Chruściński, A. Messina

   Published in Journal of Russian Laser Research 39, 422, (2018).

Chapter 1

Introduction

Pattern formation and cold atom physics: the context

The spontaneous appearance of highly organized states characterized by a decrease in entropy is a universal feature distinguishing the physics of systems with drive and dissipation from those at thermodynamic equilibrium [1]. Pursuant to such a universality, spatially and temporally ordered structures known as *patterns* can occur in a variety of contexts involving, e.g., biological and chemical systems, hydrodynamic convection, optical systems etc. [2]. All such systems share the same underlying mechanism, namely, the balance between the effect of *nonlinearity* as a source of inhomogeneity, and a linear *spatial coupling* among separated parts of the system, acting as an opposing, re-distributive tendency. Concurrently, such order in the system emerges due to the wider balance between gain and losses, inherent to systems exposed to drive and dissipation in the interaction with the external environment [3].

Among the most relevant contexts for pattern formation, coupled light-matter systems have provided excellent platforms for the observation of spatial pattern formation, after the pioneering works of Lugiato and Lefever in 1987 [4], and Firth and D'Alessandro in 1990-92 [5–7], showing that spatial dissipative structures can spontaneously emerge in the transverse profile of a passive optical resonator or optical feedback configuration, where the nonlinearity is provided by the optical medium itself and the spatial coupling by optical diffraction. The study of *transverse optical patterns* later became a burgeoning research topic throughout the 1990's and 2000's and detailed review papers can be found in Refs. [8, 9].

Along with the major developments in the field of nonlinear optics, formidable progress in the experimental control of light-atom interaction enabled the possibility of cooling a gas of neutral atoms to sub-Kelvin temperatures [10–12]. The basic principles of *laser cooling*, introduced in the next chapter, are based on the well-known mechanical action exerted by electromagnetic (e.m.) radiation onto atoms, i.e., so-called *optomechanical forces*. Such concepts, together with the achievement of kinetic temperatures well below the mK regime, were crucial to the observation and corresponding theoretical efforts in understanding the physics of Bose-Einstein condensation [13]. This paved the way to the era of cold/ultracold atoms, where the manipulation of coherence and quantum correlations at a many-particle level enable technological applications in quantum information processing and communication, with

profound impact on future technologies [14, 15].

A common feature in all the systems considered so far is that the laser-cooled atoms can be also trapped into arrays or spatial geometries that are fixed, i.e., chosen at will for a specific target. The issue of *static* vs. *dynamical* potentials/fields allows to draw a connection between cold atom physics and the concept of self-organization and, as such, it represents one among the key topics in modern quantum simulation [16, 17]. As discussed below, when the optical field is spatially confined by a cavity or other diffractive feedback configurations, the emerging potential for dispersively coupled atoms can create a modulated density profile, maximizing a certain scattering condition and leading to optomechanical self-structured states [18]. For the case of ultracold atoms[1], such a collectively generated dynamics has been of fundamental importance in the experimental realizations of the Dicke-model phase transitions [19], super-solidity with breaking of continuous symmetries [20–23], tunable range interactions [24], and structural phase transitions among different crystalline configurations [25].

Atoms in optical cavities and dynamical potentials

Let us recall here two among the most important landmarks concerning collective effects in cold atoms and optical cavities, with focus on self-organization via spatial instabilities and its potential applications. The first one is the so-called self-organization into a *Bragg crystal*, originally predicted by Domokos and Ritsch in Ref. [26] for atoms interacting with a single mode of a transversely pumped cavity, and the second one is the *collective atomic recoil lasing* (CARL), involving atoms in a ring resonator and introduced by Bonifacio *et al.* in Ref. [27].

The first setup is sketched in Fig. 1.1, where the atomic ensemble scatters photons from a standing-wave pump field into a single cavity mode, oriented perpendicular to the pump axis. Below a threshold value of input intensity I_{cr}, the homogeneous cloud is stable and the random scattering of photons does not build a photon population of the cavity (Fig. 1.1 - a). Above I_{cr}, the growth of cavity field induces the organization of the atomic cloud into a periodic checker-board lattice (Fig. 1.1 - b). This is induced by the dipole potential that arises from the inter-ference of the pump and the cavity fields and maximizes the Bragg scattering condition. The strong localization of the atoms into the potential wells ensures a high efficiency of scattering which is thus *superradiant*, i.e., scaling with N_{at}^2, with N_{at} being the atom number. The whole process can also be understood in terms of a *positive feedback* picture, since the build-up of the cavity field induces localization of the atoms which, in turn, contributes to the maximiza-tion of photon scattering into the cavity. Superradiant scattering due to self-organization of cold atoms in a cavity was first observed by Black *et al.* in Ref. [28] and later adapted to Bose-Einstein condensates by Baumann *et al.* and Mott *et al.* in Refs. [19, 22, 29]. In particular, as shown in [19], the symmetry breaking during the self-organization of the atom condensate in choosing the Bragg planes and the corresponding superradiance reveals close analogies with the $\mathbb{Z}_2$-*Dicke phase transition* [30]. The analogy between the self-organization transition and the Dicke model is based on the effective quantum-mechanical coupling scheme between ground and excited momentum states of the condensate.

---

[1]Namely, for temperatures below the Doppler limit (see Eq. 2.22).
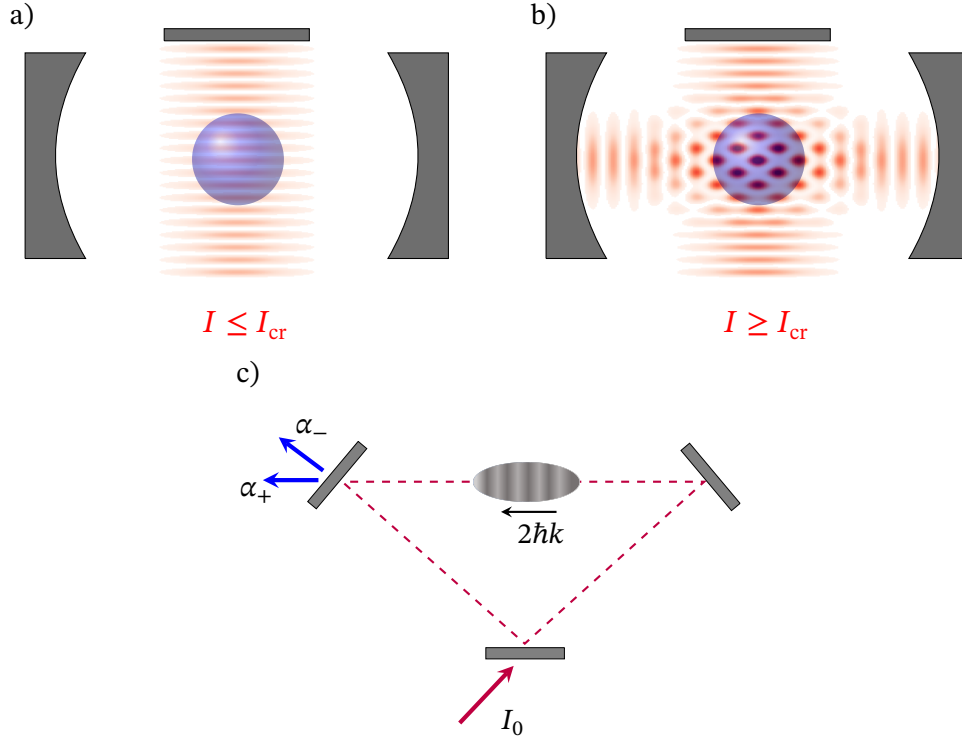
Fig. 1.1. Sketch of the transversely pumped cavity setup. a) The homogeneous atomic cloud is placed inside a single-mode cavity with zero average scattering on the cavity mode below threshold. b) The atom-light system undergoes a superradiant phase transition and the cloud spontaneously self-organizes into a regular checkerboard lattice built by the interference of the pump lattice and the cavity field for a strong enough pumping, i.e., $I \geq I_{cr}$. c) CARL schematics in a ring cavity setup. The ring cavity supports two counter-propagating fields whose amplitudes are denoted by $\alpha_{\pm}$. The interference between the two fields, generated by the back-scattering of photons into the probe α_-, results in longitudinal grating formation and acceleration of the elongated atomic cloud.

On the other hand, a setup for CARL can be realized by means of a bi-directional ring cavity[2], which supports two counter-propagating modes coupled with the atomic cloud [31]. The underlying instability mechanism based on Bragg scattering is shared with the previous setup but, in this case, the bunching of the atoms occurs along the cavity axis, due to the interference between the two counter-propagating cavity modes. The whole process results in an exponential amplification of the probe beam amplitude and an accelerating longitudinal lattice of atoms. This effect can be stabilized by introducing a further dissipative channel (optical molasses), realizing momentum damping and allowing the system to attain a steady-state [32].

Finally, it is worth remarking on the importance of the symmetry breaking aspect shared by such dynamical instabilities. Indeed, self-organized condensates of bosonic atoms represent a candidate for observing the features of *supersolidity* [20], an exotic phase of matter that can be regarded as a superfluid state displaying (off-diagonal) long-range spatial ordering [33, 34].

---

[2]Where the field has running modes instead of the standing waves in the Fabry-Pérot resonator.

Structured light and orbital angular momentum

In 1992, Allen *et al.* provided the ground-breaking intuition that one of the most commonly used families of light modes, i.e., the so-called *Laguerre-Gauss* modes, carry a net angular momentum flux through the plane orthogonal to the direction of propagation, due to their singular phase structure [35]. As discussed later in Ch. 3, this angular momentum, denoted with the term *orbital* or OAM, has an origin that is distinct from the *spin* angular momentum, that originates from the circular polarization state of the light field [36].

The recognition of Laguerre-Gauss modes as carriers of OAM and their relatively simple generation procedures and high degree of control, prepared the ground for numerous applications, for example, in the context of optical manipulation and information and communication technologies [37, 38]. Such important developments in the optics community also had a significant impact in cold atom physics and atom optics [39]. Indeed, the use of OAM carried by light modes allows for an effective transfer of angular momentum to both motional and internal atomic degrees of freedom. For the physical scenario of interest for this thesis, i.e., atoms coupled dispersively to an optical field, one can achieve macroscopic rotational states of atoms by means of ring-shaped optical lattices as trapping potentials [40–42]. Such ring lattice geometries were used to engineer classical and quantum transport and in the simulation of prominent topological phenomena such as artificial gauge fields [43] and fractional quantum Hall condensed matter physics [44–46]. Finally, beside the possibility of shaping the phase structure of a light field, polarization structuring also attracted notable interest in the contexts of trapping and optical manipulation [47, 48]. Novel research frontiers in this direction constitute the field of *fully structured light* [49, 50].

Thesis outline

The main themes in this thesis are novel phenomena and potential applications in schemes for optomechanical self-organization of light and atoms, involving phase structured input fields. Due to the intrinsic nature of OAM, stemming from a vortex-like phase structuring in the transverse plane, the configurations of interest are those characterized by a single distinguished axis of the injected field, where the self-organization transition occurs in the transverse plane. For cold atomic systems, similar schemes such as longitudinally pumped cavities or single-feedback-mirror systems [5–7] have been widely investigated by the Strathclyde and Nice groups in a series of works, achieving coupled patterns of light and atoms where the atomic patterns involve either density structures (formed by optomechanical forces) [51–55], electronic (population) structures [56, 57], or magnetic structures[3] [59–61]. Other schemes of interest involve optical fields counter-propagating along the major axis of a cigar-shaped atomic cloud [62–65]. The main findings concerning the cold-atom optomechanical model within the chapters 3, 4, 5 of this thesis are summarized below.

---

[3]Combined optomechanical and magnetic effects have been recently investigated theoretically in Ref. [58].

1. *Rotational dynamics and atomic transport in a ring cavity.*

   The idea of studying the effect of phase-structured input fields in an optical pattern forming systems was introduced in Ref. [66], for drifting dissipative solitons in a saturable medium within an optical cavity, and in Ref. [67] for the stabilization of domain walls states in degenerate optical parametric oscillators. Transverse rotational dynamics of dissipative solitons and optical patterns induced by the vortex structure of the pump was reported in Refs. [68, 69]. However, a systematic treatment of such an effect was developed only recently in Ref. [70] for a Kerr-cavity, including fully structured light effects in the *vectorial* model, i.e. by means of coupled Lugiato-Lefever equations. The effect of such drifting pattern dynamics is still unexplored for the cold-atom optomechanical model, where the coupling mechanism is based on atomic transport. A theoretical and computational investigation of such a problem for a ring cavity configuration is the subject of Ch. 3, where the emergence of stable atomic currents induced by OAM is demonstrated in correspondence with the rotation of ring lattices of light and atoms.

2. *Multiple phases in a single-feedback-mirror setup.*

   Recent theoretical and experimental investigations of cold-atom optomechanical instabilities have shown self-structuring into atom density states with hexagonal symmetry in a parameter regime where the nonlinear self-focusing is relatively close to that of an *effective-Kerr* medium [53]. However, by means of a weakly nonlinear analysis and a variational formalism discussed in Ch. 4, one can show that, for sufficiently low values of the optical susceptibility, the system behaviour shows a substantial deviation from that observed in a Kerr medium. This is demonstrated by the fact that the light-atom structures exhibit a non trivial recovery of inversion symmetry and, thus, structural transitions among hexagonal, stripe, and honeycomb patterns which are forbidden by the standard effective-Kerr approach to transverse pattern formation [7]. This striking observation has consequences for the atomic transport induced by OAM, and this is explored for different parameter regions of the phase stability diagram.

3. *Rotating and interacting optomechanical dissipative solitons.*

   A general feature of the optomechanical nonlinearity, shared by the ring cavity and the single-mirror-configurations, is the appearance of bright or dark hexagonal patterns far from the special inversion symmetric point found in Ch. 4. Such phases have subcritical character and, thus, dissipative optomechanical cavity solitons as coupled light-atom wavepackets were observed numerically when the system pump was below threshold [71]. The existence of such solitons is discussed for the single-feedback system in the blue detuning regime, in correspondence with the two hexagon/honeycomb phases. For the honeycomb field phase, the feedback solitons can be regarded as self-sustained dark atomic traps that can be effectively transported by means of externally controlled phase gradients. Moreover, it is shown how OAM-carrying input profiles are used to induce rotating and spiralling transverse motion of bright intensity/atom-density cavity solitons and interacting soliton chains.

Chapter 2

Preliminary concepts

The first chapter provides the essential introductory concepts, divided into three main areas in atomic and optical physics representing well established research themes: cold atom physics and optomechanical effects (Sec. 2.1), structured light modes and orbital angular momentum of light (Sec. 2.2) and self-organization phenomena in coupled light-atom systems (Sec. 2.3). Within each section, the material will be divided into short paragraphs aimed at summarizing technical tools used in the later chapters of this thesis. In addition, each section contains an overview of the state of the art in the respective fields, paving the way to the novel research contributions discussed in Ch. 3, 4 and 5.

2.1 Cold atoms and optomechanics

In this first section, a short introduction to the principles of laser cooling and cold-atom physics is provided, starting with a derivation of optical forces on atoms coupled to a light field via *dipole interaction*. This sets the stage for understanding collective optomechanical effects observed in cold/ultracold atom experiments, which constitute the core of the present work.

2.1.1 Cooling and trapping neutral atoms

To discuss cold atom optomechanics, one needs to recall first two fundamental concepts in quantum theory, namely, the description of the quantum state of an atomic ensemble by means of the *density matrix* and its dynamical evolution induced by interaction with classical light (*optical Bloch equations*). Both concepts are presented in the following paragraphs.

Density matrices

The standard scheme describing light-atom interaction is based on a quantum description of the internal or *electronic* degrees of freedom. Although the basic principles used here are valid for any possible multi-level atomic structure, in this thesis, the simplest possible picture of a two-level atom coupled to a monochromatic e.m. field is assumed. The two-level electronic structure is simply described by a complex Hilbert space $\mathcal{H}$ such that $\dim(\mathcal{H}) = 2$, with a

natural basis provided by the *ground* and *excited* states, $\hat{H}_{at}|1\rangle = \hbar\omega_1|1\rangle$ and $\hat{H}_{at}|2\rangle = \hbar\omega_2|2\rangle$, where ω_1, ω_2 indicate the frequency of the energy levels and $\omega_{at} = \omega_2 - \omega_1 > 0$ the transition frequency. However, such state definition only is inadequate for a broader description of atomic ensembles in statistical mixtures. This is achieved by constructing a *density operator*[1]:

$$\hat{\rho} = \sum_{i=1}^{k} p_k |\psi_k\rangle\langle\psi_k|, \tag{2.1}$$

where $\{p_k\}$ is a probability distribution[2] and $\hat{P}_k = |\psi_k\rangle\langle\psi_k|$ are projection operators onto states identified by $|\psi_k\rangle$, i.e, any superposition of $|1\rangle$ and $|2\rangle$. Moreover, the convex construction used in Eq. (2.1) imposes that a generic density matrix $\hat{\rho}$ is a positive semidefinite operator represented by a matrix of unit trace. Based on such concept, one can introduce the main building blocks in the derivation of optomechanical phenomena, namely, the atomic dynamics (*optical Bloch equations*), and the forces induced by the interaction with the optical field.

The optical Bloch equations

Let us start our analysis with the semi-classical dynamics of a two-level atom of mass m and transition frequency ω_{at}, coupled to classical e.m. radiation, represented here by an oscillating electric field of frequency ω_0 and wavenumber k_0 propagating along the z direction, i.e.:

$$\mathbf{E}(\mathbf{r}, t) = i\left[\mathcal{E}(\mathbf{r})\exp\left[-i(\omega_0 t - k_0 z)\right]\mathbf{e}_r - \text{c.c.}\right], \tag{2.2}$$

where $\mathcal{E}(\mathbf{r})$ is a complex amplitude encoding the spatial structure of the field (its details will be discussed in Sec. 2.2.2) and $\mathbf{e}_r$ is the complex polarization vector. Defining with $\hat{\mathbf{R}}$ and $\hat{\mathbf{P}}$ the atomic center-of-mass position and momentum operators, the corresponding Hamiltonian, in the Coulomb gauge and dipole approximation[3], reads [72]:

$$\hat{H}_{tot} = \hat{H}_{cm} + \hat{H}_{at} + \hat{H}_{int} = \frac{\hat{\mathbf{P}}^2}{2m} + \hbar\delta_{at}\hat{\sigma}^+\hat{\sigma}^- - \hat{\mathbf{d}} \cdot \mathbf{E}\left(\langle\hat{\mathbf{R}}\rangle, t\right), \tag{2.3}$$

where $\sigma^- = |1\rangle\langle2|$ and $\sigma^+ = (\sigma^-)^\dagger$, $\hat{\mathbf{d}} = q(\hat{\mathbf{R}} - \langle\hat{\mathbf{R}}\rangle)$ is the atomic dipole operator, and q the electron charge. Note from the presence of the light-atom detuning $\delta_{at} = \omega_{at} - \omega_0$ that an interaction picture with respect to a term $\hbar\omega_0\hat{\sigma}^+\hat{\sigma}^-$ is employed. Expressing now the atomic dipole $\hat{\mathbf{d}}$ in terms of the matrix elements $d\mathbf{e}_{at} = q\langle g|\hat{\mathbf{R}}|e\rangle$, where $\mathbf{e}_{at}$ is the unit vector representing the atomic transition polarization, one obtains the following, purely off-diagonal, form of the interaction Hamiltonian $\hat{H}_{int}$ in Eq. (2.3):

$$\hat{H}_{int} = -i\hbar\left(\Omega_{\langle\hat{\mathbf{R}}\rangle}\hat{\sigma}^+ - \Omega^*_{\langle\hat{\mathbf{R}}\rangle}\hat{\sigma}^-\right), \quad \Omega_{\langle\hat{\mathbf{R}}\rangle} = \frac{d\mathcal{E}(\langle\hat{\mathbf{R}}\rangle)\,e^{ik_0 z}}{\hbar}\,\mathbf{e}^*_{at} \cdot \mathbf{e}_r \tag{2.4}$$

---

[1] Any deviation from a pure state can be measured by the *purity* $\mathcal{P} = \text{Tr}\rho^2$, where $\mathcal{P} < 1$ for a mixed state.
[2] That is, any set of numbers such that $0 \le p_k \le 1$ and $\sum_k p_k = 1$.
[3] $\lambda_0 = 2\pi/k_0 \gg a_0$, with a_0 being the Bohr radius.

where $\Omega_{\langle\hat{\mathbf{R}}\rangle}$ is the spatially dependent *Rabi frequency*[4]. The second assumption is a classical limit for the position and momentum operators. This means that the operators are simply replaced by their average values $\langle\hat{\mathbf{R}}\rangle$ and $\langle\hat{\mathbf{P}}\rangle$ and that the quantum state description (density matrix) of the atom involves the internal states only. The quantities of interest will be considered at steady state so one first needs to figure out the full equation for $\hat{\rho}(t)$. The standard approach to the internal atomic dynamics is given by the so-called *optical Bloch equations*:

$$\frac{d}{dt}\hat{\rho}(t) = \mathcal{L}[\hat{\rho}(t)] = -\frac{i}{\hbar}\left[\hat{H}_{\text{at}} + \hat{H}_{\text{int}}, \hat{\rho}(t)\right] + \Gamma\left(\hat{\sigma}^-\hat{\rho}(t)\hat{\sigma}^+ - \frac{1}{2}\{\hat{\sigma}^+\hat{\sigma}^-, \hat{\rho}(t)\}\right), \qquad (2.5)$$

where the first commutator term $\left[\hat{H}_{\text{at}} + \hat{H}_{\text{int}}, \hat{\rho}(t)\right]/i\hbar$ describes the *closed* system (conservative) evolution due to the atom-field Hamiltonian while the second is a term of dissipative nature[5], describing *spontaneous emission* with rate Γ, due to the broader coupling with the e.m. environment [73, 74]. The whole system in Eq. (2.5) assumes the following matrix form (Bloch picture):

$$\frac{d}{dt}\begin{bmatrix} \rho_{21}(t) \\ \rho_{12}(t) \\ \rho_{22}(t) \end{bmatrix} = \begin{bmatrix} -\frac{\Gamma}{2} + i\delta_{\text{at}} & 0 & 2\Omega_{\langle\hat{\mathbf{R}}\rangle} \\ 0 & -\frac{\Gamma}{2} - i\delta_{\text{at}} & 2\Omega^*_{\langle\hat{\mathbf{R}}\rangle} \\ -\Omega^*_{\langle\hat{\mathbf{R}}\rangle} & -\Omega_{\langle\hat{\mathbf{R}}\rangle} & -\Gamma \end{bmatrix} \cdot \begin{bmatrix} \rho_{21}(t) \\ \rho_{12}(t) \\ \rho_{22}(t) \end{bmatrix} + \begin{bmatrix} -\Omega_{\langle\hat{\mathbf{R}}\rangle} \\ -\Omega^*_{\langle\hat{\mathbf{R}}\rangle} \\ 0 \end{bmatrix}, \qquad (2.6)$$

where the 3×3 linear system above represents the action of the superoperator $\mathcal{L}$ in Eq. (2.5) and $\rho_{11}(t)$ is omitted, since $\text{Tr}[\hat{\rho}(t)] = 1$. However, the above master equation for ρ is strictly valid for an atom at rest. Indeed, the appropriate Doppler-corrected expression for a moving atom requires the effective velocity dependent detuning:

$$\delta_{\mathbf{V}} = \delta_{\text{at}} - \mathbf{k} \cdot \mathbf{V} = \delta_{\text{at}} - k_0\frac{\langle\hat{\mathbf{P}}\rangle_z}{m}, \qquad (2.7)$$

where only the z-component $\langle\hat{\mathbf{P}}\rangle_z$ is present, due to the assumed form of the incoming electric field $\mathbf{E}(\mathbf{r}, t)$. From Eq. (2.6) and (2.7), and recalling the Hermiticity of the density matrix $\hat{\rho}$, i.e., that $\rho_{12} = \rho^*_{21}$, one easily obtains the steady state linear relations between the atomic coherences $\tilde{\rho}_{12}$ and the excited state population $\tilde{\rho}_{22}$ as follows:

$$\tilde{\rho}_{12} = -\left(\frac{\Gamma}{2} + i\delta_{\mathbf{v}}\right)^{-1}\Omega^*_{\langle\hat{\mathbf{R}}\rangle}(1 - 2\tilde{\rho}_{22}), \qquad (2.8)$$

$$\tilde{\rho}_{22} = -\frac{1}{\Gamma}\left(\Omega_{\langle\hat{\mathbf{R}}\rangle}\tilde{\rho}_{12} + \Omega^*_{\langle\hat{\mathbf{R}}\rangle}\tilde{\rho}_{21}\right). \qquad (2.9)$$

Substituting Eq. (2.8) into Eq. (2.9), one finally obtains:

---

[4]Note that, in Eq. (2.4), the fast oscillating terms (frequency $2\omega_0$) are neglected (rotating-wave approximation).
[5]In the standard Lindblad form, where $\{\hat{A}, \hat{B}\} = \hat{A}\hat{B} + \hat{B}\hat{A}$.

$$\tilde{\rho}_{12} = \frac{2}{\Gamma(1 + i\Delta_{\mathbf{v}})}\left(\frac{1}{1+s}\right)\Omega^{*}_{\langle\hat{\mathbf{R}}\rangle}, \tag{2.10}$$

$$\tilde{\rho}_{22} = \frac{4\left|\Omega_{\langle\hat{\mathbf{R}}\rangle}\right|^{2}}{\Gamma^{2}(1 + \Delta_{\mathbf{v}}^{2}) + 8\left|\Omega_{\langle\hat{\mathbf{R}}\rangle}\right|^{2}} = \frac{1}{2}\left(\frac{s}{1+s}\right), \tag{2.11}$$

where it is convenient to define the following adimensional quantities: the spatially dependent *saturation parameter* and the *atomic detuning*[6] (measured in units of $\Gamma/2$) as follows:

$$s(\mathbf{r}, t) = \frac{8\left|\Omega_{\langle\hat{\mathbf{R}}\rangle}\right|^{2}}{\Gamma^{2}(1 + \Delta_{\mathbf{v}}^{2})}, \quad \Delta_{\mathbf{v}} = \frac{2\delta_{\mathbf{v}}}{\Gamma}. \tag{2.12}$$

Eq. (2.10) and (2.11) can now be used to compute steady state expectation values for all quantities of interest. In what follows, the two main contributions to the optical force acting on the atom are derived, i.e. the *scattering force* and the *dipole force*.

Optical forces on neutral atoms

Extensive literature reviews of the principles and experimental achievements of optical trapping by means of optical forces on neutral atoms can be found in Refs. [75, 76]. The semi-classical approach to the force $\mathbf{F}$ arising from light-atom interaction and acting on the atom center of mass is introduced here by means of Ehrenfest's theorem as follows:

$$\mathbf{F}(t) = \frac{d}{dt}\langle\hat{\mathbf{P}}(t)\rangle = -\frac{i}{\hbar}\left\langle[\hat{\mathbf{P}}, \hat{H}_{\mathrm{at}} + \hat{H}_{\mathrm{int}}]\right\rangle = -\left\langle\nabla\hat{H}_{\mathrm{int}}\right\rangle = -\mathrm{Tr}[\hat{\rho}(t)\,\nabla\hat{H}_{\mathrm{int}}], \tag{2.13}$$

where the standard expression of the momentum operator $\hat{\mathbf{P}}$ is used in the coordinate representation, namely $\langle\mathbf{r}|\hat{\mathbf{P}}|\psi\rangle \equiv -i\hbar\nabla\psi(\mathbf{r})$, where $\psi(\mathbf{r})$ is the atom wavefunction. The obtained expression in the RHS of Eq. (2.13) depends on the internal state $\hat{\rho}(t)$. One can easily show that, according to Eqs. (2.4), the total force at steady state involves the coherences $\tilde{\rho}_{12} = \tilde{\rho}_{21}^{*}$ only, and reads as follows:

$$\tilde{\mathbf{F}} = \mathbf{F}(t \to \infty) = -i\hbar\left(\nabla\Omega_{\langle\hat{\mathbf{R}}\rangle}\tilde{\rho}_{12} - \text{c.c.}\right). \tag{2.14}$$

Given the expression of the Rabi frequency $\Omega_{\langle\hat{\mathbf{R}}\rangle}$ in Eq. (2.4), one obtains the following:

$$\nabla\Omega_{\langle\hat{\mathbf{R}}\rangle} = ik_{o}\Omega_{\langle\hat{\mathbf{R}}\rangle}\mathbf{e}_{z} + \frac{d\nabla\mathcal{E}(\langle\hat{\mathbf{R}}\rangle)\,e^{ik_{0}z}}{\hbar}\mathbf{e}^{*}_{\mathrm{at}}\cdot\mathbf{e}_{r} \tag{2.15}$$

$$= \left[ik_{0}\mathbf{e}_{z} + \frac{\nabla\mathcal{E}(\langle\hat{\mathbf{R}}\rangle)}{\mathcal{E}(\langle\hat{\mathbf{R}}\rangle)}\right]\Omega_{\langle\hat{\mathbf{R}}\rangle}. \tag{2.16}$$

This gives rise to the two following contributions in the force $\tilde{\mathbf{F}} = \tilde{\mathbf{F}}_{\mathrm{diss}} + \tilde{\mathbf{F}}_{\mathrm{dip}}$, acting on the

---

[6]The quantity Δ is simply referred to as *detuning* from now on.

atom center of mass and resulting from the spatial variation of the envelope $\mathcal{E}(\langle \hat{\mathbf{R}} \rangle)$ and the propagation phase $k_o z$ respectively:

$$\tilde{\mathbf{F}}_{\text{diss}} = \frac{2\hbar k_o}{1+s} \left| \Omega_{\langle \hat{\mathbf{R}} \rangle} \right|^2 \left[\frac{1}{\Gamma(1+i\Delta_{\mathbf{v}})} + \text{c.c.} \right] \mathbf{e}_z = \frac{\hbar k_o \Gamma}{2} \left(\frac{s}{1+s} \right) \mathbf{e}_z = \hbar k_o \Gamma \tilde{\rho}_{22} \mathbf{e}_z \tag{2.17}$$

$$\tilde{\mathbf{F}}_{\text{dip}} = -i \frac{2\hbar}{1+s} \left| \Omega_{\langle \hat{\mathbf{R}} \rangle} \right|^2 \left[\frac{1}{\Gamma(1+i\Delta_{\mathbf{v}})} - \text{c.c.} \right] \frac{\nabla \mathcal{E}(\langle \hat{\mathbf{R}} \rangle)}{\mathcal{E}(\langle \hat{\mathbf{R}} \rangle)} = -\frac{\hbar \Gamma \Delta_{\mathbf{v}}}{2} \frac{s}{1+s} \frac{\nabla \mathcal{E}(\langle \hat{\mathbf{R}} \rangle)}{\mathcal{E}(\langle \hat{\mathbf{R}} \rangle)}. \tag{2.18}$$

The first one $\tilde{\mathbf{F}}_{\text{diss}} = \hbar k_o \Gamma \tilde{\rho}_{22} \mathbf{e}_z$ represents a dissipative or *scattering force* due to the incoherent process of spontaneous emission. Indeed, quanta of momentum $\hbar k_o \mathbf{e}_z$ are absorbed by the atom and subsequently lost with a rate Γ into the surrounding e.m. environment in a random direction. Thus, a net momentum transfer along the $\mathbf{e}_z$ direction must occur, with a probability of the whole process given by the excited state population $\tilde{\rho}_{22}$. The second term is instead known as the *dipole force* and arises as an average of the coherent processes of stimulated emission. In a purely classical picture, this can be understood as the induced dipole moment $\hat{\mathbf{d}}$ interacting dispersively with the intensity gradient of the light field [75]. This conservative contribution to the total force on the atom originates from the following potential[7]:

$$U_{\text{dip}}(\mathbf{r}, t) = -\frac{\hbar \Gamma \Delta_{\mathbf{v}}}{4} \ln \left[1 + s(\mathbf{r}, t) \right]. \tag{2.19}$$

Note the crucial dependence of Eq. (2.19) on the atomic detuning $\Delta_{\mathbf{v}}$. This implies that the atom behaves as a bright-intensity seeking particle for $\Delta_{\mathbf{v}} > 0$ (red detuning) and dark-light-intensity seeking particle for $\Delta_{\mathbf{v}} < 0$ (blue detuning). The forces derived above in Eq. (2.17) and (2.18) are graphically represented in Fig. 2.1 for the case of an atom interacting with a red detuned beam having a Gaussian envelope $\mathcal{E}(\mathbf{r})$ (defined later in Sec. 2.2.2).

Let us now assume for the moment the simplest case of a plane wave, namely, a constant envelope profile of amplitude $\mathcal{E}(\mathbf{r}) = \mathcal{E}_0$ in Eq. (2.2). In this case, only scattering forces are present since the gradient term in Eq. (2.18) vanishes. Recalling now the Doppler correction in Eq. (2.7), and the definition of the saturation parameter in Eq. (2.12), one obtains:

$$\frac{|\tilde{\mathbf{F}}_{\text{diss}}|}{\hbar k_o \Gamma} = \frac{1}{2} \left(\frac{s}{1+s} \right) = \frac{4 \left| \Omega_{\langle \hat{\mathbf{R}} \rangle} \right|^2}{\Gamma^2 (1+\Delta_{\mathbf{v}}^2) + 8 \left| \Omega_{\langle \hat{\mathbf{R}} \rangle} \right|^2} = \frac{4 \left| \Omega_{\langle \hat{\mathbf{R}} \rangle} \right|^2}{\Gamma^2 \left[1 + \left(\Delta_0 - \frac{2}{\Gamma} \mathbf{k} \cdot \mathbf{V} \right)^2 \right] + 8 \left| \Omega_{\langle \hat{\mathbf{R}} \rangle} \right|^2}. \tag{2.20}$$

where $\Delta_0 = 2\delta_{\text{at}}/\Gamma$. Let us expand the above at first order in the atom velocity $\mathbf{V}$, namely:

$$\frac{|\tilde{\mathbf{F}}_{\text{diss}}|}{\hbar k_o \Gamma} = \frac{1}{2} \frac{s_0}{1+s_0} \left[1 + \frac{4\Delta_0}{\Gamma(1+\Delta_0^2)} \frac{k_0 \cdot \langle \mathbf{V} \rangle_z}{1+s_0} \right]. \tag{2.21}$$

Therefore, as seen from Eq. (2.21), the $\mathbf{V}$-dependent correction can be used in order to provide momentum damping on the atom. Indeed, assuming a configuration that involves two

---

[7]Let us recall that $s \propto I(\mathbf{r}) = |\mathcal{E}(\mathbf{r})|^2$.

a)

$I(x, z)$

b)
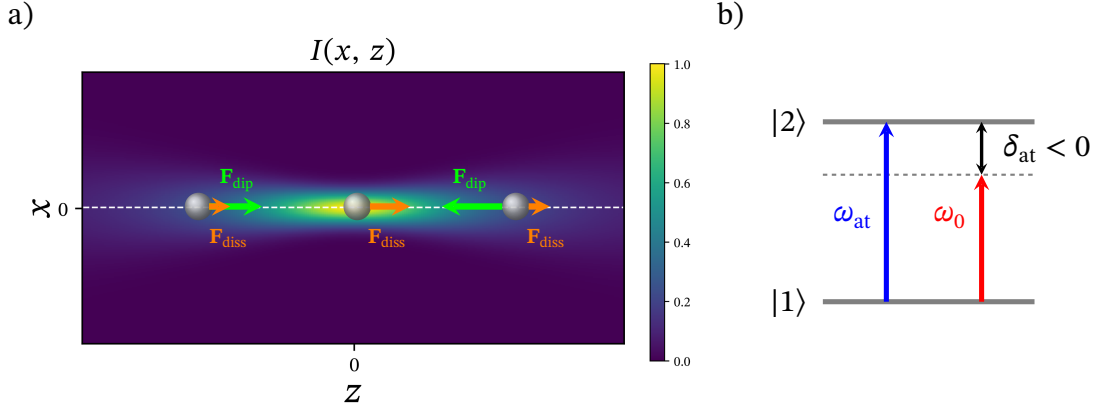
Fig. 2.1. Pictorial representation of light-induced forces on an atom illuminated by a single Gaussian mode of frequency ω_0. a) The normalized 2-d longitudinal intensity profile $I(x, z)$ of the beam is represented in the plane (x, z) only, due to the rotational symmetry of the transverse profile. b) Two level scheme of light-atom interaction. The field of frequency ω_0 is red detuned $\delta_{at} < 0$ with respect to the atomic transition ω_{at} so that the atom is attracted by dipole forces $\mathbf{F}_{dip}$ a), green) towards the maximum in the $(0, 0)$ point. Scattering forces $\mathbf{F}_{diss}$ (in orange) are proportional to the field intensity (saturation) and always oriented along the z direction.

counter-propagating plane waves, and that the two fields act independently on the atom[8], the total effect would result in a net frictional force on the atomic motion. Such configuration has been termed *optical molasses* in the context of Doppler cooling, in order to emphasize the similarity with the motion of a particle in a viscous fluid [77–80]. The Doppler cooling process based on optical molasses has a theoretical limit temperature provided by the atomic transition decay rate Γ, namely:

$$k_B T_D = \frac{\hbar \Gamma}{2}. \tag{2.22}$$

The above temperature, known as the *Doppler temperature* can be explained by considering momentum fluctuations and the relaxation of the probability distribution towards equilibrium [81]. Such stochastic methods are briefly introduced later in Sec. 2.3.1. Sub-Doppler cooling methods, such as *evaporative cooling*, are needed to reach *Bose-Einstein condensation* of the atomic gas [82, 83]. The manipulation and control of matter wave coherence in dilute gases of ultracold atoms represents nowadays the experimental workhorse in the exploration of many-body quantum effects and condensed matter phenomena [84, 85].

So far it was implicitly assumed that the radiation field is weakly affected by the interaction with the atoms. The situation strongly changes when one considers light modes of *high-finesse* optical resonators or other boundary conditions such as, e.g., a single reflecting mirror. In such conditions, the back action of the atomic motion onto the optical field has to be taken into account and the dynamics of the whole system becomes nonlinear[9] [18]. Such concepts are briefly discussed in the following subsections.

---

[8]Note that this assumption is valid only in the *low saturation limit*, i.e., $s \ll 1$ [77].

[9]And the spontaneous appearance of self-organized states comes into play.

2.2 Structured light and orbital angular momentum

This section is aimed at introducing the reader to the interaction between structured light and matter. The term *structured* is generally used to emphasize that the incident light carries a nontrivial phase or amplitude dependence such as, e.g., a net angular momentum along the direction of propagation[10]. Let us start reviewing the concept of OAM in classical electrodynamics in Sec. 2.2.1, and introduce the two common families of Gaussian light-modes, namely the Hermite-Gauss ($\mathcal{HG}$) and Laguerre-Gauss modes ($\mathcal{LG}$) in Sec. 2.2.2. Finally, in Sec. 2.2.3, OAM exchange mechanisms between light and atoms including optical forces will be discussed.

2.2.1 Spin and orbital angular momentum of arbitrary fields

In this subsection, the fundamental background to the OAM of light modes is introduced, namely, how one can generate light beams which manifestly exhibit such a property. In particular, after the introduction of the relevant quantities, a derivation of the angular momentum density of an electromagnetic field is presented, within the framework of Refs. [90, 91]. This shows how the total angular momentum of a light mode can be separated into *spin* and *angular* parts. Starting from the definition of two arbitrary fields $\mathbf{E}$ and $\mathbf{B}$ in the presence of external charges and currents, the local conservation of quantities of interest derived from such fields is generally described in terms of a continuity equation:

$$\partial_t \rho(\mathbf{r}, t) + \nabla \cdot \mathbf{J}(\mathbf{r}, t) = q(\mathbf{r}, t), \tag{2.23}$$

where $\rho(\mathbf{r}, t)$ indicates the density of the corresponding conserved quantity (e.g. energy, charge, linear or angular momentum), and $\mathbf{J}(\mathbf{r}, t)$ and $q(\mathbf{r}, t)$ represent the flux density and a source term respectively. For example, when considering the e.m. energy, Eq. (2.23) is known as the *Poynting's theorem* and assumes the following form [92]:

$$-\mathbf{j} \cdot \mathbf{E} = \partial_t \left(\frac{\epsilon_0}{2} \mathbf{E}^2 + \frac{1}{2\mu_0} \mathbf{B}^2 \right) + \nabla \cdot \left(\frac{1}{\mu_0} \mathbf{E} \times \mathbf{B} \right), \tag{2.24}$$

with $\mathbf{j}$ being the charge current density and ϵ_0 and μ_0 the free space electric and magnetic permittivities. Therefore, one recognizes the quantity:

$$\rho^E = \frac{\epsilon_0}{2} \mathbf{E}^2 + \frac{1}{2\mu_0} \mathbf{B}^2, \tag{2.25}$$

as the e.m. energy density, and the *Poynting vector* $\mathbf{S}$ (energy flux density) as follows:

$$\mathbf{S} = \frac{1}{\mu_0} \mathbf{E} \times \mathbf{B}. \tag{2.26}$$

Eq. (2.23) can be generalized to the case of the linear momentum carried by an e.m. field.

---

[10]More generally, it is also used to include polarization structuring, see Refs. [48, 50, 86–89]

Adopting Einstein's index notation, which conveniently encodes the vectorial nature of the momentum density[11] ρ_k^P, the continuity equation becomes:

$$\partial_t \rho_k^P + \partial_i J_{ik}^{(P)} = q_k^P, \tag{2.27}$$

where the sum involves the repeated indices. Defining also a generic charge density σ, it is the Lorentz force acting on σ that generates a source term in the RHS of Eq. (2.27) and its density reads as follows:

$$q_k^P = -[\rho\mathbf{E} + \mathbf{j}\times\mathbf{B}]_k = -(\sigma E_k + \varepsilon_{klm}j_l B_m), \tag{2.28}$$

where ρ is the scalar charge density and ε_{klm} is the completely anti-symmetric tensor arising from the cross product. Moreover, let us also recall that the momentum density is given by [93]:

$$\rho_k^P = \frac{1}{c^2}[\mathbf{E}\times\mathbf{B}]_k = \frac{1}{c^2}\varepsilon_{klm}E_l B_m = \frac{\mu_0}{c^2}S_k, \tag{2.29}$$

and the related flux density is described by the *Maxwell* or *Energy-Stress tensor*:

$$J_{ik}^P = \epsilon_0\left(\frac{1}{2}\mathbf{E}^2 - \delta_{ik} - E_i E_k\right) + \frac{1}{\mu_0}\left(\frac{1}{2}B^2 - \delta_{ik} - B_i B_k\right), \tag{2.30}$$

where δ_{ik} is the Kronecker symbol. Finally, one has now all the necessary ingredients to consider the angular momentum case. Indeed, this is achieved by means of a vector multiplication of the (vectorial) momentum density ρ^P with the position vector $\mathbf{r}$. Therefore, the total angular momentum is simply obtained by integrating the resulting density, namely:

$$\mathbf{J} = \int d^3\mathbf{r}\ \mathbf{r}\times\rho^P = \int d^3\mathbf{r}\ \epsilon_0\mathbf{r}\times(\mathbf{E}\times\mathbf{B}). \tag{2.31}$$

Similarly for all the remaining quantities involved in Eq. (2.27), one has:

$$J_{ik}^J = \epsilon_{ijl}r_j J_{lk}^P, \tag{2.32}$$

$$q_k^J = \epsilon_{klm}r_l q_m^P. \tag{2.33}$$

It can already be seen from Eq. (2.31) that the total angular momentum $\mathbf{J}$ can be separated into a sum of an orbital part $\mathbf{L}$ (OAM) and a spin part $\mathbf{S}$ (SAM), with a different interpretation. Indeed, taking the vector potential $\mathbf{A}$ into account[12], Eq. (2.31) can be generally decomposed as the following sum [73, 94]:

$$\mathbf{J} = \int d^3\mathbf{r}\ \epsilon_0\left[E_i(\mathbf{r}\times\nabla)A_i - E_i\partial_i(\mathbf{r}\times\mathbf{A}) + \mathbf{E}\times\mathbf{A}\right]. \tag{2.34}$$

One shows that, integrating by parts and using Gauss theorem, the second term in Eq. (2.34)

---

[11]As well as the tensorial nature of the momentum density flux.
[12]such that $\mathbf{B} = \nabla\times\mathbf{A}$.

leads eventually to a vanishing surface integral. Thus, the two following contributions remain:

$$\mathbf{L} = \int d^3\mathbf{r} \; \epsilon_0 \, E_i(\mathbf{r} \times \nabla) A_i, \tag{2.35}$$

$$\mathbf{S} = \int d^3\mathbf{r} \; \epsilon_0 \, \mathbf{E} \times \mathbf{A}, \tag{2.36}$$

which are interpreted as the *orbital* component (**L** - OAM) and the *spin* component (**S** - SAM) respectively. The same concept will be shown later in a more physically concrete fashion, by means of the flux density J_{ik}^J, directly computed from Eqs. (2.32) and (2.33):

$$J_{ik}^J = \epsilon_{ilk} r_l \rho^E - \epsilon_{ilm} r_l \left(\epsilon_0 E_m E_k + \frac{1}{\mu_0} B_m B_k \right). \tag{2.37}$$

By means of Eq. (2.37), one demonstrates that higher order $\mathcal{LG}$-modes already possess a non-vanishing angular momentum flux along the direction of propagation. Indeed, simply assuming the z axis as such direction, J_{zz}^J is integrated in the transverse plane $\mathbf{r}_\perp = (x, y)$:

$$\Phi_{zz}^J = \int d^2\mathbf{r}_\perp \; J_{zz}^J(x, y). \tag{2.38}$$

In the following subsection, the full expression of a Gaussian beam as a fundamental mode of free-space propagation equation is presented. Moreover, one observes that higher-order modes of the same equation directly provide the two commonly used families of transverse modes, i.e., the $\mathcal{HG}$ and the $\mathcal{LG}$-modes.

2.2.2 Gaussian modes and optical vortices

The well known wave equations describing the propagation of the e.m. field in free space are derived by means of standard manipulations of Maxwell's equations. Inserting the usual unidirectionally propagating ansatz[13] of Eq. (2.2), one is left with the Helmoltz equations for the field envelopes $\mathcal{E}(\mathbf{r})$ and $\mathcal{B}(\mathbf{r})$, namely:

$$\nabla^2 \mathcal{E}(\mathbf{r}) + k_0^2 \mathcal{E}(\mathbf{r}) = 0, \tag{2.39}$$

$$\nabla^2 \mathcal{B}(\mathbf{r}) + k_0^2 \mathcal{B}(\mathbf{r}) = 0, \tag{2.40}$$

with the wavenumber satisfying $k_0 = \omega_0/c$. Eqs. (2.39) and (2.40) represent the starting point of our analysis but, in order to describe realistic configurations, one includes two well-known approximations called *paraxial* and *slowly varying envelope*, namely [95, 96]:

$$\left| \partial_z^2 \mathcal{E}(\mathbf{r}) \right| \ll |2k_0 \partial_z \mathcal{E}(\mathbf{r})|, \; |\partial_x^2 \mathcal{E}(\mathbf{r})|, \; |\partial_y^2 \mathcal{E}(\mathbf{r})| \tag{2.41}$$

where the electric field is expanded in a plane wave basis by means of the components $\mathbf{k} \equiv (k_x, k_y, k_z)$, and it is assumed that the field amplitude variation is much smaller than the car-

---

[13]Separated in space and time.
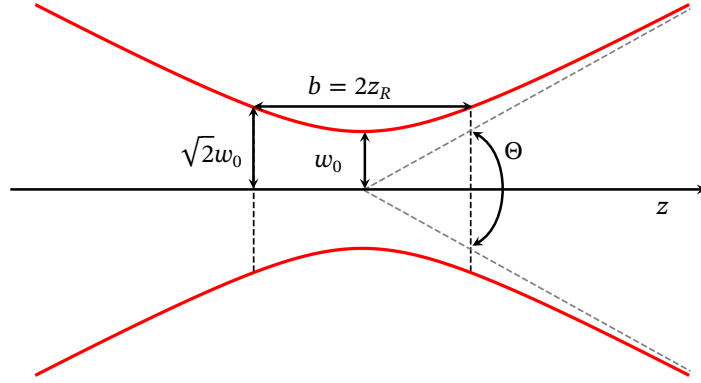
Fig. 2.2. Illustrated longitudinal profile of the width of a Gaussian beam. The parameter $b = 2z_R$ is called *confocal range*. The angular total angular spread $\Theta = 2 \lim_{z \to +\infty} w(z)/z$.

rier wave. It is straightforward to show now that, under such approximations, the Helmoltz Eqs. (2.39) and (2.40) transform as follows:

$$\nabla^2_\perp \mathcal{E}(\mathbf{r}) + 2ik_0 \partial_z \mathcal{E}(\mathbf{r}) = 0. \tag{2.42}$$

Eq. (2.42) is commonly denoted as *paraxial wave equation* and its solutions are used to approximate the envelope profile of a laser beam. The fundamental solution of Eq. (2.42) is given by the Gaussian mode, defined as[14] [97]:

$$\mathcal{E}(\mathbf{r}) \propto \frac{e^{-i\phi(z)}}{\sqrt{1 + \frac{z^2}{z_R^2}}} \exp\left(\frac{ik_0(x^2 + y^2)}{2R(z)}\right) \exp\left(-\frac{(x^2 + y^2)}{w^2(z)}\right), \tag{2.43}$$

where the three functions $R(z)$, $w(z)$ and $\varphi(z)$ (*Gouy phase shift*) read:

$$R(z) = z + \frac{z_R^2}{z}, \quad w(z) = w_0\sqrt{1 + \left(\frac{z}{z_R}\right)^2}, \quad \varphi(z) = \tan^{-1}\left(\frac{z}{z_R}\right). \tag{2.44}$$

The two parameters z_R and w_0, known as *Rayleigh range* and *beam waist* respectively, are linked by the relation $z_0 = \pi w_0^2/\lambda$, and their geometrical meaning can be recognized graphically in Fig. 2.2. Transverse higher-order modes of Eq. (2.42) can also be obtained by simply imposing the following separate spatial dependence in the ansatz:

$$\mathcal{E}(\mathbf{r}) \propto \frac{w_0}{w(z)} g\left[\frac{x}{w(z)}\right] h\left[\frac{y}{w(z)}\right] \exp\left(\frac{ik_0(x^2 + y^2)}{2q(z)}\right) e^{ip(z)}, \tag{2.45}$$

where $q(z) = z + iz_R$ (*complex beam parameter*). Such separation of variables has an essential

---

[14]Eq. (2.43) yields a good approximation of a laser transverse profile and it is also known as the *transverse electromagnetic mode* (TEM$_{00}$).
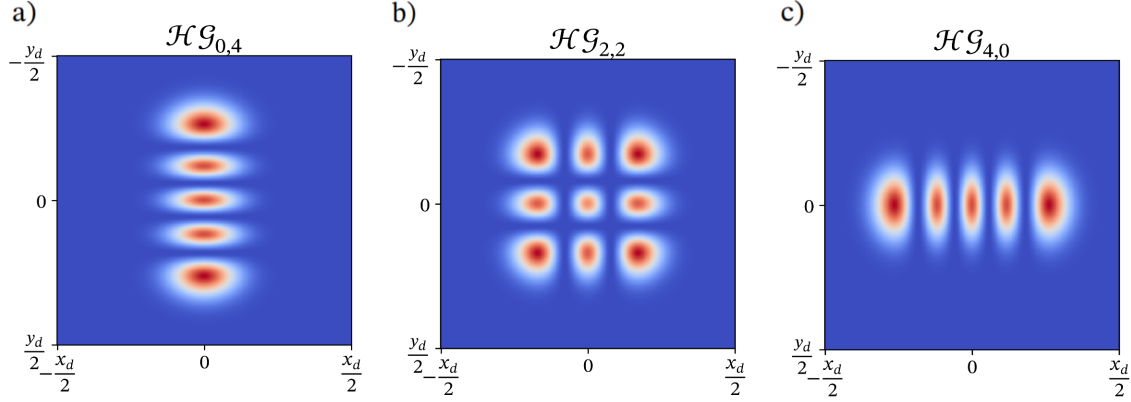
Fig. 2.3. a), b), c) Characteristic normalized intensity profiles $I = |\mathcal{E}(\mathbf{r}_\perp)|^2$ of Hermite-Gaussian light modes as defined in Eq. (2.45). In particular, the three cases corresponding to the subspace defined by the condition $m + n = 2$ are shown here.

role since it can be shown that both functions g and h satisfy an Hermite differential equation, whose solutions are given by the namesake series of polynomials[15] [98]:

$$g\left[\frac{x}{w(z)}\right] = H_m\left[\sqrt{2}\frac{x}{w(z)}\right], \quad h\left[\frac{x}{w(z)}\right] = H_n\left[\sqrt{2}\frac{x}{w(z)}\right] \tag{2.46}$$

$$H_0(u) = 1, \quad H_1(u) = 2u, \quad H_2(u) = 4u^2 - 2, \quad \dots \tag{2.47}$$

so that the Gouy phase now reads $p(z) = (m + n + 1)\varphi(z)$. Examples of transverse intensity structures of such modes are shown in Fig. 2.3, where one recognizes the characteristic rectangular symmetry. The spatial structure of the transverse higher-order modes also changes significantly if one introduces the same paraxial equation (2.42) in cylindrical coordinates $\mathbf{r} = (r, \phi, z)$, that is:

$$\left(\partial_r^2 + \frac{1}{r}\partial_r + \frac{1}{r^2}\partial_\phi^2 + 2ik_0\partial_z\right)\mathcal{E}(r, \phi, z) = 0. \tag{2.48}$$

An analogous separation of the two transverse variables yields, this time, an azimuthal phase dependence in $\exp(il\phi)$ with $l \in \mathbb{Z}$, and and a radial-only part. Both are encoded in the following profile[16] [100]:

$$\mathcal{E}(\mathbf{r})_{p,l} \propto \frac{r^{|l|}}{\omega^{|l|+1}(z)} \exp\left(-\frac{r^2}{w^2(z)}\right)\mathcal{L}_p^{|l|}\left(\frac{2r^2}{w^2(z)}\right)\exp(il\phi)\exp\left(\frac{ik_0r^2z}{2R(z)}\right)e^{-i\varphi(z)}, \tag{2.49}$$

where the Gouy phase is now multiplied by the factor $-i(2p + |l| + 1)$. The radial part depends this time on the *associated Laguerre polynomials* $\mathcal{L}_p^{|l|}$, obtained from the ordinary ones as [37]:

$$\mathcal{L}_p^{|l|}(x) = (-1)^{|l|}\frac{d^{|l|}}{dx^{|l|}}L_{|l|+p}(x). \tag{2.50}$$

---

[15]For this reason such modes are also called Hermite-Gaussian.
[16]A normalization constant is given by $\mathcal{C}_{l,p} = (2p!/\pi(p + |l|)!)^{1/2}$, so that $\mathcal{C}_{l,p}\int_{\mathbb{R}^2}\mathcal{E}(\mathbf{r})_{p,l}d^2\mathbf{r} = 1$ [99].

As already anticipated in the introduction, the main feature of such light modes is the presence of the azimuthal phase factor $\exp{(il\phi)}$, which generates l intertwined phase fronts and a non-trivial topological structure due to the presence of a *phase singularity*, i.e. a point[17] where the phase is not defined and the intensity vanishes accordingly (See Fig. 2.4). In the next section it is shown how a non zero orbital angular momentum flux arises from Eq. (2.49), applying the concepts previously introduced in Sec. 2.2.1.

2.2.3 Exchange of orbital angular momentum

The aim of this subsection is to show that $\mathcal{LG}$-modes carry a net OAM and that this can be exchanged in light-atom interactions, involving optically induced forces on atoms introduced previously in Sec. 2.1. A detailed review of the principles and applications of OAM-carrying light modes in cold atom and atom optics experiments can be found in Ref. [39].

OAM and the azimuthal phase $e^{il\phi}$

Let us start from the angular momentum flux density tensor in Eq. (2.37). Since one deals now with oscillating terms, the expression for J_{zz}^{J} needs to be averaged over a period $T = 2\pi/\omega_0$. After some algebra, one obtains two distinct contributions[18] for Φ_{zz}^{J} :

$$
\begin{aligned}
\Phi_{zz}^{J} = \Phi_{zz}^{J(1)} + \Phi_{zz}^{J(2)} = \frac{\epsilon_0 c^2}{2\omega_0} \mathrm{Re} \Bigg[\int d^2\mathbf{r}_\perp (\mathcal{E}_x \mathcal{B}_x^* + \mathcal{E}_y \mathcal{B}_y^*) + \\
\frac{1}{2} \int d^2\mathbf{r}_\perp \left(-\mathcal{B}_x^* \partial_\phi \mathcal{E}_y + \mathcal{E}_y \partial_\phi \mathcal{B}_y^* - \mathcal{E}_x \partial_\phi \mathcal{B}_y^* - \mathcal{B}_y^* \partial_\phi \mathcal{E}_x \right) \Bigg],
\end{aligned}
\tag{2.51}
$$

represented here in terms of generic electric field amplitudes ($\mathcal{E}_x, \mathcal{E}_y, \mathcal{E}_z$ etc.) in the cylindrical coordinate representation $\mathbf{r} = (r, \phi, z)$. Such a separation can be understood by means of the following argument. Let us consider propagation through a certain bi-refringent optical element of length L. The phase shifts of the electric and magnetic fields (assuming x and y as the *fast* the *slow* directions respectively) affect only $\Phi_{zz}^{J(1)}$ in Eq. (2.51). Instead, the second term is modified if, for example, one considers an azimuthal phase shift $\exp{(il\phi)}$ applied to the fields, such as in the case of propagation through a spiral phase plate, namely:

$$
\tilde{\Phi}_{zz}^{J(2)} = \Phi_{zz}^{J(2)} + l\frac{\epsilon_0 c^2}{2\omega_0} \mathrm{Re} \int d^2\mathbf{r}_\perp (\mathcal{E}_x \mathcal{B}_x^* + \mathcal{E}_y \mathcal{B}_y^*).
\tag{2.52}
$$

This means that the above phase shift increases the total angular momentum by l times the flux amount $\Phi_{zz}^{J(1)}$. This observation suggests an interpretation of $\Phi_{zz}^{J(2)}$ as an orbital part of the total angular momentum (OAM) flux and, instead, the first term as the *spin* angular momentum, i.e, depending on the polarization of the field only.

Although the above reasoning suggests a way to generate OAM beams experimentally, several other procedures for phase only structuring are commonly adopted in laboratories involv-

---

[17]Or locii of points (e.g. a circumference).
[18]See the complete derivation by Barnett in Ref. [90].
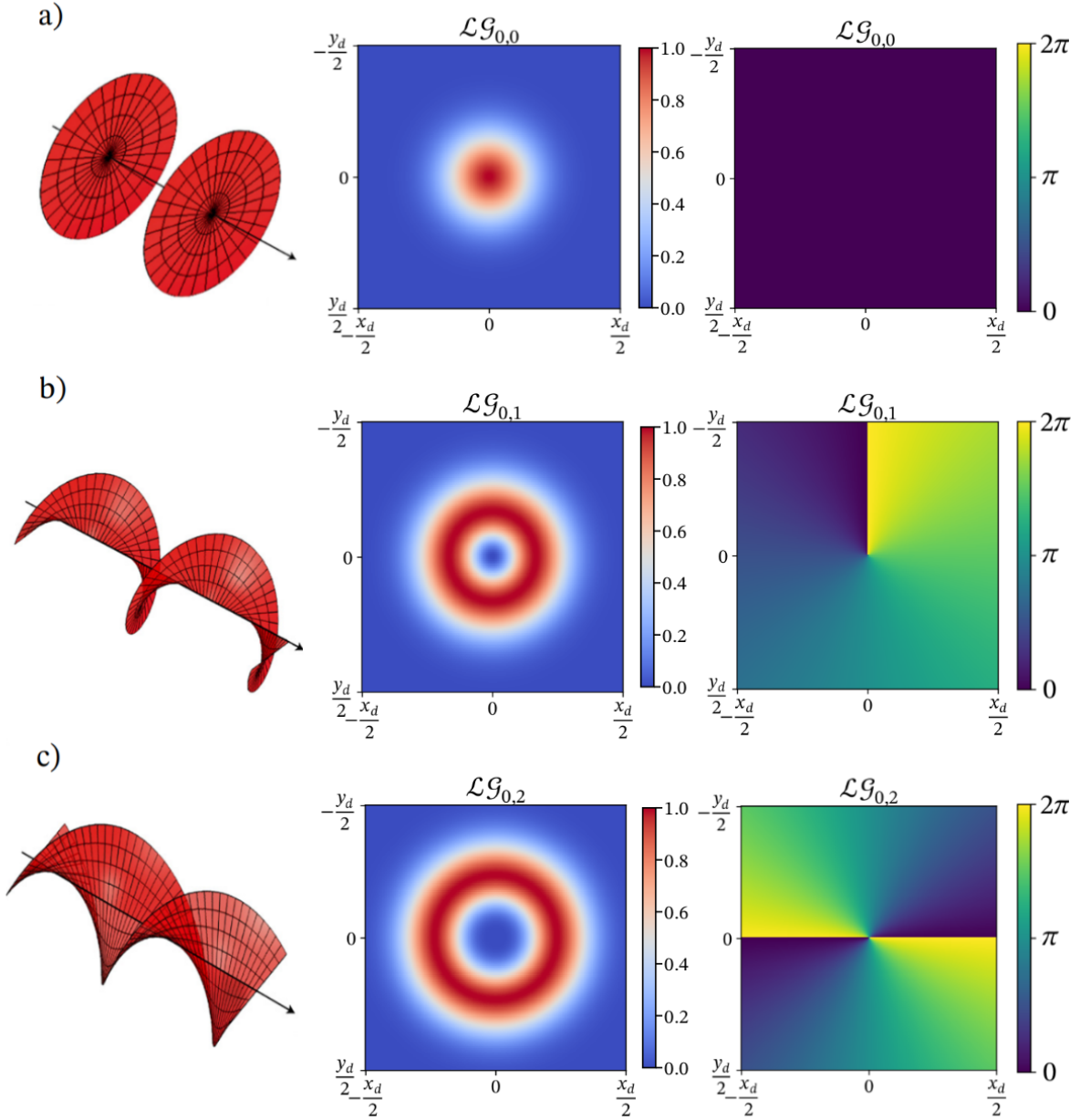
Fig. 2.4. Illustrated wavefronts, transverse normalized intensity and phase profiles for different Laguerre-Gauss light modes with different topological charges $l = 0$ (a), 1 (b), 2 (c) and fixed $p = 0$. Note that with $l = 0$ a), the expression in Eq. (2.49) reduces to the fundamental (Gaussian) transverse e.m. mode TEM$_{00}$. Image adapted from Ref. [37]. Note the phase singularities for $l \neq 0$ at $(x, y) = (0, 0)$ which causes the intensity to vanish, providing the typical ring-shaped (doughnut) profiles.

ing spatial light modulators [37, 101]. In particular, one typically combines the desired phase structure with a linear phase variation. The diffractive optical element yields the desired beam profile in the first diffraction order. Besides the OAM flux as a physical quantity, the use of OAM-carrying modes has also attracted interest in quantum information, since the production of pairs of entangled high-dimensional photons using spontaneous parametric down conversion has been demonstrated experimentally [102–104].

OAM and rotating atoms

Let us now come back to light-induced forces on neutral atoms and assume the ideal case of an atom at rest, illuminated by a $\mathcal{LG}$-beam of topological charge l. According to Eq. (2.17), in this case, the scattering force is shown to display two contributions[19] [105]:

$$\mathbf{F}_{\text{diss}} = \frac{4\hbar\Gamma \left|\Omega_{\langle\hat{\mathbf{R}}\rangle,p,l}\right|^2}{\Gamma^2(1+\Delta_0^2) + 8\left|\Omega_{\langle\hat{\mathbf{R}}\rangle,p,l}\right|^2} \left(k_0\hat{\mathbf{e}}_z + \frac{l}{r}\hat{\mathbf{e}}_\phi\right). \quad (2.53)$$

Assuming high intensities[20] $\left|\Omega_{\langle\hat{\mathbf{R}}\rangle,p,l}\right|^2 \gg \Delta_0, \Gamma$, the total *torque* $\mathbf{T}$ on the atom amounts to[21]:

$$\mathbf{T} = \mathbf{r} \times \mathbf{F}_{\text{diss}} \approx \frac{\hbar l\Gamma}{2}\hat{\mathbf{e}}_z. \quad (2.54)$$

This result was derived by Babiker *et al.* in Ref. [106]. However, due to the incoherent nature of the process and the effect of temperature, such a scattering induced torque is difficult to observe experimentally for thermal atomic clouds. For a BEC trapped in annular geometries, one can instead achieve persistent currents of atoms by means of 2-photon Raman processes [107, 108], or moving optical lattices [109, 110]. Rotating condensates of atoms are also an experimental platform for probing topological effects such as the emergence of fractional quantum Hall states [111]. In the dispersive regime, on the contrary, one can induce and control macroscopic rotation of thermal atoms by means of trapping dipole potentials (*optical ferris wheels*), generated by means of superposition of $\mathcal{LG}$-modes [40, 42]. In such a regime, a novel platform for realizing controlled currents of atomic wavepackets by means of dynamical, self-organized potentials will be introduced in Ch. 3. This arises from the spontaneous breaking of a continuous rotational symmetry in the transverse plane via an optomechanical instability.

2.3 Self-organization in light-matter systems

This section is aimed at describing the main theoretical tools used to address the formation of self-organized optomechanical structures and review the known experimental realizations using transverse optical systems. The material is ordered as follows: a technical introduction

---

[19]The subscripts p and l are added to $\Omega_{\langle\hat{\mathbf{R}}\rangle}$.

[20]More precisely, in the high saturation limit or when the field frequency is close to the atomic resonance, i.e., $(\delta_{\text{at}} \ll 1)$.

[21]Note that the z-component only contribute to the total torque $\mathbf{T}$.

to stochastic processes and the Fokker-Planck equations is provided in Sec. 2.3.1, together with a concise introduction to pattern formation methods in Sec. 2.3.2. This will guide the reader to the core of the work, providing essential tools to understand the results presented in later chapters. Finally, in Sec. 2.3.3, the main features of previous achievements of transverse optomechanical self-organization in light-atom systems are also discussed.

2.3.1 Stochastic processes and collective effects

The aim of this subsection is to introduce the reader to the methods used to describe transport effects in cold atoms. The starting point is given by a formal derivation of the *Fokker-Planck equation*, in order to provide a mean-field phase-space description to the non-equilibrium optomechanical dynamics. The importance of such methods is twofold: to address analytical calculations on the optomechanical instability and to avoid computationally expensive simulations with a large number of atoms.

The Fokker-Planck Equation

Let us now recall some aspects of the formal derivation of the Fokker-Planck equation which are useful for our aims. The material presented here is largely inspired by Ref. [112]. One starts from the usual set of Langevin equations for a classical atom/particle in a viscous environment and subject to a fixed dipole trapping potential[22] $U_{\text{dip}}(\mathbf{r})$, assumed time-independent for the moment:

$$\dot{\mathbf{r}} = \frac{\mathbf{p}}{m}, \quad \dot{\mathbf{p}} = -\nabla_{\mathbf{r}} U_{\text{dip}}(\mathbf{r}) - \frac{\gamma}{m}\mathbf{p} + \xi(t), \tag{2.55}$$

where m is the atomic mass, γ represents momentum damping and $\xi(t)$ is a white noise variable, i.e., such that $\langle \xi(t) \rangle = 0$ and $\langle \xi(t)\xi(t') \rangle = 2D_{\mathbf{p}}\delta(t - t')$, where $D_{\mathbf{p}}$ is the momentum diffusion constant[23]. Since it is not possible to solve Eq. (2.55) for all possible realizations of $\xi(t)$, one would like to guess the master equation for a smooth, normalized distribution function $f(\mathbf{r}, \mathbf{p}, t)$ representing the probability of the particle being in a certain point of the phase space $(\mathbf{r}, \mathbf{p})$, averaged on the realizations of $\xi(t)$. The probability flow in phase space, for a specific $\xi(t)$, is described by a continuity equation for a function $\rho(\mathbf{r}, \mathbf{p}, t)$, such that $f(\mathbf{r}, \mathbf{p}, t) = \langle \rho(\mathbf{r}, \mathbf{p}, t) \rangle$, namely:

$$\partial_t \rho(\mathbf{r}, \mathbf{p}, t) + \nabla_{\mathbf{r}} \cdot (\dot{\mathbf{r}}\,\rho(\mathbf{r}, \mathbf{p}, t)) + \nabla_{\mathbf{p}} \cdot (\dot{\mathbf{p}}\,\rho(\mathbf{r}, \mathbf{p}, t)) = 0. \tag{2.56}$$

By substituting the Langevin equations above, Eq. (2.56) can be conveniently expressed as the sum of two terms:

$$\partial_t \rho(\mathbf{r}, \mathbf{p}, t) = \hat{L}_0 \rho(\mathbf{r}, \mathbf{p}, t) + \hat{L}_1(t)\rho(\mathbf{r}, \mathbf{p}, t), \tag{2.57}$$

with the following differential operators $\hat{L}_0 = m^{-1} \left[\mathbf{p} \cdot \nabla_{\mathbf{r}} - \gamma(1 - \mathbf{p} \cdot \nabla_{\mathbf{p}}) \right] - \nabla_{\mathbf{r}} U_{\text{dip}}(\mathbf{r}) \cdot \nabla_{\mathbf{p}}$,

---

[22]See Eq. (2.19) for its definition.
[23]The reason why it is termed so will be clarified later on.

and $\hat{L}_1(t) = \xi(t) \cdot \nabla_{\mathbf{p}}$. The advantage of such re-arrangement is evident if one defines the function $\phi(\mathbf{r}, \mathbf{p}, t) = \exp(\hat{L}_0 t)\rho(\mathbf{r}, \mathbf{p}, t)$. Indeed, Eq. (2.57) now reads:

$$\partial_t \phi(\mathbf{r}, \mathbf{p}, t) = \hat{G}(t)\phi(\mathbf{r}, \mathbf{p}, t), \tag{2.58}$$

where $\hat{G}(t) = \exp(\hat{L}_0 t)\hat{L}_1(t)\exp(-\hat{L}_0 t)$. Note, from the form of Eq. (2.58), that this procedure resembles the interaction representation one often uses in quantum dynamics. A formal integration of the above yields[24]:

$$\phi(\mathbf{r}, \mathbf{p}, t) = \exp\left[-\int_0^t \hat{G}(\tau)d\tau\right]\phi(\mathbf{r}, \mathbf{p}, 0). \tag{2.59}$$

By means of the definition of the exponential operator in Eq. (2.59), the following ensemble average is obtained:

$$\langle \phi(\mathbf{r}, \mathbf{p}, t)\rangle = \left[\sum_{i=1}^{+\infty} \frac{1}{(2n)!}\left\langle\left(\int_0^t \hat{G}(\tau)d\tau\right)^{2n}\right\rangle\right]\phi(\mathbf{r}, \mathbf{p}, 0), \tag{2.60}$$

since the variable $\xi(t)$ in $\hat{L}_1(t)$ is of Gaussian type and has vanishing odd moments. Moreover, one can demonstrate that the same average in Eq. (2.60) decomposes into a sum of $(2n)!/(n!\,2^n)$ identical terms made by products of n pairwise integrals, namely [113]:

$$\langle \phi(\mathbf{r}, \mathbf{p}, t)\rangle = \left[\sum_{i=1}^{+\infty} \frac{1}{n!}\left(\frac{1}{2}\int_0^t \int_0^t \langle \hat{G}(\tau_1)\hat{G}(\tau_2)\rangle\, d\tau_1 d\tau_2\right)^n\right]\phi(\mathbf{r}, \mathbf{p}, 0) = \tag{2.61}$$

$$= \exp\left[\frac{1}{2}\int_0^t \int_0^t \langle \hat{G}(\tau_1)\hat{G}(\tau_2)\rangle\, d\tau_1 d\tau_2\right]\phi(\mathbf{r}, \mathbf{p}, 0). \tag{2.62}$$

The reason for such manipulation is that one can now exploit the assumptions on $\xi(t)$, namely, that $\langle \xi(\tau_1)\xi(\tau_2)\rangle = 2D_{\mathbf{p}}\delta(\tau_1 - \tau_2)$, in order to show that the generator of the dynamical equation for Eq. (2.62) simply reads:

$$\partial_t \langle \phi(\mathbf{r}, \mathbf{p}, t)\rangle = D_{\mathbf{p}}\exp(\hat{L}_0 t)\nabla_{\mathbf{p}}^2 \exp(-\hat{L}_0 t)\langle \phi(\mathbf{r}, \mathbf{p}, t)\rangle. \tag{2.63}$$

In other words, the effect of diffusion is recovered in momentum space, characterized by the temporal correlation strength $D_{\mathbf{p}}$. By simply recalling that $f(\mathbf{r}, \mathbf{p}, t) = \exp(-\hat{L}_0 t)\langle \phi(\mathbf{r}, \mathbf{p}, t)\rangle$, one finally obtains the Fokker-Planck equation:

$$\partial_t f(\mathbf{r}, \mathbf{p}, t) = -\frac{\mathbf{p}}{m} \cdot \nabla_{\mathbf{r}} f(\mathbf{r}, \mathbf{p}, t) + \nabla_{\mathbf{p}} \cdot \left[\left(\frac{\gamma}{m}\mathbf{p} + \nabla_{\mathbf{r}}U_{\text{dip}}(\mathbf{r})\right)f(\mathbf{r}, \mathbf{p}, t)\right] + D_{\mathbf{p}}\nabla_{\mathbf{p}}^2 f(\mathbf{r}, \mathbf{p}, t). \tag{2.64}$$

Eq. (2.64) is also known in the literature as Kramers-Chandrasekhar equation [114]. Al-

---

[24]Only commutative generators are considered here, i.e., $[\hat{G}(t), \hat{G}(t')] = 0$ for any $t, t' > 0$.

though it was derived for one particle only, it is widely used to describe mass transport and collective effects in a variety of systems such as dilute clouds of cold thermal atoms[25] [18, 115] or water suspensions of dielectric colloidal microspheres [116], and transport in plasmas [117].

The Smoluchowski Equation and the Gibbs distribution

Let us consider now the simpler case in which the momentum damping rate γ in the Langevin Eqs. (2.55) is large enough that the frictional force dominates over inertia. In this case, the momentum is assumed at equilibrium ($\dot{\mathbf{p}} = 0$), namely:

$$\dot{\mathbf{r}} = \frac{\mathbf{p}}{m} = -\frac{1}{\gamma}\left[\nabla_{\mathbf{r}}U_{\mathrm{dip}}(\mathbf{r}) + \xi(t)\right]. \tag{2.65}$$

Therefore, it is enough to describe here the probability flow for the atom in its configuration space only, i.e., based on the density distribution $\tilde{\rho}(\mathbf{r},t) = \int_{-\infty}^{+\infty}\rho(\mathbf{r},\mathbf{p},t)\,d\mathbf{p}$. Following the same derivation as in Eq. (2.57), one obtains:

$$\partial_t\tilde{\rho}(\mathbf{r},t) = \hat{L}_0\tilde{\rho}(\mathbf{r},t) + \hat{L}_1(t)\tilde{\rho}(\mathbf{r},t), \tag{2.66}$$

where, this time, the operators read $\hat{L}_0 = -\gamma^{-1}\left[\nabla_{\mathbf{r}}^2 U_{\mathrm{dip}}(\mathbf{r}) - \nabla_{\mathbf{r}}U_{\mathrm{dip}}(\mathbf{r})\cdot\nabla_{\mathbf{r}}\right]$ and $\hat{L}_1(t) = -\gamma^{-1}\xi(t)\cdot\nabla_{\mathbf{r}}$. One shows that the corresponding dynamical equation for the atom density $n(\mathbf{r},t) = \langle\tilde{\rho}(\mathbf{r},t)\rangle$ reads:

$$\partial_t n(\mathbf{r},t) = \nabla_{\mathbf{r}}\cdot\mathbf{J}(\mathbf{r},t) = \frac{1}{\gamma}\nabla_{\mathbf{r}}\cdot\left[\nabla_{\mathbf{r}}U_{\mathrm{dip}}(\mathbf{r})\,n(\mathbf{r},t) + \frac{D_{\mathbf{p}}}{\gamma}\nabla_{\mathbf{r}}n(\mathbf{r},t)\right], \tag{2.67}$$

where a real space diffusion constant is defined here as $D_{\mathbf{r}} = \gamma^{-2}D_{\mathbf{p}}$. Eq. (2.67) is known as the Smoluchowski or Drift + Diffusion equation, in light of the two contributions appearing in the total probability current $\mathbf{J}(\mathbf{r},t)$, induced by the dipole potential $U_{\mathrm{dip}}(\mathbf{r})$ and the stochastic forces $\xi(t)$ respectively. Its stationary solution, i.e, identified by $\partial_t n_{\mathrm{eq}}(\mathbf{r}) = 0$, is provided by a canonical Gibbs distribution[26], namely:

$$n_{\mathrm{eq}}(\mathbf{r}) = \frac{\exp\left[-\beta U_{\mathrm{dip}}(\mathbf{r})\right]}{\int_{-\infty}^{+\infty}\exp\left[-\beta U_{\mathrm{dip}}(\mathbf{r})\right]d\mathbf{r}}, \tag{2.68}$$

where $\beta = (k_B T)^{-1}$, and the integral in the denominator has the role of preserving the normalization of $n_{\mathrm{eq}}(\mathbf{r})$. The fact that the dissipative evolution of the atom density $n(\mathbf{r},t)$ in Eq. (2.67) always converges asymptotically to Eq. (2.68) can also be proven more rigorously by means of an extremum principle [118]. At this stage, it is enough to show that the Boltzmann factor

---

[25]When illuminated by a far detuned beam.

[26]Such a statement can be also extended to the coupling with dynamical equations for the optical field, provided that there is a separation of timescales.

$\exp\left[-\beta U_{\mathrm{dip}}(\mathbf{r})\right]$ satisfies the equilibrium condition $\mathbf{J}(\mathbf{r}, t) = 0$, that is to say:

$$0 \equiv \left[\frac{1}{\gamma}\nabla_{\mathbf{r}}U_{\mathrm{dip}}(\mathbf{r}) + D_{\mathbf{r}}\nabla_{\mathbf{r}}\right]\exp\left[-\beta U_{\mathrm{dip}}(\mathbf{r})\right] = (1 - \beta D_{\mathbf{r}}\gamma)\nabla_{\mathbf{r}}U_{\mathrm{dip}}(\mathbf{r})\exp\left[-\beta U_{\mathrm{dip}}(\mathbf{r})\right]. \quad (2.69)$$

Therefore, the above statement is valid if and only if $\beta D_{\mathbf{r}}\gamma = (k_B T)^{-1}D_{\mathbf{p}}\gamma^{-1} = 1$. Such a celebrated identity reflects one of the many facets of the *fluctuation-dissipation* theorem, providing a link between the amplitude of stochastic and damping forces [119, 120]. In addition, the Smoluchowski equation can also be obtained directly from Eq. (2.64) with the appropriate limit $t \gg \gamma^{-1}$, meaning that the late time behaviour is nevertheless captured by Eq. (2.67) [121]. Spatial optomechanical instabilities in driven, dilute, clouds of cold atoms can be predicted by coupling dynamical equations for modulated densities, derived with a Fokker-Planck approach, to those of the optical field. To characterize instead the features of the ordered steady states of such systems out of equilibrium, a review of the essential methods in pattern formation and dynamical systems theory is provided in the following subsection.

2.3.2 Pattern formation outside equilibrium

The formation of spatio-temporal ordered structures or *patterns*, resulting from nonlinear dynamics, is a major feature of physical systems driven far from thermodynamic equilibrium [2]. A classical example of stationary pattern-forming behaviour occurs in so-called *reaction-diffusion systems*, predicted in the seminal work by Turing in 1952 [122]. Motivated originally by the developments in fluid dynamics, the main approaches were successfully extended to the study of chemical/biological systems [123], liquid crystals [124], ecosystems [125], active matter [126] etc. Adopting the non-equilibrium thermodynamics picture, steady states characterized by an *order parameter*, and induced from external driving, can be maintained for arbitrarily long times if the system dissipates energy into the environment [127]. The process resulting in the growth of spatial modulations is known as *modulation* instability (MI) and is briefly discussed below.

Modulation instabilities

Due to the absence of equilibrium and relative extremum principles, detailed nonlinear *microscopic models* are required to describe the evolution to steady states of such systems. As an illustrating example, the typical two component reaction-diffusion picture in chemical kinetics deals with two densities $u(\mathbf{r}, t)$ and $v(\mathbf{r}, t)$, whose dynamical evolution read as follows [128]:

$$\partial_t \begin{bmatrix} u(\mathbf{r}, t) \\ v(\mathbf{r}, t) \end{bmatrix} = \begin{bmatrix} D_u\nabla_{\mathbf{r}}^2 & \cdot \\ \cdot & D_v\nabla_{\mathbf{r}}^2 \end{bmatrix} \cdot \begin{bmatrix} u(\mathbf{r}, t) \\ v(\mathbf{r}, t) \end{bmatrix} + \begin{bmatrix} \mathcal{F}(u, v) \\ \mathcal{G}(u, v) \end{bmatrix}, \quad (2.70)$$

where D_u and D_v are two spatial diffusion constants and $\mathcal{F}$ and $\mathcal{G}$ are nonlinear functionals containing the details of the system, e.g., of the chemical reaction. In the case of stationary
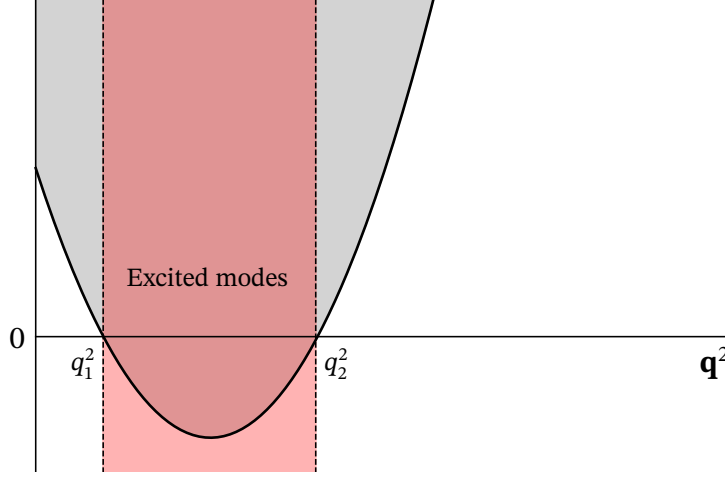
Fig. 2.5. Typical Fourier space MI scenario for Turing patterns in systems governed by Eq. (2.70). The quadratic function, derived from $P(0, \mathbf{q}^2) = 0$, (solid black line) represents the threshold condition in Eq. (2.74), delimiting the instability domain above (grey area). An unstable region is selected if and only if $P(0, \mathbf{q}^2) \leq 0$ (pink area). The figure is adapted from Ref. [128].

(non-oscillatory) MIs, one deals with a *linearized* version of Eq. (2.70), for the vector $\tilde{\mathbf{r}} = (\tilde{u}, \tilde{v})^{\mathrm{T}}$ representing perturbations around homogeneous steady states u_0 and v_0, namely:

$$\partial_t \tilde{\mathbf{r}} = \left[\hat{\mathcal{D}}_{u,v} + \hat{\mathcal{J}}(u_0, v_0) \right] \tilde{\mathbf{r}}, \tag{2.71}$$

where $\hat{\mathcal{D}}_{u,v}$ is the diffusion operator above and $\hat{\mathcal{J}}(u_0, v_0)$ is the Jacobian matrix evaluated at the point (u_0, v_0). For Turing-like instabilities, the Jacobian belongs to the following class[27]:

$$\hat{\mathcal{J}}(u_0, v_0) = \begin{bmatrix} a & -b \\ c & -d \end{bmatrix}, \tag{2.72}$$

where $a, b, c, d \geq 0$. MI regimes in Eq. (2.71) are identified by parametrizing the perturbations in Fourier space, i.e., $\tilde{u} = \alpha \exp(i\mathbf{q} \cdot \mathbf{r} + \gamma t) + \text{c.c}$ and $\tilde{v} = \beta \exp(i\mathbf{q} \cdot \mathbf{r} + \gamma t) + \text{c.c}$, where $\alpha, \beta \in \mathbb{C}$. Indeed, from Eq. (2.71) and (2.72), the *dispersion relation* is simply obtained as a root of the following characteristic polynomial:

$$P(\gamma, \mathbf{q}^2) = \gamma^2 + \left[(D_u + D_v)\mathbf{q}^2 - \mathrm{Tr}\, \hat{\mathcal{J}}(u_0, v_0) \right] \gamma + (D_u \mathbf{q}^2 - a)(D_v \mathbf{q}^2 + d) + bc, \tag{2.73}$$

and the Turing instability condition, namely:

$$P(0, \mathbf{q}^2) = (D_u \mathbf{q}^2 - a)(D_v \mathbf{q}^2 + d) + bc \leq 0. \tag{2.74}$$

If the condition in Eq. (2.74) is satisfied, a whole range of modes, identified by $q_1^2 \leq \mathbf{q}^2 \leq q_2^2$, are excited in the system, i.e., their growth rate is positive. This is graphically represented in

---

[27]This justifies the term *activator* for $u(\mathbf{r}, t)$ and *inhibitor* for $v(\mathbf{r}, t)$ in chemical kinetics.

Fig. 2.5, where the excited band is identified by the pink region, and the *critical* wavevector by the minimum threshold as follows:

$$q_{\text{cr}}^2 = \frac{1}{2}\left(\frac{a}{D_u} - \frac{d}{D_v}\right), \tag{2.75}$$

where the necessary condition for a Turing instability reads[28]: $a/D_u > d/D_v$. Despite the differences in the details of the model, the class of optomechanical instabilities analyzed in this thesis falls in the same class of Turing-like (stationary) instabilities, as discussed in Ref. [51]. Other classes of spatial instabilities are usually given in terms of the characteristics of the dispersion relation at threshold [2]. In what follows, instead, the general role of nonlinearities in a dynamical system is addressed. As described by the amplitude equation formalism, the presence of such terms is needed in order to counterbalance the exponential growth of the unstable modes in the system.

Amplitude Equations

Pattern forming dynamics is typically described by partial differential equations capturing the essential physical behaviour in a variety of physical scenarios. However, despite those differences, several phenomena close to the instability threshold can be addressed by means of methods falling into a small set of universality classes [129, 130]. For example, restricting ourselves to the case of stationary instabilities in 2-d for a generic real field $u(\mathbf{r}, t)$, where $\mathbf{r} = (x, y)$, one of the paradigmatic models is the so-called *Ginzburg-Landau equation*[29], namely [132]:

$$\partial_t u(\mathbf{r}, t) = (b + ic)\nabla_{\mathbf{r}}^2 u(\mathbf{r}, t) + f(|u(\mathbf{r}, t)|^2) u(\mathbf{r}, t), \tag{2.76}$$

where $b, c \in \mathbb{R}$ and f is a generic complex function of the modulus square $|u(\mathbf{r}, t)|^2$. Excited stable modes of Eq. (2.76), in the vicinity of the MI threshold, are assumed to have the following stripe form (**S**) along the y direction:

$$u(\mathbf{r}, t) = u_0 A(\mathbf{r}, t) \exp(iq_{\text{cr}}x + \gamma t) + \text{c.c.} + O(\mu), \tag{2.77}$$

where μ is a control parameter that provides a measure of the distance from the MI threshold. Assuming μ slightly above the MI threshold, i.e. $0 < \mu \ll 1$, one shows that the spatial envelope function $A(\mathbf{r}, t)$ satisfies a dynamical equation in the following form [2]:

$$\tau_o \partial_t A(\mathbf{r}, t) = \mu A(\mathbf{r}, t) + \xi_0^2 \left[\partial_x - \frac{i}{2q_{\text{cr}}}\partial_y^2\right]^2 A(\mathbf{r}, t) - g_0 |A(\mathbf{r}, t)|^2 A(\mathbf{r}, t), \tag{2.78}$$

where τ_0, ξ_0, g_0 are constants defining temporal, spatial and amplitude scales. Equations in the form (2.78) are known as *amplitude equations* and represent a suitable method to study

---

[28]This is not sufficient since one also needs the minimum threshold to be negative.

[29]The name Ginzburg-Landau equation arises from the strong analogy between the family of pattern forming models and the mean field theory of superconductivity [131].

the stability of spatial modulations in 2-d, such as the stripes in Eq. (2.77) [133]. Moreover, Eq. (2.78) reproduces the expected growth rate in the vicinity of the MI threshold, namely [30]:

$$\gamma(\mathbf{q}) = \frac{1}{\tau_0} \left[\mu - \xi_0^2 (\mathbf{q} - q_{cr}\mathbf{e}_x)^2 \right] \approx \frac{1}{\tau_0} \left[\mu - \xi_0^2 \left(k_x + \frac{1}{2q_{cr}} k_y^2 \right)^2 \right], \qquad (2.79)$$

where the vector $\mathbf{k} = \mathbf{q} - q_{cr}\mathbf{e}_x$ is introduced. In principle, more complex situations can be represented as superposition of critical stripe states at different orientations ($|\mathbf{q}_i| = q_{cr}$), such as:

$$u(\mathbf{r}, t) = u_0 \sum_{i=1}^{n} [A_i(\mathbf{r}, t) \exp(i\mathbf{q}_i \cdot \mathbf{r}) + \text{c.c.}] + O(\mu). \qquad (2.80)$$

However, leaving the spatial variation of the amplitudes aside, i.e. $A_i(\mathbf{r}, t) = A_i$, and adopting the rescaling rule $\tilde{A} = \sqrt{g_0}A$, $\tilde{q}_{cr} = \xi_0 q_{cr}$, $\tilde{t} = \tau^{-1}t$, the competition of all modes in Eq. (2.80) can be described in terms of coupled ordinary differential equations in the following form [129]:

$$\partial_{\tilde{t}} \tilde{A}_i = \mu \tilde{A}_i - \sum_{j=1}^{n} g_{ij} |\tilde{A}_j|^2 \tilde{A}_i, \quad i = 1, \dots, n, \qquad (2.81)$$

where the constants $g_{ij}(\theta_{ij})$ are functions of the relative angles $\cos(\theta_{ij}) = \tilde{\mathbf{q}}_i \cdot \tilde{\mathbf{q}}_j$. Of particular interest for this work is the competition between stripes (**S**) and hexagons (**H**) patterns, where one has instead three modes only, satisfying the condition [31] $\tilde{\mathbf{q}}_1 + \tilde{\mathbf{q}}_2 + \tilde{\mathbf{q}}_3 = 0$. In this case, an additional quadratic nonlinear term comes into play [32] and the three coupled amplitude equations read as follows [134]:

$$\partial_{\tilde{t}} \tilde{A}_1 = \mu \tilde{A}_1 + \lambda \tilde{A}_2^* \tilde{A}_3^* - \gamma_1 (|\tilde{A}_2|^2 + |\tilde{A}_3|^2) \tilde{A}_1 - \gamma_2 |\tilde{A}_1|^2 \tilde{A}_1, \qquad (2.82)$$

$$\partial_{\tilde{t}} \tilde{A}_2 = \mu \tilde{A}_2 + \lambda \tilde{A}_3^* \tilde{A}_1^* - \gamma_1 (|\tilde{A}_3|^2 + |\tilde{A}_1|^2) \tilde{A}_2 - \gamma_2 |\tilde{A}_2|^2 \tilde{A}_2, \qquad (2.83)$$

$$\partial_{\tilde{t}} \tilde{A}_3 = \mu \tilde{A}_3 + \lambda \tilde{A}_1^* \tilde{A}_2^* - \gamma_1 (|\tilde{A}_1|^2 + |\tilde{A}_2|^2) \tilde{A}_3 - \gamma_2 |\tilde{A}_3|^2 \tilde{A}_3. \qquad (2.84)$$

Eqs. (2.82), (2.83) and (2.84) are known as *real Ginzburg-Landau amplitude equations* (rGLE) and generally hold for systems that do not posses inversion symmetry ($u \to -u$). For small, nonzero values of the quadratic coefficient λ, the pattern competition described by the system above admits **H**-solutions ($\tilde{A}_1 = \tilde{A}_2 = \tilde{A}_3 = A_{\mathbf{H}}$) for values of the control parameter μ in the following range:

$$\mu_{SN} = -\frac{\lambda^2}{4(\gamma_2 + 2\gamma_1)}, \quad \mu_{\mathbf{H}}^< = \frac{\lambda^2 (2\gamma_2 + \gamma_1)}{(\gamma_1 - \gamma_2)^2}, \qquad (2.85)$$

where $\mu_{SN} < 0$ is the subcritical point in which the **H**-solution originates in a *saddle-node*

---

[30] As in the case of the Turing instability in Fig. 2.5.
[31] Three wavevectors at angles of $\theta_{12} = \theta_{23} = \theta_{31} = 2\pi/3$.
[32] This is also denoted as *non-Boussinesq effect* in hydrodynamic systems.
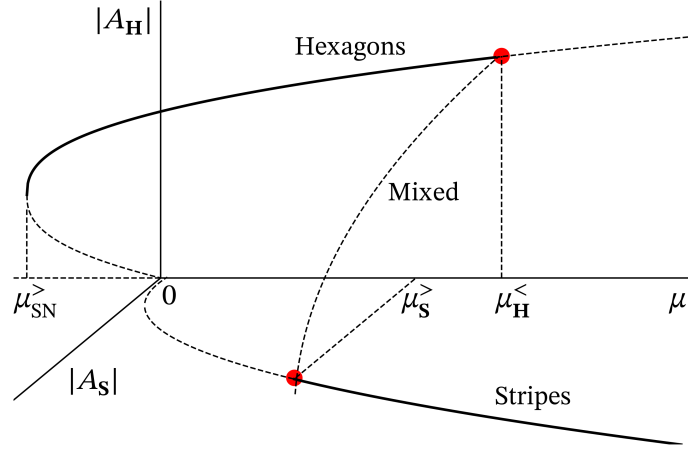
Fig. 2.6. Bifurcation scheme for systems described by the rGLE in Eqs. (2.82), (2.83) and (2.84). Two branches of hexagonal and stripe solutions originate in the parameter space $(A_{\mathbf{H}}, A_{\mathbf{S}}, \mu)$. $\mathbf{H}$-solutions arise sub-critically at $\mu_{\mathrm{SN}}^{>}$ and continue up to $\mu_{\mathbf{H}}^{<}$ where they lose stability against $\mathbf{S}$-solutions. Within the intermediate region $\mu_{\mathbf{S}}^{>} < \mu < \mu_{\mathbf{H}}^{<}$ one can observe unstable mixed states. Figure adapted from Ref. [134].

bifurcation and it is stable up to the critical value $\mu_{\mathbf{H}}^{<}$. In addition, $\mathbf{S}$-solutions ($\tilde{A}_1 = A_{\mathbf{S}}$, $\tilde{A}_2 = \tilde{A}_3 = 0$) also exist and are stable above the following critical value of linear growth μ:

$$\mu_{\mathbf{S}}^{>} = \frac{\lambda^2 \gamma_2}{(\gamma_1 - \gamma_2)^2}. \tag{2.86}$$

Eq. (2.85) and (2.86) give rise to the universal bifurcation scheme represented in Fig. 2.6, including the stability limits of the two solution branches, and a region of competition of $\mathbf{H}-\mathbf{S}$ solutions. In particular, this last situation can lead to unstable $\mathbf{H} - \mathbf{S}$ fronts[33] where a final state is selected by means of free-energy minimization arguments [128]. This is discussed in detail in Ch. 4, where the possibility of structural phase transitions is addressed in the light-atom optomechanical model. Finally, in dependence on the sign of the quadratic coefficient λ, one obtains 2 different $\mathbf{H}$-solutions, denoted as $\mathbf{H}^{\pm}$. Indeed, writing the hexagonal state as follows:

$$u(\mathbf{r}, t) = u_0 \sum_{i=1}^{3} [A_i \exp{(i\Phi_i)} + \text{c.c.}] + O(\mu), \tag{2.87}$$

together with generic phases $\Phi_i = \tilde{\mathbf{q}}_i \cdot \mathbf{r} + \nu_i$, one shows that the case of $\Phi_1 + \Phi_2 + \Phi_3 = \pi$ is the stable $\mathbf{H}$-solution[34] of the rGLE for $\lambda < 0$. At the point $\lambda = 0$, the system described by rGLE becomes inversion symmetric, admitting $\mathbf{S}$-states as the only stable solutions. Examples of $\mathbf{H}^{\pm}$ and $\mathbf{S}$ patterns are shown in Fig. 2.7, where one notes the lack of inversion symmetry

---

[33]Namely, the unstable mixed branch in Fig. 2.6.

[34]This kind of solutions are called honeycombs (negative hexagons).
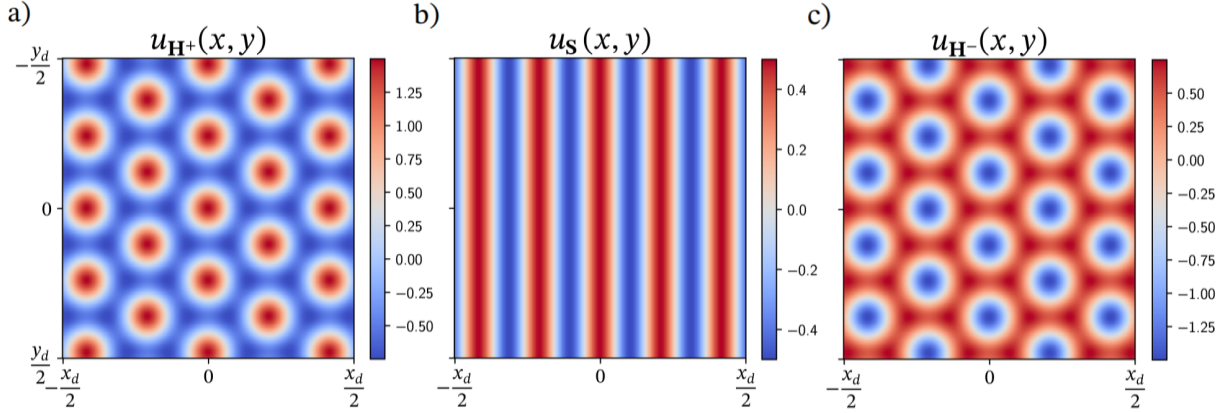
Fig. 2.7. $\mathbf{H}^{\pm}$ and $\mathbf{S}$ states as solutions of the rGLE equations. a) - c) Hexagonal and honeycomb solutions $\mathbf{H}^{\pm}$ obtained with $\tilde{A}_1 = \tilde{A}_2 = \tilde{A}_3 = 1/2$, $\tilde{\mathbf{q}}_1 = (1,0), \nu_1 = 0, \pi$, $\tilde{\mathbf{q}}_2 = (-1/2, \sqrt{3}/2), \nu_2 = 0$, $\tilde{\mathbf{q}}_3 = (-1/2, -\sqrt{3}/2), \nu_3 = 0$. b) Stripe solutions $\mathbf{S}$ obtained with $\tilde{A}_1 = 1/2, \tilde{A}_2 = \tilde{A}_3 = 0$, $\tilde{\mathbf{q}} = (1,0), \nu = 0$.

of hexagonal states[35] $\mathbf{H}^{\pm}$. So far, only spatial self-organization arising from modulation instabilities in driven-dissipative systems was considered. A deeply connected research theme concerns the study of localized structures known as *dissipative solitons*.

Dissipative solitons

Extensive reviews on the properties of dissipative solitons (DS) and their applications in the context of nonlinear optical devices can be found in Refs. [135–137]. The concept of DS was introduced as an attempt to generalize that of solitary wave-like solutions (solitons) in non-integrable systems, i.e., in the presence of gain and losses [135]. While for standard soliton theory the stationarity of a localized solution is simply guaranteed by the competition between dispersion (diffraction) and a nonlinearity, the balance between gain and losses is also essential in the dissipative case [127]. Such difference between the two soliton concepts is represented pictorially in Fig. 2.8. Note that, despite the common view of DS as fixed points of a dynamical system, one can also have non-stationary pulsating solitons (limit cycles).

One of the main features that are well captured by transverse nonlinear optical models is the bi-stability between two so-called *on* and *off* states, namely, that optical DS can be excited and switched off by external addressing beams. Such characteristic is explained by the sub-critical behaviour of the hexagonal branch already discussed before. Therefore, in such case, a patterned state can be excited locally in the form of single or multiple clustered peaks[36] [136].

A useful approximation in order to describe the properties and dynamics of DS is to consider an asymptotic expansion and to model the profile of a DS as superposition of generalized Bessel functions [139]. This enables to study the oscillatory behaviour of the DS tails

---

[35]Whereas the two states are related by the inversion operation.
[36]See Ref. [138] for an introduction to the phenomenon of *homoclinic snaking* in the Swift-Hohenberg model.
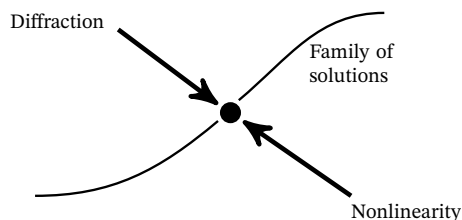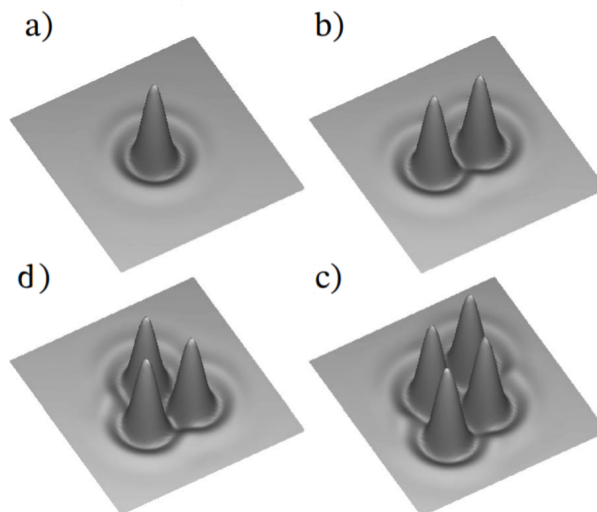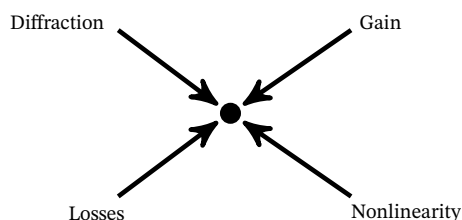
Fig. 2.8. Different mechanism for self-localization in conservative and dissipative systems. (Left) In the conservative/Hamiltonian case, soliton-like states typically arise as a few-parameter families of solutions, so that local convergence of the localized states to such families is guaranteed by the balance of diffraction (dispersion) and the system nonlinearity. The double balance mechanism in the dissipative case involves also gain and losses and, thus, DS solutions are fixed points in the system phase space (figure adapted from Ref. [135]). a) - d) Spatial profiles of single and multipeaked optical DS in a cavity model with saturable absorber (figure adapted from Ref. [141]).

and their dependence on the model parameters, to model DS interactions and to single out translational neutral or *Goldstone* modes, whose excitation induces stable motion of the localized structure in the transverse plane, as shown in Ref. [140]. The following subsection provides the reader with a brief introduction to the experimental realization of optomechanical instabilities, by means of two common transverse nonlinear optical schemes, namely, a longitudinally pumped ring cavity and the single-feedback-mirror configurations.

2.3.3 Experimental realizations of transverse optomechanical instabilities

Transverse optomechanical self-structuring of light and atomic densities has been achieved experimentally by means of a single-feedback-mirror (SFM) scheme[37] (see Fig. 4.1) [53]. The theoretical principles of such a scheme, based on the Talbot effect, are introduced in detail in Ch. 4, specifically for the cold atom optomechanical nonlinearity. The central new ingredient enabled by laser cooling the cloud is that the dipole forces induced by the optical field modulations highly affect the atom center-of-mass dynamics and provide the corresponding back-action on the optical field behaviour. This strongly coupled picture gives rise to an additional

---

[37]Where the input pump is far-detuned from any internal atomic transition.
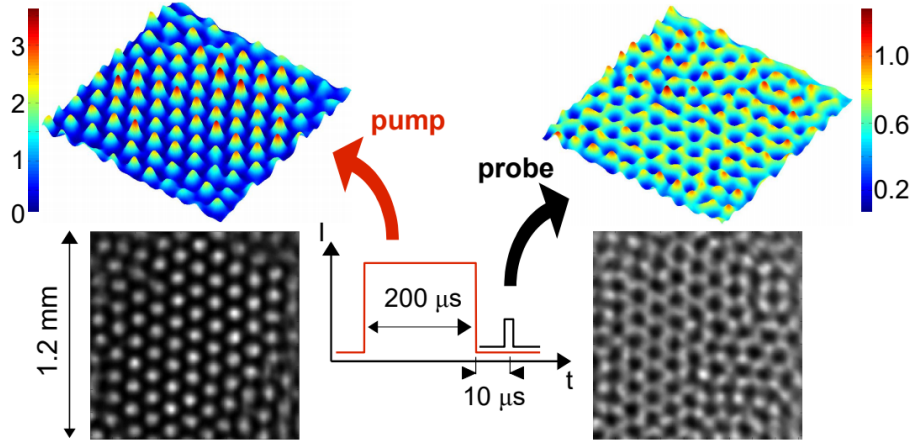
Fig. 2.9. Experimental observation of light-atom self-organization in a single-feedback-mirror scheme with a blue detuned pump. Transverse intensity profiles in arbitrary units of the transmitted near field (left - pump), and of the probe field (right - probe), showing an anticorrelated hexagonal modulation in the transmitted beam ($\mathbf{H}^+$) and the atomic density ($\mathbf{H}^-$). Both images were acquired by a CCD camera, according to the scheme discussed from Ref. [53].

self-focusing nonlinearity, analogous to the *artificial-Kerr* medium case, originally proposed by Ashkin for a water suspension of dielectric microparticles [142, 143] and the CARL instability of cold atoms in a ring cavity. Denoting with $n(\mathbf{r})$ the transversely inhomogeneous atomic density, the spatially dependent nonlinear index of refraction of the atomic cloud, including both electronic and optomechanical nonlinear effects, reads [53]:

$$\eta(\mathbf{r}, s) = 1 - \frac{3\lambda^3}{4\pi^2} \frac{\Delta}{2(1 + \Delta^2)} \frac{n(\mathbf{r}, s)}{1 + s(\mathbf{r})}, \tag{2.88}$$

where the atomic saturation depends on the optical intensity itself. The coupled light-density structuring was demonstrated for blue atomic detuning[38] ($\Delta > 0$), as visible from the images of the transmitted beam in Fig. 2.9, carrying the hexagonal structure of the pump field, together with a red detuned probe pulse, which shows an anticorrelated, honeycomb-like, structuring. Important insight into such optomechanical phenomenon was shown by considering the decay and switching-on dynamics, where the latter is relevant when measured in dependence of the input pump. In particular, the observed decay time of the patterns is not consistent with the typical timescales of the electronic nonlinearity, i.e., $\tau \approx \Gamma^{-1}(25 \text{ ns})$. Instead, such a decay is much slower ($\tau \approx 80 \ \mu$s) and consistent with natural relaxation timescales measured by means of simulating atomic diffusive transport [52].

Even more relevant is the switching-on dynamics which shows that, for high enough values of the input pump (400 mW cm^{-2}) one has a net separation in the structure formation

---

[38]$\Delta \approx 15$ together with optical density at resonance $b_0 \approx 150$ in the experiment.

timescales for the transmitted and the probe beams, meaning that the much faster electronic processes are responsible for driving the instability in that case. On the other hand, the optical and density structures appear with the same slower timescales below a certain threshold (200 mW cm^{-2}), meaning that the only relevant nonlinear processes there are the optomechanical ones. In the next chapter, one of the main questions of interest for this thesis is addressed, namely, the effect of a structured pump field carrying OAM on the optomechanical pattern-forming dynamics. For this investigation, the proposed configuration is that of a ring-cavity (see Fig. 3.1). However, this difference is not crucial and much of the same physical phenomena also apply to the SFM configuration. Details on the current status of the experimental cavity setup at Strathclyde are discussed in Ref. [144].

Chapter 3

Atom optomechanics and structured light I: ring cavity setup

In this chapter, the first original contribution regarding optomechanical self-structuring involving structured light is discussed. In particular, the present configuration for the cold-atom optomechanical instability involves a cold atomic ensemble within a ring optical resonator pumped by a spatially structured input beam. For transverse optical pattern formation, any spatial dependence of the input phase profile is known to induce drifting dynamics of the self-organized structures, as shown experimentally for patterns in a photorefractive system [69, 145], and localized states [146]. For coupled light-atom systems, such an angular drift induced by the OAM phase profile is shown to generate controllable atomic currents in ring lattices, introducing a novel OAM transfer mechanism of potential interest in atomtronic devices. Part of the present research material is published in Ref. [147]

3.1   Transverse cavity nonlinear optics with two-level atoms

In this section, a formal derivation of the equations describing the transverse dynamics of the electric field inside an optical resonator is provided. Such model equations are essential to describe the main effect of interest for this thesis, namely, spontaneous pattern formation transversely to the optical axis. Detailed literature reviews can be found in Refs. [9, 148].

As introduced in Sec. 2.3.2, stationary modulation instabilities within the Turing class are generally obtained by means of a combined effect of a nonlinearity and spatial diffusion, which provide coupling between points of a spatial domain. In optical systems, such coupling is provided by diffraction in the paraxial approximation, as in the case of Eq. (2.42), described by the transverse Laplacian operator [4]. Commonly used nonlinear optical media are able to give rise to several nonlinear effects such as *second harmonic generation* or *four wave mixing*, depending on the order on which the polarization depends on the electric field [149]. In our model, part of the nonlinear coupling is realized by considering the population dynamics of an ensemble of two-level atoms coupled to the e.m. field of an *optical resonator*. This is analogous to the saturation effect describing gain in laser systems [95]. Indeed, according to the

optical Bloch equations introduced previously (2.5), the atomic polarization density is simply obtained as the following expectation value:

$$\mathbf{P}(\mathbf{r}, t) = N_0 \langle \hat{\mathbf{d}} \rangle = N_0 \text{Tr}[\hat{\mathbf{d}} \rho(t)] = 2N_0 d \, \text{Re}[\rho_{12}(t)] \, \mathbf{e}_r, \qquad (3.1)$$

where N_0 is the homogeneous density of the cloud and, for the sake of simplicity, the atomic transition is assumed to have the same polarization as the incoming field. Assuming also a slow time dependence of the field envelope $\mathcal{E}(\mathbf{r}, t)$ and the presence of a cloud of atoms, the paraxial wave equation describing transverse effects in the field envelope $\mathcal{E}(\mathbf{r}, t)$ now reads:

$$\frac{1}{2ik_0} \nabla_\perp^2 \mathcal{E}(\mathbf{r}, t) + \partial_z \mathcal{E}(\mathbf{r}, t) + \frac{1}{c} \partial_t \mathcal{E}(\mathbf{r}, t) = i \frac{\mu_0 \omega_0^2 N_0}{2k_0} \mathcal{P}(\mathbf{r}, t), \qquad (3.2)$$

where one can represent as well the atomic medium polarization as a propagating vector field[1] $\mathbf{P}(\mathbf{r}, t) = N_0 \mathcal{P}(\mathbf{r}, t) \exp\left[-i(\omega_0 t - k_0 z)\right] \mathbf{e}_r + \text{c.c.}$ In terms of the polarization envelope $\mathcal{P}(\mathbf{r}, t)$ and the population inversion $\mathcal{D}(\mathbf{r}, t) = \rho_{22} - \rho_{11}$, the optical Bloch equations can be rescaled conveniently as follows:

$$\partial_t \mathcal{P}(\mathbf{r}, t) = -\frac{\Gamma}{2} (1 + i\Delta) \mathcal{P}(\mathbf{r}, t) + \frac{d^2}{\hbar} \mathcal{E}(\mathbf{r}, t) \mathcal{D}(\mathbf{r}, t), \qquad (3.3)$$

$$\partial_t \mathcal{D}(\mathbf{r}, t) = -\Gamma \left[\mathcal{D}(\mathbf{r}, t) - 1\right] - \frac{2}{\hbar} \left[\mathcal{P}(\mathbf{r}, t) \mathcal{E}^*(\mathbf{r}, t) + \mathcal{P}^*(\mathbf{r}, t) \mathcal{E}(\mathbf{r}, t)\right]. \qquad (3.4)$$

The system made by Eq. (3.2) coupled with Eqs. (3.3) and (3.4) is known as *Arecchi-Bonifacio*[2] equations or, alternatively, the *Maxwell-Bloch equations* and, together with the inclusion of transverse effects, represent a paradigmatic model for optical pattern formation where modulation instabilities are induced by the two-level nonlinearity [8]. Let us briefly recall, following Ref. [152], that the approximations used to describe the field inside a so called *ring* optical resonator in the rest of this section.

Effective field-only description

Eq. (3.2), seen as a single partial differential equation for $\mathcal{E}(\mathbf{r}, t)$, becomes closed if one eliminates the polarization $\mathcal{P}(\mathbf{r}, t)$ by solving the optical Bloch equations (3.3) and (3.4) at steady state. The steady state expression of the fast atomic variables, i.e., the excited state population $\tilde{\rho}_{22}$ and atomic coherence $\tilde{\rho}_{12}$ was already found in Eq. (2.10) and (2.11). Thus, the corresponding polarization and population difference here read:

$$\tilde{\mathcal{P}}(\mathbf{r}, t) = \frac{2id^2(1 - i\Delta)}{\hbar\Gamma(1 + \Delta^2)} \left(\frac{1}{1 + s}\right) \tilde{\mathcal{E}}(\mathbf{r}, t), \qquad (3.5)$$

$$\tilde{\mathcal{D}}(\mathbf{r}, t) = \frac{1}{1 + s}, \qquad (3.6)$$

---

[1]The slowly varying envelope approximation is also applied to the polarization envelope $\mathcal{P}(\mathbf{r}, t)$.
[2]Introduced for the first time in 1965 in Ref. [150, 151].
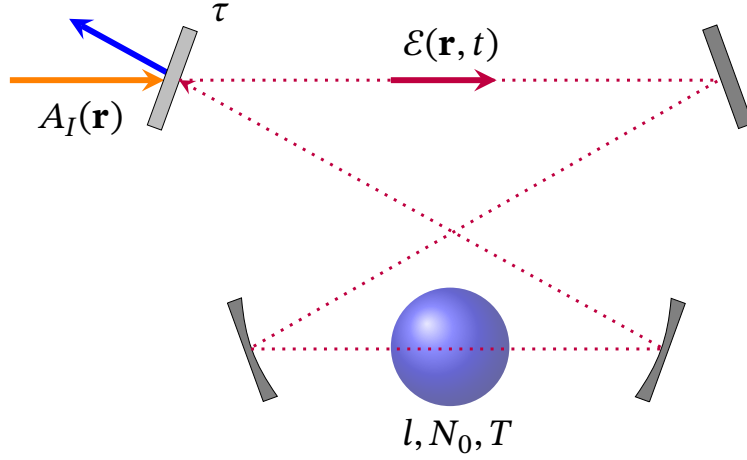
Fig. 3.1. Schematic representation of a "bow-tie" cold-atom cavity setup. A spatially structured incident field (pump) of amplitude $A_I(\mathbf{r}_\perp)$ drives a single mode ring cavity of effective length L. In the present configuration, only one mirror is assumed to have transmittivity τ. A cloud of Doppler-cooled atoms of thickness l and density N_0 interacts with the cavity field, represented by its envelope function $\mathcal{E}(\mathbf{r}, t)$.

where s represents the saturation parameter defined in Eq. (2.12). By substituting the above back in Eq. (3.15), one obtains[3]:

$$\frac{1}{2ik_0}\nabla_\perp^2 \mathcal{E}(\mathbf{r},t) + \partial_z \mathcal{E}(\mathbf{r},t) + \frac{1}{c}\partial_t \mathcal{E}(\mathbf{r},t) = -\alpha(1 - i\Delta)\frac{\mathcal{E}(\mathbf{r},t)}{1+s}, \quad \alpha = \frac{\mu_0 c^2 k_0 d^2 N_0}{\hbar\Gamma(1+\Delta^2)}. \quad (3.7)$$

The typical situation considered here is that of a *ring resonator*, characterized by the closed path sketched in Fig. 3.1. Defining with $\mathbf{r}_\perp \equiv (x,y)$ the transverse coordinate and identifying with $z = 0$ and $z = L$ the extremes of the equivalent optical path in the cavity, a first step to the complete equation for $\mathcal{E}(\mathbf{r},t)$ is obtained by considering the following boundary condition[4]:

$$\mathcal{E}(\mathbf{r}_\perp, 0, t) = \sqrt{\tau}A_I(\mathbf{r}_\perp) + \sqrt{R}e^{-i\delta_0}\mathcal{E}(\mathbf{r}_\perp, L, t) = \sqrt{\tau}A_I(\mathbf{r}_\perp) + \sqrt{R}e^{-i\delta_0}e^{i(L-l)\nabla_\perp^2/2k_0}\mathcal{E}(\mathbf{r}_\perp, l, t),$$
$$(3.8)$$

where $A_I(\mathbf{r}_\perp)$ is the spatially dependent input amplitude, $R = 1 - \tau$ is the reflectivity of the first mirror, i.e., at $z = 0$, and $\delta_0 = (\omega_{\text{cav}} - \omega_0)L/c$ is the cavity-pump detuning, with ω_{cav} being the frequency of the closest cavity resonance with respect to ω_0. The differential operator $\exp\left[i(L-l)\nabla_\perp^2/2k_0\right]$ represents the total amount of diffraction within the cavity path. It is now helpful to consider the following replacement rule for the field envelope $\mathcal{E}(\mathbf{r},t)$:

---

[3]The quantity $\alpha_0 = \mu_0 c^2 k_0 d^2 N_0/\hbar\Gamma$ represents the absorption coefficient at resonance $\Delta = 0$.
[4]In Ref. [152], the authors assumed two imperfect mirrors whereas here only one is assumed.

$$\tilde{\mathcal{E}}(\mathbf{r}, t) = \exp\left[\frac{z}{L}\left(\ln\sqrt{R} - i\delta_0 + i\frac{(L-l)}{2k_0}\nabla_\perp^2\right)\right]\mathcal{E}(\mathbf{r}, t) + \frac{\sqrt{\tau}z}{L}A_I(\mathbf{r}_\perp), \tag{3.9}$$

so that the boundary condition in Eq. (3.8) simply reads $\tilde{\mathcal{E}}(\mathbf{r}_\perp, 0, t) = \tilde{\mathcal{E}}(\mathbf{r}_\perp, L, t)$. Defining the exponential operator $\hat{\Xi} = \exp(\hat{D}z/L) = \exp\left[\left(\ln\sqrt{R} - i\delta_0 + i(L-l)\nabla_\perp^2/2k_0\right)z/L\right]$, the equation for the field $\tilde{\mathcal{E}}(\mathbf{r}, t)$ now reads:

$$\partial_z\tilde{\mathcal{E}}(\mathbf{r}, t) = \frac{\hat{D}}{L}\hat{\Xi}\mathcal{E}(\mathbf{r}, t) + \hat{\Xi}\partial_z\mathcal{E}(\mathbf{r}, t) + \frac{\sqrt{\tau}}{L}A_I(\mathbf{r}_\perp) = \tag{3.10}$$

$$= \frac{\hat{D}}{L}\hat{\Xi}\mathcal{E}(\mathbf{r}, t) + \hat{\Xi}\left[-\alpha(1-i\Delta)\frac{\mathcal{E}(\mathbf{r}, t)}{1+s} - \frac{1}{2ik_0}\nabla_\perp^2\mathcal{E}(\mathbf{r}, t) - \frac{1}{c}\partial_t\mathcal{E}(\mathbf{r}, t)\right] + \frac{\sqrt{\tau}}{L}A_I(\mathbf{r}_\perp) = \tag{3.11}$$

$$= \frac{1}{L}\left(-\frac{\tau}{2} - i\delta_0 + i\frac{(L-l)}{2k_0}\nabla_\perp^2\right)\left(\tilde{\mathcal{E}}(\mathbf{r}, t) - \frac{\sqrt{\tau}z}{L}A_I(\mathbf{r}_\perp)\right) - \frac{\alpha L(1-i\Delta)}{1+s}\left(\frac{\tilde{\mathcal{E}}(\mathbf{r}, t)}{L} - \frac{\sqrt{\tau}z}{L^2}A_I(\mathbf{r}_\perp)\right) +$$

$$- \frac{1}{c}\partial_t\tilde{\mathcal{E}}(\mathbf{r}, t) - \frac{L}{2ik_0}\nabla_\perp^2\left(\frac{\tilde{\mathcal{E}}(\mathbf{r}, t)}{L} - \frac{\sqrt{\tau}z}{L^2}A_I(\mathbf{r}_\perp)\right). \tag{3.12}$$

Let us consider a simplified version of the above by neglecting all those terms displaying an explicit dependence on the longitudinal coordinate[5] z. This limit is commonly expressed by assuming $\alpha L, \tau, \delta_0, L/2k_0 \approx O(\epsilon)$, with $\epsilon \ll 1$ and $l \approx L$, so that Eq. (3.12) now reads:

$$\partial_t\tilde{\mathcal{E}}(\mathbf{r}, t) + c\partial_z\tilde{\mathcal{E}}(\mathbf{r}, t) =$$
$$\kappa\left[-\left(1 + i\frac{\delta_0}{\tau}\right)\tilde{\mathcal{E}}(\mathbf{r}, t) + A_I(\mathbf{r}_\perp) - \frac{\alpha L}{\tau}\frac{1-i\Delta}{1+s}\tilde{\mathcal{E}}(\mathbf{r}, t)\right] + \frac{ic}{2k_0}\nabla_\perp^2\tilde{\mathcal{E}}(\mathbf{r}, t), \tag{3.13}$$

where the quantity $\kappa = c\tau/L$ represents the cavity decay rate. The last commonly used approximation corresponds to considering cavities where, in the modal expansion, the relevant light-atom coupling occurs only with the fundamental e.m. mode, denoted with $\mathcal{E}_0(\mathbf{r}, t)$[6]. For such a *single-longitudinal-mode* approximation, the z derivative term in Eq. (3.13) drops out and one is left with the final result:

$$\partial_t\tilde{\mathcal{E}}_0(\mathbf{r}, t) = \kappa\left[-(1 + i\theta)\tilde{\mathcal{E}}_0(\mathbf{r}, t) + A_I(\mathbf{r}_\perp) - \frac{C(1-i\Delta)}{1+s}\tilde{\mathcal{E}}_0(\mathbf{r}, t) + ia\nabla_\perp^2\tilde{\mathcal{E}}_0(\mathbf{r}, t)\right], \tag{3.14}$$

where $\theta = \delta_0/\tau$, $C = \alpha L/\tau$ is denoted as *cooperativity parameter* and $\sqrt{a} = \sqrt{cL/2k_0\kappa}$ as the *diffraction length*. By a suitable rescaling of the field envelope $\mathcal{E}(\mathbf{r}, t)$, such that the saturation $s = |\mathcal{E}(\mathbf{r}, t)|^2$, Eq. (3.14) finally reads:

$$\partial_t\mathcal{E}(\mathbf{r}, t) = \kappa\left[-(1 + i\theta)\mathcal{E}(\mathbf{r}, t) + A_I(\mathbf{r}_\perp) - \frac{C(1-i\Delta)}{1+|\mathcal{E}(\mathbf{r}, t)|^2}\mathcal{E}(\mathbf{r}, t) + ia\nabla_\perp^2\mathcal{E}(\mathbf{r}, t)\right], \tag{3.15}$$

---

[5]This assumption is known in the literature as *mean field limit* and has the great advantage of eliminating any dependence on the z coordinate in the model [153].

[6]The fundamental mode will be simply denoted with $\mathcal{E}(\mathbf{r}, t)$ in the rest of the thesis.
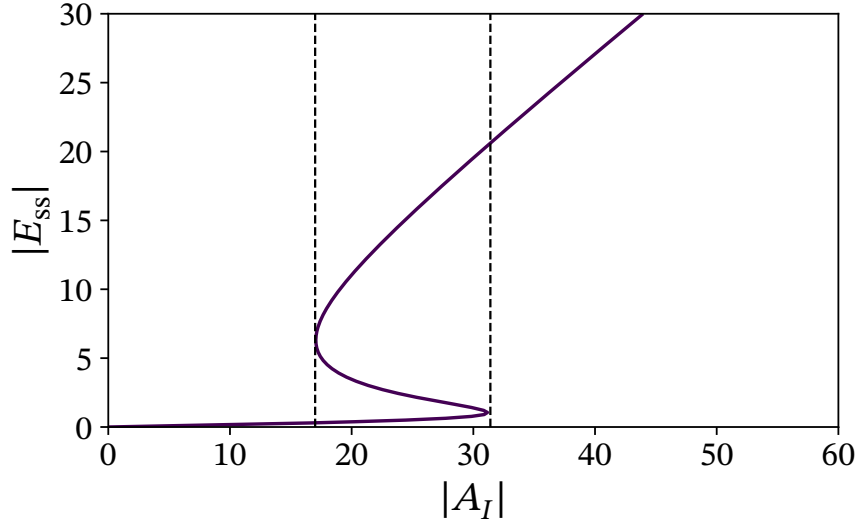
Fig. 3.2. Steady state characteristic $\mathcal{E}_{ss}(|A_I|)$ of an optical resonator coupled to a saturable two-level medium. The bistable curve is obtained for the following values of the parameters $\theta = 1, \Delta = 15, C = 4$. The vertical lines identifies the corresponding bistable range $A_{min} < A_I < A_{max}$. Laser-cooling the atomic cloud enables the observation of purely optomechanical phenomena for $A_I \ll A_{min}$.

where one can recognize the typical dependence of a two-level saturable nonlinearity. One of the direct consequences of such nonlinearity can be seen by assuming a perfect plane-wave (spatially constant) pumping, i.e. $A_I(\mathbf{r}_\perp) = A_I$, and analyzing Eq. (3.15) at steady state, i.e., $\partial \mathcal{E}_{ss}/\partial t = 0$ and $\nabla_\perp^2 \mathcal{E}_{ss} = 0$ in Eq. (3.15), namely:

$$A_I = \left[1 + i\theta + \frac{C(1 - i\Delta)}{1 + |\mathcal{E}_{ss}|^2} \right] \mathcal{E}_{ss}. \tag{3.16}$$

Eq. (3.16) provides the steady state relation between the the cavity field $\mathcal{E}_{ss}$ (output) constant input field A_I and it is multi-valued when the cooperativity C exceeds a certain threshold $C_{min}(\theta, \Delta)$ [152]. The effect of such an *optical bistability* is represented in Fig. 3.2, where one recognizes the typical s-shaped characteristic $\mathcal{E}_{ss}(|A_I|)$ of the nonlinear optical resonator [154]. However, as quantitatively discussed in the next section, the threshold for the appearance optomechanical pattern-forming effects involves pumping and saturation values well below the bistable regime. By appropriately considering the purely dispersive limit in this regime, one can show that the nonlinear term in Eq. (3.15) reduces to a Kerr form:

$$\alpha \mathcal{P}(\mathbf{r}, t) = i\eta |\mathcal{E}(\mathbf{r}, t)|^2 \mathcal{E}(\mathbf{r}, t), \tag{3.17}$$

where η is a nonlinear susceptibility term, determining the self-focusing (self-defocusing) nature of the optical medium for $\eta > 0 \, (\eta < 0)$. This yields the celebrated *Lugiato-Lefever* model, originally introduced to describe modulation instabilities leading to spontaneous optical pat-

tern forming dynamics [4]. The same model is also adopted in a variety of such as involving optical frequency combs based on ring micro-resonators [155, 156], and quantum squeezing realized on ring optical parametric oscillators [157, 158]. Stationary patterns and dissipative solitons are also predicted to occur for Eq. (3.15) in the purely absorptive case [66, 159]. So far, only the case of a hot ensemble of two-level atoms was considered. The following section focuses on the main model of interest for the present work, namely, when the transverse cavity field dynamics is able to induce density redistributions $n(\mathbf{r}, t)$ in an ensemble of laser-cooled atoms via the optical forces discussed previously in Ch. 2.

3.2 Optomechanical self-structuring in a ring cavity

The class of optomechanical pattern-forming processes that are considered in this work[7] share some features with *collective self-focusing* phenomena of light and atoms. Indeed, soon after the first experimental observation of self-focusing of an atomic beam with optical forces by Bjorkholm *et al.* in Ref. [160], it was realized by Klimontovich and Luzgin that density inhomogeneities can lead to a significant back-action to the optical field dynamics [161]. Moreover, the direct observation, by Ashkin *et al.*, of four-wave mixing and collective self-focusing phenomena in liquid suspensions of dielectric spheres led to the introduction of the term *artificial Kerr medium* [142, 143]. Collective optomechanical phenomena and nonlinear focusing were also observed in cold atomic gases [162, 163], and predicted to induce transverse filamentation instability of light propagating through a quantum degenerate gas [164].

3.2.1 The optomechanical instability: model equations

The main theoretical model describing optomechanical self-structuring in a cold, thermal, atomic gas involve the paraxial description of a single mode ring cavity in Eq. (3.15), coupled to an inhomogeneous atomic density distribution $N(\mathbf{r}, t) = N_0\, n(\mathbf{r}, t)$, where N_0 is the average density of the atomic cloud[8]. Therefore, one simply expects the nonlinear term to contain an explicit dependence on the atom density $n(\mathbf{r}, t)$:

$$\partial_t \mathcal{E}(\mathbf{r}, t) = \kappa \left[-(1 + i\theta)\, \mathcal{E}(\mathbf{r}, t) + A_I(\mathbf{r}) - \frac{C(1 - i\Delta)}{1 + |\mathcal{E}(\mathbf{r}, t)|^2} n(\mathbf{r}, t)\mathcal{E}(\mathbf{r}, t) + ia\nabla^2 \mathcal{E}(\mathbf{r}, t) \right]. \quad (3.18)$$

Density redistributions are described here by a mean-field Fokker-Planck-Smoluchowski description of overdamped atomic motion (See Sec. 2.3.1), in the limit when the population of the excited atomic state is negligible, so that scattering forces on atoms due to the cavity field are discarded[9]. This is captured by the saturation parameter, assumed $s(\mathbf{r}, t) \ll 1$. Thus, momentum exchange with the light beam is primarily represented by the dipole force field

---

[7]I.e. involving atomic transport induced by optical forces.
[8]From now on, $\mathbf{r}$ is used to represent the transverse coordinate only.
[9]This assumption is generally valid for large detuning $\Delta \gg 1$.

$\mathbf{F}_{\text{dip}}(\mathbf{r}, t)$, derived as follows from the AC stark potential introduced in Eq. (2.19):

$$\mathbf{F}_{\text{dip}}(\mathbf{r}, t) = -\nabla U_{\text{dip}}(\mathbf{r}, t) = -\frac{\hbar \Gamma \Delta}{4} \nabla s(\mathbf{r}, t). \tag{3.19}$$

The center-of-mass classical dynamics for a collection of N atoms is described by the usual set of stochastic differential equations, as in Eq. (2.55):

$$\frac{d\mathbf{r}_j}{dt} = \frac{\mathbf{p}_j}{m}, \quad \frac{d\mathbf{p}_j}{dt} = \mathbf{F}_{\text{dip}}(\mathbf{r}_j, t) - \gamma \frac{\mathbf{p}_j}{m} + \xi_j(t), \tag{3.20}$$

where the microscopic parameters m, γ and the stochastic force $\xi_j(t)$ were already introduced in Sec. 2.3.1. In the thermodynamic limit ($N \to \infty$), the optomechanical dynamics of the considered atomic ensemble is well described by Kramers-Chandrasekhar equation for a smooth 1-particle distribution function $f(\mathbf{r}, \mathbf{p}, t)$:

$$\partial_t f(\mathbf{r}, \mathbf{p}, t) = -\frac{\mathbf{p}}{m} \cdot \nabla f(\mathbf{r}, \mathbf{p}, t) + \nabla_{\mathbf{p}} \cdot \left[\left(\frac{\gamma}{m} \mathbf{p} - \mathbf{F}_{\text{dip}}(\mathbf{r}, t) \right) f(\mathbf{r}, \mathbf{p}, t) \right] + D_{\mathbf{p}} \nabla_{\mathbf{p}}^2 f(\mathbf{r}, \mathbf{p}, t), \tag{3.21}$$

where $\beta = 1/k_B T$. In addition, as introduced in Sec. 2.3.1, Eq. (3.21) in the limit of strong viscous damping, maps to the Smoluchowski equation for the real space density distribution:

$$\partial_t n(\mathbf{r}, t) = -\beta D_{\mathbf{r}} \nabla \cdot \left[n(\mathbf{r}, t) \mathbf{F}_{\text{dip}}(\mathbf{r}, t) \right] + D_{\mathbf{r}} \nabla^2 n(\mathbf{r}, t), \tag{3.22}$$

$$= \frac{\hbar \Gamma \Delta}{4 k_B T} D_{\mathbf{r}} \nabla \cdot \left[n(\mathbf{r}, t) \nabla s(\mathbf{r}, t) \right] + D_{\mathbf{r}} \nabla^2 n(\mathbf{r}, t), \tag{3.23}$$

where the diffusion constant $D_{\mathbf{r}} = 1/\gamma\beta$ represents the spatial macroscopic effect of optical molasses and the atom density $n(\mathbf{r}, t)$ is obtained by direct integration of the distribution function $f(\mathbf{r}, \mathbf{p}, t)$ in momentum space, namely:

$$n(\mathbf{r}, t) = \int_\Omega f(\mathbf{r}, \mathbf{p}, t) \, d\mathbf{p}, \tag{3.24}$$

with Ω being the integration domain. It is useful to introduce here a coupling strength $\sigma = \hbar\Gamma\Delta/4k_B T$, representing a competition between the drift generated by the optical force, which induces inhomogeneities in $n(\mathbf{r}, t)$, and diffusion, which tends to spread such modulations in the spatial domain[10]. A similar self-consistent model was derived by considering light propagation in an ensemble of cold Cs atoms, damped with optical molasses, in order to describe dissipative soliton formation and longitudinal modulation instabilities [165, 166].

Generally speaking, pattern-forming instabilities in the present system are due to a competition between two-level and density-driven nonlinearities [51]. However, the novelty aspect of our scheme consists in showing that any significant coupling with the internal level is not necessary in order to achieve modulation instability. Therefore, in this condition, the saturation nonlinearity can be neglected and the nonlinear effects arise entirely from the coupled

---

[10]One easily sees that in the hot atoms case $\sigma \to 0$ and optomechanical effects caused by the drift term are suppressed.

light-density dynamics, elucidated by Eqs (3.18) and (3.23) in the low saturation limit. This is shown in the next section by means of a linear stability analysis. Finally, it is worth remarking the role of the spatially structured pump $A_I(\mathbf{r})$ in the present model, which enables the realization dynamical (drifting) light-density patterns, allowing robust control of atomic transport in the transverse profile. This aspect will be extensively discussed in Sec. 3.3.

3.2.2 Linear stability analysis

Let us start this section by recalling the form of the model equations above in the low saturation limit. It is useful to introduce here the adimensional coordinate rescaling $t' = \kappa t$, $\mathbf{r}' = \mathbf{r}/\sqrt{a}$, $D' = D/\kappa a$, so that Eqs. (3.15) and (3.23) now read:

$$\partial_{t'}\mathcal{E}(\mathbf{r}',t') = -(1+i\theta)\mathcal{E}(\mathbf{r}',t) + A_I(\mathbf{r}') - 2iC\Delta\, n(\mathbf{r}',t)\,\mathcal{E}(\mathbf{r}',t) + i\nabla^2\mathcal{E}(\mathbf{r}',t), \tag{3.25}$$

$$\partial_{t'}n(\mathbf{r}',t') = \sigma D'\nabla\cdot\left[n(\mathbf{r}',t)\nabla|\mathcal{E}(\mathbf{r}',t)|^2\right] + D'\nabla^2 n(\mathbf{r}',t). \tag{3.26}$$

Spatial perturbations around the homogeneous steady state solutions $\mathcal{E}_{\mathrm{ss}}$ and $n_{\mathrm{ss}} = 1$ are simply parametrized in Fourier space as follows:

$$\delta\mathcal{E}(\mathbf{q}',t') = a\, e^{i(\mathbf{q}'\cdot\mathbf{r}'+\lambda t')} + b^*\, e^{-i(\mathbf{q}'\cdot\mathbf{r}'+\lambda^* t')}, \tag{3.27}$$

$$\delta n(\mathbf{q}',t') = c\, e^{i(\mathbf{q}'\cdot\mathbf{r}'+\lambda t')} + c^*\, e^{-i(\mathbf{q}'\cdot\mathbf{r}'+\lambda^* t')}, \tag{3.28}$$

where $\mathbf{q}'$ is the transverse wavevector, $a,b,c \in \mathbb{C}$, and the quantity $-\mathrm{Im}[\lambda]$ identifies the linear *growth rate* of such spatial modulations[11]. Therefore, the linearized equations read:

$$\partial_{t'}\delta\mathcal{E}(\mathbf{q}',t') = -\left[1+i\theta+i\mathbf{q}'^2\right]\delta\mathcal{E}(\mathbf{q}',t') - 2iC\Delta\left[1+\delta n(\mathbf{q}',t')\right]\left[\mathcal{E}_{\mathrm{ss}}+\delta\mathcal{E}(\mathbf{q}',t')\right],$$
$$\partial_{t'}\delta n(\mathbf{q}',t') = -\sigma D'\mathbf{q}'^2\left[\mathcal{E}_{\mathrm{ss}}^*\delta\mathcal{E}(\mathbf{q}',t') + \mathcal{E}_{\mathrm{ss}}\delta\mathcal{E}^*(\mathbf{q}',t)\right] - D'\mathbf{q}'^2, \tag{3.29}$$

where the steady state $\mathcal{E}_{\mathrm{ss}}$ is a function of the pump intensity A_I, as seen previously in Eq. (3.16). Moreover, one defines the vector variable $\mathbf{x} = (a,b,c)^{\mathrm{T}}$ so that the linearized system (3.29) can be cast in the usual secular form $\left[\mathbf{M}(\mathbf{q}') - \lambda\mathbb{1}\right]\cdot\mathbf{x} = \mathbf{0}$, where the corresponding 3×3 stability matrix $\mathbf{M}(\mathbf{q}')$ reads as follows:

$$\mathbf{M}(\mathbf{q}') = i^{-1}\begin{pmatrix} -1-i(\mathbf{q}'^2-2C\Delta-\theta) & 0 & -2iC\Delta\mathcal{E}_{\mathrm{ss}} \\ 0 & -1+i(\mathbf{q}'^2+2C\Delta+\theta) & 2iC\Delta\mathcal{E}_{\mathrm{ss}}^* \\ -D'\mathbf{q}'^2\sigma\mathcal{E}_{\mathrm{ss}}^* & -D'\mathbf{q}'^2\sigma\mathcal{E}_{\mathrm{ss}} & -D'\mathbf{q}'^2 \end{pmatrix}. \tag{3.30}$$

Eigenvectors of $\mathbf{M}(\mathbf{q}')$ corresponding to $-\mathrm{Im}[\lambda_i] > 0$ represent the band of excited modes in the system for a certain value of the pump above threshold, and the growth rate is defined as $\min\{-\mathrm{Im}[\lambda_i]\}$. A partial understanding of the marginal stability condition, i.e., when at least one eigenvalue vanishes, is readily found by imposing $\det[\mathbf{M}(\mathbf{q}')] = 0$, leading to the

---

[11]Note that stationary instabilities are identified by purely imaginary $\lambda = -i\nu$, $\nu \in \mathbb{R}$.

a)

$$\min\{-\mathrm{Im}[\lambda_i]\}$$

b)

$$\min\{-\mathrm{Im}[\lambda_i]\}$$
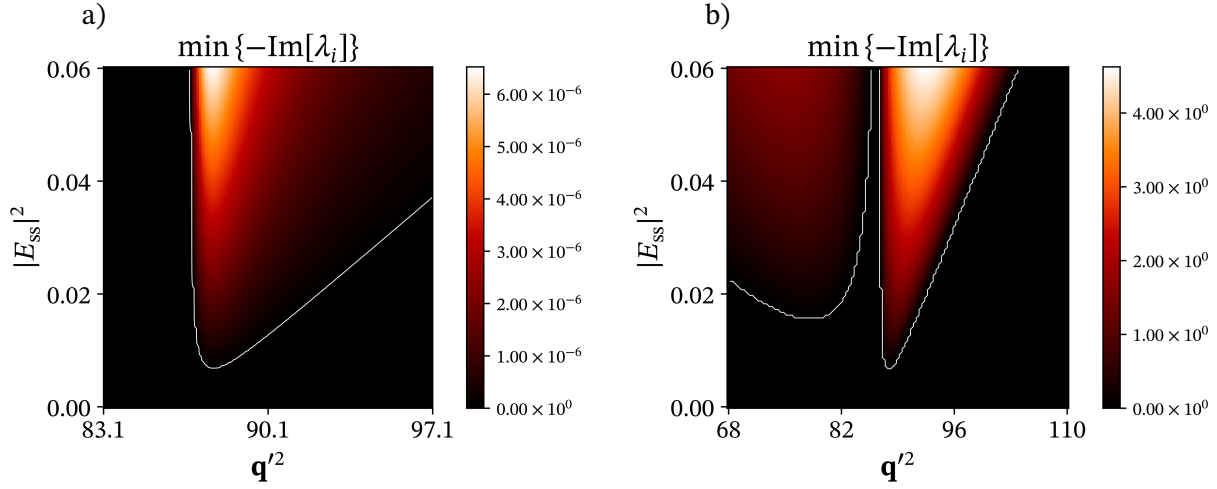
Fig. 3.3. Instability domains represented in the space spanned by $(|\mathcal{E}_{\mathrm{th}}|^2, \mathbf{q}'^2)$, for two values of the rescaled diffusion coefficient, i.e. $D' = 10^{-8}$ (a - slow) and $D' = 10^{-2}$ (b - fast). Other model parameters chosen as follows: $\theta = -100$, $\Delta = 15$, $b_0 = 20$ and $\tau = 0.1$ (such that the cooperativity parameter $C \approx 0.44$) and $\sigma = 12$ (such that $T \approx 100\,\mu\mathrm{K}$). Note the presence of a secondary instability domain for faster diffusion in b). Such unstable modes however are not excited at threshold (white solid lines).

following analytical instability threshold:

$$|\mathcal{E}_{\mathrm{th}}|^2(\mathbf{q}') = \frac{1 + (\mathbf{q}'^2 + \theta + 2C\Delta)^2}{4C\Delta\sigma(\mathbf{q}'^2 + \theta + 2C\Delta)}, \tag{3.31}$$

and the critical wavenumber[12] $\mathbf{q}'^2_c = 1 - (\theta + 2C\Delta)$. Note also that the threshold lines described by Eq. (3.31) do not depend on the diffusion coefficient D'.

As in the case of reaction-diffusion systems described in Sec. 2.3.3, one is able to describe the instability domain in Fourier space by studying numerically the spectrum of eigenvalues and eigenvectors of $\mathbf{M}(\mathbf{q}')$ in Eq. (3.30), for all model parameters fixed to a certain reference value. This is shown in the two diagrams in Fig. 3.3, where the minimum imaginary part among the eigenvalues of Eq. (3.30) is plotted as a function of the steady state intensity $|\mathcal{E}_{\mathrm{ss}}|^2$ and the transverse wavenumber $\mathbf{q}'^2$. For slow atomic diffusion (see Fig. 3.3 - a), a typical Turing instability scenario is obtained, with an instability domain bounded by the analytical threshold curve in Eq. (3.31). One also finds $\mathrm{Re}[\lambda_i] = 0$ throughout the unstable region, recovering the stationary character of the modulation instability, expected for a pattern-forming system of our class. Interestingly, a secondary non-stationary instability is found for values of $\mathbf{q}'^2 < -(\theta + 2C\Delta)$, i.e., below the threshold divergence in Eq. (3.31)[13]. However, such modes are never excited at threshold and, as shown later in Sec. 3.3.1 by means of numerical simulations, they are never observed due to the nonlinear saturation, which typically results in the selection

---

[12]This is simply obtained as the minimum of $|\mathcal{E}_{\mathrm{th}}|^2$ as a function of $\mathbf{q}^2$

[13]The boundary corresponding to the secondary instability domain in Fig. 3.3 - b is found numerically as a contour line.
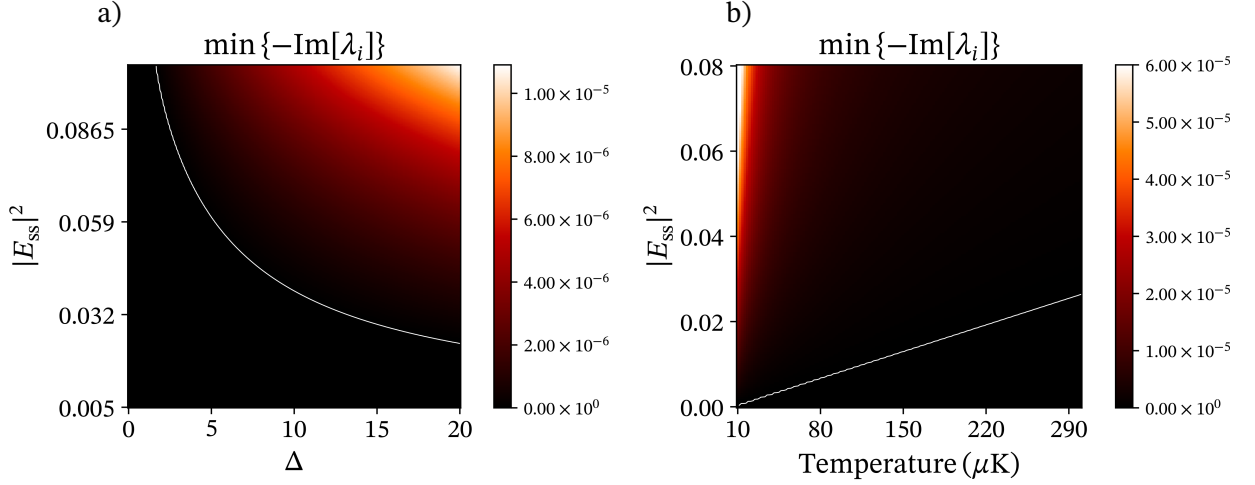
Fig. 3.4. 2-d linear stability plots showing the growth rate $\min\{-\mathrm{Im}[\lambda_i]\}$ in dependence of the following two-parameter spaces. a) Growth rate as a function of $|E_{\mathrm{ss}}|^2$ and Δ, with a a range of Δ sufficiently far from the internal atomic resonance and at $\sigma = 12$. b) Growth rate dependence on $|E_{\mathrm{ss}}|^2$ and temperature T, obtained at $|\Delta| = 20$. Consistently with the plots in Fig. 3.3, other model parameters are chosen in both cases as follows: $\theta = -100$, $D' = 10^{-8}$ and critical wavenumber. The analytical threshold from Eq. (3.31) is represented by the solid white line.

of three competing resonant modes and the emergence of an hexagonally patterned state (see also Sec. 2.3.3).

Furthermore, the linear stability properties of our system are also studied by spanning two other experimentally interesting parameters regions, namely, as a function of $|E_{\mathrm{ss}}|^2$ vs. the adimensional detuning[14] Δ (in Fig. 3.4 - a), and $|E_{\mathrm{ss}}|^2$ vs. temperature T (Fig. 3.4 - b). For those two cases, the growth rate is obtained at the critical wave vector[15], i.e., $\mathbf{q}'^2 = \mathbf{q}_c'^2$. Such results provide evidence for the spontaneous emergence of purely optomechanical structures via modulation instability in our system. This prediction, however, is based on the assumption that two-level saturation effects are negligible and, therefore, for values of the injected field intensity in the proximity of the threshold. Far from threshold, instead, effects arising the electronic nonlinearity become predominant and the corresponding spatial scales of the symmetry broken state are not anymore dictated by the optomechanical instability [56]. Finally, although the instability threshold does not depend on the diffusivity D', it is interesting to plot the dependence of the growth rate on D' at various temperatures T above threshold. Indeed, as a general trend, any increase of D' in such a condition result in a faster growth of spatial modulations. Such increasing trend of the growth rate however saturates for high enough D'. As shown later in Sec. 3.3.2, a similar dependence on D' is recovered by the rotation speed of the pattern in the presence of an OAM-carrying pump. In the following section the role of a spatially structured pump is addressed, with emphasis on phase structure that carries OAM.

---

[14]It is enough to consider here the case $\Delta > 0$ only, since the behaviour is symmetric $\Delta < 0$.

[15]Assumed to be the dominant unstable mode in the system dynamics.
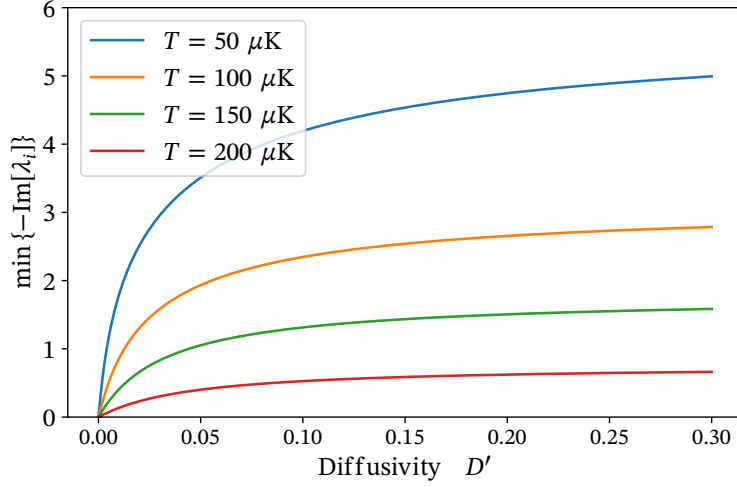
Fig. 3.5. Growth rate dependence of critical modulations, i.e., calculated at $\mathbf{q}' = \mathbf{q}'_c$, on the atomic gas diffusivity D' above threshold for various temperatures, i.e., $T = 50, 100, 150, 200\,\mu$K. Fixed model parameters chosen as follows: $\theta = -100$, $\Delta = 15$, $b_0 = 20$, $\tau = 0.1$ and critical saturation value $s = |\mathcal{E}_{\mathrm{ss}}|^2 \approx 0.03$. A similar saturating behaviour as a function of the atomic diffusivity D' is also recovered from later numerical simulations in Fig. 3.10

As introduced first in the case of dissipative solitons, phase gradients applied on the input pump result into convective motion of the corresponding structures [66]. This phenomenon is particularly relevant for the optomechanical instability, since it provides an effective way to engineer transport of the transverse atomic density structures in our system.

3.3 Rotating light-atom lattice dynamics

The configuration including a nonlinear optical resonator pumped with an helically phased field in the $\mathcal{LG}$-form was considered first in Ref. [67], in order to stabilize domain walls states in optical parametric oscillators and later applied induce rotational motion of dissipative solitons in semiconductor microcavities [68]. In this section, results concerning the dynamics of patterned states in the transverse optomechanical cavity model are discussed.

3.3.1 Pattern dynamics with structured phase

Let us start recalling that, in order to address the effect of OAM in the input field in our ring cavity system, the pump rate $A_I(\mathbf{r}')$ must possess the following topologically non-trivial azimuthal phase structure:

$$A_I(\mathbf{r}') = \mathcal{A}_I(r')\exp(il\phi), \tag{3.32}$$

where $\mathcal{A}_I(r')$ is a generic radial profile and $l \in \mathbb{Z}$. Indeed, the factor $\exp(il\phi)$ generates l intertwined phase fronts and a non-trivial topological structure due to the phase singularity

at $\mathbf{r}' = 0$. Following Ref. [70], one can simplify the analysis by using the Gibbs distribution as a stationary solution of the Smoluchowski Eq. (3.26), namely:

$$n_{\mathrm{eq}}(\mathbf{r}') = \frac{\exp[-\beta U_{\mathrm{dip}}(\mathbf{r}')]}{\int_{\Omega} \exp[-\beta U_{\mathrm{dip}}(\mathbf{r}')]d\mathbf{r}'} = \frac{\exp[-\sigma|\mathcal{E}(\mathbf{r}')|^2]}{\int_{\Omega} \exp[-\sigma|\mathcal{E}(\mathbf{r}')|^2]d\mathbf{r}'}. \tag{3.33}$$

This assumption reduces the coupled system to the field equations only and yields an effective closed form of the optomechanical (Kerr-like) nonlinearity[16], induced by density redistribution as follows[17] [51]:

$$\partial_{t'}\mathcal{E}(\mathbf{r}',t') = -(1+i\theta)\mathcal{E}(\mathbf{r}',t') + A_I(\mathbf{r}') - 2i\,C\Delta\,n_{\mathrm{eq}}(\mathbf{r}')\,\mathcal{E}(\mathbf{r}',t') + i\nabla^2\mathcal{E}(\mathbf{r}',t'). \tag{3.34}$$

One can show that the nonlinear term is always of self-focusing kind [167]. As demonstrated below, the use of a Gibbs distribution provides a way to describe the steady states of the coupled system (3.25) and (3.26) in numerical simulations[18]. One can easily prove that Eq. (3.34) and, in general, all models belonging to the same family of the Lugiato-Lefever in Sec. 3.1, possess a *gauge invariance* with respect to phase shifts of both the optical field and the input pump. Thus, by considering the local transformation defined by $\mathcal{E}(\mathbf{r}',t') = \tilde{\mathcal{E}}(\mathbf{r}',t')\exp(il\phi)$, the corresponding equation for $\tilde{\mathcal{E}}(\mathbf{r}',t')$ reads now as follows:

$$\begin{aligned}
\partial_{t'}\tilde{\mathcal{E}}(\mathbf{r}',t') + \frac{2l}{r'}\nabla\tilde{\mathcal{E}}(\mathbf{r}',t') &= -\tilde{\mathcal{E}}(\mathbf{r}',t') - i\left(\theta + \frac{l}{r'^2}\right)\tilde{\mathcal{E}}(\mathbf{r}',t') \\
&\quad + \mathcal{A}_I(r') - 2i\,C\Delta\,n_{\mathrm{eq}}(\mathbf{r}')\,\tilde{\mathcal{E}}(\mathbf{r}',t') + i\nabla^2\tilde{\mathcal{E}}(\mathbf{r}',t').
\end{aligned} \tag{3.35}$$

The LHS of Eq. (3.35) displays a so-called *convective derivative*[19], i.e., a time-derivative expressed in the locally co-moving reference frame defined by the following transverse velocity vector field:

$$\mathbf{v}_{\mathrm{dr}}(\mathbf{r}') = 2l\nabla\phi = \frac{2l}{r'}\hat{\phi}. \tag{3.36}$$

The above Eqs. (3.35) and (3.36) now motivate the statement that, in the presence of OAM, the same patterned solutions of Eq. (3.34) are stationary in a rotating frame and, thus, in the laboratory frame are simply observed to drift at velocity given by $\mathbf{v}_{\mathrm{dr}}(\mathbf{r}')$. Furthermore, the presence of the azimuthal phase $\exp(il\phi)$ results in a modification of the geometry of the patterned states. Insight on this aspect can be gained by considering the additional spatially dependent contribution to the cavity phase shift in the RHS of Eq. (3.35). In this case, one expects the typical spatial rigidity of the ordered phase to be broken, according to the new spatial sym-

---

[16]See Sec. 4.2.2 for a careful discussion of such comparison.

[17]Note that the presence of the integral at the denominator of Eq. (3.33) yields a non-local nonlinearity.

[18]Note that this does not correspond to a proper adiabatic elimination. Indeed, the role of the diffusive timescales is discussed in detail in Sec. 3.3.2.

[19]The term *convective* is borrowed from fluid dynamics [2].

metry of the pump $A_I(\mathbf{r}')$, and due to the radially dependent angular frequency defined by:

$$\tilde{\phi}(r',t') = \phi - \omega(r')t', \quad \omega(r') = \frac{2l}{r'^2}. \tag{3.37}$$

Such differential rotation dynamics of concentric patterns was introduced and discussed for the case of a purely Kerr resonator (Lugiato-Lefever model) in Ref. [70]. In what follows, such general qualitative considerations are shown to be supported as well for the cold-atom optomechanical cavity model by an extensive set of numerical observations.

Numerical Results I - Homogeneous pump

The steady states of the coupled system can be obtained by integrating Eq. (3.34) numerically using a pseudo-spectral split-step method [168]. For the reader's convenience, the first case considered is that of plane-wave pumping, previously discussed in Ref. [51]. The chosen spatial domain size is of 5 critical wavelengths, discretized in a square grid of 256×256 points, with a time step of the order of $dt' = 4 \times 10^{-3}$. Two cases corresponding to opposite atomic detunings are considered, in order to show the differences in the corresponding density distribution with respect to the cavity intensity. Focusing here on the super-critical behaviour, the value of the pump amplitude is chosen with respect to the following minimum threshold:

$$|\mathcal{E}_{\text{th}}|^2 \geq \frac{1}{2C\Delta\sigma}, \tag{3.38}$$

obtained for the critical wavenumber $\mathbf{q}'^2 = \mathbf{q}_c'^2$. Numerical results are displayed in Figs. (3.6), where the cavity field intensity $|\mathcal{E}(\mathbf{r}')|^2$ is plotted together with the density at equilibrium $n_{\text{eq}}(\mathbf{r}')$. One clearly identifies both positive hexagonal states $\mathbf{H}^+$ of cavity field and atomic density in the red detuned case ($\Delta < 0$) and the opposite[20] configuration observed for blue atomic detuning ($\Delta > 0$). Note that, in the case $\Delta < 0$, and in absence of saturation effects, Fourier filtering by means of a rapidly decaying hyperbolic tangent function is necessary in order to damp the growth of shorter wavelengths and observe stable patterns. Such *blow-up* of the numerically found solution is due to a catastrophic collapse analogous to the well known cases of localized states in the nonlinear Schrödinger equation and cavity solitons in the Lugiato-Lefever model [169–171].

Numerical Results II - Tophat with OAM

In the rest of this section, the role of the azimuthal phase factor $\exp(il\phi)$ in the input field phase is addressed by considering a 2-d radial finite-size "top hat" profile, i.e., a hyperbolic tangent function possessing rapidly vanishing tails. A widely used input field including tophat function is given by the following [172]:

$$A_I(\mathbf{r}') = \frac{A_I}{2}\{1 - \tanh[\eta(r' - r_0')]\}\exp(il\phi), \tag{3.39}$$

---

[20]I.e. hexagonal states $\mathbf{H}^\pm$ with opposite signs.
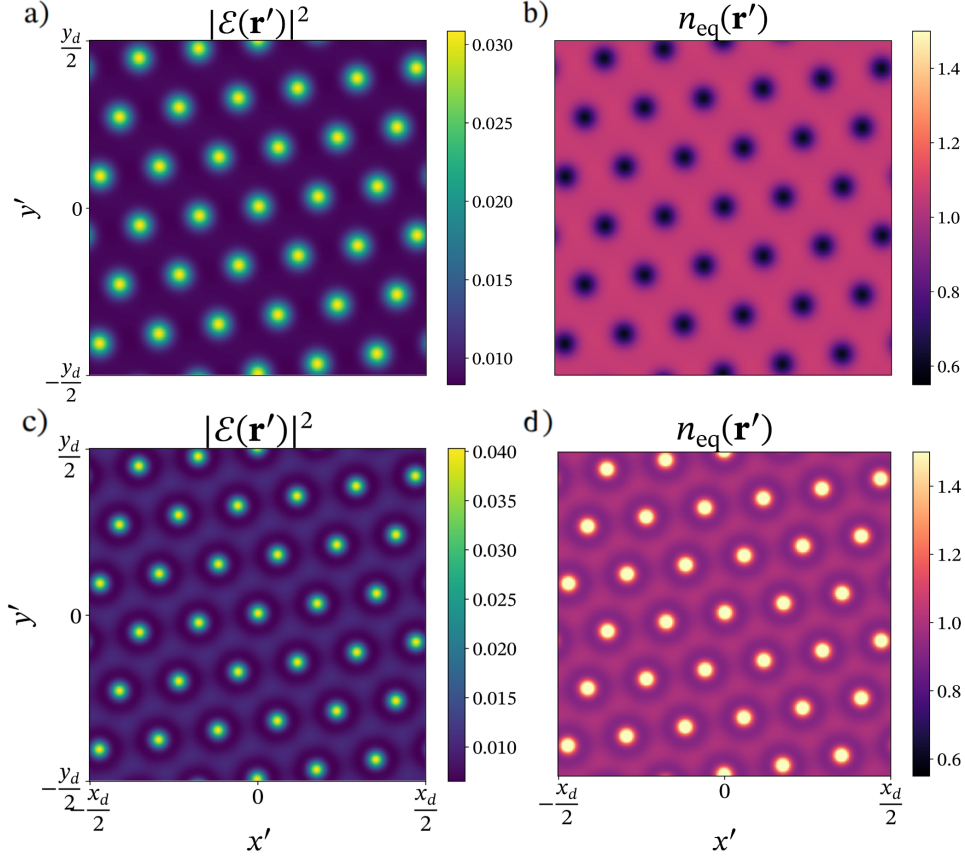
Fig. 3.6. Cavity intensity (left) and atomic density (right) steady state distributions above threshold at $|\mathcal{E}|^2/|\mathcal{E}_{\text{th}}|^2 = 1.05$. a), b) Model parameters chosen as follows $C\Delta = 1.75$ (blue detuning), $\theta = -3.3$, $\sigma = 25$ ($T = 176\,\mu K$ and $\Delta = 20$). The cavity field self-organizes into a $\mathbf{H^+}$ state with anticorrelated ($\mathbf{H^-}$) atomic density structuring. c), d) Red detuned configuration with $C\Delta = -1.75$, $\theta = 3.7$, $\sigma = -25$ and correlated atomic density structuring.

where the complex azimuthal phase carrying OAM is multiplied by the real radial part, and the two constants $\eta > 0$ and r'_0 determine the steepness of the decaying region and the radius of the flat region respectively. The use of the tophat function in Eq. (3.39) has two advantages. Indeed, the choice of boundary conditions in simulations do not affect numerical results with the presence of OAM and, on the other hand, it allows the study of transverse effects induced by the helical input phase $\exp(il\phi)$ on an effective domain much larger than by using a standard Gaussian profile (a total square domain of 10 critical wavelengths is chosen in this case). Examples of optomechanically self-structured states with OAM indices $l = 1, 3$ and for various integration times are shown in Figs. (3.7) and (3.8).

A first consequence of the presence of an helical phase $\exp(il\phi)$ in the pump profile (3.39) is that the field vanishes at $\mathbf{r'} = 0$, due to phase singularity. Together with the circular size of the pump, this induces the formation of diffractive rings whose maximum intensity exceeds the MI threshold locally. The size of the spatial domain is tuned such that the spacing among
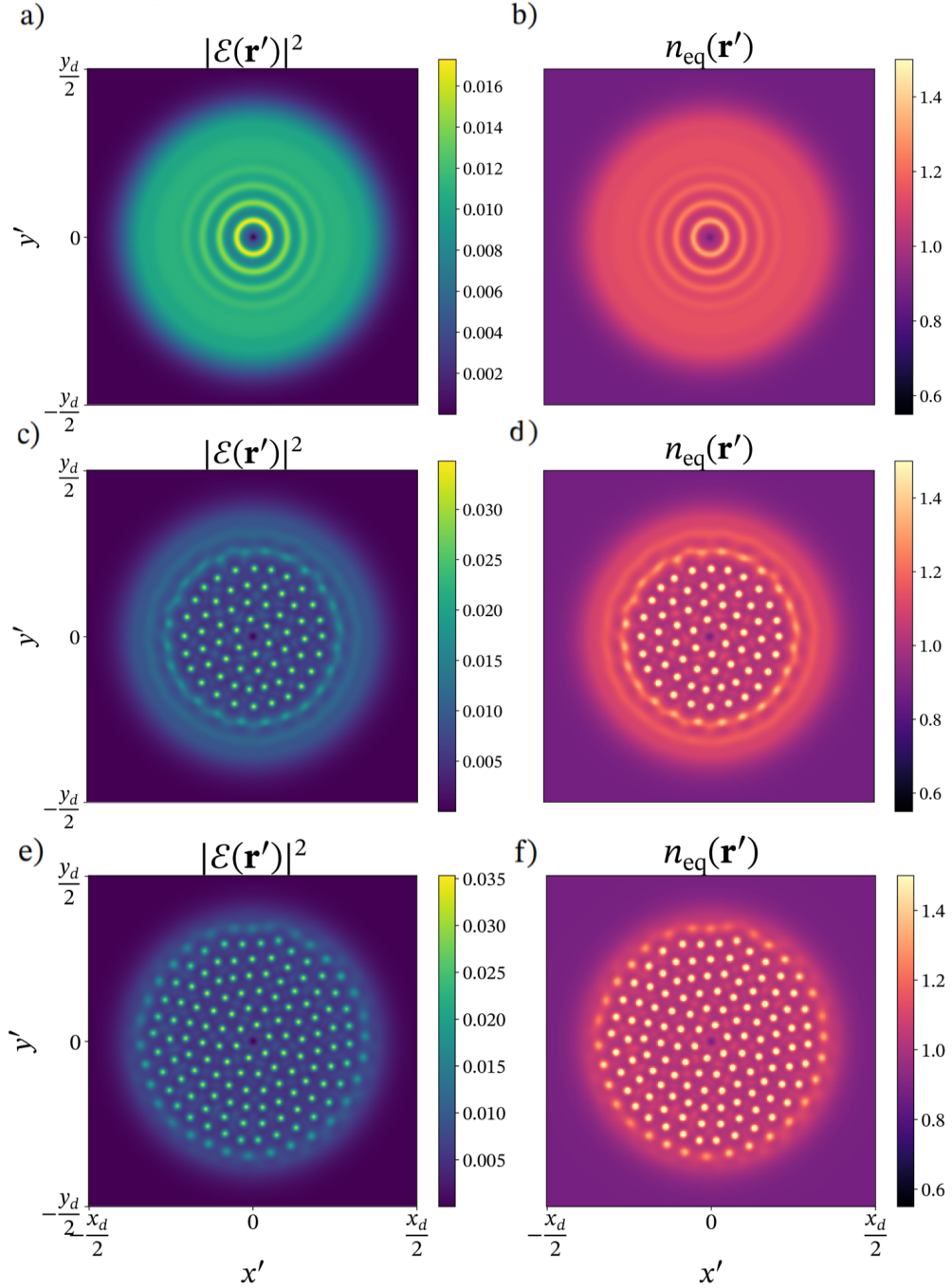
Fig. 3.7. Bright self-organized optomechanical ring lattice formation with $|\mathcal{E}|^2/|\mathcal{E}_{\mathrm{th}}|^2 = 1.05$ and in the presence of an OAM input pump ($l = 1$). Cavity intensity (left) and equilibrium atom density $n_{\mathrm{eq}}(\mathbf{r})$ (right) distribution at different times, i.e. $\kappa t = 20$ a), $\kappa t = 80$ b), $\kappa t = 200$ c). Model parameters chosen as follows: $\theta = 3.7$, $C\Delta = -3.5$ (red detuning $\Delta < 0$), $\sigma = -25$.
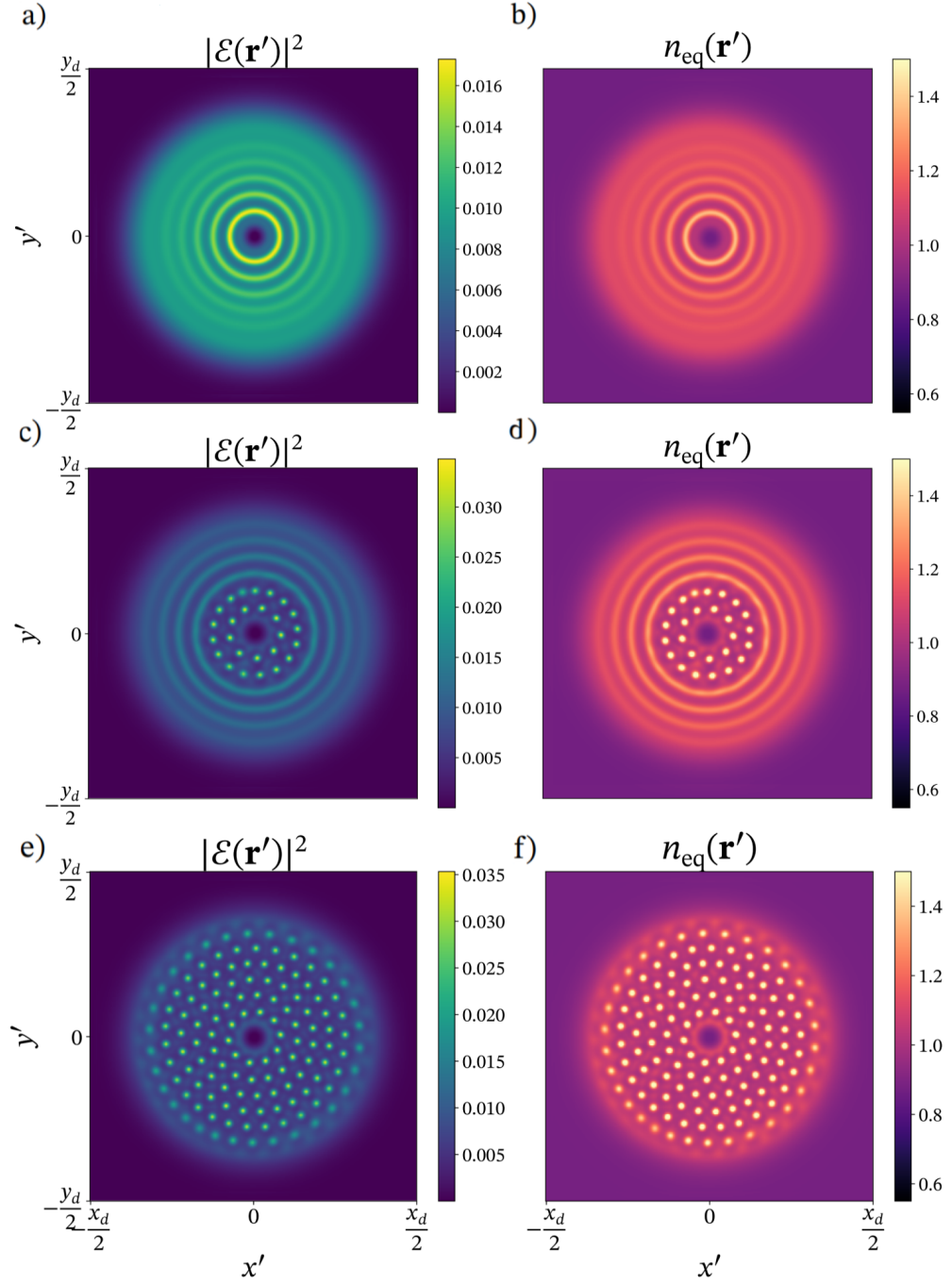
Fig. 3.8. Bright self-organized optomechanical ring lattice formation with $|\mathcal{E}|^2/|\mathcal{E}_{\text{th}}|^2 = 1.05$ and with a higher charged OAM pump ($l = 3$). Cavity intensity (left) and atomic density $n_{\text{eq}}(\mathbf{r})$ (right) steady state distribution at different times, i.e. $\kappa t = 20$ a), $\kappa t = 50$ b), $\kappa t = 200$ c). Note that the number of ring lattices is smaller due to the increased size of the inner optical vortex.

rings is roughly the same as the critical wavelength of the transverse MI[21]. The diffractive radial modulation is such that the local intensity minima lie below the MI point and, therefore, pattern formation is expected to take place independently in a set of concentric ring-lattices [70]. Moreover, the ring lattice formation dynamics can also be influenced by the shape of the tophat profile. For example, one can increase the steepness η, leading to outer diffraction rings achieving MI on faster timescales. However, for a wide parameter span, varying the tophat parameters in order to host several ring lattices always results in a steady state described by independently rotating light-density lattices above threshold. Similar results are found for higher values of the OAM index l.

As anticipated before, numerical simulations show the occurrence of differential rotation of the light-density ring lattice structures. The observed angular frequency is compared with the predicted $\omega(r')$ in Eq. (3.37) by considering an effective 1-d angular version of Eq. (3.34), i.e. at a fixed radius $r' = r'_0$ and with the input pump of the form $A_I(\phi) = A_I e^{il\phi}$, namely:

$$\partial_{t'}\mathcal{E}(\phi, t') = -(1 + i\theta)\mathcal{E}(\phi, t') + A_I(\phi) - 2i\,C\Delta\,n_{\text{eq}}(\phi)\,\mathcal{E}(\phi, t') + \frac{i}{r'_0}\frac{\partial^2}{\partial\phi^2}\mathcal{E}(\phi, t'). \qquad (3.40)$$

where the transverse azimuthal coordinate $\phi \in [0, 2\pi]$ and $\mathcal{E}(0, t') = \mathcal{E}(2\pi, t')$[22]. Eq. (3.40) is numerically integrated with different 1-d domain sizes in order to provide a more accurate estimate of the rotation frequency observed in simulations for several radial distances r'_0. Fig. 3.9 shows a comparison, for $l = 1, 2, 3$, of the rotation frequency estimated at several radial distances and showing good agreement with the predicted $\omega(r')$ by simply measuring the slope of the pattern in a (t', ϕ) with the relative propagated uncertainty (See error bars in Fig. 3.9). As shown in Ch. 5, analogous control of rotational dynamics can be generalize to the case of bistable optomechanical dissipative solitons, as those found in [71].

Finally, other more complex phase structured input fields can be effectively used in this case to control the motion and study the effective interactions of localized dissipative transverse structures of cold atoms in an optical cavity. As considered in detail in [70], for the case of a single ring in a $\mathcal{LG}$-mode, one has a maximum intensity radius $r'_{\text{max}} = w_0\sqrt{l/2}$ where w_0 is the usual beam waist introduced in 2.2.2. Therefore, one expects the angular frequency of the ring to be independent of l, namely $\omega_{\pm}(r'_{\text{max}}) = \pm 4/w_0^2$. Vectorial superpositions of counter-rotating $\mathcal{LG}$-modes are also shown to provide continuous control of the rotation frequency between the two extremal values $\omega_{\pm}$.

3.3.2 Diffusive drag and its microscopic origin

The above discussion is based upon the assumption that the overdamped dynamics of atom density can be simply replaced by the Gibbs density distribution in Eq. (3.33). While this procedure is effective in determining the features of the steady states, it misses one of the cru-

---

[21]This is simply found by measuring peak distances in the radial profiles in Fig. 3.7.

[22]In other words, the azimuthal variation at fixed radius is mapped to a 1-d model with periodic boundary conditions.
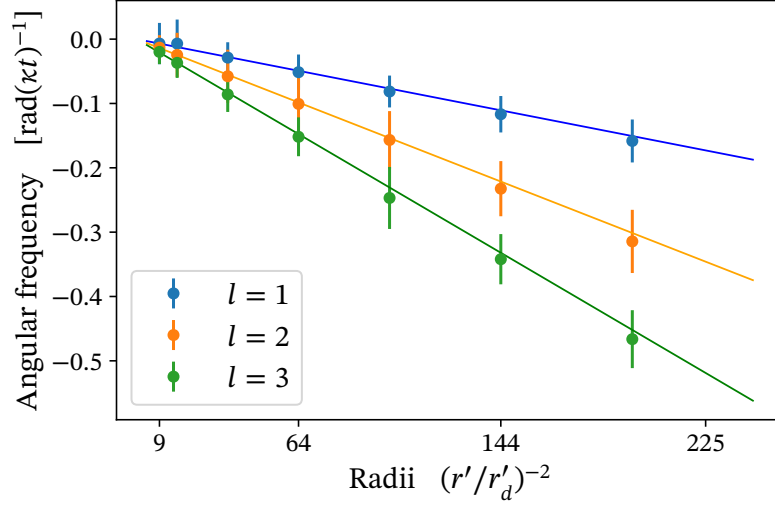
Fig. 3.9. Numerical results from the integration of Eq. (3.40). The angular frequency of rotation of the patterned states is obtained at different radii (in units of half the domain size $r'_d = L_d/2$). Radial distances are chosen by adjusting the size of the 1-d integration domain. Solid lines represent the predicted angular frequency radial dependence $\omega(r')$ with OAM indices $l = 1, 2, 3$.

cial aspects of the optomechanical nonlinearity in the presence of structured phase profiles, i.e. any possible dependence of the observed rotation speed on the thermal diffusivity of the gas[23]. In order to take such effect into account and obtain values of the angular rotation frequency comparable with experimental conditions, it is necessary to integrate numerically the full system described by Eqs. (3.25) and (3.26). This is realized by means of a second order Crank-Nicolson scheme for coupled equations, discussed in detail in appendix A.1.

Let us start here by recalling the fluctuation-dissipation relation $\beta D_{\mathbf{r}}\gamma = 1$, introduced in Sec. 2.3.1, where $\beta = (k_B T)^{-1}$, $D_{\mathbf{r}}$ is the gas diffusivity, and γ is the momentum damping rate. This implies that varying the diffusivity at constant temperature must correspond to an inversely proportional variation of γ, since their product is constant. Fig. (3.10) show numerical results of the observed rotation angular frequency[24] (modulus), as a function of the rescaled diffusion coefficient $D'_\phi = D_\phi/\kappa a$ in the coupled model. Firstly, one overall notices smaller values of the rotation angular frequency which are a consequence of the convergence of the atomic density to the Gibbs distribution in a finite timescale. Moreover, one observes that the azimuthal ring lattices rotate faster when increasing D'_ϕ (and decreasing γ) and that such growth eventually saturates to a certain value, seemingly proportional to the OAM index l. On the other hand, increasing the momentum damping γ introduces an effective drag, which eventually compensates the phase gradient of the input pump carrying OAM in the limit of $D'_\phi \to 0$, where the ring lattices are stationary[25]. An interesting comparison of the

---

[23]More generally, on the optical molasses parameters

[24]Measured with the same method as in Sec. 3.3.2

[25]Note the the atom density is also forced to be stationary, i.e., $\partial_{t'} n = 0$.
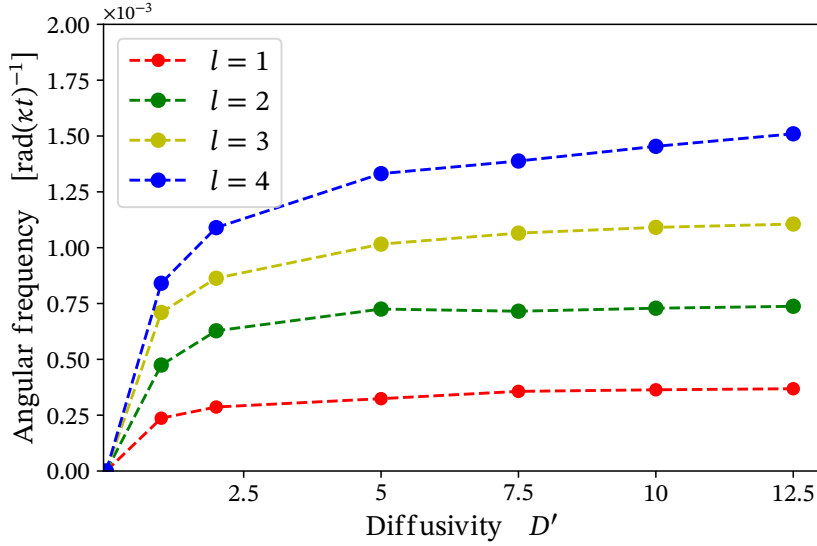
Fig. 3.10. Numerical results from the the 1-d full cavity-atom density model of Eqs. (3.25, 3.26). Estimated values of the lattice angular rotation frequency plotted against the rescaled diffusivity D' (at fixed temperature T), with OAM index $l = 1, \dots, 4$. Besides the proportionality of the ring-lattice rotation speed on the pump OAM, a faster diffusion processes imply a higher value of the observed angular frequency.

results shown above in Fig. 3.10 can be drawn by recalling the dependence of linear growth rate on D', analyzed in detail Sec. 3.2.2, Fig. 3.5, since the same saturation with the atom diffusivity D'_ϕ is observed here for the angular rotation frequency of the ring-lattice. The roots of such connection are to be found in the coupled nature of the two model equations and, in particular, to the difference in the relative timescales, i.e. of the cavity field and diffusive dynamics.

As discussed in the following section, such observations derived with a simple mean field model carry a number of profound consequences from the point of view of the dynamics of the atom center of mass, since the rotation of the self-organized modulations of the cavity intensity and atomic density induces transport of the atoms.

3.4 Optomechanical transport

Although the observed rotation of the self-organized ring lattices intuitively suggests that the OAM carried by the input field induces atomic currents[26], a quantitative analysis of such effects by means of, e.g., an atomic *current*, requires an approach beyond the equilibrium distribution and the Smoluchowski equation. Such tool can be obtained by addressing the average momentum of the full atomic phase-space distribution, providing a suitable measure of the macroscopic rotation of the self-trapped atoms. For this aim, it is enough to consider the simple 1-d case of atoms effectively confined in a circular ring trap. Such configuration, however,

---

[26]As a result of the drift of the self-trapped atomic wave-packets.

can be realized experimentally in the transverse plane of the ring cavity by considering a $\mathcal{LG}$-mode exciting a single self-organized ring lattice at a fixed radius[27] [39].

3.4.1 Ring-lattice rotation and atomic currents

A first approach to quantify the atomic mass current is based on the continuous density distribution $n(\phi, t)$, where $\phi \in [0, 2\pi]$. Let us start by recalling the form of the Langevin equations for a set of atoms subject to the dipole potential and confined in a 1-d angular geometry at fixed radius r_0:

$$\frac{d}{dt}\phi_j = \frac{1}{mr_0^2}p_j^\phi, \quad \frac{d}{dt}p_j^\phi = -\frac{\hbar\Gamma\Delta}{4}\partial_\phi s(\phi, t) - \frac{\gamma}{m}p_j^\phi + \xi_j^{(\phi)}(t), \tag{3.41}$$

where ϕ_j is the azimuthal coordinate of the j-th atom and p_j^ϕ its conjugate (angular) momentum. When focusing on the overdamped case, one implicitly assumes angular momenta p^ϕ at equilibrium, i.e., a distribution $\bar{f}(p^\phi)$ described by the following Maxwell-Boltzmann function, namely [173]:

$$\bar{f}(p^\phi) = \left(\frac{\beta}{2\pi mr_0^2}\right)^{1/2}\exp\left[-\frac{\beta(p^\phi - \langle p^\phi\rangle)^2}{2mr_0^2}\right], \tag{3.42}$$

where $\langle p^\phi\rangle$ is the average (bulk) angular momentum representing the center of the Maxwell-Boltzmann distribution[28] $\bar{f}(p^\phi)$. The assumption of strong friction limit corresponds to fact that the total phase space distribution has the following factorized form [165]:

$$f(\phi, p^\phi, t) = \bar{f}(p^\phi)\,n(\phi, t). \tag{3.43}$$

Atomic transport effects induced by the dipole potential are addressed here by looking at the average angular momentum $\langle p^\phi\rangle$ of the distribution, whose dynamical equation is obtained by simply multiplying the corresponding Kramers-Chandrasekhar equation[29] by p^ϕ and integrating it over p^ϕ-space, namely [121]:

$$\frac{\partial n(\phi, t)}{\partial t}\langle p^\phi\rangle = -\frac{1}{mr_0^2}\int_{-\infty}^{+\infty}(p^\phi)^2\,\partial_\phi f\,dp^\phi + \partial_\phi U_{\text{dip}}(\phi, t)\int_{-\infty}^{+\infty}p^\phi\,\partial_{p^\phi}f\,dp^\phi$$
$$+ \frac{\gamma}{m}\int_{-\infty}^{+\infty}p^\phi\,\partial_{p^\phi}(p^\phi f)\,dp^\phi + \frac{\gamma r_0^2}{\beta}\int_{-\infty}^{+\infty}p^\phi\,\partial_{p^\phi}^2 f\,dp^\phi, \tag{3.44}$$

where $U_{\text{dip}}(\phi, t) = \hbar\Gamma\Delta\partial_\phi s(\phi, t)/4$ is the usual dipole potential in the low saturation limit. Eq. (3.44), known as the *momentum equation*, is rearranged according to the following elementary manipulations. Firstly, by exchanging the derivative and the integral in the first term

---

[27]In such a configuration, the system develops an azimuthal instability at the maximum intensity radius r_{max}.
[28]Normally, the equilibrium distribution is centered at $\langle p^\phi\rangle = 0$ but, as shown later, the OAM pump breaks this symmetry, introducing an effective atomic current.
[29]Expressed here in polar coordinates.

of the RHS of Eq. (3.44), one obtains:

$$\int_{-\infty}^{+\infty} (p^\phi)^2 \, \partial_\phi f \, dp^\phi = \partial_\phi \int_{-\infty}^{+\infty} (p^\phi)^2 \, f \, dp^\phi = \partial_\phi n(\phi,t)\langle (p^\phi)^2 \rangle, \tag{3.45}$$

with $\langle (p^\phi)^2 \rangle = r_0^2 m \beta^{-1}$ being the second moment of the distribution $\bar{f}(p^\phi)$ in Eq. (3.42). Integrating by parts, the second and third terms read:

$$\int_{-\infty}^{+\infty} p^\phi \, \partial_{p^\phi} f \, dp^\phi = -n(\phi,t), \quad \int_{-\infty}^{+\infty} p^\phi \, \partial_{p^\phi}(p^\phi f) \, dp^\phi = -n(\phi,t)\langle p^\phi \rangle, \tag{3.46}$$

and, analogously, the fourth integral vanishes, i.e., $\int_{-\infty}^{+\infty} p^\phi \, \partial_{p^\phi}^2 f \, dp^\phi = 0$. Thus, at equilibrium, the momentum equation (3.44) simply reads:

$$0 = -\frac{1}{\beta}\partial_\phi n(\phi,t) - \left[\partial_\phi U_{\text{dip}}(\phi,t) + \frac{\gamma}{m}\langle p^\phi \rangle \right] n(\phi,t). \tag{3.47}$$

Therefore, the net atomic mass current is obtained integrating Eq. (3.47) over ϕ. However, the first term in the RHS clearly vanishes[30] so that, after integration, the average angular momentum of the atoms finally reads:

$$\langle p^\phi(t) \rangle_{\text{density}} = -\frac{m}{\gamma} \int_0^{2\pi} \partial_\phi U_{\text{dip}}(\phi,t) n(\phi,t) \, d\phi. \tag{3.48}$$

Eq. (3.48) quantifies the steady state mass current along the rotating self-organized ring lattice in the overdamped momentum limit, from the knowledge of $n(\phi,t)$ only. In order to convince the reader of the consistency of the technical tools derived here, the values of $\langle p^\phi(t) \rangle_{\text{density}}$ will be compared in the next section with the ones resulting from a full model simulation, i.e., the ensemble averages obtained from simulating particle dynamics.

3.4.2 Numerical simulations (particle dynamics)

In order to introduce here the particle dynamics simulations, it is more convenient to map the azimuthal variation of $\phi \in [0, 2\pi]$ onto a 1-d segment $\Omega = [-L_d/2, L_d/2]$ of adjustable length L_d and with periodic boundary conditions[31]. Furthermore, and adopt the adimensional coordinates $\bar{r}_j = q_c r_j$ and $\bar{p} = p_j/\hbar q_c$, describing atomic positions and momenta respectively, together with the rescaled time $t' = \kappa t$ where κ is the usual cavity decay rate. Therefore, the Langevin equations read:

$$\frac{d\bar{r}_j}{dt'} = 2\omega_q \bar{p}_j, \quad \frac{d\bar{p}_j}{dt'} = -\frac{\Gamma\Delta}{4\kappa}\frac{\partial}{\partial \bar{r}}|E(\bar{r} = \bar{r}_j, t')|^2 - \bar{\gamma}\,\bar{p}_j + \bar{\xi}_j(t'), \tag{3.49}$$

---

[30]Since the atom density $n(\phi,t)$ is periodic in the azimuthal domain at fixed radius.

[31]Adjusting the domain size simply corresponds here to varying the radius of the ring trap.

where the (adimensional) recoil frequency $\omega_q = \hbar q_c^2/2m\kappa$ represents the characteristic scales of an atom oscillating in a potential generated by a standing wave modulation of the cavity field at wavenumber q_c and, also, $\bar{\gamma} = \gamma/m\omega_q$. The atomic mass current, introduced previously in Eq. (3.48), in this context reads:

$$\langle \bar{p}(t') \rangle_{\text{particles}} = -\frac{\Gamma\Delta}{4\kappa\bar{\gamma}} \left\langle \frac{\partial}{\partial \bar{r}} \left| E(\bar{r} = \bar{r}_j, t') \right|^2 \right\rangle, \tag{3.50}$$

i.e., obtained from the ensemble average on atomic momenta. An accurate comparison of the values of the atomic current in Eq. (3.50) to Eq. (3.48) requires the following relation between the parameters appearing in the mean-field Smoluchowski equation and the *microscopic* Langevin equations (3.49) (See appendix A.2):

$$\bar{D}_r = \frac{4\omega_q^2}{\bar{\gamma}^2} \bar{D}_p = \frac{4\omega_q^2}{\bar{\gamma}} \zeta_p^2, \quad \sigma = \frac{\omega_q \Gamma\Delta}{2\kappa\bar{\gamma}\bar{D}_r} = \frac{\Gamma\Delta}{8\kappa\omega_q\zeta_p^2}, \tag{3.51}$$

where $\bar{D}_p$ is the rescaled momentum diffusion constant[32]. Eqs. (3.49) are integrated numerically in the overdamped limit (See appendix A.1) by means of a particle-in-cell technique, whereas the coupling with the cavity field equation is obtained by computing numerically an atom density profile $n(\bar{r}, t')$, at all times, from the atomic positions $\bar{r}_j(t')$. To include the effect of OAM in our simulations it is enough to consider a linear phase gradient on the on the input pump, namely:

$$A_I(\bar{r}) = \mathcal{A}_I \exp\left(il\frac{2\pi}{L_d}\bar{r}\right) \tag{3.52}$$

An example of outcome of our simulations is shown below in Fig. 3.11 for two cases of $N = 5 \times 10^4$ atoms and with OAM index $l = 3, 4$, where one observes a lateral drift of the patterned intensity and atom densities, whose velocity depends on the domain size L_d. Such drift corresponds exactly to the differential rotation in the 2-d case discussed in Sec. 3.3.2.

In the rest of this section it is show that, at onset of self-organization, occurring at $t' = \kappa t \approx 5$ as visible from the space-time plots of Fig. 3.11, the atoms trapped in the 1-d geometry start developing a net mass current along the domain, induced by the presence of the phase gradient (3.52) in the input pump. This is displayed in detail in Fig. 3.12 a), where the value of the atomic current $\langle \bar{p}(t') \rangle$ for two different OAM cases ($l = 3, 4$) is computed at each t' according to both the previously discussed methods, namely, the density integral[33] in Eq. (3.48) and the ensemble average in Eq. (3.50). Both cases are characterized by an exponential-like growth of the order parameter $\langle \bar{p}(t') \rangle$. Such growth saturates around $t' = \kappa t \approx 10$, where it fluctuates around a certain steady state value. Note that the two obtained time series in each case display a highly correlated behaviour, since the statistical fluctuations are clearly not independent[34].

Fig. 3.12 b) shows instead the time evolution of the atomic current, from the initial state

---

[32]Most commonly expressed in terms of the spread of the momentum distribution ζ_p^2, i.e., $D_p' = \bar{\gamma}\zeta_p^2$.

[33]Obtained by means of the numerical density profile $n(\bar{r}, t)$.

[34]They both arise from the realizations of the same stochastic variable $\bar{\xi}_j(t')$.
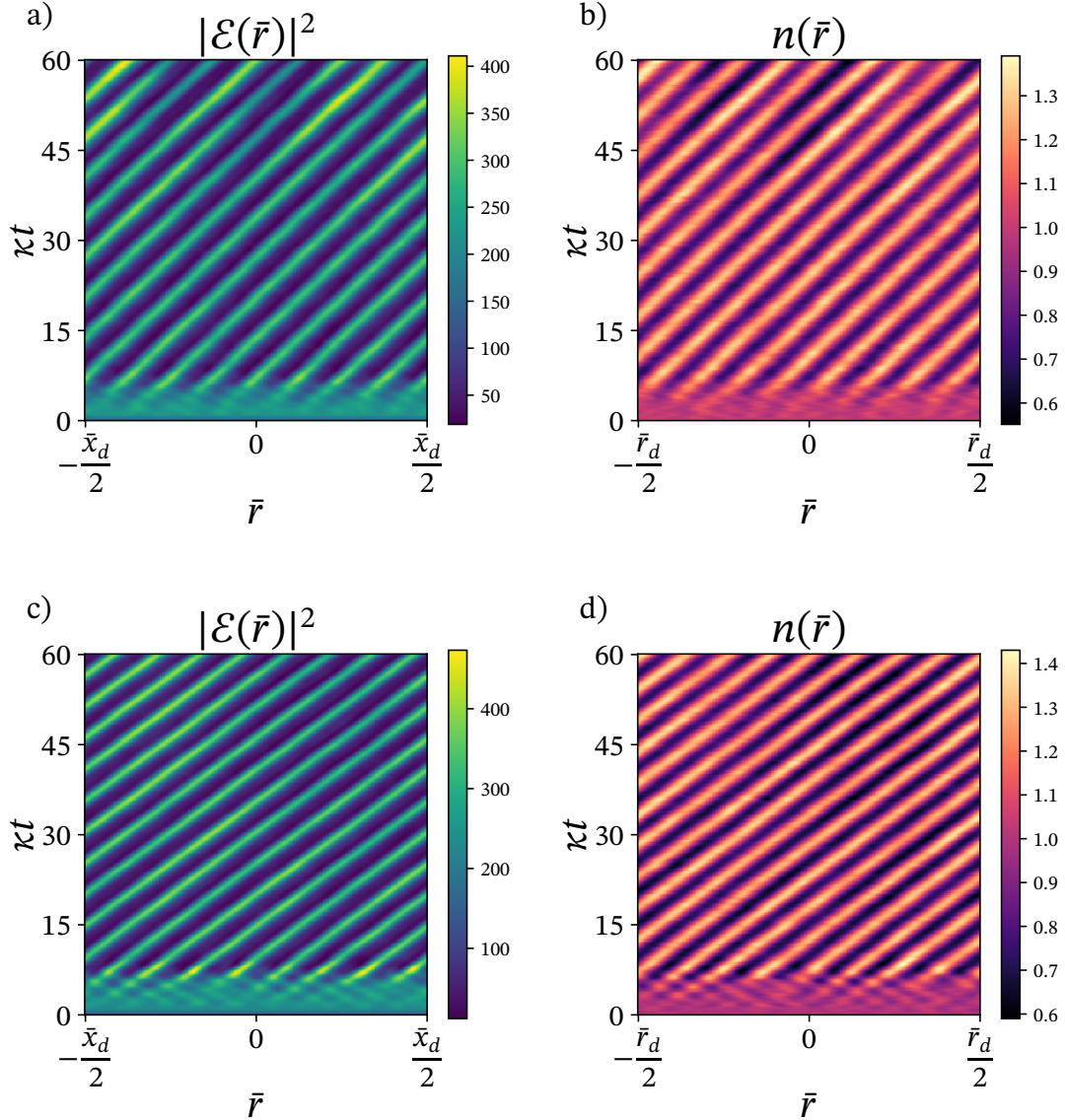
Fig. 3.11. Numerical results from the particle dynamics simulation of $N = 5 \times 10^4$ atoms with OAM. a) Space-time plot showing the evolution of the patterned 1-d cavity intensity up to $\kappa t_{max} = 60$ and with $dt' = 2 \times 10^{-2}$. b) Density self-ordering, where the function $n(\bar{r}, t)$ has been reconstructed numerically from particle trajectories $\{\bar{r}_j(t')\}$. For blue-detuned pumping ($\Delta > 0$), the atoms tend to bunch onto the minima of the cavity intensity $|\mathcal{E}(\bar{r})|^2$. The slope of the patterned phases in such plots is induced by OAM with index $l = 3$ a), b) and $l = 4$ c), d), and corresponds to the rotation of the pattern in the purely azimuthal case. Model parameters are chosen as follows: $\frac{\Gamma}{\kappa} = \bar{\omega}_p = \bar{\gamma} = 1$, $\zeta_p = 0.707$, $\Delta = 100$, such that $D' \approx 2$, $\sigma \approx 25$.
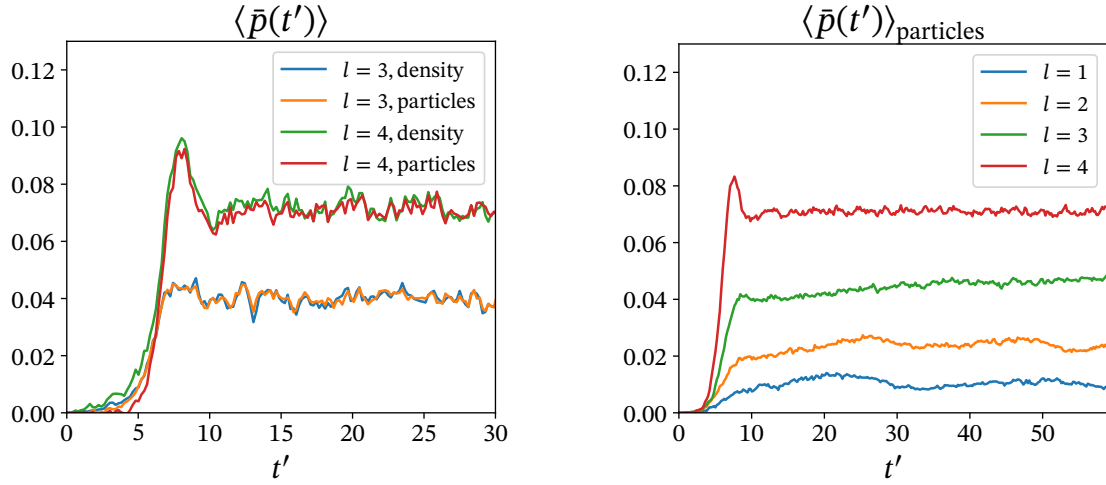
Fig. 3.12. OAM induced atomic currents along the 1-d domain measured by the average particle momentum. The atomic ensemble that is initially defined at rest and distributed homogeneously in the 1-d domain develops net current at the onset of self-organization. (Left) Time evolution of the rescaled average momentum $\langle \bar{p}_j(t') \rangle$ (in units of $\hbar q_c$), with OAM index $l = 3, 4$, obtained from both the ensemble average in Eq. (3.48) and from the reconstructed density profile $n(\bar{r}, t)$ in Eq. (3.50). (Right) Dynamics of the atomic current measured for different values of the OAM index $l = 1, \dots, 4$. In order to reduce the amplitude of fluctuations around the steady state, each line is in turn averaged over a set of 10 identical launches for each case.
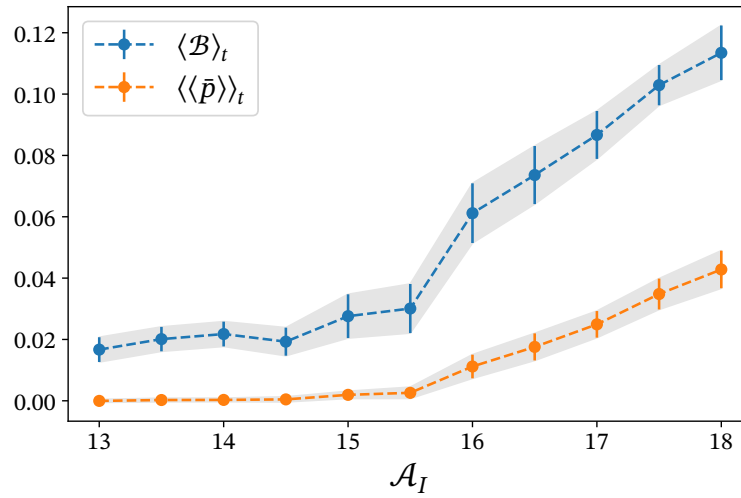
Fig. 3.13. Time averaged bunching factor vs atomic current with fixed OAM $l = 3$. Numerical integration of the cavity-atom/particle dynamics is performed up to $t'_{\max} = 60$, where both quantities are averaged in the steady state phase with uncertainty provided by the standard deviation. Both quantities are nonzero and increasing in the ordered phase above threshold, although $\langle \mathcal{B} \rangle_t$ displays a residual bunching below threshold, due to the the density fluctuations that trigger transient modulations. However, the random nature of such transient bunching does is not associated with any current and is expected to vanish for $N_{\text{atoms}} \to +\infty$.

$t' = 0$ to the equilibrium value achieved at $t' \approx 15$. In order to get more precise steady state values for each $l = 1, \ldots, 4$, one can average over a certain number of realizations. By choosing 10 launches, one observes a nonlinear increase of the steady state atomic currents with the OAM index l. At first glance, this observation might suggest that the efficiency OAM transfer mechanism that is introduced here increases quadratically with l. This conclusion, however, deserves additional investigation and a careful analysis of the angular momentum conservation, in absence of optical molasses damping. Finally, in order to emphasize the connection between the self-organization process and the building up of the atomic current it is useful to recall a commonly used order parameter for the atom density known as the *bunching factor*, defined as follows [174]:

$$\mathcal{B}(t') = \frac{\int_\Omega n(\bar{r}, t') \exp{(-i2\pi\bar{r})} d\bar{r}}{\int_\Omega n(\bar{r}, t') d\bar{r}} = \hat{n}(2\pi, t'), \tag{3.53}$$

i.e., simply representing the amplitude of the resonant component of the atomic density. Since Eq. (3.53) provides a time dependent quantity, it is worth to consider in addition a time average $\langle \mathcal{B} \rangle_t$ on a sufficiently large period at steady state. The same concept is applied to the atomic current so that one can simply span over a range of input pump amplitudes $\mathcal{A}_I$ including the threshold. This is shown in Fig. 3.13, where the two symmetry breaking parameters are plotted as a function of $\mathcal{A}_I$, displaying a common qualitative behaviour, namely, flat-like below threshold[35] and steadily increasing above threshold. This yields an evidence that the emerging atomic current is purely due to the self-trapping in the drifting light-atom lattice. As already mentioned before, possible generalizations of such effect may involve the case of an optomechanical instability without momentum damping [54], and the case of a quantum degenerate bosonic gas. In this last case, our setup potentially provides a platform to study vortex formation and issues related to quantum turbulence [175, 176].

---

[35]Roughly occurring at $\mathcal{A}_I \approx 15.5$

Chapter 4

Atom optomechanics and structured light II: SFM setup

This chapter presents novel results concerning cold atom optomechanical instabilities in a single-feedback mirror setup (SFM). Particular emphasis is given to the recent prediction of *structural transitions* among phases characterized by different geometric configurations. Such behaviour is intrinsically due to the transport generating character of the system nonlinearity and cannot be captured by a simplified nonlinear picture, e.g., the Kerr limit. Moreover, the interplay among structured light and atomic transport in self-organized ring lattices is also discussed here. The material from this chapter is partially published in Ref. [177].

4.1 Transverse instabilities with optical feedback

Spatial (modulation) instabilities in a single-feedback-mirror system were introduced and analyzed systematically by Firth in Ref. [5], as a generalization of a pattern formation experiment with a sodium vapour involving time delay, proposed by Giusfredi *et al.* [178]. After the first theoretical efforts in describing transverse hexagon formation by means of an effective-Kerr nonlinear medium [6, 7], several experimental implementations were proposed, including liquid crystal systems [179], photorefractive media [180], and alkali metal vapors [181]. The minimal scheme of the SFM system is sketched in Fig. 4.1 a), where the optical medium is assumed to be a cloud of laser cooled atoms, characterized by length L, optical density at resonance b_0 and at constant temperature T. Neglecting the effect of diffraction, the field propagation equations for $\mathcal{E}_\pm(\mathbf{r}, t)$ inside the medium read:

$$\partial_z \mathcal{E}_\pm(\mathbf{r}, t) = \pm i \frac{\chi}{L} n(\mathbf{r}, t) \, \mathcal{E}_\pm(\mathbf{r}, t), \tag{4.1}$$

where the + signs corresponds to the forward propagating field $\mathcal{E}_+$ and viceversa. Assuming low saturation and large atomic detuning Δ, the purely real susceptibility of the atomic gas reads $\chi = b_0 \Delta / 2(1 + \Delta^2)$. The main advantage of such a setup lies in the fact that it is often justified to consider the optical medium as *diffractively thin*, i.e., the effect of diffraction is only
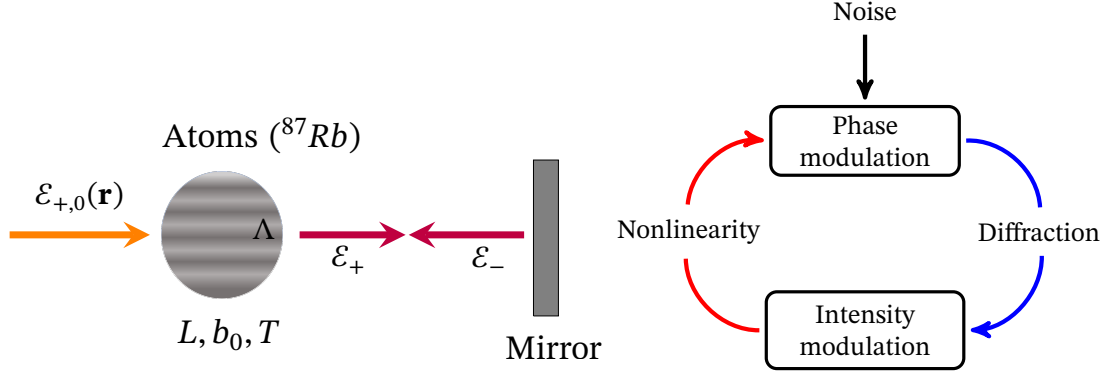
Fig. 4.1. (Left) Cold atomic cloud in a SFM scheme. A far detuned input field of amplitude $\mathcal{E}_{+,0}$ and wavenumber k_0 drives a cloud of Rubidium atoms of thickness L, optical density b_0 and temperature T. The reflected field $\mathcal{E}_-$ provides optical feedback by means of the dipole potential, leading to transverse self-organized structures. (Right) Conceptual scheme of the feedback loop leading to optomechanical self-structuring, initiated by random fluctuations (noise). The propagation in free space (diffraction) converts phase modulations into amplitude (and intensity) modulations, creating a dipole potential that dynamically enhances the original phase modulations.

accounted for in the free-space propagation to the mirror and back[1]. Moreover, the feedback loop is closed by considering paraxial propagation in free space between the atoms and the feedback mirror as follows:

$$\partial_z \mathcal{E}_\pm(\mathbf{r}, t) = \pm \frac{1}{2ik_0} \nabla_\perp^2 \mathcal{E}_\pm(\mathbf{r}, t). \tag{4.2}$$

The mechanism behind the feedback instability can be understood by adopting the simple picture by Tamburrini *et al.* involving *Talbot effect* [184, 185], namely, the fact that any phase modulation induced, e.g., by a spatial grating of wavelength Λ, is converted completely into an amplitude modulation after propagation at a quarter of the so-called Talbot distance[2], i.e., $z_T = 8\pi^2/(\Lambda k_0^2)$. In this sense, the self-structuring instability, triggered by random density fluctuations, is possible by means of diffraction, providing transverse spatial coupling via intensity modulations (in the reflected field $\mathcal{E}_-(\mathbf{r})$) and building up a dipole potential for the atoms. Therefore, pump photons are scattered by the modulated atom density $n_{\mathrm{eq}}(\mathbf{r})$ onto the sideband modes, enhancing the Talbot-converted intensity modulations. Above a certain threshold, one has positive feedback and the system spontaneously selects a (self)-structured state characterized by a critical wavelength Λ_{cr}. A generic scheme of the feedback loop instability mechanism is represented in Fig. 4.1 b). The threshold condition for the purely optomechanical instability is addressed in the rest of this section, focusing on one a distinctive feature of the SFM setup, namely the periodicity of higher order instabilities[3].

---

[1]This assumption simplifies a lot the model. See Refs. [182, 183] for the case of a diffractively thick medium.

[2]For $z = z_T$ the grating image is reproduced, whereas at $z = z_T/2$ and $z = 3z_T/4$ one has $\pi/2$-shifted phase and amplitude modulations respectively.

[3]Note that this periodicity is in general lost when considering thick medium effects as in Refs. [182, 183].

Threshold condition

Let us discuss here the derivation of the instability threshold in the optomechanical SFM system by following the original approach by Firth [5, 167]. By identifying with R the reflectivity of the mirror in the setup, and conveniently rescaling the spatial coordinates as $(\mathbf{r}', z') = D^{-1/2}(\mathbf{r}, z)$ and introducing $L' = D^{-1/2}L$, $d' = D^{-1/2}d$, one obtains the following coupled system of partial differential equations:

$$\partial_{z'}\mathcal{E}_{\pm}(\mathbf{r}', t) = \pm i\frac{b_0 \Delta}{2L'(1 + \Delta^2)}\, n(\mathbf{r}', t)\, \mathcal{E}_{\pm}(\mathbf{r}', t), \tag{4.3}$$

$$\partial_t n(\mathbf{r}', t) = \sigma \nabla'_{\perp} \cdot \left[n(\mathbf{r}', t)\, \nabla'_{\perp} s(\mathbf{r}', t)\right] + \nabla'^2_{\perp} n(\mathbf{r}', t), \tag{4.4}$$

$$\partial_{z'}\mathcal{E}_{\pm}(\mathbf{r}', t) = \pm\frac{i\eta}{2d'}\nabla'^2_{\perp}\mathcal{E}_{\pm}(\mathbf{r}', t), \tag{4.5}$$

where the two constants:

$$\eta = \frac{d}{k_0 D}, \; \sigma = \frac{\hbar\Gamma\Delta}{4k_B T}, \tag{4.6}$$

measure of the competition between diffraction and atomic diffusion and an optomechanical coupling constant respectively. Representing the homogeneous intensity as $I = |\mathcal{E}_{+,0}|^2$, the family of homogeneous steady states of the above Eqs. (4.3, 4.4, 4.5) is given as follows:

$$\begin{cases} \mathcal{E}_{+,0} = \sqrt{I}, \\ \mathcal{E}_{-,0} = \sqrt{RI}, \\ n_{\text{eq}} = 1. \end{cases} \tag{4.7}$$

Spatial modulations as perturbations to the homogeneous backwards field $\mathcal{E}_{-,0}$ are conveniently introduced in Fourier space as $\mathcal{E}_-(\mathbf{q}', t) = \mathcal{E}_{-,0}\left[\delta(\mathbf{q}') + \epsilon_1(\mathbf{q}', t)\right]$, where $\delta(\mathbf{q}')$ is the Dirac delta function and $\mathbf{q}'$ the transverse wavevector. The total optical intensity (saturation parameter) reads[4] as $s(\mathbf{r}', t) = |\mathcal{E}_{+,0}|^2 + |\mathcal{E}_-(\mathbf{r}', t)|^2$ so that the Fourier-transformed counterpart $s(\mathbf{q}', t)$ at first order simply reads:

$$s(\mathbf{q}', t) = RI\left[\epsilon_1(\mathbf{q}', t) + \epsilon_1^*(\mathbf{q}', t)\right]. \tag{4.8}$$

Such modulations due to the backwards field cause density redistributions $n(\mathbf{q}', t)$. Therefore, the expression of $b_1(\mathbf{q}', t)$ at first order in the density perturbation $n_1(\mathbf{q}', t)$ reads:

$$\epsilon_1(\mathbf{q}', t) = i\frac{b_0 \Delta}{2(1 + \Delta^2)}\exp(-i\Theta)n_1(\mathbf{q}', t), \tag{4.9}$$

where $\Theta = \eta|\mathbf{q}'|^2$ is the total diffractive phase slippage after propagation at distance $z = 2d'$.

---

[4]By doing so, it is implicitly assumed that longitudinal grating formation due to standing wave effects of the two counter-propagating fields are neglected. See the supplementary material of [53] for a detailed discussion.
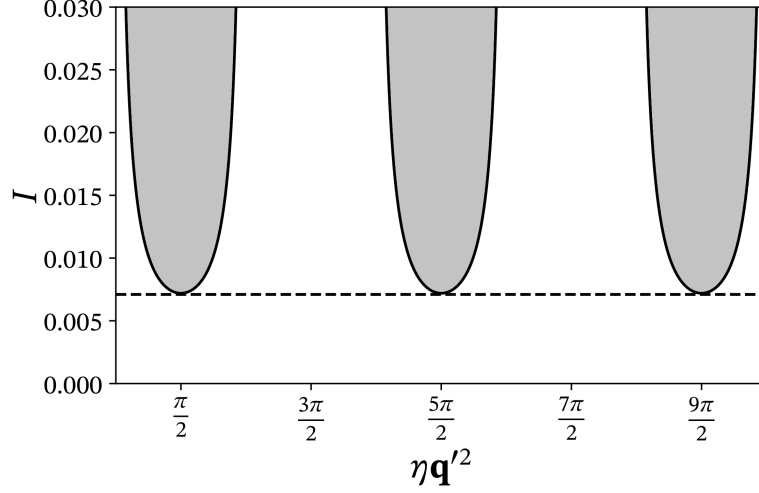
Fig. 4.2. Intensity threshold dependence on the diffractive phase shift $\Theta = \eta \mathbf{q}'^2$ (black solid line). The condition $I \geq I(\Theta)$ identifies instability domains, centered around the minima $\eta q_{cr}'^2 = (4m + 1)\pi/2$, $m \in \mathbb{N}$, as expected for a purely dispersive self-focusing medium. Note the degeneracy of the minima of $I(\Theta)$, represented by the black dashed line.

A closed linearized form of the Smoluchowski equation from Eq. (2.67) is derived as follows:

$$\partial_t n_1(\mathbf{q}', t) = -|\mathbf{q}'|^2 \left\{ n_1(\mathbf{q}', t) - \sigma RI \left[\epsilon_1(\mathbf{q}', t) + \epsilon_1^*(\mathbf{q}', t) \right] \right\} \tag{4.10}$$

$$\partial_t n_1(\mathbf{q}', t) = -|\mathbf{q}'|^2 n_1(\mathbf{q}', t) \left[1 - \frac{\sigma RI b_0 \Delta \sin \Theta}{(1 + \Delta^2)} \right]. \tag{4.11}$$

Parametrizing $n_1(\mathbf{q}', t) = a \exp(i\mathbf{q}' \cdot \mathbf{r}' + \nu t) + \text{c.c}$, one obtains the following (rescaled) linear growth rate[5] $\nu(\mathbf{q}')$ of modulations at wavenumber $\mathbf{q}'$:

$$\nu(\mathbf{q}') = -|\mathbf{q}'|^2 \left[1 - \frac{\sigma RI b_0 \Delta \sin \Theta}{(1 + \Delta^2)} \right]. \tag{4.12}$$

Imposing marginal stability, i.e., a vanishing growth rate $\nu(\mathbf{q}') = 0$, leads to the minimum threshold condition, namely:

$$I = \frac{1 + \Delta^2}{\sigma R \, b_0 \Delta \sin \Theta} \geq \frac{1 + \Delta^2}{\sigma R \, b_0 \Delta} = I_0. \tag{4.13}$$

As represented in Fig. 4.2, the term $\sin \Theta$ in the above threshold gives rise to a perfect periodicity with respect to the diffractive shift Θ of the instability domains. This implies that, in order to numerically simulate the purely optomechanical instability, a Fourier filter is necessary when integrating diffraction so that the growth of shorter wavelengths is damped[6]. The

---

[5]Note that, as in Ref. [5], one obtains a purely stationary instability so that $\text{Im}[\nu] = 0$.
[6]Such a degeneracy implies that higher order frequencies are excited above threshold and this is non-physical.

presence of such degeneracy is intrinsically due to the nonlinear form of the optomechanical transport generating product in the Smoluchowski equation. This can be removed by considering a complete theory for a diffractively thick optical medium [182, 183].

The rest of this chapter is divided into two sections. First of all, the occurrence of a multiple pattern selection mechanism in the optomechanical system and its origin is discussed by means of numerical and analytical observations. Moreover, in the second section, the occurrence of transport effects in 2-d is discussed by means of particle dynamics simulations.

4.2 Multiple self-organized phases and structural transitions

In this section, the transverse self-structuring of a cold atomic cloud in a SFM setup is analyzed for a wide range of parameters. The resulting landscape of structures due to optomechanical forces is much richer than expected for an effective-Kerr medium and displays hexagonal, stripe and honeycomb phases. Such a phase selection process depends on the linear susceptibility of the atomic cloud. Phase domains are obtain numerically and their analytical description is given by means of real Ginzburg-Landau amplitude equations.

4.2.1 Phase diagram and weakly nonlinear approach

The stability and coexistence of 2-d optomechanical patterns is addressed here by means of numerical observations. First of all, a substantial advantage, inherent to the dissipative dynamics of the Smoluchowski Eq. (2.67) with respect to the conservative case, is that, due to the typical separation of timescales, one can still use the (quasi) stationary state, given by the canonical Gibbs distribution [51]:

$$n_{\text{eq}}(\mathbf{r}',t) = \frac{\exp[-\beta U_{\text{dip}}(\mathbf{r}',t)]}{\int_\Omega d^2\mathbf{r}' \exp[-\beta U_{\text{dip}}(\mathbf{r}',t)]} = \frac{\exp[-\sigma s(\mathbf{r}',t)]}{\int_\Omega d^2\mathbf{r}' \exp[-\sigma s(\mathbf{r}',t)]}, \qquad (4.14)$$

where Ω indicates the integration domain. The feedback loop is numerically integrated according to the following simple scheme:

1. Propagate the input beam through the atomic cloud, namely: $\mathcal{E}_+(z' = L', \mathbf{r}', t) = \mathcal{E}_{+,0} \exp\left[i\chi n(\mathbf{r}',t)\right]$.

2. Solve free-space propagation for the reflected field $\mathcal{E}_-(z' = L', \mathbf{r}', t)$ in Fourier space with wavenumber filtering.

3. Update the atomic density by means of the equilibrium distribution in Eq. (4.14).

The above feedback loop is iterated until the reflected field $\mathcal{E}_-(\mathbf{r}')$ adjusts itself to its stationary state[7]. As expected for a Kerr-like medium and based on the experimental observations in

---

[7]Such integration time varies in general but a $N_{max} = 150$ is enough for our aim.

a) $|\mathcal{E}_-(\mathbf{r}')|^2$ b) $|\mathcal{E}_-(\mathbf{r}')|^2$ c) $|\mathcal{E}_-(\mathbf{r}')|^2$

d) $n_{eq}(\mathbf{r}')$ e) $n_{eq}(\mathbf{r}')$ f) $n_{eq}(\mathbf{r}')$
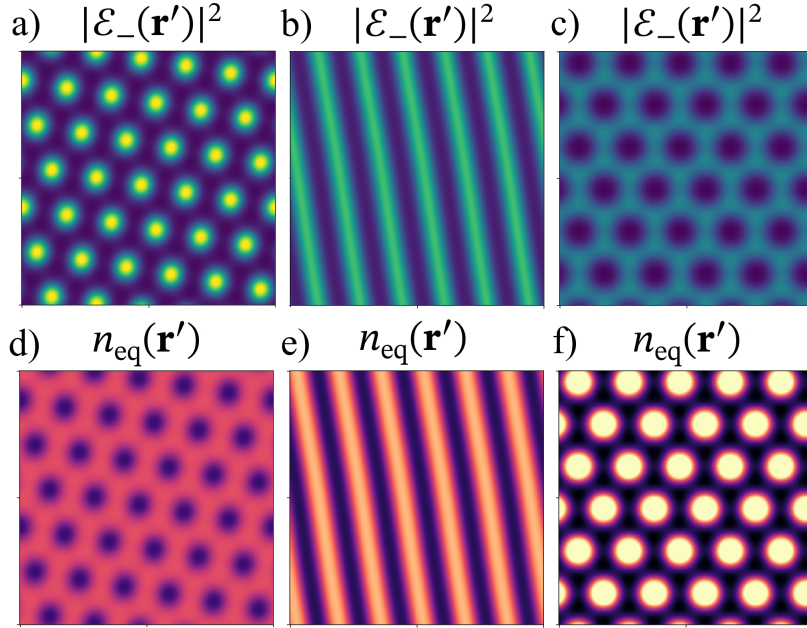
Fig. 4.3. Multiple self-structured phases obtained from an homogeneous initial state with fixed optical density $b_0 = 110$ and temperature $T = 300\ \mu$K. a),d) $\mathbf{H}^-$ phase at $\Delta = 25$. b),e) $\mathbf{S}$ phase at $\Delta = 55$. b),e) $\mathbf{H}^+$ phase at $\Delta = 90$.

Ref. [53], the emergent spatial instability typically leads to an hexagonally patterned state in the backwards field $\mathcal{E}_-(\mathbf{r}')$ above threshold and, thus, the atom density is expected to choose an hexagonal (honeycomb) configuration for $\Delta < 0$ ($\Delta > 0$). From now on, the labels $\mathbf{H}^\pm$ and $\mathbf{S}$ are used to indicate positive/negative hexagon and stripe atom density states respectively. The presence of multiple stable self-structured phases is shown in Fig. 4.3, for different values of atomic detuning ($\Delta > 0$) and at fixed optical density of the cloud b_0.

Transitions between different phases are observed in simulations by tuning the values of the two main parameters in the cloud susceptibility χ, namely b_0 and Δ. Therefore, it is useful to span numerically the two dimensional space (Δ, b_0), within the experimentally achievable ranges[8] of $\Delta = [10, 110]$ and $b_0 = [50, 150]$. The corresponding phase stability diagram is obtained from numerical integration of the feedback loop by seeding an $\mathbf{S}$ state as the initial state and iterating it until convergence to the stable steady state structure is reached. In order to distinguish between phases, it is enough to count the number of peaks in the resonant circle of the far field[9]. Results are shown in Fig. 4.4, where one distinguishes a region of stable stripe states $\mathbf{S}$, sandwiched between two domains of stable hexagons with opposite signs $\mathbf{H}^\pm$.

A crucial observation is that the phase boundaries in Fig. 4.4 match with lines of constant linear susceptibility χ. Such behaviour is analyzed in detail in the rest of this section, by means of the weakly nonlinear expansion. This approach leads to a simplified description of

---

[8]See Ref. [53] for the details of the experimental realization.
[9]Indeed, one sees that the corresponding Fourier transform of a generic n-mode pattern in Fig. 4.3 displays the same number of peaks.
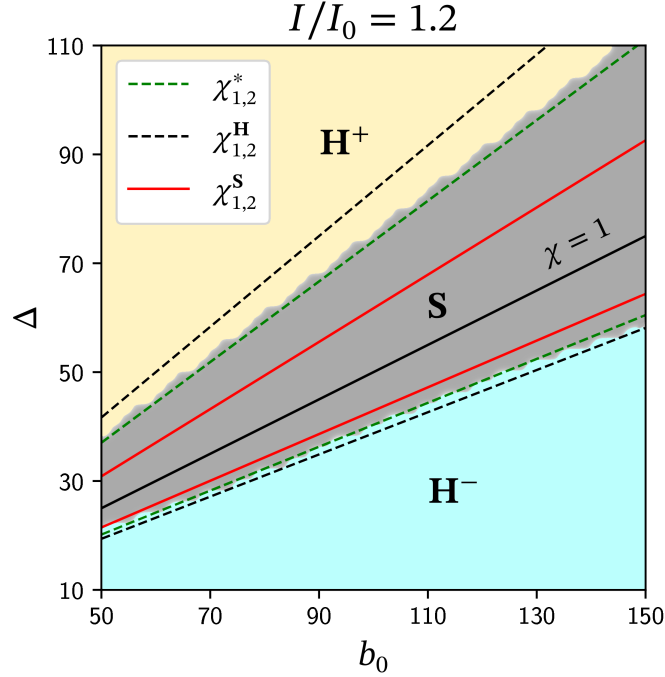
Fig. 4.4. Numerically observed stability domains of the stripe **S** and hexagonal $\mathbf{H}^\pm$ atom density phases at fixed I/I_0. Stripe states **S** (grey) are absolutely stable on a domain sandwiched between lines corresponding to the values $\chi_{1,2}^{\mathbf{S}}$ (red lines), around $\chi = 1$ (solid black line). Stripe states **S** coexist with hexagons $\mathbf{H}^\pm$ and minimize a free energy functional in the region between the $\chi_{1,2}^{\mathbf{H}}$ (dashed-black lines) and $\chi_{1,2}^*$ points (dashed-green lines). $\mathbf{H}^\pm$ phases are stable within the yellow-cyan domains and absolutely stable outside the region delimited by $\chi_{1,2}^{\mathbf{H}}$. The specific values of χ corresponding to the phase boundaries are derived in the next section.

our system in terms of amplitude equations, and is a commonly used method to characterize pattern transitions in transverse nonlinear optical systems [7, 186–189]. Applied to our case, the weakly nonlinear expansion provides an estimation of the phase boundaries in excellent agreement with the numerical observation, establishing a theoretical framework to describe such structural transitions in a self-structured cold atomic gas[10].

Nonlinear and slow-scale expansions

A first step to introduce the weakly nonlinear approach is given by a formal integration of the equation for the backwards field in the presence of a homogeneous pump, namely:

$$\mathcal{E}_-(\mathbf{r}',t) = \sqrt{RI}\,\hat{\mathcal{L}}e^{i\chi n(\mathbf{r}',t)}, \tag{4.15}$$

where the differential operatorial notation $\hat{\mathcal{L}} = e^{-id'\nabla_\perp'^2/k_0} = e^{-i\eta\nabla_\perp'^2}$ is adopted. Thus, substituting Eq. (4.15) into the Smoluchowski equation, one is left with one, formally exact, equa-

---

[10]See Ref. [190] for an introduction to structural phase transitions in condensed matter.

tion[11] for the atom density perturbation $\delta n(\mathbf{r}', t)$:

$$(-\nabla_\perp'^2 + \partial_t) \chi \delta n(\mathbf{r}', t) = R\sigma I \chi \nabla_\perp' \cdot \left[(1 + \delta n(\mathbf{r}', t)) \nabla_\perp' |\hat{\mathcal{L}} e^{i\chi \delta n(\mathbf{r}', t)}|^2 \right]. \qquad (4.16)$$

Similarly, one can use the same approach in order to derive a closed equation capturing the features of the long-range interactions mediated by feedback in a SFM scheme [191]. Expanding now the backwards intensity term $|\hat{\mathcal{L}} e^{i\chi \delta n}|^2$ up to order $O\left[(\chi \delta n)^3 \right]$, one obtains:

$$\begin{aligned}
\hat{\mathcal{D}} \chi \delta n = R\sigma D I \nabla_\perp' \cdot \Bigg\{ &(\chi + \chi \delta n) \nabla_\perp' \left[i \left(\mathcal{L} - \hat{\mathcal{L}}^\dagger \right) \chi \delta n - \frac{1}{2} \left(\mathcal{L} + \hat{\mathcal{L}}^\dagger \right) (\chi \delta n)^2 + (\hat{\mathcal{L}} \chi \delta n)(\hat{\mathcal{L}}^\dagger \chi \delta n) \right. \\
&\left. - \frac{i}{6} \left(\mathcal{L} - \hat{\mathcal{L}}^\dagger \right) (\chi \delta n)^3 + ... \right] \Bigg\} + O\left[(\chi \delta n)^4 \right],
\end{aligned}$$
$$(4.17)$$

where $\hat{\mathcal{D}} = (-\nabla_\perp'^2 + \partial_t)$ is the diffusion differential operator. At a linear level $O(\chi \delta n)$, our problem is restated in the following form:

$$\hat{\mathcal{G}}(\chi \delta n) = \left[\hat{\mathcal{D}} - R\sigma I \chi \nabla_\perp' \cdot \nabla_\perp' i \left(\mathcal{L} - \hat{\mathcal{L}}^\dagger \right) \right] \chi \delta n = \left[\hat{\mathcal{D}} - 2R\sigma I \chi \nabla_\perp'^2 \sin\left(\eta \nabla_\perp'^2 \right) \right] \chi \delta n = 0. \qquad (4.18)$$

This is solved in Fourier space[12] and leads us to recover the linear growth rate $\nu(\mathbf{q})$ in Eq. (4.12). An accurate description of pattern competition phenomena due to weak nonlinear terms are captured by introducing a formal slow-scale expansion up to third order contributions in a generic parameter ϵ as follows [7, 192]:

$$\chi \delta n(\mathbf{r}', t) = \sum_{i=1}^{3} \epsilon^i n_i(\mathbf{r}', t) + O(\epsilon^4), \quad \nabla_\perp' = \sum_{i=0}^{3} \epsilon^i \nabla_i, \quad \partial_t = \sum_{i=1}^{3} \epsilon^i \partial_{T_i},$$

$$\nabla_\perp'^2 = \nabla_\perp' \cdot \nabla_\perp' = \sum_{i+j \leq 3} \epsilon^{i+j} \nabla_i \cdot \nabla_j, \quad I = I_0 p = I_0 \left(1 + \sum_{i=1}^{3} \epsilon^i p_i \right) + O(\epsilon^4),$$

$$(4.19)$$

where $\chi \delta n$ is already first order in ϵ by definition, and I_0 represents the minimum threshold. Such a separation of spatial and temporal scales is essential in order to distinguish variations of the carrier terms (fast) and amplitude (slow) modulations, in a generic ansatz for atom density modulations $\delta n(\mathbf{r}', t)$. Furthermore, the purely nonlinear character of pattern selection is embedded in the the so-called *solvability conditions* for higher order terms of the slow-scale expansion. Those contributions generally appear in the form $\hat{\mathcal{G}} n_i = S_i$, where $\hat{\mathcal{G}}$ is the linear operator in Eq. (4.18) and S_i typically include slow derivatives and, most importantly, other nonlinear terms in n_j, $j < i$, which potentially lead to the presence of secular growth. Therefore, the solvability conditions are derived by simply imposing that such terms vanish.[13]

---

[11]In such an approach, the feedback time delay ($\approx 10^{-9}s$) is neglected, since the medium diffusive timescales are much slower in our case.

[12]By means of the usual replacement rules $\nabla_\perp' \to i\mathbf{q}'$, $\hat{\mathcal{D}} \to |\mathbf{q}|^2 + \nu$ for a purely stationary instability.

[13]In other words, by applying Fredholm's alternative theorem, one has that, in order for $\hat{\mathcal{G}} n_i = S_i$ to hold at each order, the resonant Fourier components of S_i belonging to its orthogonal complement $\ker(\hat{\mathcal{G}}^\dagger)^\perp$ must vanish

In what follows, the procedure leading to the solvability conditions is applied to our case, i.e., the nonlinear expansion in Eq. (4.17). At second order $O(\epsilon^2)$, one starts by considering the slow-scale expansion of the linear operator, namely $\mathcal{G} = \hat{\mathcal{G}}_0 + \epsilon\hat{\mathcal{G}}_1$, where:

$$\hat{\mathcal{G}}_1 = \hat{\mathcal{D}}_1 - iR\sigma I_0\chi\left[\nabla_0^2\left(\hat{\mathcal{L}}_1 - \hat{\mathcal{L}}_1^\dagger\right) + 2\nabla_0\cdot\nabla_1\left(\hat{\mathcal{L}}_0 - \hat{\mathcal{L}}_0^\dagger\right) + p_1\nabla_0^2\left(\hat{\mathcal{L}}_0 - \hat{\mathcal{L}}_0^\dagger\right)\right], \qquad (4.20)$$

and $\hat{\mathcal{L}}_1 = i\eta\hat{\mathcal{L}}_0\nabla_0\cdot\nabla_1$. It is useful to group the following remaining terms at order $O(\epsilon^2)$ from Eq. (4.17):

$$\mathcal{R}_1 = R\sigma I_0\left[i\nabla_0\cdot\left(n_1\nabla_0\left(\hat{\mathcal{L}}_0 - \hat{\mathcal{L}}_0^\dagger\right)n_1\right) - \frac{\chi}{2}\nabla_0^2\left(\hat{\mathcal{L}}_0 + \hat{\mathcal{L}}_0^\dagger\right)n_1^2 + \chi\nabla_0^2(\hat{\mathcal{L}}_0 n_1)(\hat{\mathcal{L}}_0^\dagger n_1)\right]. \qquad (4.21)$$

Thus, Eqs. (4.20) and (4.21) combined provide the source term $S_2 = -\hat{\mathcal{G}}_1 n_1 + \mathcal{R}_1$ at second order in the slow-scale expansion. However, as anticipated in Sec. 2.3.3, the $\mathbf{H}^\pm - \mathbf{S}$ competition involves cubic coefficients and terms in the amplitude equations which can be derived only by means of a third-order slow-scale expansion only. Such a procedure involves in principle also a non-resonant term n_2. Therefore, at orders $O(\epsilon^2)$ and $O(\epsilon^3)$, the solvability conditions for our optomechanical nonlinear problem are obtained by imposing $S_2 = 0$ and $S_3 = 0$, where the source term $S_3 = -\hat{\mathcal{G}}_1 n_2 - \hat{\mathcal{G}}_2 n_1 + \mathcal{R}_2$ reads:

$$\hat{\mathcal{G}}_2 = \hat{\mathcal{D}}_2 - iR\sigma I_0\chi p_2\nabla_0^2\left(\hat{\mathcal{L}}_0 - \hat{\mathcal{L}}_0^\dagger\right),$$

$$\mathcal{R}_2 = p_1\mathcal{R}_1 + iR\sigma I_0\chi\nabla_0^2\left\{\frac{1}{2}\left[(\hat{\mathcal{L}}_0 n_1^2)(\hat{\mathcal{L}}_0^\dagger n_1) - (\hat{\mathcal{L}}_0 n_1)(\hat{\mathcal{L}}_0^\dagger n_1^2)\right] - \frac{1}{6}\left(\hat{\mathcal{L}}_0 - \hat{\mathcal{L}}_0^\dagger\right)n_1^3\right\} +$$
$$R\sigma I_0\left\{\nabla_0\cdot\left(n_1\nabla_0\left[(\hat{\mathcal{L}}_0 n_1)(\hat{\mathcal{L}}_0^\dagger n_1) - \frac{1}{2}\left(\hat{\mathcal{L}}_0 + \hat{\mathcal{L}}_0^\dagger\right)n_1^2\right]\right)\right\} + \dots \text{nonlinear terms in } n_2. \qquad (4.22)$$

However, in order to capture the essential physics of structural phase transitions, it is enough to adopt here a less rigorous procedure by simply neglecting all slow derivatives and non-resonant terms[14] n_j, $j \geq 2$ [7, 186]. Thus, the solvability condition would simply read $S_3 = 0$ at $O(\epsilon^3)$. Such conditions contain already all the necessary ingredients to arrive to the amplitude equations for our system in the canonical real Ginzburg-Landau form.

Amplitude equations coefficients

Let us recall from Eq. (2.80) the form of the general hexagonal (three-mode) ansatz for the resonant terms n_1:

$$n_1 = \frac{1}{2}\left[\sum_{i=1}^3 A_i\exp\left(i\mathbf{q}_i\cdot\mathbf{r}'\right) + \text{c.c.}\right], \qquad (4.23)$$

---

identically [192].

[14]Such an assumption significantly reduces computational complexity.
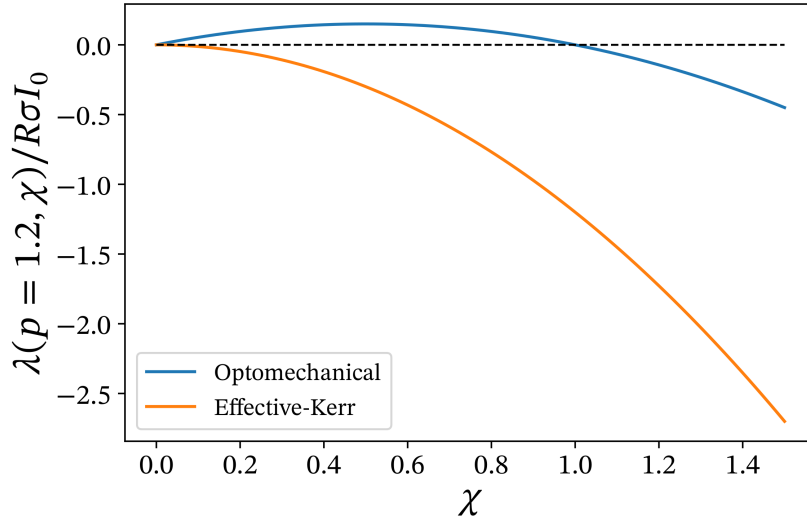
Fig. 4.5. Quadratic coefficient $\lambda(p, \chi)$ dependence on the purely dispersive susceptibility χ ($\Theta_c = \pi/2$) and fixed $p = 1.2$ for the cold-atom optomechanical system (solid blue line) and the effective-Kerr medium (solid orange line). Note the sign change for $\chi = 1$, determining the emergence of an $\mathbf{H}^+$ atom-density phase for $\chi = 1$.

where the tree wavevectors must obey the phase matching condition $\mathbf{q}_1 + \mathbf{q}_2 + \mathbf{q}_3 = 0$ with $|\mathbf{q}_i| = q_c^2$, and the complex variables A_i satisfy the amplitude equations as follows:

$$\partial_t A_i = \mu A_i + \lambda A_j^* A_k^* - \gamma_1 \sum_{j \neq i} |A_j|^2 A_i - \gamma_2 |A_i|^2 A_i, \tag{4.24}$$

where $i, j, k = 1, 2, 3$ and $i \neq j \neq k$. The solvability conditions allows to identify an expression for the coefficients $\mu, \lambda, \gamma_1, \gamma_2$ in terms of model parameters. As already stated above, at order $O(\epsilon^2)$, one obtains the source term $S_2 = -\hat{\mathcal{G}}_1 n_1 + \mathcal{R}_1 = 0$, where:

$$\hat{\mathcal{G}}_1 n_1 = -\partial_t n_1 + iR\sigma I_0 \chi \left[p_1 \nabla_\perp'^2 \left(\hat{\mathcal{L}} - \hat{\mathcal{L}}^\dagger \right) \right] n_1, \tag{4.25}$$

$$\mathcal{R}_1 = R\sigma I_0 \left[i\nabla_\perp' \cdot \left[n_1 \nabla_\perp' \left(\hat{\mathcal{L}} - \hat{\mathcal{L}}^\dagger \right) n_1 \right] - \frac{\chi}{2} \nabla_\perp'^2 \left(\hat{\mathcal{L}} + \hat{\mathcal{L}}^\dagger \right) n_1^2 + \chi \nabla_\perp'^2 (\hat{\mathcal{L}} n_1)(\hat{\mathcal{L}}^\dagger n_1) \right]. \tag{4.26}$$

Recalling that $p = I/I_0$ and assuming a generic critical shift[15] Θ_c, the linear growth and three-mode mixing coefficients can be obtained from Eqs. (4.26) (See appendix A.3) and read:

$$\mu(p, \chi) = 2RI_0\sigma (p - 1)\chi \sin \Theta_c, \tag{4.27}$$

$$\lambda(p, \chi) = \frac{RI_0\sigma p\chi}{2} \left[\sin \Theta_c + \chi(\cos \Theta_c - 1) \right]. \tag{4.28}$$

Focusing on the coefficient $\lambda(p, \chi)$, two important considerations already arise from an expansion at $O(\epsilon^2)$. Firstly, one observes a change of sign around the point $\chi = \cot(\Theta_c/2)$ ($\chi = 1$

---

[15]Note that this generalizes the treatment to the case of an absorptive system.

with the usual $\Theta_c = \pi/2$), shown in Fig. 4.5. As already introduced in Sec. 2.3.3, this special feature, due to a shifted quadratic dependence on the cloud susceptibility[16] χ, determines a change in the family of hexagonal states observed ($\mathbf{H}^+$ for the case $\lambda > 0$ and vice versa) [7]. Secondly, since the sign change occurs only for $\chi > 0$, structural transitions are expected to occur in the blue side of the atomic resonance ($\Delta > 0$) only[17].

As also demonstrated later, a complete description of phase competition processes, including the observed one in Fig. 4.4 for the cold-atom optomechanical system, is based on the variational nature of Eqs. (4.24) and requires the so-called Lyapunov or *free energy* functional [128]. To this aim, the self and cross-cubic coefficients of the amplitude equations are computed as follows (See appendix A.3):

$$\gamma_1(p, \chi) = \frac{RI_0\sigma p\chi^2}{4}\left[\chi\sin\Theta_c + 2 - \frac{1}{2}\left(\cos 3\Theta_c + \cos\Theta_c\right)\right] \tag{4.29}$$

$$\gamma_2(p, \chi) = \frac{RI_0\sigma p\chi^2}{8}\left[\chi\left(\sin\Theta_c - \sin 3\Theta_c + \frac{2}{3}\right) + 2(1 - \cos 4\Theta_c)\right], \tag{4.30}$$

For a wide variety of nonlinear systems, the selection of patterns/structures close to threshold is described by means of the critical points introduced in Sec. 2.3.3, that crucially depend on the coefficients of the amplitude Eqs. (4.27, 4.28, 4.29, 4.30) [2, 128]. Such stability limits are discussed in the rest of this section.

4.2.2 Free energy and stability of the self-structured phases

Let us introduce here the Lyapunov functional $\mathcal{F}[\{A_i\}]$ in order to describe pattern competition of the optomechanical self-structured phases. Such quantity can be interpreted as a configurational free energy density for our pattern forming system. Firstly, one shows that the dynamics of the amplitude equations in Eq. (4.24) is variational, i.e., it can be derived via the following gradient rule [2]:

$$\partial_t A_i = -\frac{\partial\mathcal{F}}{\partial A_i^*}. \tag{4.31}$$

The functional $\mathcal{F}[\{A_i\}]$ is represented in the following quartic form, as in the weak crystallization [193, 194], and dipolar condensate cases [195]:

$$\mathcal{F}[\{A_i\}] = -\mu\sum_{i=1}^{3}|A_i|^2 - \lambda\left(A_1^*A_2^*A_3^* + \text{c.c.}\right) + \frac{\gamma_2}{2}\sum_{i,j=1}^{3}|A_i|^2|A_j|^2 + \frac{\gamma_1}{2}\sum_{i=1}^{3}|A_i|^4, \tag{4.32}$$

where $i = 1, 2, 3$ and $i \neq j$. Moreover, the Lyapunov functional is minimized during time evolution, namely:

$$\frac{d}{dt}\mathcal{F} = -2\sum_{i=1}^{3}\left|\frac{\partial A_i}{\partial t}\right|^2 \leq 0. \tag{4.33}$$

---

[16]The dependence is purely quadratic, i.e., $\lambda \propto \chi^2$, in the effective-Kerr model (see Ref. [7]).

[17]Vice versa, only $\mathbf{H}^-$ atom-density states are expected at threshold for red-detuning.
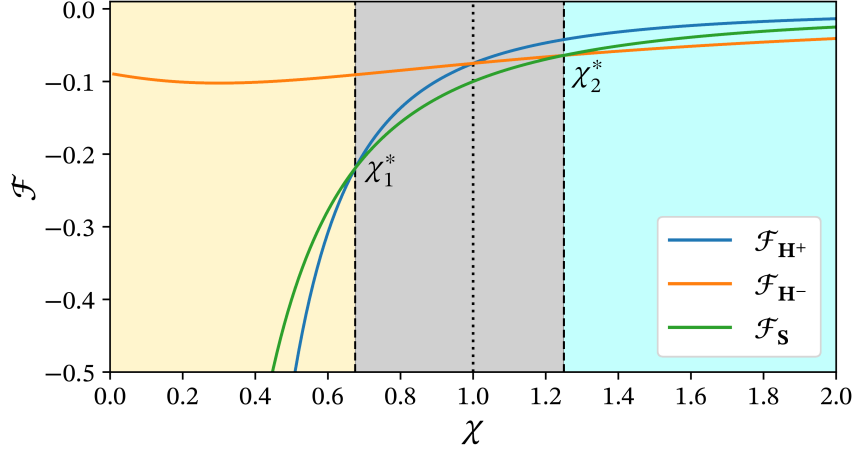
Fig. 4.6. Lyapunov/free energy functional in dependence of the cloud susceptibility χ of the self-structured phases at fixed $p = 1.2$: $\mathcal{F}_{\mathbf{H}^+}(\chi)$ (solid blue line), $\mathcal{F}_{\mathbf{H}^-}(\chi)$ (solid orange line), $\mathcal{F}_{\mathbf{S}}(\chi)$ (solid green line). The minimum determines the observed atom-density phase in each domain while the intersections χ_1^* and χ_2^* (dashed black lines) correspond to the phase boundaries in Fig. 4.4. Note that $\mathcal{F}_{\mathbf{H}^-} = \mathcal{F}_{\mathbf{H}^+}$ at $\chi = 1$.

Eq. (4.33) justifies the abuse of notation in identifying the functional in Eq. (4.32) as a (configurational) free energy density[18]. For the hexagonal states $\mathbf{H}^\pm$, one considers the perfectly balanced ansatz where the amplitudes $A_1 = A_2 = A_3 = \mathcal{A}_\pm$ are defined as roots of the quadratic equation $(\gamma_2 + 2\gamma_1)\mathcal{A}_\pm^2 - \lambda\mathcal{A}_\pm - \mu = 0$. This gives rise to the following free energy densities [128]:

$$\mathcal{F}_{\mathbf{H}^\pm} = -3\mu\mathcal{A}_\pm^2 - 2\lambda\mathcal{A}_\pm^3 + \frac{3}{2}(\gamma_2 + 2\gamma_1)\mathcal{A}_\pm^4. \tag{4.34}$$

For the $\mathbf{S}$ phase instead $A_1 = \mathcal{A}_{\mathbf{S}} = \sqrt{\mu/\gamma_2}, A_2 = A_3 = 0$, as well as:

$$\mathcal{F}_{\mathbf{S}} = -\mu\mathcal{A}_{\mathbf{S}}^2 + \frac{\gamma_2}{2}\mathcal{A}_{\mathbf{S}}^4. \tag{4.35}$$

The dependence of $\mathcal{F}_{\mathbf{H}^\pm}$ and $\mathcal{F}_{\mathbf{S}}$ on the cloud susceptibility χ and corresponding minima are shown in Fig. 4.6, together with the intersections χ_1^* and χ_2^*, identified by the following condition:

$$\mu = \frac{\lambda^2[\gamma_2^2 + 3\gamma_2\gamma_1 + \sqrt{2\gamma_2}(\gamma_1 + \gamma_2)^{3/2}]}{2(\gamma_2 + 2\gamma_1)(\gamma_2 - \gamma_1)^2}, \tag{4.36}$$

which represent points of equal free energy of the $\mathbf{S}$ and $\mathbf{H}^\pm$ phase, corresponding to the transition points between different minima[19]. For the choice of model parameters in Fig. 4.4, one obtains the estimates $\chi_1^* \approx 0.675$ and $\chi_2^* \approx 1.24$, providing a satisfactory agreement with the boundaries observed by means of numerical integration. In addition, as already introduced

---

[18]Note that our system is out of equilibrium and, thus, the analogy works at a mathematical level only.

[19]As well as perfectly stationary phase fronts in the transverse domain.
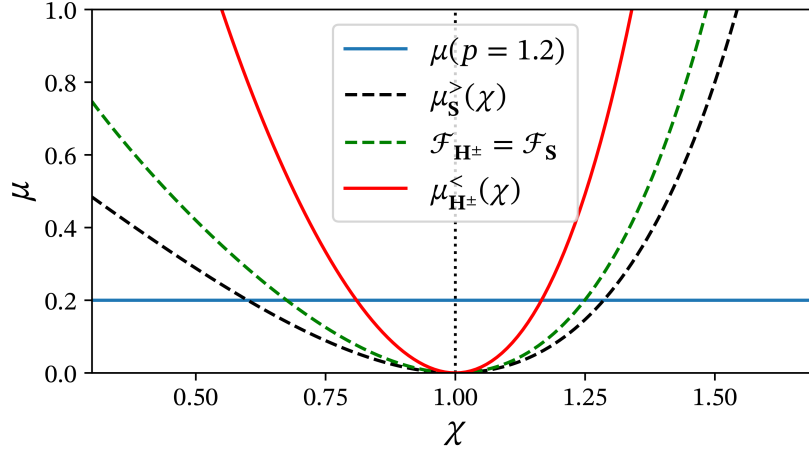
Fig. 4.7. Critical points $\mu_S^>$ and $\mu_{H^\pm}^>$ from Eqs. (4.37) (dashed-black/red lines) and phase boundaries (dashed-green line) from Eq. (4.36) as functions of the cloud susceptibility χ. Intersections with $\mu(\chi)$ (constant blue line) determine the size of the **S/H**-phase competition domains as reported in Fig. 4.4.

in Sec. 2.3.3, the critical limits read [134]:

$$\mu_S^> = \frac{\lambda^2 \gamma_2}{(\gamma_1 - \gamma_2)^2}, \quad \mu_{H^\pm}^< = \frac{\lambda^2 (2\gamma_2 + \gamma_1)}{(\gamma_1 - \gamma_2)^2}, \tag{4.37}$$

representing the lower stability limit of the **S** phase and the higher stability limit of $\mathbf{H}^\pm$ phases respectively. Those two conditions generate in our case two other pairs of intersections as shown in Fig. 4.7 and reported in the phase diagram Fig. 4.4. The rest of this section is aimed at discussing a second interesting consequence of a vanishing quadratic coefficient in the amplitude equation, namely, the nontrivial recovery of *inversion symmetry*.

Inversion symmetry of optomechanical structures

Pattern forming instabilities in systems described by Ginzburg-Landau amplitude equations and that lack inversion symmetry ($\delta n(\mathbf{r}') \to -\delta n(\mathbf{r}')$), typically result in a non zero quadratic coefficient λ and are shown to prefer $\mathbf{H}^\pm$ states depending on the sign of λ [2]. In our case, the optomechanical system displays **S** states that satisfy inversion symmetry in the vicinity of the critical susceptibility $\chi = 1$ point[20], whereas both hexagonal phases $\mathbf{H}^+$ and $\mathbf{H}^-$ states break such symmetry and are related by the inversion symmetry transformation.

The recovery of inversion symmetry is a known phenomenon in dissipative pattern formation [134]. Interestingly, in the cold-atom optomechanical system, the recovery of such a symmetry ($\lambda = 0$) results from self-tuning, in dependence on an coupling strength provided by the cloud susceptibility χ, whereas, in other systems, transitions to inversion symmetric states typically results from a change in the boundary conditions such as in the mass transport cases of

---

[20]From now on, the point $\chi = 1$ will be denoted as *inversion symmetric point*.

Marangoni and Rayleigh-Bénard convections [196]. In atomic systems, similar transitions can be controlled by symmetry-breaking external fields [61] or polarization imbalances [186, 197], and strong changes in the homogeneous solution [159, 198–200].

As pointed out before, the cold-atom optomechanical model exhibits a richer behavior with respect to an effective-Kerr model, namely, the presence of structural transitions and the recovery of inversion symmetry. This difference between the two models can be identified by considering the specific form of the nonlinear term. Indeed, the analogue of Eq. (4.16) for the refractive index perturbation[21] $\delta n(\mathbf{r}', t)$ in the effective-Kerr case in a SFM configuration reads as follows [7]:

$$(\hat{\mathcal{D}} + 1)\delta n(\mathbf{r}', t) = RI\chi \left[|\mathcal{L}e^{i\chi\delta n(\mathbf{r}',t)}|^2 - 1 \right]. \tag{4.38}$$

where χ indicates here a generic Kerr medium susceptibility and the nonlinear part in the RHS involves the field intensity only via the term $|\hat{\mathcal{L}}e^{i\chi\delta n(\mathbf{r}',t)}|^2$. A necessary and sufficient condition for a third-order perturbation theory to display a nontrivial recover of inversion symmetry of spatial modulation is that the quadratic term of the expansion vanishes for a value of the coupling constant $\chi \neq 0$ [2]. One can show that, expanding the RHS of Eq. (4.38), such condition is never achieved and thus, no **S** state is possible in the system.

The optomechanical nonlinearity displays instead a drift-generating product $n(\mathbf{r}', t)\nabla'_\perp s(\mathbf{r}', t)$ in the Smoluchowski equation, and recalling the hexagonal ansatz in Eq. (4.23), one observes that the quadratic term of the nonlinear expansion in Eq. (4.17) reads:

$$\chi\delta n \left[\nabla'_\perp i \left(\mathcal{L} - \hat{\mathcal{L}}^\dagger \right) \chi\delta n \right] - \frac{\chi}{2} \left[\left(\mathcal{L} + \hat{\mathcal{L}}^\dagger \right)(\chi\delta n)^2 - 2(\mathcal{L}\chi\delta n)(\hat{\mathcal{L}}^\dagger\chi\delta n) \right] =$$
$$- \sin\Theta_c \mathcal{A}^2\Xi(\nabla'_\perp\Xi) - \frac{\chi}{2}\left[\cos\Theta_c\mathcal{A}^2\nabla'_\perp\Xi^2 - \mathcal{A}^2\nabla'_\perp\Xi^2 \right] \tag{4.39}$$

where $A_1 = A_2 = A_3 = \mathcal{A}$ for the perfectly balanced case and $\Xi = \sum_i (\exp(\phi_i) + \text{c.c.})$. Therefore, recalling the critical shift $\Theta_c = \pi/2$ for the purely dispersive medium and that $\nabla'_\perp\Xi^2 = 2\,\Xi(\nabla'_\perp\Xi)$, Eq. (4.39) simply reduces to:

$$(-1 + \chi)\mathcal{A}^2\Xi(\nabla'_\perp\Xi) = 0. \tag{4.40}$$

Eq. (4.40) vanishes, i.e., the system is inversion-symmetric, if and only if $\chi = 1$, in accordance with the above calculation involving the symmetry-breaking coefficient $\lambda(p, \chi)$ in the Ginzburg-Landau amplitude equations (4.24).

4.3 Optomechanical transport across multiple phases

This last section is aimed at addressing further aspects of atomic transport in the cold-atom optomechanical model in a single-feedback-mirror configuration. In particular, the content is divided into two subsections dedicated to the existence of the novel phases in the 2-d model,

---

[21]In the effective-Kerr case, such modulation is encoded in the carrier excitation density in semiconductors.

predicted previously in Sec. 4.2, in the *conservative limit* and the study of atomic mass transport properties in the phases with different inversion symmetry, by means of 1-d particle dynamics simulations.

Conservative limit

In order to understand whether the momentum dissipation plays any role in the structural phase transitions occurring in the optomechanical model, one can start with preliminary considerations, by means of 2-d numerical simulations of the purely Hamiltonian case, i.e., in absence of both momentum damping and stochastic forces. In this case, the kinetic temperature of the ensemble is entirely determined by the momentum distribution[22]. Purely Hamiltonian equations of motion for a set of classical undamped atoms are introduced as follows ($j = 1, \dots, N_{\text{atoms}}$):

$$\dot{\mathbf{r}}_j = \frac{\mathbf{p}_j}{m}, \quad \dot{\mathbf{p}}_j = \mathbf{f}_{\text{dip}}(\mathbf{r}, t), \tag{4.41}$$

where m is the atomic mass. Note that the stochastic variable introduced previously is missing in (4.41) since, in absence of damping, the initial temperature of the ensemble is determined by the initial momentum distribution which is conserved by the Hamiltonian dynamics. At the onset of transverse instability, the cold-atom optomechanical system spontaneously selects the critical wavenumber $q_c = \sqrt{\pi k_0 / 2d}$ for the purely self-focusing case. One thus defines $\bar{\mathbf{r}}_j = q_c \mathbf{r}_j$ and $\bar{\mathbf{p}} = \mathbf{p}_j / \hbar q_c$, such that Eqs. (4.41) become:

$$\frac{\partial \bar{\mathbf{r}}_j}{\partial \bar{t}} = 2\bar{\mathbf{p}}_j, \quad \frac{\partial \bar{\mathbf{p}}_j}{\partial \bar{t}} = -\frac{\Gamma \Delta}{4\omega_q} \frac{d}{d\bar{\mathbf{r}}} |\mathcal{E}_-(\bar{\mathbf{r}}, \bar{t})|^2, \tag{4.42}$$

where $\omega_q = \hbar q_c^2 / 2m$ represents a recoil frequency associated with a standing wave potential of modulation q_c and $\bar{t} = \omega_q t$. As introduced in Ch. 3, the two terms describing the effect of momentum dissipation in the Kramers-Chandrasekhar equation (3.21) vanish and the particle dynamics is effectively described by a Vlasov equation in the thermodynamic limit $N_{\text{atoms}} \to \infty$, by means of the 1-particle probability distribution $f(\bar{\mathbf{r}}, \bar{\mathbf{p}}, \bar{t})$, such that the probability integral $\int_\Omega d\bar{\mathbf{r}} \, d\bar{\mathbf{p}} \, f(\bar{\mathbf{r}}, \bar{\mathbf{p}}, \bar{t}) = 1$, namely [173]:

$$\frac{\partial}{\partial \bar{t}} f(\bar{\mathbf{r}}, \bar{\mathbf{p}}, \bar{t}) = -2\bar{\mathbf{p}} \frac{d}{d\bar{\mathbf{r}}} f(\bar{\mathbf{r}}, \bar{\mathbf{p}}, \bar{t}) + \frac{\Gamma \Delta}{4\omega_p} \left[\frac{d}{d\bar{\mathbf{r}}} s(\bar{\mathbf{r}}, \bar{t}) \cdot \frac{d}{d\bar{\mathbf{p}}} f(\bar{\mathbf{r}}, \bar{\mathbf{p}}, \bar{t}) \right]. \tag{4.43}$$

Two cases corresponding to different values of the linear susceptibility, namely $\chi \approx 0.1$[23] and $\chi = 1$ (inversion symmetric point) are considered, since the novel $\mathbf{H}^+$ and $\mathbf{S}$ atom density phases have been observed and predicted in the mean-field dissipative overdamped model. Particle dynamics simulations, shown in Fig. 4.8, provide instead a preliminary evidence that the novel stable phases of the cold-atom optomechanical system are also found in the purely

---

[22]For this reason, one typically defines the initial state the atoms as normally distributed in momentum space, where the width of the distribution corresponds to the observed kinetic temperature.

[23]Largely beyond the absolute stability oh the $\mathbf{H}^+$ atom density phase (See the phase diagram of Fig. 4.4).
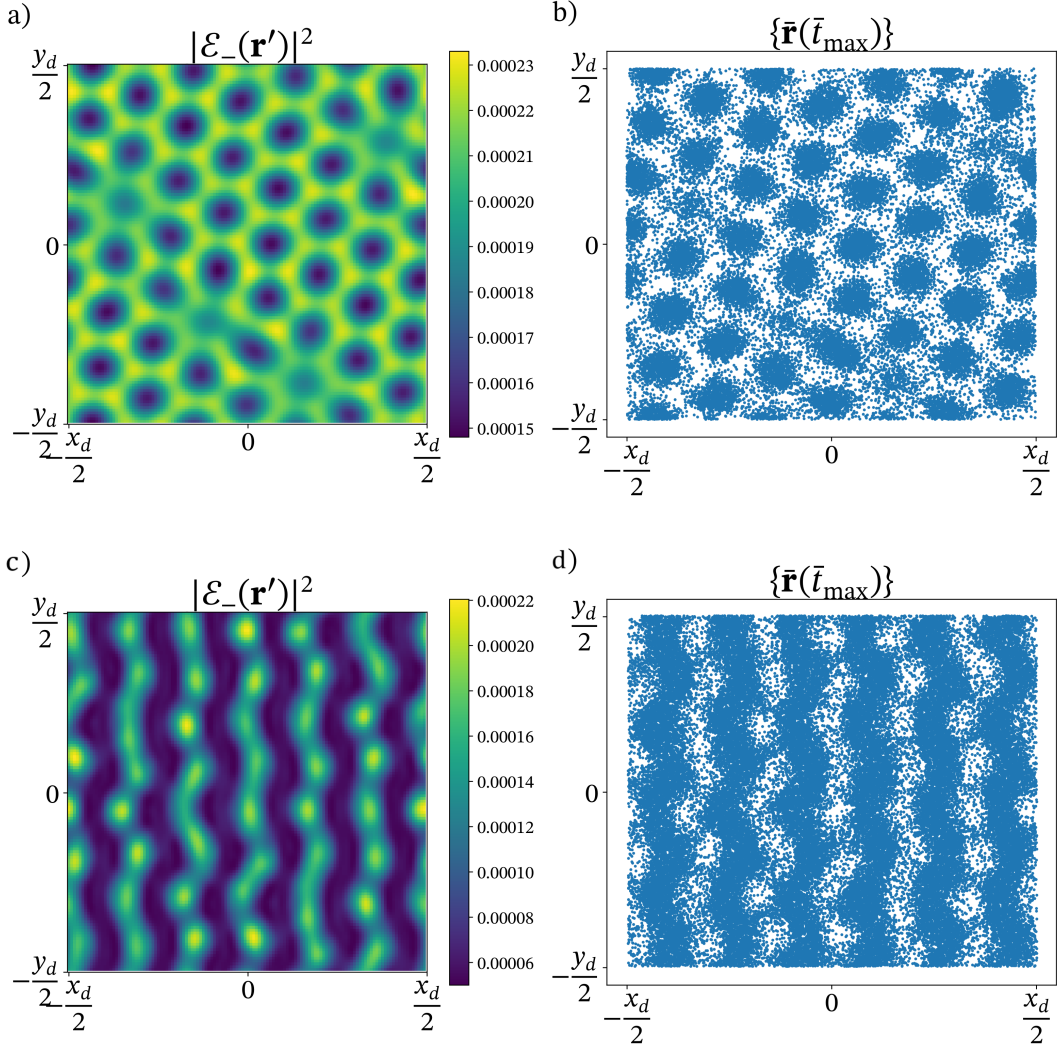
Fig. 4.8. Results from 2-d particle dynamics numerical simulations for a set of 5×10^4 atoms and above threshold for $\bar{t}_{\max} = 250$. a) - b) Backwards intensity $|\mathcal{E}_-(\bar{\mathbf{r}}, \bar{t}_{\max})|^2$ in a $\mathbf{H}^-$ (left) and $\mathbf{H}^+$ particle distribution $\{\bar{\mathbf{r}}_j(\bar{t}_{\max})\}$ ($\mathbf{H}^+$ phase). Model parameters: $b_0 = 20, \Delta = 100$, such that $\chi = 0.1$, mirror reflectivity $R = 1$. c) - d) Backwards intensity $|\mathcal{E}_-(\bar{\mathbf{r}}, \bar{t}_{\max})|^2$ and particle distribution in a $\mathbf{S}$ phase for $b_0 = 100, \Delta = 50$, such that $\chi = 1$ (inversion symmetry point).

conservative limit. The numerical simulations are performed up to $\bar{t}_{\max} = 250$ and with the choices $d\bar{t} = 0.5, \omega_q = 0.378$, where the intensity fields and atom densities are defined on a grid of size 128×128. In particular, Figs. 4.8 a), b) clearly show the formation of an $\mathbf{H}^+$ state from an homogeneous initial state with $\chi = 0.1$ whereas, in Figs. 4.8 c), d), the initially seeded $\mathbf{S}$ state survives with the appearance of modulations along the connected stripes and local distortions of the initial stripe geometry[24], and are expected to disappear in the thermodynamic limit $N_{\text{atoms}} \to +\infty$.

---

[24]Such an effect however is expected to represent a numerical artifact, induced by atom density fluctuations due to the relatively small number of atoms
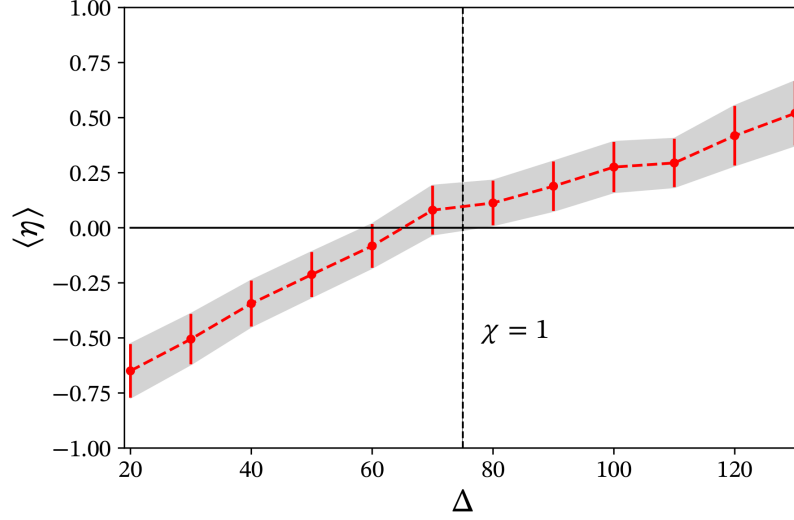
Fig. 4.9. Average displacement of the atomic density from the homogeneous value ($n = 1$, $\langle\eta\rangle = 0$) across the inversion symmetry state at susceptibility $\chi = 1$. Results measured from 1-d particle dynamics simulations at fixed $b_0 = 150$, from densities reconstructed from the trajectories of a set of $N_{\text{atoms}} = 10^4$ at different detunings Δ. Note that $\langle\eta\rangle$ changes sign around $\chi = 1$ and, as expected from 2-d simulations, $\langle\eta\rangle < 0$ for values of Δ such that $\chi > 1$ and viceversa.

Transport in blue detuned lattices

A further interesting application of the structural transitions, at different susceptibilities χ, is the study of atomic currents induced by OAM in effectively 1-d light-atom lattices in the two phases $\mathbf{H}^{\pm}$ with broken inversion symmetry. A footprint of the change in inversion symmetry of the atomic lattice can be found also in a 1-d model. Indeed, by means of particle-in-cell simulations in the SFM system, one can measure the onset of self-organization in the 1-d atomic lattice for various detunings Δ and fixed optical densities b_0, in order to span within a range of values of the linear susceptibility χ centered at the inversion symmetric point $\chi = 1$. The results are shown in Fig. 4.9, where the displacement of the atomic lattice with respect to the homogeneous value $n_{\text{eq}} = 1$ is computed by simply defining $\langle\eta\rangle$ as an average on the noisy spatial profile of the atomic density and subtracting the homogeneous background, namely:

$$\langle\eta\rangle = \frac{1}{2}\left[\max_{\Omega} n_{\text{eq}}(\mathbf{r}) + \min_{\Omega} n_{\text{eq}}(\mathbf{r})\right] - 1. \tag{4.44}$$

As expected from the general argument involving the recovery of inversion symmetry in Sec. 4.2.2, the figure of merit $\langle\eta\rangle$ is negative (positive) for $\chi < 1$ ($\chi > 1$) meaning that the 1-d density is regarded as an array of negative (positive) density peaks.

To analyze the influence of the structural transition on the behaviour of the atomic transport induced by OAM, steady-state atomic currents $\langle\langle p\rangle\rangle_t$ are measured by a further time average, as introduced in Fig. 3.13 of the Ch. 3. This is shown in Fig. 4.10, where a general increasing trend as a function of the atomic detuning Δ is expected since, at fixed distance from threshold,
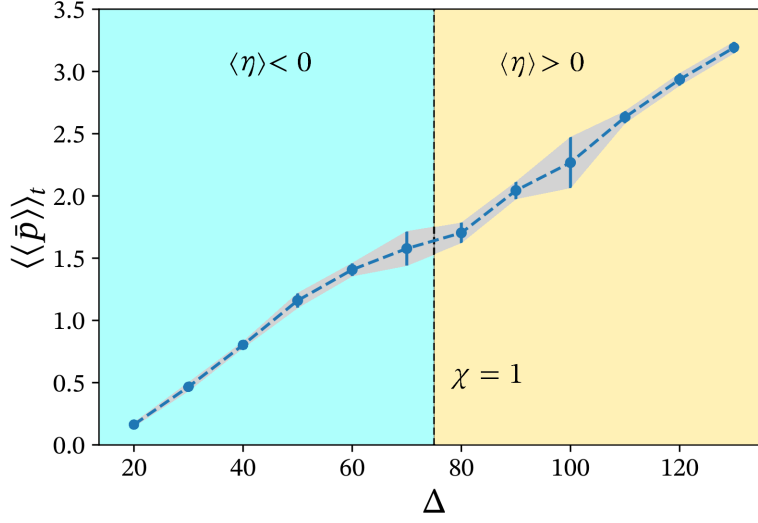
Fig. 4.10. Steady state and time-averaged atomic current $\langle\langle p \rangle\rangle_t$ measured from particle simulations across the range $\Delta \in [20, 130]$ at fixed $b_0 = 150$ (meaning that the inversion symmetric point $\chi = 1$ lies at $\Delta^* \approx 75$) and OAM index $l = 1$. Note that the linear increase of $\langle\langle p \rangle\rangle_t$ is interrupted within a certain range in correspondence of the inversion symmetric lattice.

stronger bunching of atoms on the self-organized lattice sites leads to higher steady-state currents for drifting patterns induced by OAM[25]. Interestingly, the behaviour of $\langle\langle p \rangle\rangle_t$ around the inversion symmetric point $\chi = 1$ reveals a distinct trend since the linear increase is slowed down on a certain range centered at $\Delta^* \approx 75$. This result, together with those in Fig. 4.9, seems to suggest that the inversion symmetric lattice in the 1-d is effectively *locked* in a certain range including Δ^*, unveiling a possible fingerprint of the 2-d structural transition also in the 1-d model. Such an intuition stemming from preliminary observations, however, needs to be verified with further numerical simulations in both the SFM and the ring cavity models and a weakly nonlinear expansion. Due to the technical difficulty involved, such an approach is left to future studies addressing the recovery of inversion symmetry in the 1-d cold atom optomechanical model.

---

[25]This is expected to saturate for Δ high enough to prevent particle hopping between neighboring sites, since the drifting velocity of the lattice does not depend on Δ.

Chapter 5

Dynamics and transport of optomechanical dissipative solitons

The present chapter summarizes several original contributions regarding dissipative solitons in the cold-atom optomechanical model in both ring cavity and single-feedback-mirror configurations. In particular, Sec. 5.1 addresses an interesting further consequence of the structural phase transitions widely discussed in the Ch. 4, namely, the existence of a novel kind of coupled light-density soliton for blue light-atom detuning which is characterized by a dark spot, hosting a bright density peak of atoms. This is called *dark light optomechanical soliton*. The role of structured input beams in transporting optomechanical cavity solitons is addressed in Sec. 5.2, where the spatial dependence of the pump profile is shown to effectively induce soliton motion in closed (rotating) or open (spiralling) orbits in the transverse plane.

5.1 Feedback solitons and atomic transport

The concept of optomechanical dissipative soliton as a coupled light-atom localized structure was introduced by Tesio *et al.* in Ref. [71], for the cold-atom ring-cavity model [51]. In this section, it is shown that the same feature occurs in the SFM model with novel consequences stemming from the structural phase transitions discussed in Ch. 4. A historical introduction to the concept is found below.

5.1.1 Collective self-focusing and light-atom solitons

Let us start by providing an overview of the basic mechanism behind dissipative soliton formation in driven clouds of cold atoms, namely, the collective self-focusing due to spatial inhomogeneities of the atomic density[1]. As anticipated already in Sec. 3.1, the possibility of a mutual self-focusing effects occurring in the coupled dynamics of light and matter waves was introduced by Klimontovic and Luzgin in 1979 [161]. The treatment adopted here follows instead Ref. [165, 202]. The nonlinear index of refraction of the two-level atomic cloud can be

---

[1]See Ref. [201] for a general review of self-focusing and instabilities in spatial solitons.

obtained directly from its nonlinear susceptibility and takes the following form [53]:

$$\eta(\mathbf{r}, s) = 1 - \frac{3\lambda_0^3}{4\pi^2} \frac{\Delta}{2(1 + \Delta^2)} \frac{n(\mathbf{r}, s)}{1 + s(\mathbf{r})}, \tag{5.1}$$

where λ_0 is the radiation wavelength. Focusing on the field dependent part $\eta_E(\mathbf{r}, s)$ only, and using the Gibbs equilibrium distribution in Eq. (2.68), one obtains:

$$\eta_E(\mathbf{r}, s) = -\frac{3\lambda_0^3 n_0}{4\pi^2} \frac{\Delta}{2(1 + \Delta^2)} \left(\frac{\exp\left[-\sigma s(\mathbf{r})\right]}{1 + s(\mathbf{r})} - 1 \right), \tag{5.2}$$

where $n_0 = (\int_\Omega \exp\left[-\sigma s(\mathbf{r})\right] d\mathbf{r})^{-1}$ denotes the usual normalization integral over the spatial integration domain Ω. One can see that, regardless of the sign of the atomic detuning Δ, the nonlinear contribution to the total refractive index η is always positive. This clarifies the meaning of *collective self-focusing* for coupled light matter systems. Clearly, for the blue detuned atoms case, i.e., $\Delta > 0$, atomic waves are defocused, while *mutual* self-focusing is possible for $\Delta < 0$, if and only if the following condition is satisfied:

$$\frac{\exp\left[-\sigma s(\mathbf{r})\right]}{1 + s(\mathbf{r})} > 1 \iff \sigma = \frac{\hbar|\Delta|\Gamma}{4k_B T} < 1. \tag{5.3}$$

This simple condition corresponds exactly to the result predicted by Klimontovic and Luzgin for the mutual self-focusing of light and atoms [161]. Remarkably, it was shown by Wang and Saffman that Eq. (5.3) can be also considered as an existence criterion of transverse solitons solutions in the paraxial propagation of an optical field through a cold atomic cloud subject to dipole forces, described by Eqs. (3.7) and (3.23), as follows [165]:

$$\frac{1}{2ik_0} \nabla^2 \mathcal{E}(\mathbf{r}, t) + \partial_z \mathcal{E}(\mathbf{r}, t) = i\chi n(\mathbf{r}, t) \frac{\mathcal{E}(\mathbf{r}, t)}{1 + |\mathcal{E}(\mathbf{r}, t)|^2}, \tag{5.4}$$

$$\partial_t n(\mathbf{r}, t) = -\beta D_{\mathbf{r}} \nabla \cdot \left[n(\mathbf{r}, t) \mathbf{F}_{\text{dip}}(\mathbf{r}, t) \right] + D_{\mathbf{r}} \nabla^2 n(\mathbf{r}, t), \tag{5.5}$$

which gives rise to a modified saturable (or *super-Kerr*) nonlinear susceptibility[2]:

$$\chi_{\text{NL}} \sim \frac{1}{(1 + |\mathcal{E}(\mathbf{r}, t)|^2)^{1+\sigma}}. \tag{5.6}$$

The models of interest in this thesis involve Eqs. (5.4) and (5.5) with appropriate boundary conditions as in a ring cavity or SFM configurations. Thus, the main focus in this chapter is represented by dissipative solitons[3] whose stability is purely provided by the optomechanical self-focusing mechanism and, in contrast to their longitudinally propagating counterpart, exist on a wide range of values of $|\Delta|$, as long as the stable phase corresponds to $\mathbf{H}^{\pm}$ states, as described by the phase diagram in Fig. 4.4. Optomechanical dissipative solitons were ob-

---

[2]Note that Eq. (5.6) reduces to the simple saturable nonlinearity for hot atoms, i.e., $\sigma \to 0$.

[3]From now on, we simply refer to them as cavity or feedback solitons.
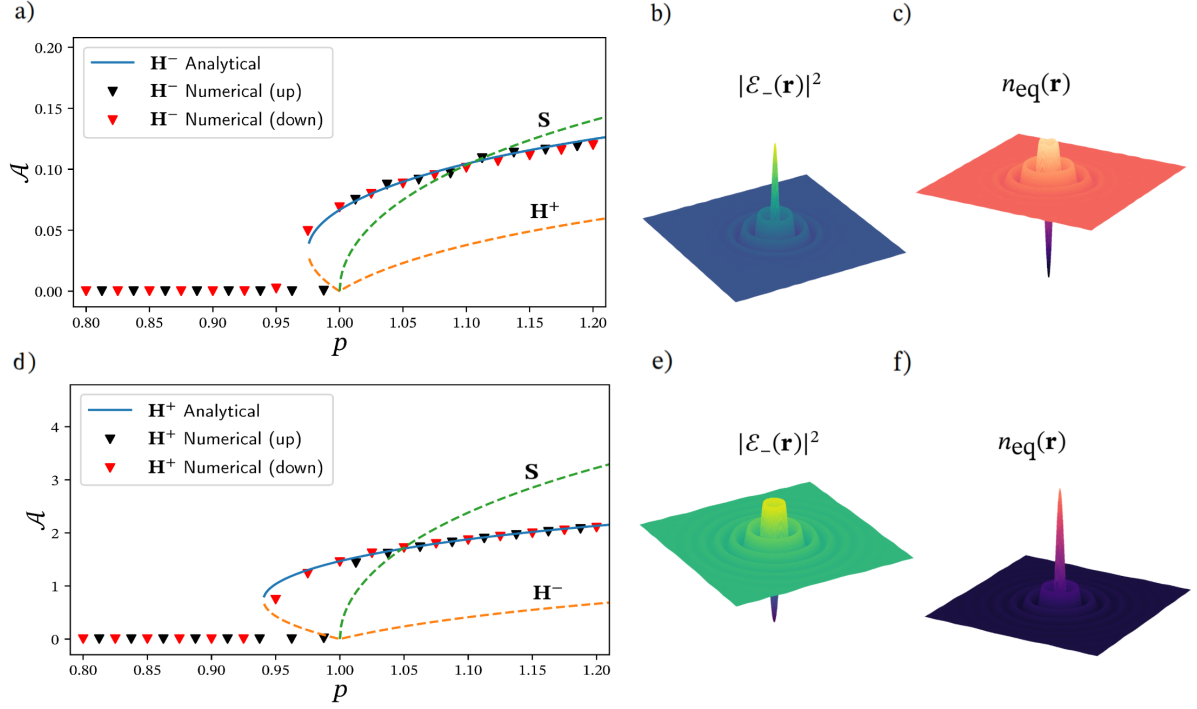
Fig. 5.1. Optomechanical feedback solitons for blue detuning. a), d) Analytical hexagon amplitudes of the $\mathbf{H}^{\pm}$, $\mathbf{S}$ branches as functions of p for $\chi \approx 0.31$ ($b_0 = 50, \Delta = 80, \sigma \approx 78.3$) and $\chi \approx 7.42$ ($b_0 = 150, \Delta = 10, \sigma \approx 2.45$), plotted together with the numerically observed amplitudes (black/red triangles). b), e) Corresponding backwards intensity $|\mathcal{E}_-(\mathbf{r})|^2$ and c), f) equilibrium atom density $n_{\mathrm{eq}}(\mathbf{r})$ localized states at $p = I/I_0 = 0.98$.

served numerically in Ref. [71] for the ring cavity model, in virtue of the subcriticality of the $\mathbf{H}^+$ pattern branch below the MI threshold. The rest of this section addresses the properties of such spatial solitons in a SFM system (*optomechanical feedback solitons*).

5.1.2 Bright and dark light optomechanical feedback solitons

As already introduced in Sec. 2.3.2 and anticipated above, the cold-atom optomechanical model displays coupled light-density spatial solitons when the symmetry breaking coefficient of the amplitude equations is nonvanishing[4], namely, $\lambda \neq 0$ [71, 136]. Therefore, one among the universal features of models described by amplitude equations in a real Ginzburg-Landau form (4.24) in the weakly nonlinear limit is the subcriticality of both the $\mathbf{H}^{\pm}$ branches. This means that stable hexagons/honeycombs can be observed throughout a parameter range identified by a linear growth $\mu_{\mathrm{SN}} < \mu < 0$. The extremal value of the linear growth coefficient μ_{SN} corresponds to the saddle-node bifurcation point occurring below MI at:

$$\mu_{\mathrm{SN}} = -\frac{\lambda^2}{4(\gamma_2 + 2\gamma_1)}, \tag{5.7}$$

---

[4]Let us recall that this is different from the input radiation wavelength λ_0.

where γ_1 and γ_2 are the self and cross-cubic coefficients of the amplitude equations, computed previously for the SFM case in Eqs. (4.29) and (4.30).

One among the most interesting features of the optomechanical dissipative solitons observed in the ring cavity model is its dependence on the light-atom detuning Δ, enabling both bright and dark atom density soliton configurations for equal and opposite Δ relatively close to resonance. The same dependence on Δ, however, leads to structural transitions[5], as discussed in Ch. 4. The stability of the novel $\mathbf{H}^+$ density phase, for cloud susceptibilities χ below a certain threshold value, enables the observation of a bright atom density feedback soliton which is self-trapped by a dark field profile. Such solitons are similar to the optical and matter-wave counterparts observed in Refs. [203–205], by means of radially symmetric trapping potentials[6]. The difference between the two soliton configurations is shown in Fig. 5.1, where the stable $\mathbf{H}^{\pm}$ branches $A_1 = A_2 = A_3 = \mathcal{A}$ (blue line), computed analytically from the AEs coefficients in Sec. 4.2.1, are in good agreement with the ones observed in numerical simulations, i.e., $(\max(n_{\text{eq}}) - \min(n_{\text{eq}}))/2$ for $p \in [0.8, 1.2]$. In addition, the observed $\mathbf{H}^-$ amplitude displays values and subcritical ranges comparable to the one observed in the cavity model in Ref. [71]. The rest of this chapter addresses different aspects of the control of soliton transverse motion by means of external phase gradients.

5.1.3 Transport of the self-localized atomic wavepackets

As widely discussed in Ch. 3, the drift velocity of light-atom patterned states in the transverse plane by means of spatially structured input beams leads to robust atomic transport [147]. The same concept is extended here to self-localized optomechanical dissipative solitons in the SFM configuration. This is shown by performing of a set of 1-d particle dynamics simulations, where the electric field couples to a continuous density reconstructed from atomic positions. Model parameters are chosen to match those of Fig. 5.1 in the thermodynamic limit ($N \rightarrow \infty$). By imposing periodic boundary conditions on the 1-d segment, atomic motion is again equivalent to the case of an annular trap and, therefore, the analogue of an OAM-carrying input field is represented by a linear azimuthal phase gradient.

By defining position and momenta as x_j and p_j ($j = 1, \ldots, N_{\text{atoms}}$), one constructs the set of Langevin equations for classical atoms in a 1-d domain including dipole force and dissipation as follows :

$$\dot{x}_j = \frac{p_j}{m}, \quad \dot{p}_j = f_{\text{dip}} - \gamma \frac{p_j}{m} + \xi_j(t), \tag{5.8}$$

where m is the atomic mass, γ the momentum damping rate and $\xi_j(t)$ is the stochastic variable such that $\langle \xi_j(t) \rangle = 0$ and $\langle \xi_j(t)\xi'_j(t') \rangle = 2D_p \delta_{jj'}\delta(t - t')$, where $D_p = \gamma k_B T$ is the momentum diffusion constant. At the onset of the transverse optomechanical instability, the system spontaneously selects a critical wavenumber $q_c = \sqrt{\pi k_0/2d}$, so we define $\bar{x}_j = q_c x_j$ and

---

[5]With $\mathbf{H}^+$ densities stable for high detuning with respect to fixed optical densities.
[6]In the present case, the self-organized potential has the same local radial symmetry in the neighborhood of the excitation.
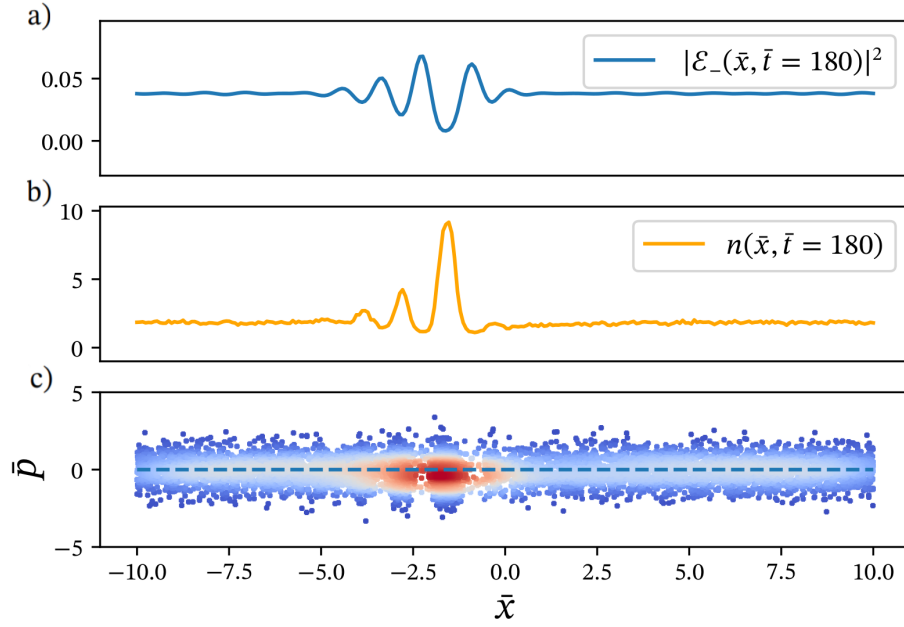
Fig. 5.2. Snapshot of a 1-d angular particle dynamics simulation of a traveling soliton with $N_{\text{at}} = 4{\times}10^4$ OAM index $l = 1$ at at $\bar{t} = 180$. a) Backwards field $|\mathcal{E}_-(\bar{x}, \bar{t})|^2$ and b) atom density $n(\bar{x}, \bar{t})$, numerically reconstructed from particle positions. c) Phase-space distribution of the atomic ensemble at $\bar{t} = 180$. Each point is coloured according to the local probability density. Note the nonzero momentum of the traveling localized structured, with respect to the vanishing average of the ensemble (dashed blue).

$\bar{p} = p_j/\hbar q_c$, such that Eqs. (5.8) become:

$$\frac{\partial \bar{x}_j}{\partial \bar{t}} = 2\bar{p}_j, \quad \frac{\partial \bar{p}_j}{\partial \bar{t}} = -\frac{\Gamma\Delta}{4\omega_p}\frac{d}{d\bar{x}}s(\bar{x}, \bar{t}) - \bar{\gamma}\,\bar{p}_j + \bar{\xi}_j(t), \tag{5.9}$$

where $\omega_q = \hbar q_c^2/2m$ represents the atomic recoil frequency in a standing wave potential of wavenumber q_c and $\bar{t} = \omega_q t$, $\bar{\gamma} = \gamma/m\omega_q$, $\bar{\xi}_j(t) = \xi_j(t)/\hbar q_c\omega_q$. To obtain the thermodynamic quantities purely in terms of microscopic parameters[7] in Eq. (5.9), we exploit the (rescaled) relation between the two diffusion constants $\bar{D}_{\bar{x}}$ and $\bar{D}_{\bar{p}}$ as in Ch. 3 and Ref. [147].

$$\bar{D}_{\bar{x}} = \frac{4}{\bar{\gamma}^2}\bar{D}_{\bar{p}}, \quad \sigma = \frac{\bar{U}_0\bar{\gamma}}{2\bar{D}_{\bar{p}}}. \tag{5.10}$$

where $\bar{U}_0 = \Gamma\Delta/4\omega_q$. Numerical results are shown in Fig. 5.2, obtained for a set of $N_{\text{atoms}} = 10^4$, $d\bar{t} = 10^{-4}$ and the following parameters[8] $\Delta = 80$, $b_0 = 30$, $p = I/I_0 = 0.98$, $\bar{\gamma} = 1$, $\bar{D}_{\bar{p}} = 2$, $\bar{U}_0 = 100$, such that a constant $\sigma = 25$ corresponding to an effective kinetic temperature of $T \approx 940\,\mu\text{K}$. In order to excite a localized perturbation, an initial atom density peak is prepared by defining a Gaussian particle distribution, centered at some point $\bar{x}_0$, for

---

[7]See appendix A.2
[8]Same Dark light/bright density configuration of Fig. 5.1.

a fraction of N_{atoms}, i.e., $\bar{x}_{c*j} = \bar{x}_0 + \alpha\eta$, where c is an arbitrary integer ($j = 1, \dots, N_{\text{atoms}}/c$) and η is a random variable normally distributed in the interval $[0, 1]$. The remaining $N_{\text{atoms}} - N_{\text{atoms}}/c$ are left instead homogeneously distributed in the 1-d domain. Moreover, a linear phase gradient representing the effect of OAM is added to the input field as follows:

$$\mathcal{E}_+(\bar{x}) = |\mathcal{E}_{+,0}| \exp\left(\frac{2\pi}{\bar{X}_d} il\bar{x}\right), \tag{5.11}$$

where $\bar{X}_d$ is the domain length[9]. Assuming periodic boundary conditions, Eq. (5.11) corresponds to the 1-d azimuthal limit of a transverse field carrying OAM with charge l [70].

As shown in Fig. 5.3 a) - d) for different parameter choices, the OAM provides transverse acceleration until the optomechanical soliton, initially defined as a density peak of atoms at rest, reaches a steady state drift velocity. Such transient behaviour is described by the relaxation of the momentum distribution and is not captured by the Smoluchowski equation only in the overdamped limit. Note also that the different spatial diffusivities of the gas cause the asymmetric formation of a second peak of confined atoms due to the displacement of the main peak. However, this is primarily due to the reduced dimensionality of the system and the lack of symmetric density redistribution around the main peak. Interestingly, one observes in Fig. 5.3 e), f), with no OAM, a decay of the self-localized light-density structure by decreasing the rescaled momentum damping rate $\bar{\gamma} = 1$ at fixed $\bar{D}_{\bar{p}}$. This corresponds to an increase of the effective temperature and spatial diffusion[10] and, conversely, a lower kinetic temperature results in a change of the instability threshold which causes the growth of spatial modulations.

5.2 Control of soliton trajectories in a ring cavity

As discussed thoroughly in Ch. 3, the use of spatially structured phase fronts as driving beams of optical cavities is a viable mechanism to induce and control rotational effects and transport phenomena involving transverse self-organized light-atom structures. Important applications of such effects can be extended to the case of self-localized dissipative solitons which will be the focus of the present section. Indeed, previous results shown for a SFM system apply also to the cavity case and, thus, one can identify regions where transverse $\mathbf{H}^\pm$ states are bi-stable with homogeneous solutions, meaning that dissipative solitons can be observed [71].

5.2.1 Rotating and spiralling solitons

The parameter regions of interest for transporting optomechanical solitons are those in which one expects bright peaks of atom density $n(\mathbf{r}')$. This would mean any configuration for $\Delta < 0$ (red atomic detuning)[11] and its inversion symmetric counterpart at $\Delta \geq \Delta^* > 0$ (see Fig. 4.4). The first case corresponds to a condition of mutual self-focusing of the cavity field and atomic

---

[9]We choose a domain of 20 critical wavelengths here.

[10]Note that, $T \to \infty$ for $\bar{\gamma} \to 0$. Thus, for a conservative system, one should set $\bar{D}_{\bar{p}} = 0$.

[11]Recall that the low saturation assumption implies pumping far from the atomic resonance at $\Delta = 0$.
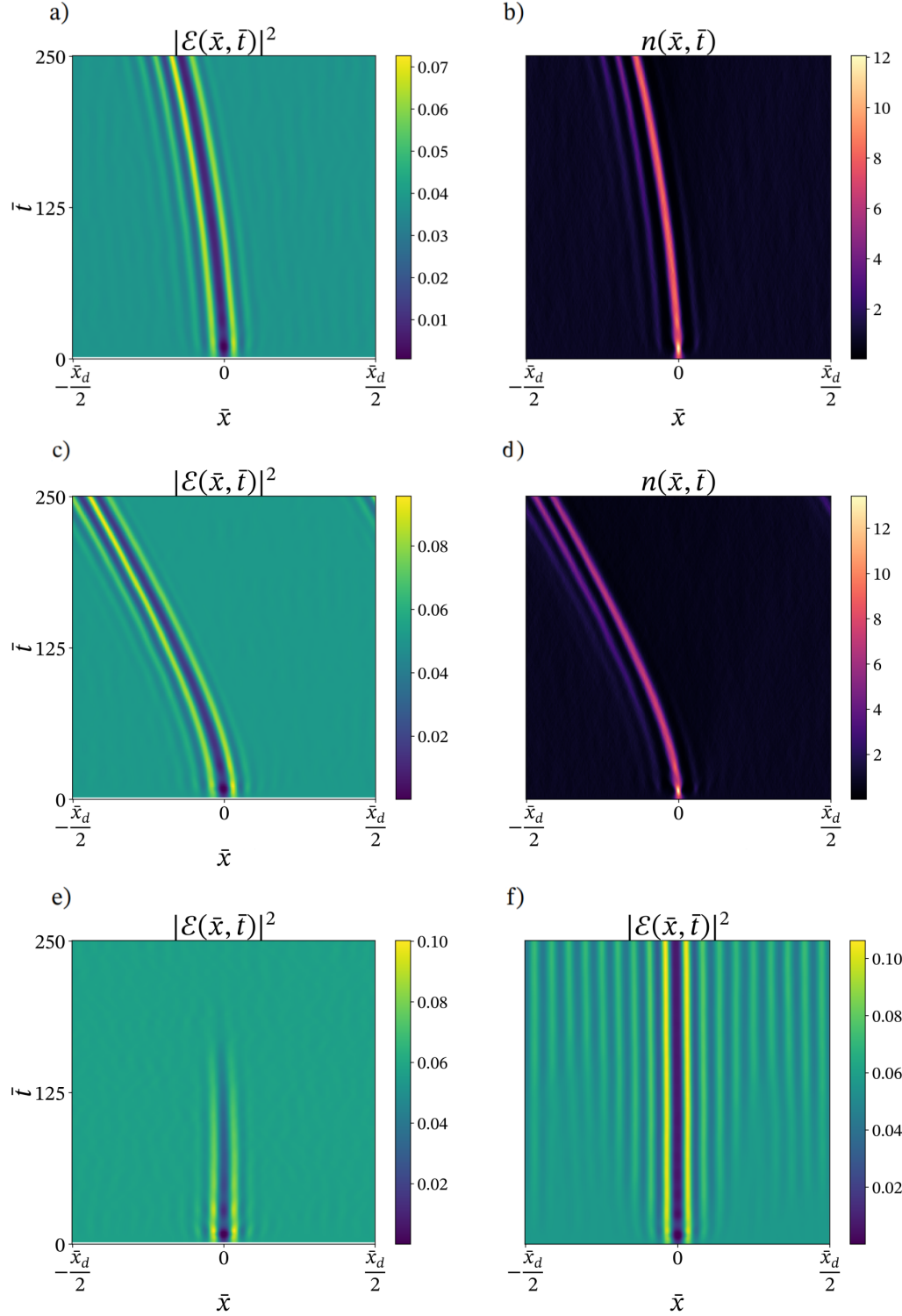
Fig. 5.3. a), b) Time evolution of the backwards intensity $|\mathcal{E}(\bar{x},\bar{t})|^2$ and numerical particle density $n(\bar{x},\bar{t})$ for $l = 1$ and model parameters as in Fig. 5.2. c), d) A shorter transient with a faster drift velocity is reached for higher order OAM $l = 2$ and slightly higher momentum diffusion $\bar{D}_{\bar{p}} = 2.25$. e), f) Effect of varying the momentum damping rate $\bar{\gamma}$ on the backwards intensity with no OAM carried in the input pump (soliton decay for $\bar{\gamma} = 1$ in e) and modulation growth for $\bar{\gamma} = 3$ in f)).
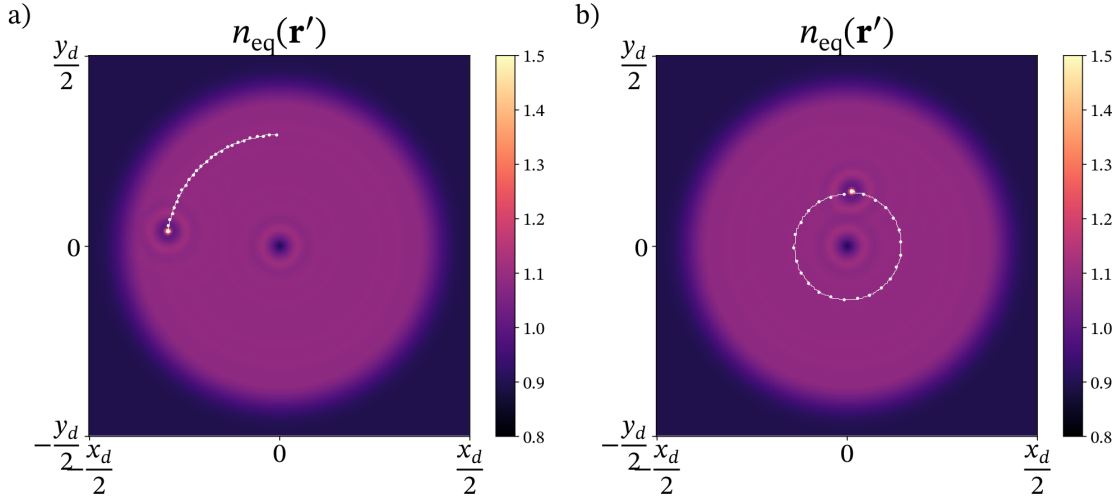
Fig. 5.4. Rotating optomechanical cavity solitons for red atomic detuning $\Delta < 0$ and for a period $\kappa t_{\max} = 300$ and $\alpha = 0$ (purely azimuthal drift within closed orbits with OAM index $l = 1$). a) The solitary structure is initially excited at $\mathbf{r}_0 = (0, y_0)$ with $y_0 > y_d/4$ and covers roughly a quarter of the orbit at $t_{\max}$. b) For $y_0 < y_d/4$ the soliton achieves faster rotation speed, completing a cycle within $t_{\max}$. Model parameters chosen as follows: $I/I_{\mathrm{th}} \approx 0.67$, $\theta = 5.1$, $C\Delta = -2.25$, $\sigma = 25$.

density (so that dissipative solitons are realized in the form of bright light peaks). Moreover, as discussed later in this section, there is a numerical evidence of the existence of structural phase transitions $\mathbf{H^+ - S - H^-}$ of the atomic cloud also in the ring cavity model, enabling realizations of traveling dark light solitons of the same kind of those reported in Fig. 5.1.

Bright light - bright density optomechanical solitons

Rotational motion of propagating (conservative) optical solitons induced by an azimuthal phase twist was predicted for solitons supported by Bessel lattices in cubic media in Ref. [206], and observed experimentally in Ref. [207]. In addition to the angular drift generated by the azimuthal phase factor $e^{il\phi}$ of the input beam, one can introduce simultaneous control of angular and radial motion of the localized structured by means of the following phase:

$$A_I(\mathbf{r}') = \mathcal{A}(r') \exp\left[i\alpha\psi(r')\right] \exp\left[il\phi\right]. \tag{5.12}$$

Here, $\mathcal{A}(r')$ represents the usual radial profile such as the tophat function in Eq. (3.39) and $\psi(r')$ represents a generic concave function such that, if $\alpha > 0$, dissipative solitons are guided towards the center of the transverse domain, since the corresponding phase gradient is directed towards the maximum at $\mathbf{r}' = 0$. Numerical simulations in 2-d of soliton dynamics in the optomechanical ring cavity model are performed by means of the same Fourier split-step method as in Sec. 3.3.2 where, this time, a larger spatial domain size of 10 critical wavelengths is chosen in order to explore several trajectories in the transverse plane. The purely rotating case is shown in Fig. 5.4, where the self-trapped density peak is excited at two different radii,
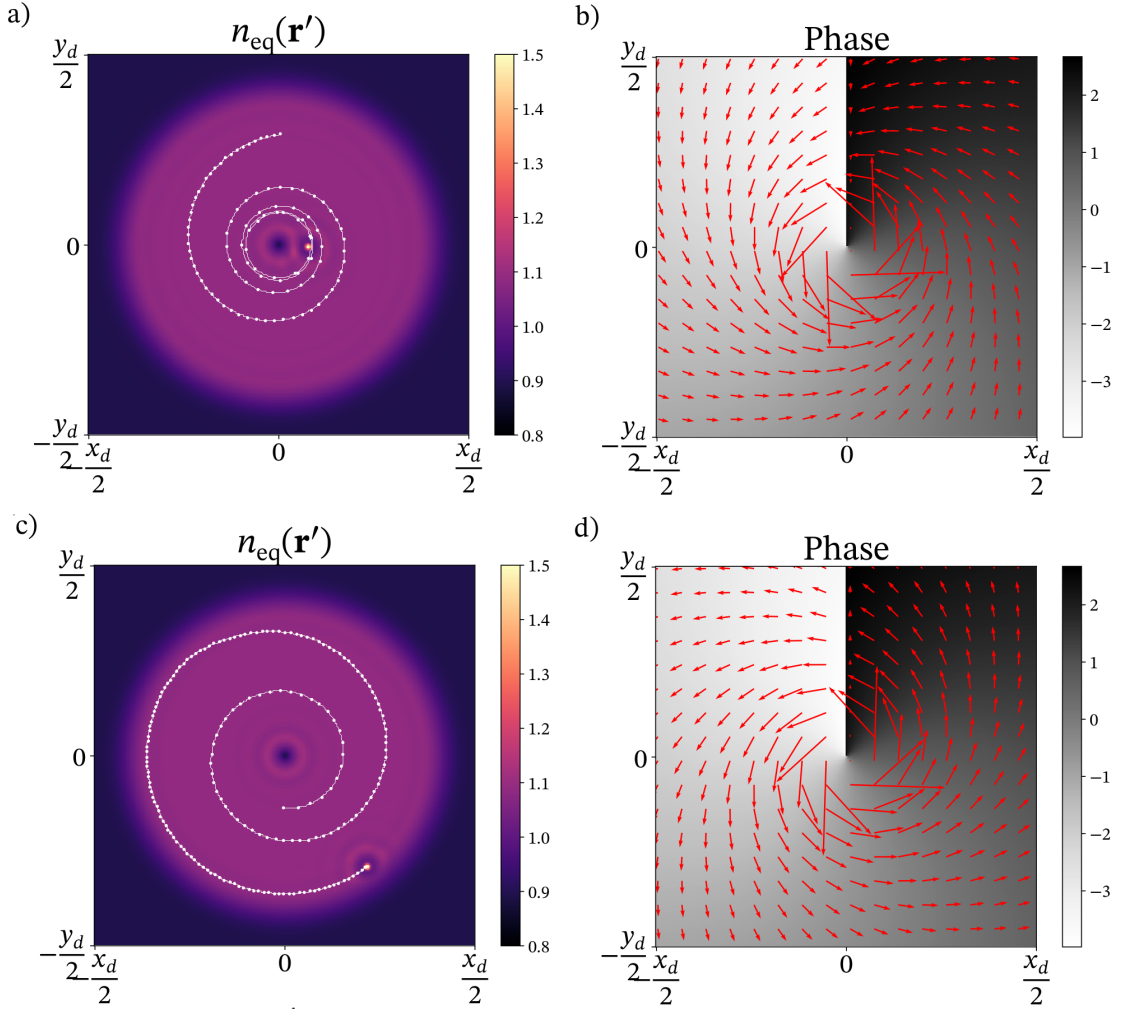
Fig. 5.5. Spiralling cavity soliton evolution for a period of $\kappa t_{\max} = 750$ and $\alpha \neq 0$ inducing spiral trajectories until the soliton interacts with the boundaries. a) Density soliton undergoing inward spiral motion for positive $\alpha = 1.2$. b) Total input phase profile $\alpha \psi(r') + \phi$ (OAM index $l = 1$), including contour lines and gradient field, indicating soliton velocity. c) Outward spiraling soliton for $\alpha = -1.2$. d) Corresponding phase and velocity field, inducing outward spiral trajectories. Model parameters chosen as follows: $I/I_{\text{th}} \approx 0.672$, $\theta = 5.1$, $C\Delta = -2.25$, $\sigma = 25$.

realizing perfectly circular trajectories with different angular frequencies[12]. This difference is shown by the white dots representing the position of the maximum of the equilibrium density peak $n_{eq}(\mathbf{r}')$ in the transverse domain, measured at regular intervals of $\kappa t = 10$.

Stable cavity solitons below the MI threshold are supported by an homogeneous state displaying much weaker radial modulations (induced by the finite size profile $\mathcal{A}(r')$) with respect to the self-organized ring lattices observed above threshold in Sec. 3.3.1. This opens the possibility of a smooth radial drift for $\alpha \neq 0$, as shown in Fig. 5.5. In particular, a choice of $\alpha > 0$

---

[12]One expects in this case exactly the same scaling with the transverse radius r as in Eq. (3.37)

induces inward spiralling motion of the cavity soliton, until an effective repulsive interaction at the inner domain boundary, due to the phase singularity at $\mathbf{r} = 0$, takes place and forces the soliton into a stable circular orbit, as shown by the evolution of the density peak in Fig. 5.5 a). Similarly, the outward spiralling trajectory for $\alpha < 0$ is shown in Fig. 5.5 c), where, this time, the effective interaction occurs with the outer boundary of the tophat profile[13]. The spiraling evolution can be seen by recalling the drift velocity in Eq. (3.36) which, in this case reads:

$$\mathbf{v}_{\mathrm{dr}}(\mathbf{r}') = \alpha \partial_r \psi(r') \hat{r}' + \frac{2l}{r'} \hat{\phi}. \tag{5.13}$$

In other words, a radial component arises from $\psi(r')$, in addition to the azimuthal one induced by the OAM and introduced previously. The drift velocity vector field $\mathbf{v}_{\mathrm{dr}}(\mathbf{r}')$ is represented graphically in Fig. 5.5 b), where the numerical gradient of the input phase used in numerical simulations is plotted as a vector field together with the total phase. The curvature of the spiral obtained can be controlled by the features of the function $\psi(r')$. In the present case, $\psi(r')$ is chosen as a radial hyperbolic tangent so that, by increasing the steepness of such function one obtains a spiralling trajectory with increased curvature and viceversa.

Dark light - bright density optomechanical solitons

As anticipated above, preliminary numerical evidence of the existence of $\mathbf{H}^+ - \mathbf{S} - \mathbf{H}^-$ structural transitions can be provided also in the ring cavity model. Although a detailed analysis of this mechanism in such a configuration is out of the aim of this thesis and will be investigated in future studies, a strong correspondence exists between the linear susceptibility χ introduced in Ch. 4 and the cavity cooperativity parameter C, which can be conveniently expressed as follows:

$$C = \frac{b_0}{2\tau(1 + \Delta^2)}. \tag{5.14}$$

Therefore, significant differences from the effective-Kerr medium case, at fixed optical density b_0, are expected to arise when the product $C\Delta$ lies below a certain threshold value which in general also depends on the cavity detuning θ. For this reason, it is convenient to assume from now on that the product $C\Delta$ as a free tunable parameter in numerical simulations.

As shown in Sec. 5.1.1, the stability of $\mathbf{H}^+$ atom density for blue detuning implies the existence of spatial solitons characterized by a bright density peak trapped in a dark field region. For example, stable $\mathbf{H}^-$ states of the intracavity intensity with corresponding anticorrelated ($\mathbf{H}^+$) atom density are found numerically, assuming a fixed cavity detuning $\theta \approx -4.5$, for a value of $C\Delta \approx 0.6$. An example of dark-light/bright-density solitons is shown in Fig. 5.6 a) - c) with the characteristic diffraction rings already observed in the single-feedback-mirror model. However, an intriguing characteristic, specific to the ring cavity model is the observation of *pulsating* behaviour of the localized structure, shown in Fig. 5.6 b) by simply measuring the

---

[13]Note the sudden change of direction in Fig. 5.5 c).
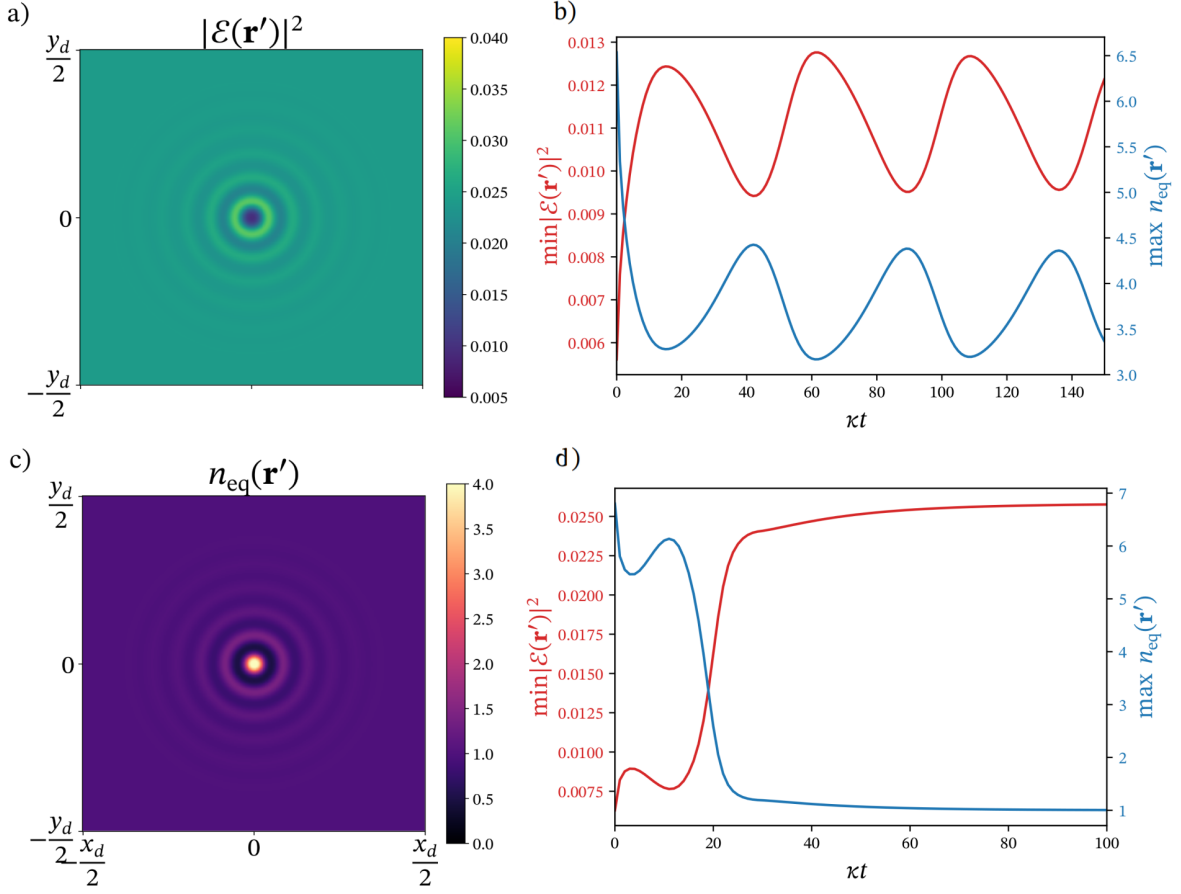
Fig. 5.6. Dark light - bright density pulsating soliton in the ring cavity model. a) - c) Spatial profiles of intracavity intensity and atomic density with a plane wave pump for $I/I_{\text{th}} = 0.97, \theta = -4.45, C\Delta = 0.2$, $\sigma = 100$ in the peak of a density oscillation cycle $kt \approx 40$. b) - d) Characteristic dynamic soliton behavior obtained by monitoring the density maximum (blue lines) and intensity minimum (red lines). Pulsating soliton in b) for $C\Delta = 0.2$ and sudden death in c) after the first cycle for $C\Delta = 0.185$.

evolution of both $\min_\Omega |\mathcal{E}(\mathbf{r}', t')|^2$ and $\max_\Omega n(\mathbf{r}', t')$. Note that such behavior is susceptible to variations of $C\Delta$ resulting in a sudden death, as show in Fig. 5.6 d).

In the rest of the section, the possibility of exciting travelling dark-light/bright-density solitons on a structured phase profile is addressed. First of all, the main problem to deal with is that the parameter regions of interest are characterized by a low cooperativity/large atomic detuning meaning that, if one assumes any finite size tophat pump, the equilibrium density distribution of the atoms may be effectively negligible in the flat part[14], meaning that it is not possible to reach sufficient light-density coupling leading to transverse instabilities. Therefore, we introduce by hand here an additional radial confinement for atoms which is effectively realized by means of a tophat-like function in the atom density, preventing atoms escaping from the tophat beam domain as well as accumulating in the intensity minimum at $\mathbf{r}' = 0$. The

---

[14]This means that the atoms are simply pushed away from the interaction region.
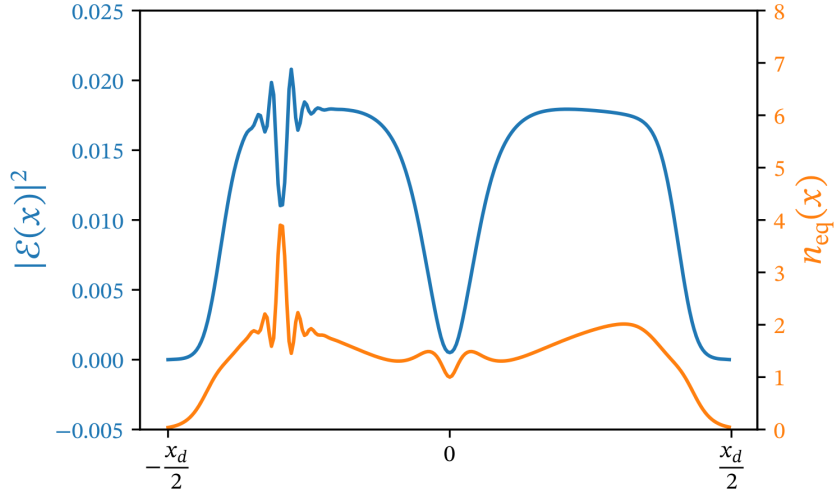
Fig. 5.7. Rotating dark-light/bright-density soliton excited on a finite size pump. 1-d section of cavity field $|\mathcal{E}(x)|^2$ (blue line) intensity with a soliton positioned at $\left(x = -\frac{x_d}{2}, y = 0\right)$ and corresponding atom density $n_{\mathrm{eq}}(x)$ modulation (orange line). Note that the atomic density is vanishing at the integration domain boundaries and no density maximum is present at $\mathbf{r}' = 0$. This is due to the additional radial confinement introduced within the region of interaction with the cavity field.
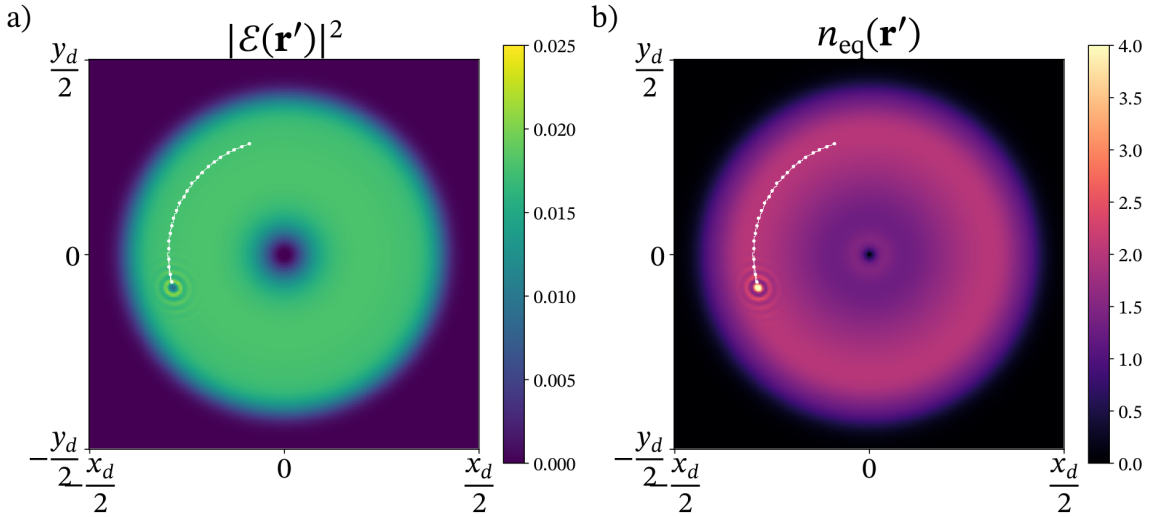
Fig. 5.8. Rotating dark-light/bright-density cavity solitons corresponding to the 1-d section in Fig. 5.7 for a period $\kappa t_{\mathrm{max}} = 10^3$ and higher OAM index $l = 5$. Model parameters chosen as follows: $I/I_{\mathrm{th}} \approx 0.495, \theta = -0.43, C\Delta = 0.14, \sigma = 100$. The position of the soliton is indicated by white dots showing a perfectly circular trajectory.

effect of such a choice on the final density distribution profile is shown in Fig. 5.7 so that it is relatively easier to excite stable localized structures in the desired position.

The observation of steady drift motion requires larger domain sizes[15] in this case and the removal of the typical diffraction structures close to the singular point. This was achieved by inserting an additional radial dependence to the usual tophat profile $\mathcal{A}(r)$. The main result is shown in Fig. 5.8 a) - b), clearly indicating the stable azimuthal drift of a stationary (non-pulsating) structure, with a rotation speed in accordance with the theoretical predictions discussed before in Sec. 3.3. So far we have discussed numerical results concerning the properties and dynamics of single solitons. The last section of this chapter focuses instead on phenomena concerning the interaction between optomechanical cavity solitons.

5.3 Interactions between optomechanical cavity solitons

This last section is aimed at reporting and discussing some phenomena concerning the interaction of cavity solitons in the purely optomechanical cold-atom model in a ring cavity. Indeed, the spatially structured input phase can be used to engineer soliton-soliton collisions, resulting into the formation of localized patterns or bound states. Multipeaked structured can be found by means of external addressing beams, opening the possibility for effectively 1-d rotating and spiralling cavity soliton clusters or *chains*.

Bound states of optomechanical solitons

The introduction of a purely radial phase profile, capable of introducing soliton drift along the radial direction, can be exploited here in order to study soliton-soliton interactions in the cold-atom optomechanical model. A general scheme for describing cavity soliton interactions and cluster formation in the purely absorptive case was derived in Ref. [139], based on the properties of *neutral* modes of the localized structure[16] [208]. Indeed, since those modes are connected with translational symmetry, any excitation results in transverse motion so that, by defining a measure of soliton-soliton superposition, one can derive an expression of the asymptotic velocity determined by the overlap of such measure with the neutral eigenmodes. This approach leads to effective equations of motion for a representative soliton center-of.mass position which, interestingly, can be cast to a gradient form with a closed expression for the two-body interaction potential, derived by approximating solitons with Bessel functions. This general feature is represented in Fig. 5.9 a), where the typical two-soliton interaction profile is plotted against the radial distance between the two localized structures.

As also observed experimentally in Ref. [209] for a hot sodium vapor in a SFM configuration, the soliton interaction potential leads to a certain number of preferred stable positions. The first pinning distance corresponding to the global minimum leads to a multipeaked structure, as predicted theoretically in [141]. Moreover, by considering multiple interacting peaks

---

[15]Approximatively 35 critical wavelengths in our case.

[16]A careful derivation of soliton-soliton interactions is out of the aim of this thesis, since a preliminary characterization is compatible with the general picture in Fig. 5.9.
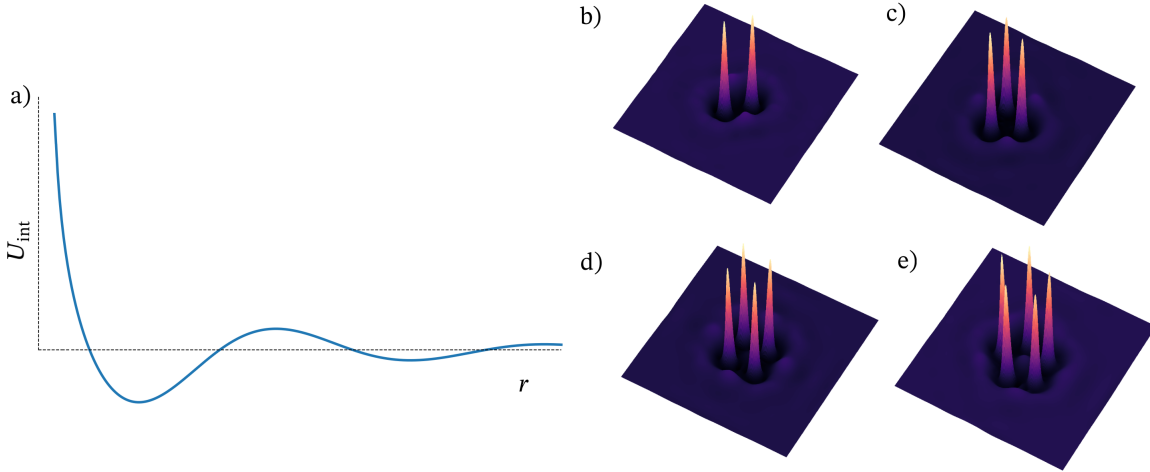
Fig. 5.9. Optomechanical soliton-soliton interactions in a ring cavity model. a) Typical two-body interaction potential U_{int} (or equivalent measure) for cavity solitons as a function of the peak distance. Note the presence of the minima which can lead to the formation of stable cluster. Fig. adapted from Ref. [139]. b) - e) Clusters of 2, 3, 4 (square), 5 (star) optomechanical cavity solitons with interacting bright density peaks. b) - c) Minimal stable configurations. d) - e) Unstable square and star configurations.

close to the same two-soliton minimum, one can achieve configurations of multiple bounded solitons (clusters). Dynamically stable clusters of two and three optomechanical cavity solitons are shown in Fig. 5.9 b) - c), while other configurations with regular square and pentagon geometries are generally unstable, due to the many-body character of the interaction among solitons causing the cluster to evolve in favour of configurations with hexagonal ordering[17].

Apart from the individual excitation by external addressing beams, it is possible to generate clusters of optomechanical solitons by inducing collision via a radially structured phase, as defined in Eq. (5.12). Note that this however depends strongly on the input pump, since above a certain threshold value, a two soliton collision might result into a localized pattern eventually spreading on the whole transverse domain. This effect is shown in Fig. 5.10 a) - c) for the cavity intensity profile, where the spatial overlap between diffraction rings creates an interference patterns which lead to the excitation of a localized pattern (self-replication). Below such an input intensity threshold, the collision leads instead to a stable bound state. Such a possibility is discussed in the rest of the section below.

Rotating and spiralling soliton chains

Another possible application of bound multi-soliton states is to exploit a structured input phase to generate rotating and spiralling *chains* of interacting solitons. This is achieved by periodical excitations of travelling solitons with a purely azimuthal phase or a combined radial + azimuthal phase such as in Eq. (5.13), at a rate such that the peak-peak distance with

---

[17]This is not surprising since the patterned state has hexagonal order.
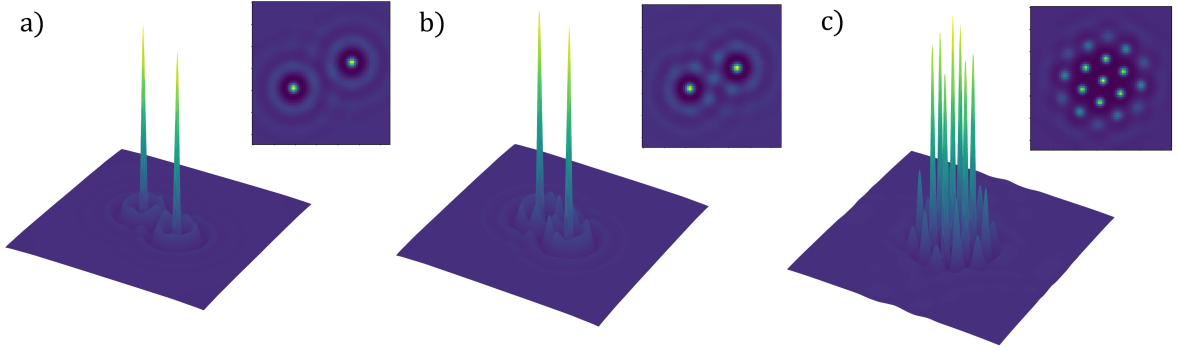
Fig. 5.10. Typical self-replication mechanism after a two-soliton collision, induced by a radially structured input phase. a) Solitons initially excited at large enough distance to have weak interactions. b) Strong interactions are provided by the overlap of the first diffraction rings. c) Stable localized hexagonal pattern at steady state.

the newly excited soliton is compatible with the 2-body potential minimum in Fig. 5.9[18]. Examples of rotating and inward spiralling chains of 10 solitons with OAM index $l = 1$ are shown in Fig. 5.11, where the one dimensional drifting chain is seen to perfectly orient itself along the same trajectories previously measured from the numerical simulations of a single rotating or spiralling soliton and shown in Fig. 5.4 and 5.5 a).

As anticipated above, such complex multi-soliton bound states forming linear chains are observed to be unstable in the long-term dynamics[19]. This due to the general tendency of the system to form structures organized in an hexagonal lattice and can be characterized rigorously in terms of higher-order moments of the soliton interactions, derived in terms of neutral modes in Ref. [139] . However, such bound states are still potentially relevant since one has a transient time in which the rotating/spiralling soliton chains can be observed in numerical simulations, depending on the most important parameter in the cavity equation, namely, the cooperativity parameter[20] C, defined previously in Eq. (5.14).

The stability of the simplest possible soliton chain, i.e., made of three interacting solitons, is studied here for the purely azimuthal rotation case, for different values of $C\Delta$. Results are shown in Fig. 5.12 a), with the maximum lifetime $\kappa t_{\max}$ in which the rotating chain is observed without any appreciable distortion other than its curvature at a certain radius (Fig. 5.12 b) - e) show the collapse of the linear chain into a triangle). Surprisingly, the minimum observed transient is of the order $\kappa t \approx 4 \times 10^3$ for $C\Delta = -2.75$, which already suggests experimentally accessible timescales. Such transient is observed to increase with $C\Delta$, i.e. moving towards the atomic resonance $\Delta = 0$ in the blue detuned regime, and required extremely long simulations up to $\kappa t \approx 6 \times 10^4$ for $C\Delta = -0.75$. Those results provide a preliminary indication that the

---

[18]Interestingly, for distances larger than the first minimum the two soliton are shown to annihilate.

[19]They tend to fold/collapse into multi-soliton clusters with hexagonal ordering, locally distorted by the radially dependent rotation speed.

[20]Together with the cavity detuning Δ, since the term $C\Delta$ is treated as an independent parameter in numerical simulations.
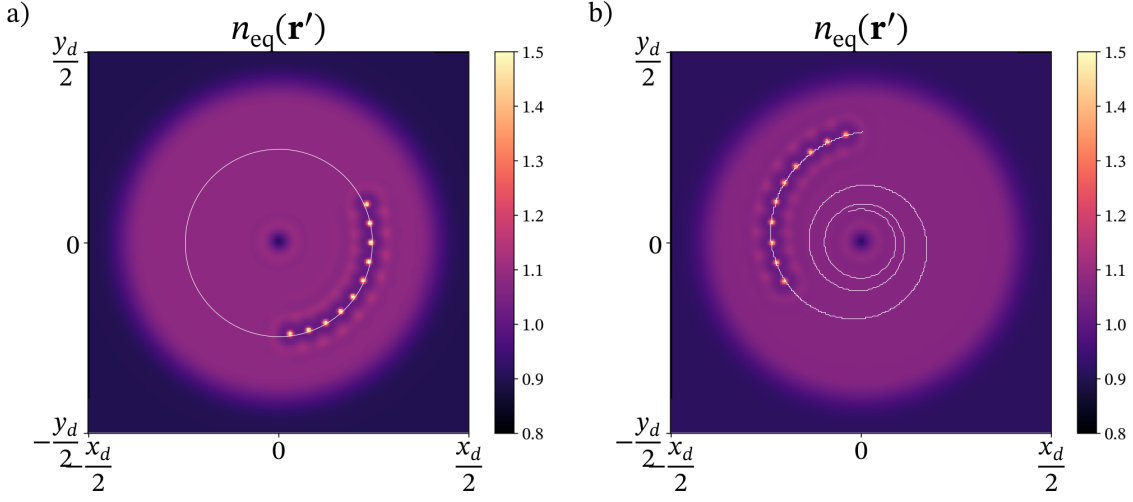
Fig. 5.11. Rotating and spiralling chains of interacting solitons. a) Rotating chain of 10 interacting cavity solitons on a purely azimuthal phase gradient ($l = 1$) provided by the input field $A_I(\mathbf{r})$. The white circle represents the perfectly circular trajectory of 1 cavity soliton at the same radial distance from the origin $\mathbf{r} = 0$. b) Spiralling chain of 10 bound cavity solitons. Model parameters $\theta = 0.6$, $C\Delta = -1.75, \sigma = -25$.
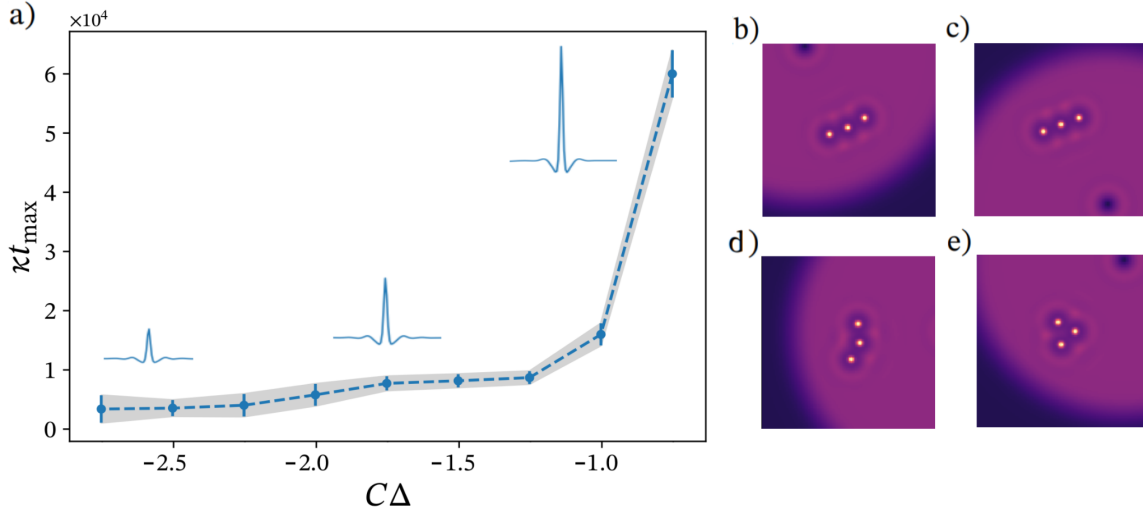
Fig. 5.12. Stability of the rotating three-soliton chain for OAM index $l = 1$. a) The maximum transient time $\kappa t_{\max}$ is measured by varying the interaction parameter $C\Delta$ for blue atomic detuning $\Delta < 0$ and is observed to increase towards the atomic resonance. Those results suggest that rotating and spiralling soliton chains are effectively stable for $C\Delta > -0.75$. b) - e) Collapse of the linear chain into a triangle.

98

structures are practically stable, i.e., $\kappa t_{\max} \to +\infty$, in correspondence of $C\Delta = -0.5$ or above[21].

Finally, it is also worth remarking that varying model parameters, such as $C\Delta$, modifies the profile of the optomechanical cavity soliton, as seen from the insets in Fig. 5.12 (see the maximum of light-intensity/atom-density peak with respect to the flat background and corresponding wiggles). The origin of such a feature can be traced back to the local energy balance, a physical characteristic of cavity solitons. Indeed, one can invoke a local energy balance principle for dissipative solitons, requiring energy gain in a circular region sustaining the central peak. In turn, this energy is transported spatially by diffraction[22]. Any possible multi-soliton interaction effect is indeed observed when the single soliton profiles have relevant overlaps between the first rings maxima surrounding their central peak. For values of $C\Delta > -1$, the secondary peaks are less present and, therefore, the interactions are expected to lose relevance in the overall soliton dynamics, providing a partial understanding of the results in Fig. 5.12.

Hamiltonian approach

A useful viewpoint to understand phenomena such as shown in Fig. 5.12 is provided by an effective-Hamiltonian approach to the multi-soliton interactions[23]. The derivation proposed here is inspired from the one in Ref. [210] for the Kerr cavity case, based on the effective Lagrangian approach introduced by Lord and Firth of Ref. [170], and generalized here to the cold-atom optomechanics case. First, one starts with the variational formulation of the driven-dissipative cavity field dynamical equation with the purely optomechanical nonlinearity by considering the following action-like mathematical functional:

$$S[\mathcal{E}, \mathcal{E}^*] = \int_{\mathbb{R}} \int_{\Omega} e^{2t} \mathcal{L}[\mathcal{E}, \mathcal{E}^*] dt\, d\mathbf{r}', \tag{5.15}$$

where the time-dependent exponential e^{2t} is introduced by hand in the action $S[\mathcal{E}, \mathcal{E}^*]$ in order to generate dissipation, and the effective (conservative) Lagrangian density reads:

$$\mathcal{L}[\mathcal{E}, \mathcal{E}^*] = \frac{i}{2} \left(\mathcal{E}^* \dot{\mathcal{E}} - \text{c.c.} \right) - |\nabla'_{\perp} \mathcal{E}|^2 - i A_I(\mathbf{r}') (\mathcal{E}^* - \mathcal{E}) - \theta |\mathcal{E}|^2 + \mathcal{L}_{\text{int}}, \tag{5.16}$$

where $\mathcal{L}_{\text{int}}$ represents the (nonlinear) interaction contribution to the Lagrangian density. For example, in the Lugiato-Lefever case for a Kerr nonlinear medium in Eq. (3.17), such an interaction term has the quartic form $\mathcal{L}_{\text{int}} = \eta |\mathcal{E}|^4 / 2$. Thus, the cavity equation follows by applying a minimum action principle by means of the functional derivative as follows [211]:

$$\frac{\delta S[\mathcal{E}, \mathcal{E}^*]}{\delta \mathcal{E}^*} = \frac{\partial \mathcal{L}}{\partial \mathcal{E}^*} - \nabla'_{\perp} \frac{\partial \mathcal{L}}{\partial (\nabla'_{\perp} \mathcal{E}^*)} - \frac{d}{dt} \frac{\partial \mathcal{L}}{\partial \dot{\mathcal{E}}^*} = 0. \tag{5.17}$$

The optomechanical case can be retrieved by using the Gibbs distribution in Eq. (2.68) for

---

[21]Recall, however, that the low saturation approximation breaks for $\Delta \to 0$.

[22]Note that this can generate many higher-order peaks, depending on the system nonlinearity. See Refs. [67, 135] for details.

[23]This is slightly less rigorous with respect to Ref. [139], based on the neutral eigenmodes.

the atomic density. Indeed, one can construct by hand the following interaction term[24]:

$$\mathcal{L}_{\text{int}}(\mathbf{r}') = \gamma \frac{\exp\left(-\sigma|\mathcal{E}(\mathbf{r}')|^2\right)}{\sigma^2 \mathcal{E}(\mathbf{r}')^2 \mathcal{J}} \left(\sigma^2|\mathcal{E}(\mathbf{r}')|^2 + 1\right), \tag{5.18}$$

where $\gamma = 2C\Delta$, $\sigma = \hbar\Gamma\Delta/4k_B T$, and $\mathcal{J}$ represents the usual normalization integral, treated here as a constant (in a functional calculus sense). The full Hamiltonian density for the cavity equation can be obtained by performing a simple Legendre transform as in Ref. [210]. However, the main focus here is in the interaction term only, rather than the full field dynamics, so that the interaction potential for two localized structures can be constructed by considering two (or more) soliton profiles separated by a distance z, namely:

$$\mathcal{E}(\mathbf{r}', z) = \mathcal{E}_0\left(\mathbf{r}' - \frac{z}{2}\right) + \mathcal{E}_0\left(\mathbf{r}' + \frac{z}{2}\right). \tag{5.19}$$

Eq. (5.19) gives rise to an additional dependence on z which leads to define a measure of the interaction energy by integrating in the transverse domain as follows[25]:

$$U_{\text{int}}(z) = -\left|\int_\Omega \mathcal{L}_{\text{int}}(\mathbf{r}', z)d\mathbf{r}'\right| \propto -\left|\int_\Omega \frac{\exp\left(-\sigma|\mathcal{E}(\mathbf{r}', z)|^2\right)}{\sigma^2 \mathcal{E}(\mathbf{r}', z)^2}\left(\sigma^2|\mathcal{E}(\mathbf{r}', z)|^2 + 1\right)d\mathbf{r}'\right|. \tag{5.20}$$

This is shown in Fig. 5.13 a), where the characteristic oscillatory behaviour as a function of the radial distance z is measured by integrating the quantity in Eq. (5.20). Contrarily to Ref. [139], the two-soliton interaction measured with the Hamiltonian approach as in Ref. [210] for the Kerr cavity and here for the purely optomechanical, displays a maximum at a certain nonzero radial distance z. However, this should not be interpreted as if there is an effective potential barrier in Fig. 5.13. Indeed, since the soliton motion here is Aristotelian, it is not possible to imagine such cavity solitons as particle-like structures with momentum/inertia and, therefore, one cannot observe two-soliton merging by collision, but only by exciting both solitons at a mutual distance within the range provided by the first maximum. For other cases such as self-propelled cavity solitons in semiconductor microcavities, where the system displays a bifurcation/transition from stationary to moving solitons [212], one can retrieve Newtonian effects in soliton motion. This motion was investigated with Laguerre-Gauss modes as input fields [213], structured profiles acting as billiards [214], multi-soliton collisions [215].

Such a measure of multi-soliton interaction can be directly generalized to the case of three (or more) localized peaks, in order to provide a partial understanding of the different stability of the multi-soliton chain observed in Fig. 5.12. For example, one can excite a single cavity soliton and span a two-dimensional potential landscape provided by two bound cavity solitons in their first pinning position. This could unveil the presence of local/global configuration minima besides the triangular cell[26], such as, for example, that of three solitons arranged on a straight line. In this framework, the presence of an angular phase gradient can be thought as

---

[24]One can simply verify that derivation with respect to $\mathcal{E}^*$ leads to the correct interaction term in Eq. 3.25 (Cavity equation in the low saturation limit).

[25]The modulus is chosen since Eq. (5.18) provides a complex expression.

[26]This corresponds to the hexagonal lattice ordering.
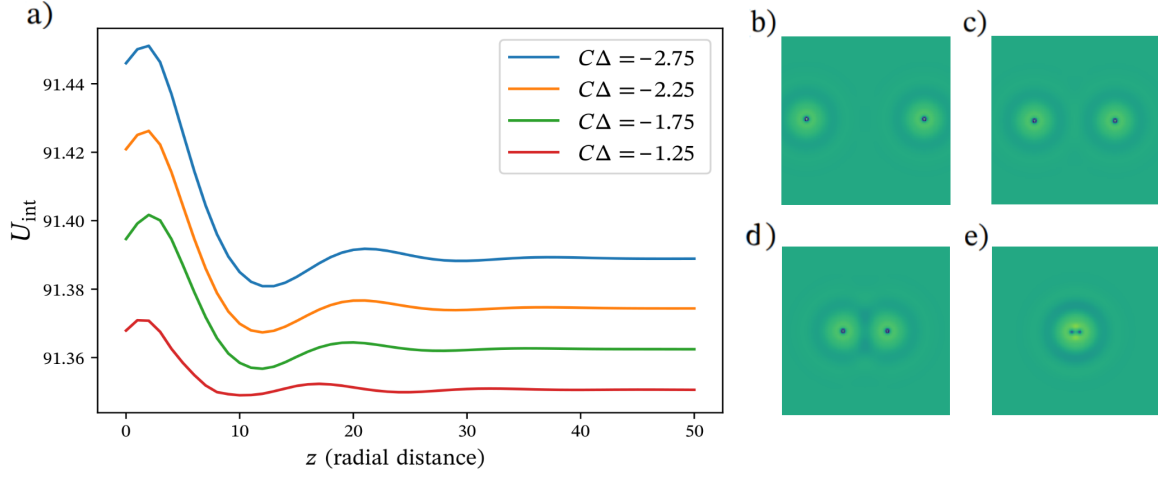
Fig. 5.13. Two-soliton interaction potentials as measured from Eq.(5.20), by exciting a single soliton at a position $(z/2, 0)$ and re-defining the cavity field according to Eq. (5.19). a) Varying z results in different interaction profiles for different values of $C\Delta$. The global minimum in each curve corresponds to the first pinning distance, often observed in numerical simulations. b) - e) Corresponding interaction $\mathcal{L}_{int}$ before numerical integration in Eq. (5.20)

an external perturbation that slightly shifts the three solitons from the local minimum configuration on the line, inducing dynamical evolution that globally minimizes the potential on the triangle. Another interesting effect observed in the simulations of Fig. 5.12, for the unstable three-soliton chain evolving in a rotating triangle, is that of tidal-like forces. This effect is caused by the differential (radially dependent) rotation induced by the azimuthal phase $e^{il\phi}$, pushing one of the solitons away from its equilibrium position. Both effect will be discussed in detail within in a further study, employing the Hamiltonian approach to the 2-d case with three interacting cavity solitons.

Chapter 6

Conclusions and Outlook

This thesis presented a collection of novel results concerning transverse optomechanical structures where the nonlinear medium is provided by a laser-cooled cloud of neutral atoms. The main new ingredient with respect to previous theoretical and experimental investigations is the use of structured input fields with spatially dependent phase profiles, from which a series of relevant physical phenomena connected to pattern dynamics, atomic transport and other applications were theoretically predicted and numerically simulated. Let us provide a brief review of the main concepts and results for each chapter below.

In Ch. 3, the spontaneous formation of rotating optomechanical lattices of light and atoms has been studied in a ring cavity configuration, where the spatially dependent rotation originates from the phase gradient of the input beam carrying OAM. The features of such a pattern rotation phenomenon have been characterized in dependence on the OAM integer index of the pump field and the kinetic parameters defining transport properties of the atomic gas in the overdamped limit. With the aid of particle-in-cell simulations, it has been shown that the corresponding OAM transfer mechanism is capable to sustain currents of bunched atoms along effectively 1-d circular lattices. In Ch. 4, numerical studies of the optomechanical self-structuring in a SFM model reveled a peculiar structural transition and pattern competition behaviour which is not described by the effective-Kerr approximation. This is shown by extensive analytical calculations probing the recovery of the inversion-symmetry and phase stability limits in the weakly nonlinear behaviour of the system at threshold. Finally, in Ch. 5, the dynamical properties of optomechanical feedback or cavity solitons have been addressed from the point of view of both atomic (classical) transport, complex trajectories in structured phase profiles and nonlinear multi-soliton interactions, showing transverse acceleration of solitary light-atom density structures[1], rotating and spiralling motion of single solitons and soliton chains, and many-soliton interactions.

Further open questions on fundamental topics and other possible research directions of interest, currently under investigation within the Strathclyde group and collaborators, are discussed in this section.

---

[1]Note that this acceleration can be tuned, in dependence on the momentum damping rate γ, externally controlled by means of optical molasses.

6.1 Further theoretical directions

Atomic transport and OAM

Firstly, the configuration in which a the atomic cloud is placed within a ring cavity setup, discussed in Ch. 3 has shown the presence of a complex[2] form of atomic transport arising from the breaking of a continuous rotational symmetry in the transverse plane and subsequent formation of rotating light-atom ring lattices due to a self-organized potential. Two interesting generalizations of such problem consist in the study of such rotational optomechanical instability in the conservative/Hamiltonian and ultracold limits. The first case can be realized by relaxing the presence of optical molasses in the atomic dynamics [54], and corresponds to the original realization of purely optomechanical structures in the Nice/Strathclyde setup [53]. Focusing on such a scenario implemented in a ring cavity may help understanding the mechanism behind the angular momentum transfer from the cavity input to the atomic currents and the dependence on the OAM index observed in Fig. 3.12. Indeed, the convergence of the coupled system to a global steady state is still ensured here by the presence of the cavity dissipation, but without additional losses due to momentum damping mechanisms.

In the ultracold/BEC case, the mean-field atomic dynamics is described by a complex function (Gross-Pitaevskij equation) and, in this sense, the proposed angular momentum exchange mechanism might share some features with *phase imprinting* mechanisms, as in Ref. [216]. OAM induced superfluid currents were introduced originally by means of two-photon Raman transfer [107, 217–219]. A connection between the OAM transfer mechanism studied here and conventional phase imprinting methods on BECs represents an interesting direction to be investigated in further studies.

Structural transitions in the SFM model and travelling solitons

Concerning the SFM setup, a clear generalization to the BEC case is given by the possible existence of structural transitions and the recovery of inversion symmetry in the model studied in Ref. [55]. This aspect is potentially useful in opening a connection with the issue of multiple supersolid phases as recently found in the case of dipolar gases or quantum ferrofluids, and described by similar variational mechanisms as in Ch. 4 [195, 220]. As already discussed in Ch. 5, this fact is deeply connected with the existence of solitons characterized by a dark-light/bright-density spatial profile. Further theoretical work is planned with the BEC model in a SFM/cavity arrangements, in order to draw a connection with the concept of quantum droplet [221–224]. Finally, the use of an OAM-carrying input field in such a model can induce rotation of the self-organized quantum gas and, thus, one can numerically observe supersolid properties/features connected with rotation in the form of deviations from the classical value of the moment of inertia of the cloud and so-called scissor modes[3] [225, 226].

Optomechanical cavity and feedback solitons have been investigated in Ch. 5, where insight

---

[2]I.e., not originating from direct angular momentum exchange by means radiation pressure/scattering forces.
[3]Such modes appear as collective oscillations of the gas around the pump symmetry axis.

about atomic transport of bright-density solitons and rotational dynamics of single and clusters of cavity solitons have been provided. A possible interesting extension would be to numerically study the collision of two solitons in a SFM model by means of particle dynamics simulations. Indeed, such method could unveil effects in the transient dynamics of the momentum distribution, not predicted by the mean-field approach. Furthermore, the preliminary results on the stability of rotating/spiralling soliton chains requires further efforts in a more rigorous theoretical characterization of the interaction among dissipative solitons, by means of a neutral mode approach as in Ref. [139], or a simpler effective variational/Hamiltonian one as in Refs. [170, 210]. Finally, one may generalize the problem to the case of a full control of complex cavity soliton transverse trajectories by means of time-dependent phase profiles.

6.2 Possibilities for experimental realizations

The aim of this small section is to provide the reader with some recent experimental advancements on transverse pattern formation setups involving the purely optomechanical nonlinearity. Current plans involve the realization of optomechanical patterns in the transverse domain of an optical cavity, interaction between magnetic and optomechanics degrees of freedom, and colloidal suspensions in a SFM setup.

Cold atoms in an optical cavity (Strathclyde)

Recent progress concerning Strathclyde current experimental setup were recently published in Ref. [144], where the chosen configuration is that of a confocal Fabry-Pérot cavity. Calculations from a linear stability analysis suggest that the purely optomechanical instability is achievable at intensities of the order of 10 mW/cm^2, with transverse structures of the order of $\Lambda_c \approx 100 \ \mu m$. However, implementing the presence of optical molasses to introduce momentum damping of the atoms demands for a careful compensation of the magnetic fields in the setup and experimental conditions for implementing such a proposition are currently under experimental investigation. This would allow the study of the effect of momentum dissipation into self-organization at various levels, i.e., from the slightly to the strongly viscous or overdamped cases. Such setup will also be used in future experiments to investigate interactions between magnetic/spin and optomechanical degrees of freedom [227], mutual self-focusing in the case of red atomic detuning, experimental realization of the structural transitions in the strong blue-detuned regime, and OAM induced rotational/spiralling dynamics of optical patterns of single and multiple/interacting dissipative solitons.

Suspensions of dielectric particles (Münster)

Further realizations of Talbot-based purely optomechanical structures are currently under investigation by the Münster group by means of colloidal suspension of dielectric particles in a SFM setup [228]. The features of the cold-atom theoretical model can be generalized to this
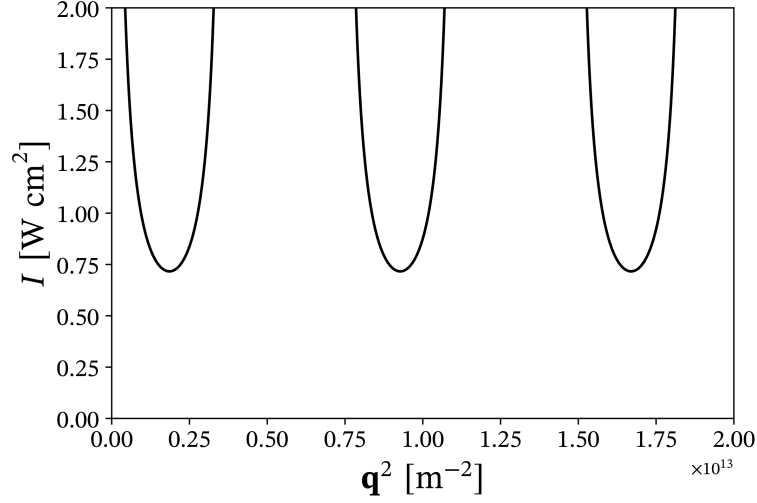
Fig. 6.1. Optomechanical pattern formation threshold (real optical intensity rescaled as $I = c\epsilon_0|E|^2/2$ [W/m^2]) for a colloidal suspension in a single-feedback-mirror model for parameter values comparable with the Münster lab experiment (see Fig. 6.2). As discussed previously in Ch. 4, additional diffusive mechanisms as well as thick medium effects and atomic saturation are expected to lift the perfect degeneracy of higher order instability domains.

case by considering the polarization **P** of a single dielectric microparticle of radius a, given by the following[4]:

$$\mathbf{P} = 4\pi\epsilon_0\nu_b^2\left(\frac{\nu^2-1}{\nu^2+2}\right)a^3\mathbf{E} = \alpha\mathbf{E}, \tag{6.1}$$

where ν_b is the refractive index of the surrounding medium, $\nu = \nu_a/\nu_b$ is the relative refractive index of the microparticle and **E** is the incoming electric field. Thus, assuming simply the presence of two counter-propagating scalar fields $\mathcal{E}_+$ and $\mathcal{E}_-$ (and neglecting as usual the longitudinal "standing wave" effects) in a SFM setup one obtains the following ponderomotive dipole-like force [229]:

$$\mathbf{F}_{\text{dip}}(\mathbf{r},t) = \frac{\alpha}{2}\nabla_\perp I(\mathbf{r},t) = \frac{\alpha}{2}\nabla_\perp|\mathcal{E}_-(\mathbf{r},t)|^2, \tag{6.2}$$

where I represents the total optical intensity. Therefore, the overdamped "density-only" dynamical equation of the colloid suspension is described by the Smoluchowski drift-diffusion equation, as used thoroughly in this thesis[5]. Note, however, that the appropriate optical susceptibility χ of the suspension parametrizing the optomechanical nonlinearity[6] reads (Maxwell-Garnett formula) [230, 231]:

$$\chi = k_0\eta(\nu_p - \nu_b), \tag{6.3}$$

---

[4]Known as the Clausius-Mossotti relation.
[5]Where the diffusion constant is linked to the fluid viscosity via the Stokes-Einstein relation.
[6]Which is effective-Kerr at the lowest nonlinear order.
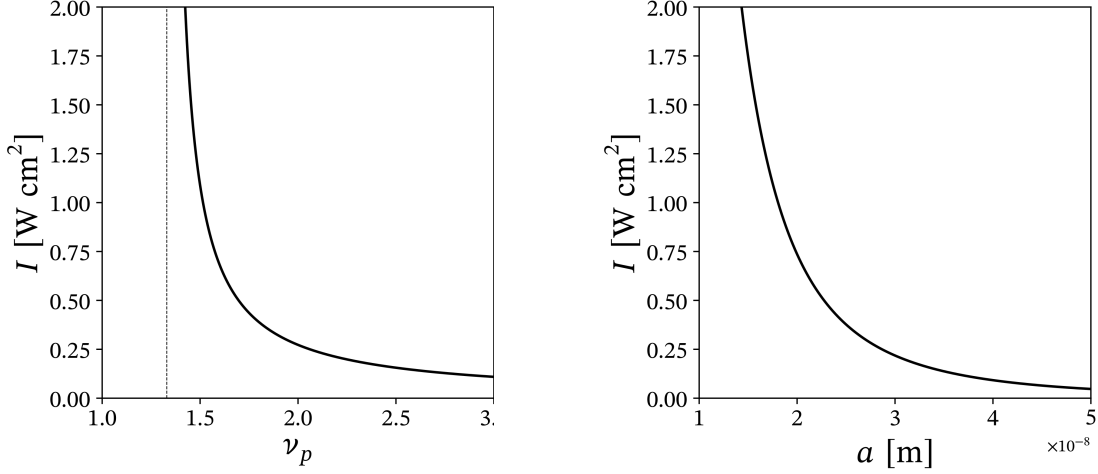
Fig. 6.2. MI intensity threshold dependence as function of two variable parameters of the colloidal suspension. (left) Threshold dependence on the particle refractive index ν_p at a typical fixed radius $a = 2 \times 10^{-8}\,m$. Note the divergence for $\nu_p = \nu_b$, where the background is simply the water refractive index $\nu_b \approx 1.33$ at 20 °C. (right) Threshold dependence on the particle radius $\propto a^{-3}$ at fixed $\nu_p \approx 1.58$, obtained for commercial polystyrene microparticles at wavelength $\lambda = 532\,nm$.

where $k_0 = 2\pi/\lambda_0$ and η is a filling factor parameter. Linear stability computations based on the previously shown approach of Sec. 4.1 for the purely dispersive SFM model with reflectivity R lead to the usual threshold condition:

$$\chi|F_0|^2 = \frac{1}{\alpha\beta R n_0 L \sin\Theta},\qquad(6.4)$$

where Θ is the total diffractive phase shift, L is the sample length, n_0 is the homogeneous particle density and $\beta = (k_B T)^{-1}$. Eq. (6.4) reveals a much higher modulation instability threshold with respect to the cold-atom case, of the order of 1 W/cm^2 for typical parameters of a water suspension of commercially available polystyrene microparticles, as seen from Fig. 6.1.

The dependence of the intensity threshold on the two relevant parameters such as the microparticle refractive index ν_p and its radius a, characteristic of such a soft-matter model, is shown in Fig. 6.2, displaying a decrease of the linear MI threshold for increasing value of both parameters[7] ν_p, a. However, stable precursors of hexagon-like optomechanical self-structuring are currently observed below the linear instability threshold by means of a slightly modified single-mirror setup [232]. Such studies have the potential to provide an interesting optical feedback based alternative to previous experimental realizations of modulation instabilities in soft-matter involving intense external fields [233], fiber optical traps [234], evanescent waveguides [235], counterpropagating Gaussian fields [236–238]. Furthermore, particle dynamics simulations and elimination of the backwards field $\mathcal{E}_-$ can be applied here to characterize effective long range photon-mediated interactions and demonstrate optically bound states of microparticles in the transverse domain [239].

---

[7]Note that one may have a degree of control here in choosing the particle size and materials with different ν_p.

Acknowledgements

This thesis is the results of almost four years of scientific research, stemming from a complex - in fact nonlinear - path, alternating moments of solitary reflection and other of strong collaborative efforts. Despite the backbone of the research progress at the early career stage is mainly given by the first, it is in the latter that the life of a researcher often finds its most pleasant and remarkable memories. For this reason, I would like to acknowledge here all the people that were involved in this route, from those who strongly contributed to my scientific and professional growth to those who were simply part of the life that comes with it.

I wish to start by thanking my supervisor Dr. Gordon R. M. Robb for being a constant and solid guide throughout my doctoral years, and for his support during times of intense and rigorous scientific work. His dedication in teaching and expertise in the field of cold-atom Physics, collective phenomena and computational methods inspired me to shape my own research work and future ambitions.

Moreover, I had the privilege of the shared second supervision of Dr. Alison M. Yao and Prof. Gian-Luca Oppo. I am grateful to them for their countless contributions to the research project and this Thesis, and for sharing their passion for the fields of structured light and nonlinear optics. Although the main interest of this research work is in the Physics of cold atomic systems, their support made me understand the importance of crossing boundaries, creativity and solid principles in scientific research.

An important role for the success of this Ph.D. project has been played by Prof. Thorsten Ackemann. I am indebted with him for sharing his expertise on pattern formation and experimental physics. His collaboration made me realize the importance of the feedback between theory and experiments, and how one positively influences the other.

As an Early Stage Researcher (ESR) within a Marie Skłodowska-Curie Action project, a special acknowledgement goes to the ColOpt ITN for the generous financial support and, in particular, to Nicola McRobbie for managing a successful and vibrant network of researchers. I greatly enjoyed academic visits and secondment experiences, which resulted in fruitful collaborations. In particular, I wish to thank Valeriia Bobkova and Adam Mazur for their collaboration during secondment projects in Münster and Berlin. I also want to thank Dr. Rolando Ayllon Salinas for the shared interests in science and all other ColOpt ESRs for the time spent together during network events. I am equally grateful to all fellow Ph.D. students in the CNQO group at Strathclyde for being part of a stimulating and fun environment.

Appendices

A.1   Further theoretical details and numerical methods

Details concerning the optomechanical model and numerical simulations presented throughout the thesis are discussed in this appendix. The first subsection focuses on the role of the 1-particle distribution function in modelling density redistribution in a many-particle system. Thereafter, the main algorithms of interest are the Split-Step and the Cranck-Nicolson schemes, useful to integrate the cold-atom optomechanical dynamics in the mean field limit and the Particle-in-cell technique, which is employed to solve the full semiclassical dynamics of the many-particle system.

Dilute gases and the 1-particle picture

In order to describe the essential physics in our scenario, i.e., a dilute cloud of cold neutral atoms, we show that it is enough to consider a phase space distribution in the 1-particle picture [173, 240]. Without loss of generality, we consider here the purely Hamiltonian case without dissipation. Let us start from the expression of a many-particle Hamiltonian of N classical atoms, interacting via a generic, short range, interatomic potential $V(|\mathbf{r}_i - \mathbf{r}_j|)$:

$$H = \sum_{i=1}^{N} \frac{\mathbf{p}_i^2}{2m} + U_{\mathrm{dip}}(\mathbf{r}_i) + \sum_{i<j} V(|\mathbf{r}_i - \mathbf{r}_j|), \tag{A.5}$$

where $U_{\mathrm{dip}}(\mathbf{r}_i)$ is an external trapping potential given by , e.g., the dipole force in our case. Analogous to the above defined function $f(\mathbf{r}, \mathbf{p}, t)$, we introduce here a more general probability distribution $f_N(\{\mathbf{r}_i, \mathbf{p}_i\}, t)$ defined in a phase space of dimension $2DN$, where $D = \{1, 2, 3\}$ is the effective dimensionality of the single-atom configuration space[8]. As for every regular distribution function, the normalization condition reads:

$$\int_{-\infty}^{+\infty} f_N(\{\mathbf{r}_i, \mathbf{p}_i\}, t) \, d\mathcal{V}_N = 1, \tag{A.6}$$

where $d\mathcal{V}_N = d\mathbf{r}_1 \dots d\mathbf{r}_N \times d\mathbf{p}_1 \dots d\mathbf{p}_N$. According to the Hamilton equations generated by Eq. (A.5), the dynamics (continuity equation) of $f_N(\{\mathbf{r}_i, \mathbf{p}_i\}, t)$ is given in terms of Poisson's

---

[8]Without loss of generality, we identify $(\mathbf{r}, \mathbf{p}) = (\mathbf{r}_1, \mathbf{p}_1)$.

brackets as follows [241]:

$$\partial_t f_N = -\sum_{i=1}^{N} \left[\nabla_{\mathbf{r}_i} \cdot (\dot{\mathbf{r}}_i f_N) + \nabla_{\mathbf{p}_i} \cdot (\dot{\mathbf{p}}_i f_N) \right] = \{H, f_N\}, \tag{A.7}$$

where $\{A, B\} = \sum_i \left(\nabla_{\mathbf{r}_i} A \cdot \nabla_{\mathbf{p}_i} B - \nabla_{\mathbf{p}_i} A \cdot \nabla_{\mathbf{r}_i} B \right)$. The 1-particle picture is thus recovered by simply integrating f_N over $N - 1$ atoms, namely, $f_1(\mathbf{r}, \mathbf{p}, t) = \int_{-\infty}^{+\infty} f_N(\{\mathbf{r}_i, \mathbf{p}_i\}, t) \, d\mathcal{V}_{N-1}$. As shown below, the general approach to the time evolution of $f_1(\mathbf{r}, \mathbf{p}, t)$ involves integrals of the interatomic potential $V(|\mathbf{r}_i - \mathbf{r}_j|)$:

$$\partial_t f_1 = \int_{-\infty}^{+\infty} \{H, f_N\} \, d\mathcal{V}_{N-1} = -\sum_{i=1}^{N} \int_{-\infty}^{+\infty} \left[\nabla_{\mathbf{r}_i} \cdot (\dot{\mathbf{r}}_i f_N) + \nabla_{\mathbf{p}_i} \cdot (\dot{\mathbf{p}}_i f_N) \right] d\mathcal{V}_{N-1} = \tag{A.8}$$

$$\sum_{i=1}^{N} \int_{-\infty}^{+\infty} \left[-\frac{\mathbf{p}_i}{m} \cdot \nabla_{\mathbf{r}_i} f_N + \nabla_{\mathbf{r}_i} U_{\text{dip}}(\mathbf{r}_i) \cdot \nabla_{\mathbf{p}_i} f_N + \sum_{j<k} \nabla_{\mathbf{r}_i} V(|\mathbf{r}_j - \mathbf{r}_k|) \cdot \nabla_{\mathbf{p}_i} f \right] d\mathcal{V}_{N-1}. \tag{A.9}$$

Integrating by parts all terms in the sum in Eq. (A.9), they all vanish except for $i = 1$, giving rise to the following equation:

$$\partial_t f_1 = \{H_1, f_1\} + \sum_{j=2}^{N} \int_{-\infty}^{+\infty} \left[\nabla_{\mathbf{r}} V(|\mathbf{r} - \mathbf{r}_j|) \cdot \nabla_{\mathbf{p}} f \right] d\mathcal{V}_{N-1}, \tag{A.10}$$

where we note the appearance of the single-particle Hamiltonian H_1. The integrals in the RHS of Eq. (A.10), often called *collision integrals* due to the short range nature of $V(|\mathbf{r} - \mathbf{r}_j|)$, are difficult to compute in full generality and one has to include several further assumptions and simplifications, e.g., leading to the Boltzmann transport equation [242]. In more general situations, the behaviour of Eq. (A.10) can be reduced to a hierarchy of equations, named after Bogoliubov, Born, Green, Kirkwood and Yvon (BBGKY), involving higher order distribution functions f_m as corrections to the dynamics of any collection of n atoms, represented by f_n, $n < m$. Such an approach is of relevance instead in the case of long-range interactions [243]. However, in many circumstances involving a dilute cloud of neutral atoms/scatterers, we can reasonably neglect collision integrals[9], i.e. $V \approx 0$, and assume that the conservative dynamics of the atoms is well described by a collisionless Boltzmann or Vlasov equation for $f_1(\mathbf{r}, \mathbf{p}, t)$ only:

$$\partial_t f_1(\mathbf{r}, \mathbf{p}, t) = \{H_1, f_1(\mathbf{r}, \mathbf{p}, t)\} = -\frac{\mathbf{p}}{m} \cdot \nabla_{\mathbf{r}} f_1(\mathbf{r}, \mathbf{p}, t) + \nabla_{\mathbf{r}} U_{\text{dip}}(\mathbf{r}) \cdot \nabla_{\mathbf{p}} f_1(\mathbf{r}, \mathbf{p}, t). \tag{A.11}$$

The prevalence of the 1-particle picture still applies entirely for the dissipative case under the action of optical molasses, where Eq. (A.11) is replaced by the above Kramers-Chandrasekhar equation or by the Smoluchowski equation in the strong friction case.

---

[9]And, more generally, all correlation functions included in f_n, $n > 1$.

Optomechanical and Electronic instabilities

The aim of this subsection is to discuss the different origin in the threshold for transverse modulation instabilities originating from the optomechanical and electronic instability mechanisms [56, 167]. Let us recall first the full optomechanical dynamics including momentum damping, described by the Kramers-Chandrasekhar equation (2.64):

$$\partial_t f(\mathbf{r}, \mathbf{p}, t) = -\frac{\mathbf{p}}{m} \cdot \nabla_\mathbf{r} f(\mathbf{r}, \mathbf{p}, t) + \nabla_\mathbf{p} \cdot \left[\left(\frac{\gamma}{m} \mathbf{p} + \nabla_\mathbf{r} U_{\mathrm{dip}}(\mathbf{r}) \right) f(\mathbf{r}, \mathbf{p}, t) \right] + D_\mathbf{p} \nabla_\mathbf{p}^2 f(\mathbf{r}, \mathbf{p}, t).$$

(A.12)

where $U_{\mathrm{dip}}(\mathbf{r}, t) = -\frac{\hbar \Gamma \Delta}{2} [1 + s(\mathbf{r}, t)]$ is the dipole force exerted on the external degrees of freedom of the atoms and $s(\mathbf{r}, t)$ is the saturation parameter which, for a SFM scheme reads $s(\mathbf{r}, t) = |\mathcal{E}_{+,0}|^2 + |\mathcal{E}_-(\mathbf{r}, t)|^2$. Note that the dipole potential expression in Eq. (A.12) arises from an adiabatic elimination of the internal atomic dynamics. As usual, the optical field evolution in free space (with k_0 being the wavenumber) is given as follows:

$$\partial_z \mathcal{E}_+(\mathbf{r}, t) = -\frac{i}{2k_0} \nabla_\perp'^2 \mathcal{E}_+(\mathbf{r}, t), \quad \partial_z \mathcal{E}_-(\mathbf{r}, t) = \frac{i}{2k_0} \nabla_\perp'^2 \mathcal{E}_-(\mathbf{r}, t).$$

(A.13)

Propagation of an optical beam of amplitude $\mathcal{E}_{+,0}$ inside the atomic cloud (including absorption) assumed of thickness L with a uniform atomic density and saturation, i.e. $n = 1$ and $s = s_0$ leads to:

$$\mathcal{E}_+(z = L) = \mathcal{E}_{+,0} \exp\left\{ -\frac{\alpha_0 L(1 - i\Delta)}{1 + s_0} \right\},$$

(A.14)

where the constant $\alpha = b_0/2L(1 + \Delta^2)$, such that the total susceptibility $\chi = \alpha_0 L \Delta$. This gives the homogeneous stationary solution for the field equations, where the saturation s_0 has to be computed self consistently from Eq. (A.14)[10], namely:

$$s_0 = |\mathcal{E}_{+,0}|^2 + |\mathcal{E}_{-,0}|^2 = |\mathcal{E}_{+,0}|^2 (1 + R\gamma_0) = |\mathcal{E}_{+,0}|^2 \left(1 + R \exp\left\{ -\frac{2\alpha_0 L}{(1 + s_0)} \right\} \right),$$

(A.15)

where the absorption factor $\gamma_0 = \exp\{-2\alpha_0 L/(1 + s_0)\}$. The family of homogeneous solutions for the distribution function in Eq. (A.12) is instead denoted with $f_0(\mathbf{v})$[11]. One introduces perturbations $f = f_0(\mathbf{v}) + f_1$ (which in turn yields $n = 1 + n_1$) and $s = s_0 + s_1$, so that the linearized expression of Eq. (A.14) reads:

$$\mathcal{E}_+'(z = L) = \mathcal{E}_{+,0} \exp\left\{ -\frac{\alpha_0 L(1 - i\Delta)}{1 + s_0 + s_1}(1 + n_1) \right\} \approx$$
$$\mathcal{E}_{+,0}\gamma_0 \left[1 - \frac{\alpha_0 L(1 - i\Delta)}{1 + s_0} \left(n_1 - \frac{s_1}{1 + s_0} \right) \right].$$

(A.16)

---

[10] Being assumed as a perfectly homogeneous component one does consider free-space diffraction
[11] I.e., depending on the atomic velocity only.

On the other hand, free space propagation to the mirror and back is solved in Fourier space so that, for the backward field $\mathcal{E}_-$, one has:

$$
\begin{aligned}
\mathcal{E}_-(\mathbf{q}, t) &= \sqrt{R} \exp\left(i \frac{d|\mathbf{q}|^2}{k_0}\right) \int_{\mathbb{R}^2} d\mathbf{r}\, e^{i\mathbf{q}\cdot\mathbf{r}}\, \mathcal{E}'_+(z = L) = \\
&= \sqrt{R} \exp\left(i \frac{d|\mathbf{q}|^2}{k_0}\right) \mathcal{E}_{+,0} \gamma_0 \left[\delta(\mathbf{q}) - \frac{\alpha_0 L(1 - i\Delta)}{1 + s_0}\left(n_1(\mathbf{q}, t) - \frac{s_1(\mathbf{q}, t)}{1 + s_0}\right)\right] = \\
&\quad\quad \mathcal{E}_{-,0}\left[\delta(\mathbf{q}) + \mathcal{E}_1(\mathbf{q}, t)\right],
\end{aligned}
\tag{A.17}
$$

where $\exp\left(id|\mathbf{q}|^2/k_0\right)$ is the usual phase slippage factor due to propagation to the mirror and back. Eq. (A.17) provides a first order expression for $\mathcal{E}_1(\mathbf{q}, t)$ in terms of $s_1(\mathbf{q}, t)$ and $n_1(\mathbf{q}, t)$. This is used to find the perturbations $s_1(\mathbf{q}, t)$ in terms of $n_1(\mathbf{q}, t)$ only:

$$
\begin{aligned}
s_1(\mathbf{q}, t) &= \gamma_0 R |\mathcal{E}_{+,0}|^2 \left[\mathcal{E}_1(\mathbf{q}, t) + \mathcal{E}_1^*(\mathbf{q}, t)\right] = \\
\gamma_0 R |\mathcal{E}_{+,0}|^2 &\left[-\frac{\alpha_0 L(1 - i\Delta)}{1 + s_0}\left(n_1(\mathbf{q}, t) - \frac{s_1(\mathbf{q}, t)}{1 + s_0}\right)\exp\left(i\Theta\right) + \text{c.c.}\right] = \\
\gamma_0 R |\mathcal{E}_{+,0}|^2 &\left[-\frac{2\alpha_0 L}{1 + s_0}\left(n_1(\mathbf{q}, t) - \frac{s_1(\mathbf{q}, t)}{1 + s_0}\right)\left[\cos\Theta + \Delta\sin\Theta\right]\right]
\end{aligned}
\tag{A.18}
$$

where $\Theta = d|\mathbf{q}|^2/k_0$. Isolating $s_1(\mathbf{q}, t)$ from the above expression, one obtains:

$$
s_1(\mathbf{q}, t) = \frac{(1 + s_0)K}{1 - K} n_1(\mathbf{q}, t) = \frac{K}{1 - K} \int_V f_1(\mathbf{r}, \mathbf{v}, t) d\mathbf{v},
\tag{A.19}
$$

where:

$$
K = \frac{2R|\mathcal{E}_{+,0}|^2 \gamma_0 \alpha_0 L}{(1 + s_0)^2}\left[\cos\Theta + \Delta\sin\Theta\right].
\tag{A.20}
$$

To obtain a closed expression for the phase space modulation $f_1(\mathbf{r}, \mathbf{v}, t)$ one needs to linearize Eq. (A.12) in Fourier (space) - Laplace (time) domain from which one is able to extract the growth rate [54, 244]. In particular, for the purely electronic case the threshold condition is obtained imposing that the growth rate diverges [12]. This is achieved when $K = 1$, namely:

$$
\frac{\gamma_0 |\mathcal{E}_{+,0}|^2}{\left[1 + (1 + \gamma_0 R|\mathcal{E}_{+,0}|^2)\right]^2} = \frac{1}{2R\alpha_0\left[\cos\Theta + \Delta\sin\Theta\right]}.
\tag{A.21}
$$

Such threshold condition above can be visualized in the parameter space (s_0, Δ) where s_0 is the value of the homogeneous saturation, showing the presence of lower and upper thresholds for the electronic instability [58]. This is shown in Fig. 3 a), where the optical density b_0 is kept fixed in the calculation. Furthermore, it is also useful to visualize the instability in terms of the linear and nonlinear phase shift (Fig. 3 b)), namely $\Phi_L = \chi/2 = \alpha_0 L\Delta$, and $\Phi_{NL} = \Phi_L s_0/(1 + s_0)$ respectively.

---

[12]This is not surprising since one typically assumes fast atomic dynamics in the purely optomechanical model.
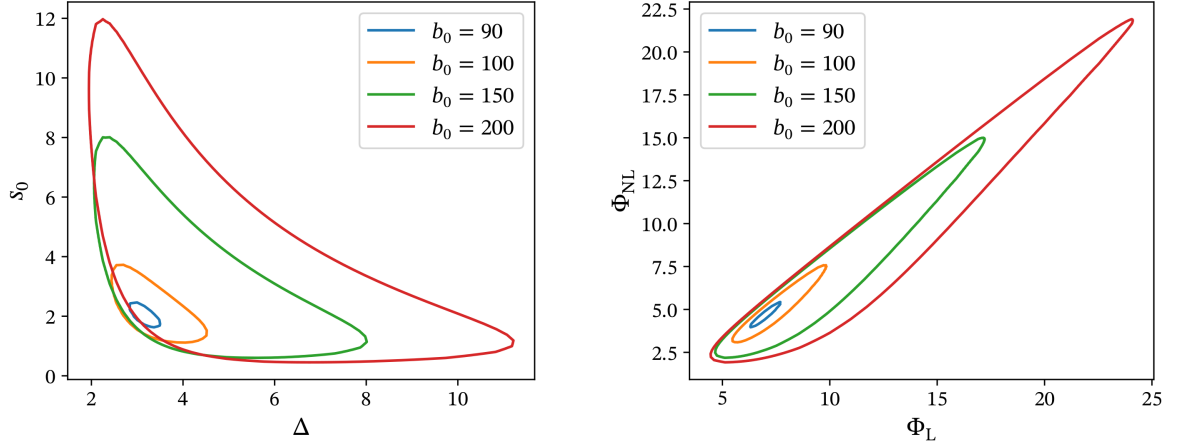
Fig. 3. Electronic instability threshold diagrams identified by $K = 1$. a) Homogeneous saturation at threshold vs Δ. b) Nonlinear Φ_{NL} vs linear Φ_L shifts according to the above definitions.

Split-step method

The split-step numerical method is a so-called *pseudo-spectral* method, commonly used to integrate nonlinear wave equations such as the nonlinear Schroedinger Eqs. or the Lugiato -Lefever Eqs. The split step is widely used in this thesis in order to numerically integrate the cavity field dynamical equation, where the nonlinear term is provided by the Gibbs density. An introduction to the split-step method can be found in Ref. [245]. The general nonlinear wave equation in our case can be represented as follows:

$$i\partial_t \mathcal{E} + \hat{L}\mathcal{E} + \hat{N}(\mathcal{E})\mathcal{E} = 0, \tag{A.22}$$

where $\hat{L}$ is a linear differential operator and $\hat{N}(\mathcal{E})$ is a nonlinear functional. Let us define $\mathcal{E}(\mathbf{r}, \delta t)$ a solution of Eq. (A.22) at time $t = \Delta t$ where r is the transverse coordinate. $\mathcal{E}(\mathbf{r}, t)$ is formally obtained from an initial condition $\mathcal{E}(\mathbf{r}, 0)$ as follows:

$$\mathcal{E}(\mathbf{r}, \delta t) = \exp\left[-i\hat{L}t + -i\int_0^{\delta t} \hat{N}(\mathcal{E}(\mathbf{r}, \tau))d\tau\right]\mathcal{E}(\mathbf{r}, 0). \tag{A.23}$$

The method is based on approximating the exponential operator as the following product:

$$\exp\left[-i(\hat{A} + \hat{B})\right] = \exp\left(-i\hat{A}/2\right)\exp\left(-i\hat{B}\right)\exp\left(-i\hat{A}/2\right) + O(\delta t^3). \tag{A.24}$$

In typical problems of interest, the nonlinear integral in Eq. (A.23) depends on the modulus square $|\mathcal{E}|^2$ which is a constant of motion so that the integral in (A.23) drops out. Thus, due to the specific form[13] of $\hat{L}$, the algorithm for integrating Eq. (A.22) numerically can be described

---

[13]Typically $\hat{L} = \nabla^2$ in our case.

in a series of steps:

$$\mathcal{E}_1(\mathbf{r}, \delta t) = \mathcal{F}^{-1}\{h(\mathbf{q}, \delta t)\mathcal{F}[\mathcal{E}(\mathbf{r}, 0)]\}, \tag{A.25}$$

$$\mathcal{E}_2(\mathbf{r}, \delta t) = e^{-i\hat{N}(|\mathcal{E}(\mathbf{r},0)|^2)\delta t}\mathcal{E}_1(\mathbf{r}, \delta t), \tag{A.26}$$

$$\mathcal{E}_3(\mathbf{r}, \delta t) = \mathcal{F}^{-1}\{h(\mathbf{q}, \delta t)\mathcal{F}[\mathcal{E}_2(\mathbf{r}, \delta t)]\}, \tag{A.27}$$

where $h(\mathbf{q}, \delta t) = e^{-i\frac{\mathbf{q}^2 \delta t}{2}}$ is the factor representing the action of the linear operator $\hat{L}$ in Fourier space and $\mathcal{F}$ represents the Fourier transform. The exponential in (A.26), representing the nonlinear step of the algorithm, is solved by a 4$^{\text{th}}$-order Runge-Kutta method [246]. Therefore, once the time step δt is established, the procedure is repeated until the final time $t_{\max}$ is reached.

Crank-Nicolson method

The Crank-Nicolson (CN) method is a finite difference method commonly used to integrate nonlinear partial differential equations [247]. In this context it is adopted as a scheme to integrate the coupled systems of Eqs. (3.34) and (3.26) in order to show the existence of a diffusive drag in the rotating lattice dynamics in a ring cavity system[14]. Let us start from the general formulation of the system for the function $u(\mathbf{r}, t) = [\text{Re}\,\mathcal{E}(\mathbf{r}, t), \text{Im}\,\mathcal{E}(\mathbf{r}, t), n(\mathbf{r}, t)]^{\text{T}}$, where $\mathcal{E}$ is the complex cavity field and n is the real atom density:

$$\partial_t u(\mathbf{r}, t) = \mathcal{F}[u],$$

where $\mathcal{F}$ is the nonlinear functional defined by Eqs. (3.34) and (3.26). The discretization is introduced as $(\{x_i\}, \{y_j\}, \{t_k\}) = (\{-x_d + i * \delta x\}, \{-y_d + j * \delta y\}, \{k * \delta t\})$, where $i, j, k \in \mathbb{N}$. Thus, the approximation of $u(\mathbf{r}, t)$ is denoted as $u_{i,j}^k$ where the subscript and superscript refer to spatial and temporal discretization respectively. The CN scheme is applied as follows:

$$\frac{u_{i,j}^{k+1} - u_{i,j}^k}{\delta t} = \frac{1}{2}\left(\mathcal{F}[u_{i,j}^{k+1}] - \mathcal{F}[u_{i,j}^k]\right), \tag{A.28}$$

where the forward derivative in time is adopted. Since the optomechanical nonlinearity depends crucially on the intensity gradient in the Smoluchowski equation, the optomechanical system can be approximated by means of a Besse-like scheme [248]:

$$\begin{cases} v(\mathbf{r}, t) = |\mathcal{E}(\mathbf{r}, t)|^2, \\ \partial_t u(\mathbf{r}, t) = \mathcal{F}[u, v], \end{cases} \tag{A.29}$$

where the function $v(\mathbf{r}, t)$ (intracavity field intensity) is typically estimated at an intermediate step. Thus, one shows that the coupled system functional $\mathcal{F}[u, v]$ can be represented by means

---

[14]See Sec.3.3.2 for the numerical results in dependence on the diffusion constant $D_{\mathbf{r}}$.

of the following compact matrix notation:

$$\mathcal{F}[u,v] = \begin{pmatrix} -1 & \hat{L} & 0 \\ -\hat{L} & -1 & 0 \\ 0 & 0 & \hat{L}_n(v) \end{pmatrix} \cdot u + 2C\Delta \left[\begin{pmatrix} 0 & 1 & 0 \\ -1 & 0 & 0 \\ 0 & 0 & 0 \end{pmatrix} \cdot u \right] \odot \begin{pmatrix} n \\ n \\ 0 \end{pmatrix} + \begin{pmatrix} \mathrm{Re}\, A_I(\mathbf{r}) \\ \mathrm{Im}\, A_I(\mathbf{r}) \\ 0 \end{pmatrix},$$

(A.30)

where the operator $\hat{L} = \nabla_\perp^2 - \theta$, $A_I(\mathbf{r})$ is the usual input pump (split into real and imaginary parts) and the symbol $\odot$ denotes the Hadamard (element-wise) product, representing the field-density coupling in the cavity equation. Moreover, due to this assumption the transport-generating coupling in the Smoluchowski equation becomes linear and it is represented by:

$$\hat{L}_n(v) = \sigma D_\mathbf{r} \left[(\nabla_\perp v) \cdot \nabla_\perp + \nabla_\perp^2 v \right] + D_\mathbf{r} \nabla_\perp^2.$$

The spatial discretization introduces coupling among spatial points, according to the central difference rules with periodic boundary conditions. The corresponding nonlinear system $\mathcal{S}[u_{i,j}^{k+1}] = 0$, obtained by applying the CN scheme, is solved by employing a standard nonlinear solver[15], where the Jacobian matrix is computed analytically from Eqs. (A.30).

Particle-in-cell codes

Originally introduced in the context of plasma physics simulations, the particle-in-cell (PIC) technique is a widely used computational method to efficiently solve a wide class of particle dynamics problems, where a large number of particles interact with a continuous e.m. field [249]. A classical introduction to PIC simulations is given in Ref. [250]. In purely general terms, denoting with the dynamical evolution of a set on N atoms or particle is given as follows:

$$\frac{d\mathbf{r}_j}{dt} = \frac{\mathbf{p}_j}{m}, \quad \frac{d\mathbf{p}_j}{dt} = \mathcal{F}(t, \{\mathbf{r}_j\}, \{A\}) \tag{A.31}$$

where $j = 1, \dots, N$ and $\{A\}$ denotes one or a set of continuous fields whose dynamics is governed by a certain prescribed rule. For example, in our case, the functional $\mathcal{F}$, which includes also the stochastic forces $\{\xi_j(t)\}$ and momentum damping, is given by the dipolar force in Eq. (4.42), where the field amplitudes $\mathcal{E}_+$ and $\mathcal{E}_-$ evolve according to the paraxial wave equation, the cavity equation, or the thin-medium model with single-feedback, depending on the specific configuration in use. Moreover, the field evolution depends on an atom/particle density $n(t, \{\mathbf{r}_j\})$ which needs to be evaluated, depending on the particle state.

For simplicity, the part of the algorithm that evolves particle equations is referred to as *particle mover*. Within our system, since neural atoms interact collectively with the radiation field only, it is enough to consider a 2$^\mathrm{nd}$ order stochastic Runge-Kutta routine (SRK2), as introduced in Ref. [251]. Recalling the coordinate rescaling in Eq. (3.49) for the ring cavity and Eq. (4.42)

---

[15]See the SCIPY function *fsolve* which adopts a modified Powell's nonlinear optimization method https://docs.scipy.org/doc/scipy/reference/generated/scipy.optimize.fsolve.html.

and given an initial condition $\{\bar{\mathbf{r}}_j^0\}$, the main integration scheme at time $\bar{t} = \Delta\bar{t}$ reads[16]:

$$\bar{\mathbf{r}}_j(\Delta\bar{t}) = \bar{\mathbf{r}}_j^0 + \frac{1}{2}\Delta\bar{t}\,(F_1 + F_2) + \sqrt{2D\Delta\bar{t}}\,\psi, \tag{A.32}$$

where the two quantities F_1 and F_2 read:

$$F_1 = \mathcal{F}\left(\bar{t} = 0, \{\bar{\mathbf{r}}_j^0\}\right), \tag{A.33}$$

$$F_2 = \mathcal{F}\left(\bar{t} = \Delta\bar{t}, \{\bar{\mathbf{r}}_j^0 + \Delta\bar{t}\,F_1 + \sqrt{2D\Delta\bar{t}}\,\psi\}\right), \tag{A.34}$$

and ψ is a random variable such that $\langle\psi\rangle = 0$ and $\langle\psi^2\rangle = 1$. Of course, the value of the system functional $\mathcal{F}$ (determined by the dipole force in the particle Eqs. 5.9) needs to be interpolated at the current positions in order to determine the forces acting on atoms. This is done in FUNCTION dy. Moreover, since the field satisfies periodic boundary conditions and no other boundary effects are present, particles must be constantly re-injected within the spatial square domain of length L according to the following simple rule:

$$\tilde{\mathbf{r}}_j = (\bar{x}_j \pm L, \bar{y}_j \pm L), \quad \tilde{\mathbf{p}}_j = \mathbf{p}_j, \tag{A.35}$$

where the $\pm$ sign depends on which side the particles escape the domain. This is accomplished by the SUBROUTINE ADJUST. Denoting now with y the system variables, the main integration loop reads:

```
y=y_0
t=0.0_WP
nextt=tperplot

CALL OUTPUT(t,y_0)
DO
    CALL UPDATE(t,y,t,y)
    IF (t>=nextt) THEN
        nextt=nextt+tperplot
        CALL OUTPUT(t,y)
    END IF
    IF (t>=maxt) EXIT
END DO
```

where the UPDATE routine, for the single-feedback-system has the following structure, as described previously in Sec. 4.2.1:

```
SUBROUTINE UPDATE(t,y,newt,newy)
IMPLICIT NONE
```

---

[16]See [251] for a formal derivation of the stochastic Runge-Kutta algorithm.

```fortran
REAL(KIND=WP),                          INTENT(IN)       :: t
REAL(KIND=WP), DIMENSION(:),  INTENT(IN)       :: y
REAL(KIND=WP),                          INTENT(OUT)      :: newt
REAL(KIND=WP), DIMENSION(SIZE(y)), INTENT(OUT) :: newy


CALL PROPAGATE_F(y,newy)        !Forward field propagation (phase shift)
CALL REFLECT(newy,newy)         !Free space propagation
CALL SRK2(t,newy,newt,newy)     !Particle mover
CALL ADJUST(newy,newy)          !Particle reinjection
```

Finally, numerical reconstruction of the continuous density profile $n(\bar{\mathbf{r}}, \bar{t})$ from the particle positions is done within `PROPAGATE_F`. For the ring-cavity case, the integration scheme is the same as the split-step method in Eqs. (A.25, A.26, A.27).

A.2   From particle dynamics to mean-field equations

The aim of this appendix is to discuss the mapping of the semiclassical evolution of a discrete set of atoms to the relative partial differential equations for phase-space distributions or atomic densities in the thermodynamic limit. This is useful whenever particle-in-cell simulations are compared with results derived from the distribution functions such as in Fig. 3.12. The argument is based on the usual set of Langevin equations for a set of N_{atoms} of mass m subject to dipole potential, momentum damping (optical molasses) and stochastic forces.

$$\dot{\mathbf{r}}_j = \frac{\mathbf{p}_j}{m}, \quad \dot{\mathbf{p}}_j = \mathbf{f}_{\mathrm{dip}}(\mathbf{r}, t) - \gamma \frac{\mathbf{p}_j}{m} + \xi_j(t), \tag{A.36}$$

where the two-dimensional stochastic variable reads $\xi_j(t) = [\xi_j^x(t), \xi_j^y(t)]^T$ with[17] $\langle \xi_j^x(t) \rangle = 0$ and $\langle \xi_j^x(t)\xi_{j'}^x(t') \rangle = 2D_{\mathbf{p}}\delta_{jj'}\delta(t - t')$, and the momentum diffusion $D_{\mathbf{p}} = \gamma k_B T$. The rescaled equations for the atomic phase-space distribution function in the limit N_{atoms} depend on the coordinate rescaling, which is slightly different for a SFM or a ring cavity model.

Ring cavity

As introduced in Sec. 3.4.2, the adopted adimensional coordinates read $\bar{\mathbf{r}}_j = q_c r_j$ and $\bar{\mathbf{p}} = \mathbf{p}_j/\hbar q_c$ with the rescaled time $t' = \kappa t$, i.e. in units of the cavity decay rate κ. In the thermodynamic limit, the rescaled Kramers-Chandrasekhar for the distribution $f(\bar{\mathbf{r}}, \bar{\mathbf{p}}, \bar{t})$ reads [173]:

$$\frac{\partial}{\partial \bar{t}} f(\bar{\mathbf{r}}, \bar{\mathbf{p}}, \bar{t}) = -2\omega_p \cdot \bar{\mathbf{p}} \frac{d}{d\bar{\mathbf{r}}} f(\bar{\mathbf{r}}, \bar{\mathbf{p}}, \bar{t}) + \frac{\Gamma\Delta}{4\kappa}\left[\frac{d}{d\bar{\mathbf{r}}} s(\bar{\mathbf{r}}, \bar{t}) \cdot \frac{d}{d\bar{\mathbf{p}}} f(\bar{\mathbf{r}}, \bar{\mathbf{p}}, \bar{t})\right] +$$

$$\bar{\gamma}\frac{d}{d\bar{\mathbf{p}}}\left[\bar{\mathbf{p}} \cdot f(\bar{\mathbf{r}}, \bar{\mathbf{p}}, \bar{t})\right] + \bar{D}_{\bar{\mathbf{p}}}\frac{d^2}{d\bar{\mathbf{p}}^2} f(\bar{\mathbf{r}}, \bar{\mathbf{p}}, \bar{t}). \tag{A.37}$$

---

[17]Analogously for the y variable.

where $\omega_p = \hbar q_c/2m\kappa$, $\bar{\gamma} = \gamma/m\kappa$, and $\bar{D}_{\bar{\mathbf{p}}} = D_{\mathbf{p}}/\hbar^2 q_c^2 \kappa$. Note that the distribution function f is now also adimensional. The corresponding Smoluchowski equation for the adimensional atomic density in the limit $\bar{t} \ll \bar{\gamma}^{-1}$ reads:

$$\frac{\partial}{\partial \bar{t}} \, n(\bar{\mathbf{r}}, \bar{t}) = \frac{\omega_p \Gamma \Delta}{2\kappa \bar{\gamma} \bar{D}_{\bar{\mathbf{r}}}} \cdot \bar{D}_{\bar{\mathbf{r}}} \frac{\partial}{\partial \bar{\mathbf{r}}} \left[\frac{\partial}{\partial \bar{\mathbf{r}}} s(\bar{\mathbf{r}}, \bar{t}) \, n(\bar{\mathbf{r}}, \bar{t}) \right] + \bar{D}_{\bar{\mathbf{r}}} \frac{\partial^2}{\partial \bar{\mathbf{r}}^2} n(\bar{\mathbf{r}}, \bar{t}), \qquad (A.38)$$

where the optomechanical coupling constant σ is now expressed in terms of the spatial diffusion $\bar{D}_{\bar{\mathbf{r}}}$. In terms of simulation parameters (momentum spread ζ_p), we exploit the (rescaled) relations between $\bar{D}_{\bar{\mathbf{r}}}$ and $\bar{D}_{\bar{\mathbf{p}}}$ to obtain:

$$\bar{D}_{\bar{\mathbf{r}}} = \frac{4\omega_p}{\bar{\gamma}^2} \bar{D}_{\bar{\mathbf{p}}}, \quad \sigma = \frac{\omega_q \Gamma \Delta}{2\kappa \bar{\gamma} \bar{D}_{\bar{\mathbf{r}}}} = \frac{\Gamma \Delta}{8\kappa \omega_q \zeta_p^2}. \qquad (A.39)$$

as shown already in Eq. (3.51).

Single-feedback mirror

For the SFM case, the coordinate rescaling slightly differs from the ring cavity case for the choice of $\bar{t} = \omega_p t$ [18]. Thus the corresponding rescaled Kramers-Chandrasekhar equation for the adimensional phase space distribution function $f(\bar{\mathbf{r}}, \bar{\mathbf{p}}, \bar{t})$ now reads:

$$\frac{\partial}{\partial \bar{t}} f(\bar{\mathbf{r}}, \bar{\mathbf{p}}, \bar{t}) = -2 \cdot \bar{\mathbf{p}} \frac{d}{d\bar{\mathbf{r}}} f(\bar{\mathbf{r}}, \bar{\mathbf{p}}, \bar{t}) + \frac{\Gamma \Delta}{4\omega_p} \left[\frac{d}{d\bar{\mathbf{r}}} s(\bar{\mathbf{r}}, \bar{t}) \cdot \frac{d}{d\bar{\mathbf{p}}} f(\bar{\mathbf{r}}, \bar{\mathbf{p}}, \bar{t}) \right] +$$
$$\bar{\gamma} \frac{d}{d\bar{\mathbf{p}}} \left[\bar{\mathbf{p}} \cdot f(\bar{\mathbf{r}}, \bar{\mathbf{p}}, \bar{t}) \right] + \bar{D}_{\bar{\mathbf{p}}} \frac{d^2}{d\bar{\mathbf{p}}^2} f(\bar{\mathbf{r}}, \bar{\mathbf{p}}, \bar{t}). \qquad (A.40)$$

Analogously, for the Smoluchowski drift-diffusion equation one has:

$$\frac{\partial}{\partial \bar{t}} \, n(\bar{\mathbf{r}}, \bar{t}) = \frac{2\bar{U}_0}{\bar{\gamma} \bar{D}} \cdot \bar{D} \frac{\partial}{\partial \bar{\mathbf{r}}} \left[\frac{\partial}{\partial \bar{\mathbf{r}}} s(\bar{\mathbf{r}}, \bar{t}) \, n(\bar{\mathbf{r}}, \bar{t}) \right] + \bar{D} \frac{\partial^2}{\partial \bar{\mathbf{r}}^2} n(\bar{\mathbf{r}}, \bar{t}), \qquad (A.41)$$

where the rescaled potential reads $\bar{U}_0 = \Gamma \Delta/4\omega_p$, and the optomechanical constant reads $\sigma = 2\bar{U}_0/\bar{\gamma} \bar{D}$. Thus, as used previously in Eq. (5.10), the two important constants in terms of simulation parameters now read:

$$\bar{D} = \frac{4}{\bar{\gamma}^2} \bar{D}_{\bar{\mathbf{p}}}, \quad \sigma = \frac{\bar{U}_0 \bar{\gamma}}{2\bar{D}_{\bar{\mathbf{p}}}}. \qquad (A.42)$$

Those recipes allows for a comparison between the two approaches, useful when observing beyond mean-field effects with a finite number of atoms.

---

[18]This is due to the fact that, neglecting the feedback delay time, the temporal dynamics is entirely defined by the medium dynamics in the SFM model.

A.3 Amplitude equations coefficients

This appendix provides the analytical details concerning the computation of the coefficients of the amplitude equations for the cold-atom optomechanical model in Sec. 4.2.1. The derivation is presented into separate subsections for successive orders in the weakly nonlinear expansion.

Derivation at $O(\epsilon^2)$

At order $O(\epsilon^2)$, one starts from the term $\hat{\mathcal{G}}_1$ in Eq. (4.25), acting on n_1 of Eq. (4.23) and $\mathcal{R}_1$ in Eq. (4.26), namely :

$$\hat{\mathcal{G}}_1 n_1 = -\partial_t n_1 + iR\sigma DI_0 \chi \left[p_1 \nabla_\perp'^2 \left(\hat{\mathcal{L}} - \hat{\mathcal{L}}^\dagger \right) \right] n_1, \tag{A.43}$$

$$\mathcal{R}_1 = R\sigma DI_0 \left[i\nabla_\perp' \cdot \left[n_1 \nabla_\perp' \left(\hat{\mathcal{L}} - \hat{\mathcal{L}}^\dagger \right) n_1 \right] - \frac{\chi}{2} \nabla_\perp'^2 \left(\hat{\mathcal{L}} + \hat{\mathcal{L}}^\dagger \right) n_1^2 + \chi \nabla_\perp'^2 (\hat{\mathcal{L}} n_1)(\hat{\mathcal{L}}^\dagger n_1) \right]. \tag{A.44}$$

where $\hat{\mathcal{L}} = e^{-id\nabla_\perp'^2/k_0}$. The action of the linear term $\hat{\mathcal{G}}_1$ on n_1 is trivial and yields the coefficient $\mu(p, \chi)$ reported in Eq. (4.27). Let us consider now the terms in $\mathcal{R}_1$, keeping in mind that only resonant terms are considered in the approach of Sec. 4.2.1:

1) First term in $\mathcal{R}_1$:

$$i\nabla_\perp' \cdot \left[n_1 \nabla_\perp' \left(\hat{\mathcal{L}} - \hat{\mathcal{L}}^\dagger \right) n_1 \right] = n_1 \nabla_\perp'^2 i \left(\hat{\mathcal{L}} - \hat{\mathcal{L}}^\dagger \right) n_1 + (\nabla_\perp' n_1) \cdot i\nabla_\perp' \left(\hat{\mathcal{L}} - \hat{\mathcal{L}}^\dagger \right) n_1 = $$
$$+ 2q_c^2 \sin \Theta_c + \frac{1}{2} \left[-2 \sin \Theta_c \nabla_\perp'^2 n_1^2 + 4 \sin \Theta_c n_1 \nabla_\perp'^2 n_1 \right] = q_c^2 \sin \Theta_c n_1^2. \tag{A.45}$$

2) Second term[19] in $\mathcal{R}_1$:

$$-\frac{\chi}{2} \nabla_\perp'^2 \left(\hat{\mathcal{L}} + \hat{\mathcal{L}}^\dagger \right) n_1^2 = \frac{q_c^2 \chi}{2} \cos \Theta_c n_1^2. \tag{A.46}$$

3) Third term in $\mathcal{R}_1$:

$$\chi \nabla_\perp'^2 (\hat{\mathcal{L}} n_1)(\hat{\mathcal{L}}^\dagger n_1) = \frac{\chi}{4} \nabla_\perp'^2 e^{i\Theta_c} \left[\sum_{i=1}^{3} A_i \exp(i\mathbf{q}_i \cdot \mathbf{r}) + c.c. \right] e^{-i\Theta_c} \left[\sum_{i=1}^{3} A_i \exp(i\mathbf{q}_i \cdot \mathbf{r}) + c.c. \right] = $$
$$- q_c^2 \chi n_1^2. \tag{A.47}$$

Finally, all contributions at $O(\epsilon^2)$ sum to the quadratic coefficient $\lambda(p, \chi)$ in Eq. (4.28).

---

[19] Note that this term vanishes for $\Theta_c = \pi/2$.

Derivation at $O(\epsilon^3)$

Let us consider now the essential third-order terms of $\mathcal{R}_2$ in Eq. (4.22), namely:

$$
\begin{aligned}
\mathcal{R}_2 =\ & iR\sigma I_0 \chi \nabla_\perp'^2 \left\{ \frac{1}{2} \left[(\hat{\mathcal{L}} n_1^2)(\hat{\mathcal{L}}^\dagger n_1) - (\hat{\mathcal{L}} n_1)(\hat{\mathcal{L}}^\dagger n_1^2) \right] - \frac{1}{6} \left(\hat{\mathcal{L}} - \hat{\mathcal{L}}^\dagger \right) n_1^3 \right\} + \\
& R\sigma I_0 \left\{ \nabla_\perp' \cdot \left(n_1 \nabla_\perp' \left[(\hat{\mathcal{L}} n_1)(\hat{\mathcal{L}}^\dagger n_1) - \frac{1}{2} \left(\hat{\mathcal{L}} + \hat{\mathcal{L}}^\dagger \right) n_1^2 \right] \right) \right\}.
\end{aligned}
\tag{A.48}
$$

1) First term in $\mathcal{R}_2$:

$$
iR\sigma I_0 \nabla_\perp'^2 \frac{1}{2} \left[(\hat{\mathcal{L}} n_1^2)(\hat{\mathcal{L}}^\dagger n_1) - (\hat{\mathcal{L}} n_1)(\hat{\mathcal{L}}^\dagger n_1^2) \right].
\tag{A.49}
$$

For the reader's convenience a lookup table of the resonant terms with their coefficients is constructed below. This is later adapted to all terms of $\mathcal{R}_2$. For instance, the third-order product $(\hat{\mathcal{L}} n_1^2)(\hat{\mathcal{L}}^\dagger n_1)$ yields the following terms:

$$
\begin{aligned}
& A_1 A_1 A_1^* e^{i3\eta \mathbf{q}_1^2} \exp(i\phi_1) + A_1 A_2 A_2^* e^{-i\eta(\mathbf{q}_2^2 + \mathbf{q}_3^2)} \exp(i\phi_1) + A_1 A_3 A_3^* e^{-i\eta(\mathbf{q}_3^2 + \mathbf{q}_2^2)} \exp(i\phi_1) + \\
& A_1 A_1^* A_1 e^{-i\eta \mathbf{q}_1^2} \exp(i\phi_1) + A_1 A_1^* A_2 e^{-i\eta \mathbf{q}_2^2} \exp(i\phi_2) + A_1 A_1^* A_3 e^{-i\eta \mathbf{q}_3^2} \exp(i\phi_3) + \\
& A_1 A_2^* A_2 e^{i\eta(\mathbf{q}_1 - \mathbf{q}_2)^2} e^{-i\eta \mathbf{q}_2^2} \exp(i\phi_1) + A_1 A_3^* A_3 e^{i\eta(\mathbf{q}_1 - \mathbf{q}_3)^2} e^{-i\eta \mathbf{q}_3^2} \exp(i\phi_1) +
\end{aligned}
$$

$$
\begin{aligned}
& A_2 A_2 A_2^* e^{i3\eta \mathbf{q}_2^2} \exp(i\phi_2) + A_2 A_1 A_1^* e^{-i\eta(\mathbf{q}_3^2 + \mathbf{q}_1^2)} \exp(i\phi_2) + A_2 A_3 A_3^* e^{-i\eta(\mathbf{q}_1^2 + \mathbf{q}_3^2)} \exp(i\phi_2) + \\
& A_2 A_2^* A_1 e^{-i\eta \mathbf{q}_1^2} \exp(i\phi_1) + A_2 A_2^* A_2 e^{-i\eta \mathbf{q}_2^2} \exp(i\phi_2) + A_2 A_2^* A_3 e^{-i\eta \mathbf{q}_3^2} \exp(i\phi_3) + \\
& A_2 A_1^* A_1 e^{i\eta(\mathbf{q}_2 - \mathbf{q}_1)^2} e^{-i\eta \mathbf{q}_1^2} \exp(i\phi_2) + A_2 A_3^* A_3 e^{i\eta(\mathbf{q}_2 - \mathbf{q}_3)^2} e^{-i\eta \mathbf{q}_3^2} \exp(i\phi_3) +
\end{aligned}
\tag{A.50}
$$

$$
\begin{aligned}
& A_3 A_3 A_3^* e^{i3\eta \mathbf{q}_3^2} \exp(i\phi_3) + A_3 A_1 A_1^* e^{-i\eta(\mathbf{q}_2^2 + \mathbf{q}_1^2)} \exp(i\phi_3) + A_3 A_2 A_2^* e^{-i\eta(\mathbf{q}_1^2 + \mathbf{q}_2^2)} \exp(i\phi_3) + \\
& A_3 A_3^* A_1 e^{-i\eta \mathbf{q}_1^2} \exp(i\phi_1) + A_3 A_3^* A_2 e^{-i\eta \mathbf{q}_2^2} \exp(i\phi_2) + A_3 A_3^* A_3 e^{-i\eta \mathbf{q}_3^2} \exp(i\phi_3) + \\
& A_3 A_1^* A_1 e^{i\eta(\mathbf{q}_3 - \mathbf{q}_1)^2} e^{-i\eta \mathbf{q}_1^2} \exp(i\phi_2) + A_3 A_2^* A_2 e^{i\eta(\mathbf{q}_3 - \mathbf{q}_2)^2} e^{-i\eta \mathbf{q}_3^2} \exp(i\phi_3),
\end{aligned}
$$

where $\phi_i = \mathbf{q}_i \cdot \mathbf{r}$. For its complex conjugate, one can see that the total summation yields a certain $\sin(...)$ factor for each piece in (A.50). Therefore, the relevant contributions to the self and cross-cubic coefficients γ_1 and γ_2 appear in terms such as, for example, $A_1 |A_2|^2$ and $A_1 |A_1|^2$ respectively[20].

---

[20]The procedure is extended identically for all other contributions in $\mathcal{R}_2$.

2) Second term in $\mathcal{R}_2$:

$$-\frac{i}{6}\nabla_{\perp}'^2\left(\hat{\mathcal{L}}-\hat{\mathcal{L}}^{\dagger}\right)n_1^3 = -\frac{q_c^2\sin(\eta q_c^2)}{3}n_1^3, \tag{A.51}$$

where the resonant terms in the simplest third order case n_1^3 just read:

$$\begin{aligned}
&A_1A_1A_1^*\exp(i\phi_1) + A_1A_2A_2^*\exp(i\phi_1) + A_1A_3A_3^*\exp(i\phi_1)+\\
&A_1A_1^*A_1\exp(i\phi_1) + A_1A_1^*A_2\exp(i\phi_2) + A_1A_1^*A_3\exp(i\phi_3)+\\
&A_1A_2^*A_2\exp(i\phi_1) + A_1A_3^*A_3\exp(i\phi_1)+\\[4pt]
\hline\\[-6pt]
&A_2A_2A_2^*\exp(i\phi_2) + A_2A_1A_1^*\exp(i\phi_2) + A_2A_3A_3^*\exp(i\phi_2)+\\
&A_2A_2^*A_1\exp(i\phi_1) + A_2A_2^*A_2\exp(i\phi_2) + A_2A_2^*A_3\exp(i\phi_3)+\\
&A_2A_1^*A_1\exp(i\phi_2) + A_2A_3^*A_3\exp(i\phi_3)+\\[4pt]
\hline\\[-6pt]
&A_3A_3A_3^*\exp(i\phi_3) + A_3A_1A_1^*\exp(i\phi_3) + A_3A_2A_2^*\exp(i\phi_3)+\\
&A_3A_3^*A_1\exp(i\phi_1) + A_3A_3^*A_2\exp(i\phi_2) + A_3A_3^*A_3\exp(i\phi_3)+\\
&A_3A_1^*A_1\exp(i\phi_2) + A_3A_2^*A_2\exp(i\phi_3).
\end{aligned} \tag{A.52}$$

3) Final terms[21] contained in $\mathcal{R}_2$:

$$\begin{aligned}
&\nabla_{\perp}'\cdot\left(n_1\nabla_{\perp}'\left[(\hat{\mathcal{L}}n_1)(\hat{\mathcal{L}}^{\dagger}n_1) - \frac{1}{2}\left(\hat{\mathcal{L}}+\hat{\mathcal{L}}^{\dagger}\right)n_1^2\right]\right) =\\
&n_1\nabla_{\perp}'^2\left[(\hat{\mathcal{L}}n_1)(\hat{\mathcal{L}}^{\dagger}n_1) - \frac{1}{2}\left(\hat{\mathcal{L}}+\hat{\mathcal{L}}^{\dagger}\right)n_1^2\right] + (\nabla_{\perp}'n_1)\cdot\nabla_{\perp}'\left[(\hat{\mathcal{L}}n_1)(\hat{\mathcal{L}}^{\dagger}n_1) - \frac{1}{2}\left(\hat{\mathcal{L}}+\hat{\mathcal{L}}^{\dagger}\right)n_1^2\right] =\\
&n_1\nabla_{\perp}'^2\left[(\hat{\mathcal{L}}n_1)(\hat{\mathcal{L}}^{\dagger}n_1) - \frac{1}{2}\left(\hat{\mathcal{L}}+\hat{\mathcal{L}}^{\dagger}\right)n_1^2\right] + \frac{1}{2}\left\{\nabla_{\perp}'^2\left[n_1(\hat{\mathcal{L}}n_1)(\hat{\mathcal{L}}^{\dagger}n_1) - \frac{1}{2}n_1\left(\hat{\mathcal{L}}+\hat{\mathcal{L}}^{\dagger}\right)n_1^2\right]+\right.\\
&\left.-\left[(\nabla_{\perp}'^2n_1)(\hat{\mathcal{L}}n_1)(\hat{\mathcal{L}}^{\dagger}n_1) - \frac{1}{2}(\nabla_{\perp}'^2n_1)\left(\hat{\mathcal{L}}+\hat{\mathcal{L}}^{\dagger}\right)n_1^2\right] - \left[n_1\nabla_{\perp}'^2(\hat{\mathcal{L}}n_1\hat{\mathcal{L}}^{\dagger}n_1) - \frac{1}{2}n_1\nabla_{\perp}'^2\left(\hat{\mathcal{L}}+\hat{\mathcal{L}}^{\dagger}\right)n_1^2\right]\right\}
\end{aligned} \tag{A.53}$$

Consider first $n_1\nabla_{\perp}'^2\left[(\hat{\mathcal{L}}n_1)(\hat{\mathcal{L}}^{\dagger}n_1) - \frac{1}{2}\left(\hat{\mathcal{L}}+\hat{\mathcal{L}}^{\dagger}\right)n_1^2\right]$. We need to evaluate the term $\nabla_{\perp}'^2(\hat{\mathcal{L}}n_1)(\hat{\mathcal{L}}^{\dagger}n_1) = \nabla_{\perp}'^2 n_1^2$ separately, that is:

$$-\sum_{i,j}(\mathbf{q}_i+\mathbf{q}_j)^2\left[A_iA_j\exp\left(i(\mathbf{q}_i+\mathbf{q}_j)\cdot\mathbf{r}\right)+c.c.\right] - \sum_{i,j}(\mathbf{q}_i-\mathbf{q}_j)^2 A_iA_j^*\exp\left(i(\mathbf{q}_i-\mathbf{q}_j)\cdot\mathbf{r}\right). \tag{A.54}$$

---

[21]Those terms describe the nonlinear mixing between first and second-order harmonics.

Let us count terms in the product $n_1 \nabla'^2_\perp n_1^2$ (red for vanishing terms)[22]:

$4q_c^2 A_1 A_1 A_1^* \exp(i\phi_1) + q_c^2 A_1 A_2 A_2^* \exp(i\phi_1) + q_c^2 A_1 A_3 A_3^* \exp(i\phi_1) +$

$A_1 A_1^* A_1 (\mathbf{q}_1 - \mathbf{q}_1)^2 \exp(i\phi_1) + A_1 A_1^* A_2 (\mathbf{q}_1 - \mathbf{q}_1)^2 \exp(i\phi_2) + A_1 A_1^* A_3 (\mathbf{q}_1 - \mathbf{q}_1)^2 \exp(i\phi_3) +$

$A_1 A_2^* A_2 (\mathbf{q}_1 - \mathbf{q}_2)^2 \exp(i\phi_1) + A_1 A_3^* A_3 (\mathbf{q}_1 - \mathbf{q}_3)^2 \exp(i\phi_1) +$

$4q_c^2 A_2 A_2 A_2^* \exp(i\phi_2) + q_c^2 A_2 A_1 A_1^* \exp(i\phi_2) + q_c^2 A_2 A_3 A_3^* \exp(i\phi_2) +$

$A_2 A_2^* A_1 (\mathbf{q}_2 - \mathbf{q}_2)^2 \exp(i\phi_1) + A_2 A_2^* A_2 (\mathbf{q}_2 - \mathbf{q}_2)^2 \exp(i\phi_2) + A_2 A_2^* A_3 (\mathbf{q}_2 - \mathbf{q}_2)^2 \exp(i\phi_3) +$

$A_2 A_1^* A_1 (\mathbf{q}_2 - \mathbf{q}_1)^2 \exp(i\phi_2) + A_2 A_3^* A_3 (\mathbf{q}_2 - \mathbf{q}_3)^2 \exp(i\phi_3) +$

$4q_c^2 A_3 A_3 A_3^* \exp(i\phi_3) + q_c^2 A_3 A_1 A_1^* \exp(i\phi_3) + q_c^2 A_3 A_2 A_2^* \exp(i\phi_3) +$

$A_3 A_3^* A_1 (\mathbf{q}_3 - \mathbf{q}_3)^2 \exp(i\phi_1) + A_3 A_3^* A_2 (\mathbf{q}_3 - \mathbf{q}_3)^2 \exp(i\phi_2) + A_3 A_3^* A_3 (\mathbf{q}_3 - \mathbf{q}_3)^2 \exp(i\phi_3) +$

$A_3 A_1^* A_1 (\mathbf{q}_3 - \mathbf{q}_1)^2 \exp(i\phi_2) + A_3 A_2^* A_2 (\mathbf{q}_3 - \mathbf{q}_2)^2 \exp(i\phi_3).$

$$(A.55)$$

For $-\frac{1}{2} n_1 \nabla'^2_\perp \left(\hat{\mathcal{L}} + \hat{\mathcal{L}}^\dagger \right) n_1^2$ we have:

$4q_c^2 \cos(4\eta q_c^2) A_1 A_1 A_1^* \exp(i\phi_1) + q_c^2 \cos(\eta q_c^2) A_1 A_2 A_2^* \exp(i\phi_1) + q_c^2 \cos(\eta q_c^2) A_1 A_3 A_3^* \exp(i\phi_1) +$

$0 * A_1 A_1^* A_1 \exp(i\phi_1) + 0 * A_1 A_1^* A_2 \exp(i\phi_2) + 0 * A_1 A_1^* A_3 \exp(i\phi_3) +$

$(\mathbf{q}_1 - \mathbf{q}_2)^2 A_1 A_2^* A_2 \cos(\eta(\mathbf{q}_1 - \mathbf{q}_2)^2) \exp(i\phi_1) + (\mathbf{q}_1 - \mathbf{q}_3)^2 A_1 A_3^* A_3 \cos(\eta(\mathbf{q}_1 - \mathbf{q}_3)^2) \exp(i\phi_1) +$

$4q_c^2 \cos(4\eta q_c^2) A_2 A_2 A_2^* \exp(i\phi_2) + q_c^2 \cos(\eta q_c^2) A_2 A_1 A_1^* \exp(i\phi_2) + q_c^2 \cos(\eta q_c^2) A_2 A_3 A_3^* \exp(i\phi_2) +$

$0 * A_2 A_2^* A_1 \exp(i\phi_1) + 0 * A_2 A_2^* A_2 \exp(i\phi_2) + 0 * A_2 A_2^* A_3 \exp(i\phi_3) +$

$(\mathbf{q}_2 - \mathbf{q}_1)^2 A_2 A_1^* A_1 \cos(\eta(\mathbf{q}_2 - \mathbf{q}_1)^2) \exp(i\phi_2) + (\mathbf{q}_2 - \mathbf{q}_3)^2 A_2 A_3^* A_3 \cos(\eta(\mathbf{q}_2 - \mathbf{q}_3)^2) \exp(i\phi_3) +$

$4q_c^2 \cos(4\eta q_c^2) A_3 A_3 A_3^* \exp(i\phi_3) + q_c^2 \cos(\eta q_c^2) A_3 A_1 A_1^* \exp(i\phi_3) + q_c^2 \cos(\eta q_c^2) A_3 A_2 A_2^* \exp(i\phi_3) +$

$0 * A_3 A_3^* A_1 \exp(i\phi_1) + 0 * A_3 A_3^* A_2 \exp(i\phi_2) + 0 * A_3 A_3^* A_3 \exp(i\phi_3) +$

$(\mathbf{q}_3 - \mathbf{q}_1)^2 A_3 A_1^* A_1 \cos(\eta(\mathbf{q}_3 - \mathbf{q}_1)^2) \exp(i\phi_2) + (\mathbf{q}_3 - \mathbf{q}_2)^2 A_3 A_2^* A_2 \cos(\eta(\mathbf{q}_3 - \mathbf{q}_2)^2) \exp(i\phi_3).$

$$(A.56)$$

Additionally, we have $(\mathbf{q}_i - \mathbf{q}_j)^2 = 2q_c^2 - 2q_c^2 \cos(\phi) = 3q_c^2$ when $i \neq j$ so that many of the terms vanish. The same applies to the rest of $\mathcal{R}_2$, leading to the coefficients in Eq. (4.29, 4.30).

---

[22]A minus sign applies to all terms.

Bibliography

[1] S. R. De Groot and P. Mazur, *Non-equilibrium thermodynamics* (Dover, New York, 1984).

[2] M. C. Cross and P. C. Hohenberg, *Pattern formation outside of equilibrium,* Rev. Mod. Phys. **65**, 851 (1993).

[3] H. Haken, *Synergetics: Introduction and advanced topics* (Springer Science & Business Media, New York, 2013).

[4] L. A. Lugiato and R. Lefever, *Spatial dissipative structures in passive optical systems,* Phys. Rev. Lett. **58**, 2209 (1987).

[5] W. J. Firth, *Spatial instabilities in a Kerr medium with single feedback mirror,* J. Mod. Opt. **37**, 151 (1990).

[6] G. D'Alessandro and W. J. Firth, *Spontaneous hexagon formation in a nonlinear optical medium with feedback mirror,* Phys. Rev. Lett. **66**, 2597 (1991).

[7] G. D'Alessandro and W. J. Firth, *Hexagonal spatial patterns for a Kerr slice with a feedback mirror,* Phys. Rev. A **46**, 537 (1992).

[8] F. T. Arecchi, S. Boccaletti, and P. Ramazza, *Pattern formation and competition in nonlinear optics,* Phys. Rep. **318**, 1 (1999).

[9] P. Mandel and M. Tlidi, *Transverse dynamics in cavity nonlinear optics (2000–2003),* J. Opt. B **6**, R60 (2004).

[10] T. W. Hänsch and A. L. Schawlow, *Cooling of gases by laser radiation,* Opt. Comm. **13**, 68 (1975).

[11] D. J. Wineland, R. E. Drullinger, and F. L. Walls, *Radiation-pressure cooling of bound resonant absorbers,* Phys. Rev. Lett. **40**, 1639 (1978).

[12] A. Ashkin, *Trapping of atoms by resonance radiation pressure,* Phys. Rev. Lett. **40**, 729 (1978).

[13] F. Dalfovo, S. Giorgini, L. P. Pitaevskii, and S. Stringari, *Theory of Bose-Einstein condensation in trapped gases,* Rev. Mod. Phys. **71**, 463 (1999).

[14] I. Bloch, J. Dalibard, and S. Nascimbene, *Quantum simulations with ultracold quantum gases,* Nature Phys. **8**, 267 (2012).

[15] I. Buluta, S. Ashhab, and F. Nori, *Natural and artificial atoms for quantum computation,* Rep. Progr. Phys. **74**, 104401 (2011).

[16] W. Zheng and N. R. Cooper, *Superradiance induced particle flow via dynamical gauge coupling,* Phys. Rev. Lett. **117**, 175302 (2016).

[17] K. E. Ballantine, B. L. Lev, and J. Keeling, *Meissner-like effect for a synthetic gauge field in multimode cavity QED,* Phys. Rev. Lett. **118**, 045302 (2017).

[18] H. Ritsch, P. Domokos, F. Brennecke, and T. Esslinger, *Cold atoms in cavity-generated dynamical optical potentials,* Rev. Mod. Phys. **85**, 553 (2013).

[19] K. Baumann, C. Guerlin, F. Brennecke, and T. Esslinger, *Dicke quantum phase transition with a superfluid gas in an optical cavity,* Nature **464**, 1301 (2010).

[20] S. Gopalakrishnan, B. L. Lev, and P. M. Goldbart, *Emergent crystallinity and frustration with Bose–Einstein condensates in multimode cavities,* Nat. Phys. **5**, 845 (2009).

[21] S. Gopalakrishnan, B. L. Lev, and P. M. Goldbart, *Atom-light crystallization of Bose-Einstein condensates in multimode cavities: Nonequilibrium classical and quantum phase transitions, emergent lattices, supersolidity, and frustration,* Phys. Rev. A **82**, 043612 (2010).

[22] R. Mottl, F. Brennecke, K. Baumann, R. Landig, T. Donner, and T. Esslinger, *Roton-type mode softening in a quantum gas with cavity-mediated long-range interactions,* Science **336**, 1570 (2012).

[23] J. Léonard, A. Morales, P. Zupancic, T. Esslinger, and T. Donner, *Supersolid formation in a quantum gas breaking a continuous translational symmetry,* Nature **543**, 87 (2017).

[24] V. D. Vaidya, Y. Guo, R. M. Kroeze, K. E. Ballantine, A. J. Kollár, J. Keeling, and B. L. Lev, *Tunable-range, photon-mediated atomic interactions in multimode cavity QED,* Phys. Rev. X **8**, 011002 (2018).

[25] X. Li, D. Dreon, P. Zupancic, A. Baumgärtner, A. Morales, W. Zheng, N. R. Cooper, T. Donner, and T. Esslinger, *First order phase transition between two centro-symmetric superradiant crystals,* Phys. Rev. Res. **3**, L012024 (2021).

[26] P. Domokos and H. Ritsch, *Collective cooling and self-organization of atoms in a cavity,* Phys. Rev. Lett. **89**, 253003 (2002).

[27] R. Bonifacio, L. De Salvo, L. M. Narducci, and E. J. D'Angelo, *Exponential gain and self-bunching in a collective atomic recoil laser,* Phys. Rev. A **50**, 1716 (1994).

[28] A. T. Black, H. W. Chan, and V. Vuletić, *Observation of collective friction forces due to spatial self-organization of atoms: from rayleigh to bragg scattering,* Phys. Rev. Lett. **91**, 203001 (2003).

[29] K. Baumann, R. Mottl, F. Brennecke, and T. Esslinger, *Exploring symmetry breaking at the Dicke quantum phase transition,* Phys. Rev. Lett. **107**, 140402 (2011).

[30] K. Hepp and E. H. Lieb, *On the superradiant phase transition for molecules in a quantized radiation field: the Dicke maser model,* Ann. of Phys. **76**, 360 (1973).

[31] D. Kruse, C. von Cube, C. Zimmermann, and P. W. Courteille, *Observation of lasing mediated by collective atomic recoil,* Phys. Rev. Lett. **91**, 183601 (2003).

[32] C. Von Cube, S. Slama, D. Kruse, C. Zimmermann, P. W. Courteille, G. R. M. Robb, N. Piovella, and R. Bonifacio, *Self-synchronization and dissipation-induced threshold in collective atomic recoil lasing,* Phys. Rev. Lett. **93**, 083601 (2004).

[33] A. J. Leggett, *Can a solid be "superfluid"? ,* Phys. Rev. Lett. **25**, 1543 (1970).

[34] M. Boninsegni and N. V. Prokof'ev, *Colloquium: Supersolids: What and where are they? ,* Rev. Mod. Phys. **84**, 759 (2012).

[35] L. Allen, M. W. Beijersbergen, R. J. C. Spreeuw, and J. P. Woerdman, *Orbital angular momentum of light and the transformation of laguerre-gaussian laser modes,* Phys. Rev. A **45**, 8185 (1992).

[36] M. Born and E. Wolf, *Principles of optics: electromagnetic theory of propagation, interference and diffraction of light* (Cambridge University Press, Cambridge, 2013).

[37] A. M. Yao and M. J. Padgett, *Orbital angular momentum: origins, behavior and applications,* Adv. Opt. Photonics **3**, 161 (2011).

[38] H. Rubinsztein-Dunlop, A. Forbes, M. V. Berry, M. R. Dennis, D. L. Andrews, M. Mansuripur, C. Denz, C. Alpmann, P. Banzer, and T. e. a. Bauer, *Roadmap on structured light,* J. Opt. **19**, 013001 (2016).

[39] S. Franke-Arnold, *Optical angular momentum and atoms,* Philos. Trans. R. Soc. A **375**, 20150435 (2017).

[40] S. Franke-Arnold, J. Leach, M. J. Padgett, V. E. Lembessis, D. Ellinas, A. J. Wright, J. M. Girkin, P. Öhberg, and A. S. Arnold, *Optical ferris wheel for ultracold atoms,* Opt. Expr. **15**, 8619 (2007).

[41] S. K. Schnelle, E. D. Van Ooijen, M. J. Davis, N. R. Heckenberg, and H. Rubinsztein-Dunlop, *Versatile two-dimensional potentials for ultra-cold atoms,* Opt. Expr. **16**, 1405 (2008).

[42] A. S. Arnold, *Extending dark optical trapping geometries,* Opt. Lett. **37**, 2505 (2012).

[43] N. Goldman, G. Juzeliūnas, P. Öhberg, and I. B. Spielman, *Light-induced gauge fields for ultracold atoms,* Rep. Prog. Phys. **77**, 126401 (2014).

[44] L. Amico, D. Aghamalyan, F. Auksztol, H. Crepaz, R. Dumke, and L. C. Kwek, *Superfluid qubit systems with ring shaped optical lattices,* Sci. Rep. **4**, 1 (2014).

[45] P. Hänggi and F. Marchesoni, *Artificial Brownian motors: Controlling transport on the nanoscale,* Rev. Mod. Phys. **81**, 387 (2009).

[46] M. Łącki, H. Pichler, A. Sterdyniak, A. Lyras, V. E. Lembessis, O. Al-Dossary, J. C. Budich, and P. Zoller, *Quantum hall physics with cold atoms in cylindrical optical lattices,* Phys. Rev. A **93**, 013604 (2016).

[47] A. La Porta and M. D. Wang, *Optical torque wrench: angular trapping, rotation, and torque detection of quartz microparticles,* Phys. Rev. Lett. **92**, 190801 (2004).

[48] Q. Zhan, *Cylindrical vector beams: from mathematical concepts to applications,* Adv. Opt. Photonics **1**, 1 (2009).

[49] F. Bouchard, H. Larocque, A. M. Yao, C. Travis, I. De Leon, A. Rubano, E. Karimi, G.-L. Oppo, and R. W. Boyd, *Polarization shaping for control of nonlinear propagation,* Phys. Rev. Lett. **117,** 233903 (2016).

[50] C. J. Gibson, P. Bevington, G.-L. Oppo, and A. M. Yao, *Control of polarization rotation in nonlinear propagation of fully structured light,* Phys. Rev. A **97,** 033832 (2018).

[51] E. Tesio, G. R. M. Robb, T. Ackemann, W. J. Firth, and G.-L. Oppo, *Spontaneous optomechanical pattern formation in cold atoms,* Phys. Rev. A **86,** 031801 (2012).

[52] E. Tesio, G. R. M. Robb, G.-L. Oppo, P. M. Gomes, T. Ackemann, G. Labeyrie, R. Kaiser, and W. J. Firth, *Self-organization in cold atomic gases: a synchronization perspective,* Phil. Trans. R. Soc. A **372,** 20140002 (2014).

[53] G. Labeyrie, E. Tesio, P. M. Gomes, G.-L. Oppo, W. J. Firth, G. R. M. Robb, A. S. Arnold, R. Kaiser, and T. Ackemann, *Optomechanical self-structuring in a cold atomic gas,* Nat. Phot. **8,** 321 (2014).

[54] E. Tesio, G. R. M. Robb, T. Ackemann, W. J. Firth, and G.-L. Oppo, *Kinetic theory for transverse optomechanical instabilities,* Phys. Rev. Lett. **112,** 043901 (2014).

[55] G. R. M. Robb, E. Tesio, G.-L. Oppo, W. J. Firth, T. Ackemann, and R. Bonifacio, *Quantum threshold for optomechanical self-structuring in a Bose-Einstein condensate,* Phys. Rev. Lett. **114,** 32 (2015).

[56] A. Camara, R. Kaiser, G. Labeyrie, W. J. Firth, G.-L. Oppo, G. R. M. Robb, A. S. Arnold, and T. Ackemann, *Optical pattern formation with a two-level nonlinearity,* Phys. Rev. A **92,** 013820 (2015).

[57] G. Labeyrie and R. Kaiser, *Kibble-Zurek Mechanism in the Self-Organization of a Cold Atomic Cloud,* Phys. Rev. Lett. **117,** 275701 (2016).

[58] T. Ackemann, G. Labeyrie, G. Baio, I. Krešić, J. G. M. Walker, A. Costa-Boquete, P. Griffin, W. J. Firth, R. Kaiser, G.-L. Oppo, and G. R. M. Robb, *Self-organization in cold atoms mediated by diffractive coupling,* Atoms **9,** 35 (2021).

[59] I. Krešić, G. Labeyrie, G. R. M. Robb, G.-L. Oppo, P. M. Gomes, P. Griffin, R. Kaiser, and T. Ackemann, *Spontaneous light-mediated magnetism in cold atoms,* Comm. Phys. **1,** 33 (2018).

[60] G. Labeyrie, I. Krešić, G. R. M. Robb, G.-L. Oppo, R. Kaiser, and T. Ackemann, *Magnetic phase diagram of light-mediated spin structuring in cold atoms,* Optica **5,** 1322 (2018).

[61] I. Krešić, G. R. M. Robb, G. Labeyrie, R. Kaiser, and T. Ackemann, *Inversion-symmetry breaking in spin patterns by a weak magnetic field,* Phys. Rev. A **99,** 053851 (2019).

[62] J. A. Greenberg, B. L. Schmittberger, and D. J. Gauthier, *Bunching-induced optical nonlinearity and instability in cold atoms,* Opt. Expr. **19,** 22535 (2011).

[63] B. L. Schmittberger and D. J. Gauthier, *Enhancing light-atom interactions via atomic bunching,* Phys. Rev. A **90,** 013813 (2014).

[64] B. L. Schmittberger and D. J. Gauthier, *Transverse optical and atomic pattern formation,* J. Opt. Soc. Am. B **33,** 1543 (2016).

[65] B. L. Schmittberger and D. J. Gauthier, *Spontaneous emergence of free-space optical and atomic patterns,* New J. Phys. **18,** 103021 (2016).

[66] W. J. Firth and A. J. Scroggie, *Optical bullet holes: Robust controllable localized states of a nonlinear cavity,* Phys. Rev. Lett. **76,** 1623 (1996).

[67] G.-L. Oppo, A. J. Scroggie, and W. J. Firth, *Characterization, dynamics and stabilization of diffractive domain walls and dark ring cavity solitons in parametric oscillators,* Phys. Rev. E **63,** 066209 (2001).

[68] R. Kheradmand, L. A. Lugiato, G. Tissoni, M. Brambilla, and H. Tajalli, *Rotating and fugitive cavity solitons in semiconductor microresonators,* Opt. Expr. **11,** 3612 (2003).

[69] V. Caullet, N. Marsal, D. Wolfersberger, and M. Sciamanna, *Vortex induced rotation dynamics of optical patterns,* Phys. Rev. Lett. **108,** 263903 (2012).

[70] A. M. Yao, C. J. Gibson, and G.-L. Oppo, *Control of spatially rotating structures in diffractive Kerr cavities,* Opt. Expr. **27,** 31273 (2019).

[71] E. Tesio, G. R. M. Robb, T. Ackemann, W. J. Firth, and G.-L. Oppo, *Dissipative solitons in the coupled dynamics of light and cold atoms,* Opt. Expr. **21,** 26144 (2013).

[72] S. Haroche and J.-M. Raimond, *Exploring the quantum: atoms, cavities, and photons* (Oxford University Press, Oxford, 2006).

[73] C. Cohen-Tannoudji, J. Dupont-Roc, and G. Grynberg, *Photons and Atoms-Introduction to Quantum Electrodynamics* (John Wiley & Sons, New York, 1997).

[74] H.-P. Breuer and F. Petruccione, *The theory of open quantum systems* (Oxford University Press, Oxford, 2002).

[75] R. Grimm, M. Weidemüller, and Y. B. Ovchinnikov, *Optical dipole traps for neutral atoms,* Adv. At. Mol. Opt. Phys. **42,** 95 (2000).

[76] H. J. Metcalf and P. Van der Straten, *Laser cooling and trapping of neutral atoms,* The Optics Encyclopedia: Basic Foundations and Practical Applications (2007).

[77] P. D. Lett, W. D. Phillips, S. L. Rolston, C. E. Tanner, R. N. Watts, and C. I. Westbrook, *Optical molasses,* J. Opt. Soc. Am. B **6,** 2084 (1989).

[78] S. Chu, L. Hollberg, J. E. Bjorkholm, A. Cable, and A. Ashkin, *Three-dimensional viscous confinement and cooling of atoms by resonance radiation pressure,* Phys. Rev. Lett. **55,** 48 (1985).

[79] W. D. Phillips, J. V. Prodan, and H. J. Metcalf, *Laser cooling and electromagnetic trapping of neutral atoms,* J. Opt. Soc. Am. B **2,** 1751 (1985).

[80] P. J. Ungar, D. S. Weiss, E. Riis, and S. Chu, *Optical molasses and multilevel atoms: theory,* J. Opt. Soc. Am. B **6,** 2058 (1989).

[81] J. T. Mendonça and H. Terças, *Physics of ultra-cold matter: atomic clouds, Bose-Einstein condensates and Rydberg plasmas* (Springer Science & Business Media, New York, 2012).

[82] K. B. Davis, M. O. Mewes, M. R. Andrews, N. J. van Druten, D. S. Durfee, D. M. Kurn, and W. Ketterle, *Bose-Einstein condensation in a gas of sodium atoms,* Phys. Rev. Lett. **75**, 3969 (1995).

[83] M. H. Anderson, J. R. Ensher, M. R. Matthews, C. E. Wieman, and E. A. Cornell, *Observation of Bose-Einstein condensation in a dilute atomic vapor,* Science **269**, 198 (1995).

[84] I. Bloch, J. Dalibard, and W. Zwerger, *Many-body physics with ultracold gases,* Rev. Mod. Phys. **80**, 885 (2008).

[85] M. Lewenstein, A. Sanpera, V. Ahufinger, B. Damski, A. Sen, and U. Sen, *Ultracold atomic gases in optical lattices: mimicking condensed matter physics and beyond,* Adv. Phys. **56**, 243 (2007).

[86] A. M. Beckley, T. G. Brown, and M. A. Alonso, *Full Poincaré beams,* Opt. Expr. **18**, 10777 (2010).

[87] E. J. Galvez, S. Khadka, W. H. Schubert, and S. Nomoto, *Poincaré-beam patterns produced by nonseparable superpositions of Laguerre–Gauss and polarization modes of light,* App. Opt. **51**, 2925 (2012).

[88] E. Otte, K. Tekce, and C. Denz, *Spatial multiplexing for tailored fully-structured light,* J. Opt. **20**, 105606 (2018).

[89] J. Wang, F. Castellucci, and S. Franke-Arnold, *Vectorial light–matter interaction: Exploring spatially structured complex light fields,* AVS Quantum Science **2**, 031702 (2020).

[90] S. M. Barnett, *Optical angular-momentum flux,* J. Opt. B **4**, S7 (2001).

[91] J. B. Götte and S. M. Barnett, Light beams carrying orbital angular momentum, in *The Angular Momentum of Light*, edited by D. L. Andrews and M. Babiker (Cambridge University Press, Cambridge, 2012) p. 1–30.

[92] J. D. Jackson, *Classical electrodynamics* (John Wiley & Sons, New York, 2007).

[93] L. D. Landau and E. M. Lifshitz, *Course of Theoretical Physics, Vol. 8: Electrodynamics of continuous media* (Pergamon Press, New York, 1984).

[94] F. J. Belinfante, *On the current and the density of the electric charge, the energy, the linear momentum and the angular momentum of arbitrary fields,* Physica **7**, 449 (1940).

[95] A. Siegman, *Lasers* (University Science Books, Sausalito, 1986).

[96] L. A. Lugiato, F. Prati, and M. Brambilla, *Nonlinear optical systems* (Cambridge University Press, Cambridge, 2015).

[97] O. Svelto and D. C. Hanna, *Principles of lasers*, Vol. 4 (Springer Science & Business Media, New York, 1998).

[98] M. Abramowitz and I. A. Stegun, *Handbook of mathematical functions with formulas, graphs, and mathematical tables* (U.S. Government Printing Office, Washington D.C., 1970).

[99] M. I. E. Kolobov, *Quantum imaging* (Springer Science & Business Media, New York, 2007).

[100] L. Allen, M. J. Padgett, and M. Babiker, *IV The orbital angular momentum of light,* Prog. Opt. **39**, 291 (1999).

[101] G. Lazarev, P.-J. Chen, J. Strauss, N. Fontaine, and A. Forbes, *Beyond the display: phase-only liquid crystal on Silicon devices and their applications in photonics,* Opt. Expr. **27**, 16206 (2019).

[102] A. Mair, A. Vaziri, G. Weihs, and A. Zeilinger, *Entanglement of the orbital angular momentum states of photons,* Nature **412**, 313 (2001).

[103] R. Fickler, R. Lapkiewicz, W. N. Plick, M. Krenn, C. Schaeff, S. Ramelow, and A. Zeilinger, *Quantum entanglement of high angular momenta,* Science **338**, 640 (2012).

[104] M. Erhard, M. Krenn, and A. Zeilinger, *Advances in high-dimensional quantum entanglement,* Nature Rev. Phys. **2**, 365 (2020).

[105] M. Babiker, D. L. Andrews, and V. E. Lembessis, *Atoms in complex twisted light,* J. Opt. **21**, 013001 (2018).

[106] M. Babiker, W. L. Power, and L. Allen, *Light-induced torque on moving atoms,* Phys. Rev. Lett. **73**, 1239 (1994).

[107] M. F. Andersen, C. Ryu, P. Cladé, V. Natarajan, A. Vaziri, K. Helmerson, and W. D. Phillips, *Quantized rotation of atoms from photons with orbital angular momentum,* Phys. Rev. Lett. **97**, 170406 (2006).

[108] C. Ryu, M. F. Andersen, P. Clade, V. Natarajan, K. Helmerson, and W. D. Phillips, *Observation of persistent flow of a Bose-Einstein condensate in a toroidal trap,* Phys. Rev. Lett. **99**, 260401 (2007).

[109] J. H. Denschlag, J. E. Simsarian, H. Häffner, C. McKenzie, A. Browaeys, D. Cho, K. Helmerson, S. L. Rolston, and W. D. Phillips, *A Bose-Einstein condensate in an optical lattice,* J. Opt. B **35**, 3095 (2002).

[110] A. V. Carpentier and H. Michinel, *A ring accelerator for matter-wave solitons,* Europhys. Lett. **78**, 10002 (2007).

[111] A. L. Fetter, *Rotating trapped Bose-Einstein condensates,* Rev. Mod. Phys. **81**, 647 (2009).

[112] L. Reichl, *A modern course in Statistical Physics* (John Wiley & Sons, New York, 1999).

[113] C. Gardiner, *Stochastic methods. A handbook for the Natural and Social Sciences, 4th ed.* (Springer, Berlin, 2009).

[114] S. Chandrasekhar, *Stochastic problems in Physics and Astronomy,* Rev. Mod. Phys. **15**, 1 (1943).

[115] T. Grießer, H. Ritsch, M. Hemmerling, and G. R. M. Robb, *A Vlasov approach to bunching and self-ordering of particles in optical resonators,* Eur. Phys. J. D **58**, 349 (2010).

[116] D. Rogovin and S. O. Sari, *Phase conjugation in liquid suspensions of microspheres in the diffusive limit,* Phys. Rev. A **31**, 2375 (1985).

[117] F. Balescu, *Statistical Mechanics of Charged Particles* (Wiley-Interscience, New York, 1963).

[118] K. Schulten, *Course on theoretical Biophysics,* Lecture notes available online at https://www.ks.uiuc.edu/Services/Class/PHYS498 (University of Illinois at Urbana-Champaign, 1999).

[119] L. D. Landau and E. M. Lifshitz, *Course of Theoretical Physics, Vol. 5: Statistical Physics* (Pergamon Press, New York, 1980).

[120] R. Kubo, *The fluctuation-dissipation theorem,* Rep. Prog. Phys. **29**, 255 (1966).

[121] R. W. Davies, *The connection between the Smoluchowski equation and the Kramers-Chandrasekhar equation,* Phys. Rev. **93**, 1169 (1954).

[122] A. M. Turing, *The chemical basis or morphogenesis.* Phil. Trans. R. Soc. B **237**, 37 (1952).

[123] P. K. Maini, K. J. Painter, and H. N. P. Chau, *Spatial pattern formation in chemical and biological systems,* J. Chem. Soc., Faraday Trans. **93**, 3601 (1997).

[124] A. Buka and L. Kramer, *Pattern formation in liquid crystals* (Springer Science & Business Media, New York, 2012).

[125] E. Meron, *Nonlinear Physics of Ecosystems* (CRC Press, Boca Raton, 2015).

[126] M. Bär, R. Großmann, S. Heidenreich, and F. Peruani, *Self-propelled rods: Insights and perspectives for active matter,* Annu. Rev. Condens. Matter Phys. **11**, 441 (2020).

[127] D. Kondepudi and I. Prigogine, *Modern thermodynamics: from heat engines to dissipative structures* (John Wiley & Sons, New York, 2014).

[128] R. Hoyle, *Pattern formation: an introduction to methods* (Cambridge University Press, Cambridge, 2006).

[129] A. C. Newell and J. A. Whitehead, *Finite bandwidth, finite amplitude convection,* J. Fluid Mech. **38**, 279 (1969).

[130] L. A. Segel, *Distant side-walls cause slow amplitude modulation of cellular convection,* J. Fluid Mech. **38**, 203 (1969).

[131] L. P. Gor'kov, *Microscopic derivation of the Ginzburg-Landau equations in the theory of superconductivity,* Sov. Phys. JETP **9**, 1364 (1959).

[132] I. S. Aranson and L. Kramer, *The world of the complex Ginzburg-Landau equation,* Rev. Mod. Phys. **74**, 99 (2002).

[133] A. C. Newell, *Envelope equations,* Lect. Appl. Math. **15**, 157 (1974).

[134] S. Ciliberto, P. Coullet, J. Lega, E. Pampaloni, and C. Perez-Garcia, *Defects in roll-hexagon competition,* Phys. Rev. Lett. **65**, 2370 (1990).

[135] N. Akhmediev and A. Ankiewicz, *Dissipative solitons: from Optics to Biology and Medicine,* Lect. Notes Phys. **751** (2008).

[136] T. Ackemann, W. J. Firth, and G.-L. Oppo, *Fundamentals and applications of spatial dissipative solitons in photonic devices,* Adv. Atom., Mol., Opt. Phys, **57**, 323 (2009).

[137] H.-G. Purwins, H. Bödeker, and S. Amiranashvili, *Dissipative solitons,* Adv. in Phys. **59**, 485 (2010).

[138] J. Burke and E. Knobloch, *Snakes and ladders: localized states in the Swift–Hohenberg equation,* Phys. Lett. A **360**, 681 (2007).

[139] A. G. Vladimirov, J. M. McSloy, D. V. Skryabin, and W. J. Firth, *Two-dimensional clusters of solitary structures in driven optical cavities,* Phys. Rev. E **65**, 046606 (2002).

[140] T. Maggipinto, M. Brambilla, G. K. Harkness, and W. J. Firth, *Cavity solitons in semiconductor microresonators: Existence, stability, and dynamical properties,* Phys. Rev. E **62**, 8726 (2000).

[141] J. M. McSloy, W. J. Firth, G. K. Harkness, and G.-L. Oppo, *Computationally determined existence and stability of transverse structures. II. Multipeaked cavity solitons,* Phys. Rev. E **66**, 046606 (2002).

[142] P. W. Smith, A. Ashkin, and W. J. Tomlinson, *Four-wave mixing in an artificial Kerr medium,* Opt. Lett. **6**, 284 (1981).

[143] A. Ashkin, J. M. Dziedzic, and P. W. Smith, *Continuous-wave self-focusing and self-trapping of light in artificial Kerr media,* Opt. Lett. **7**, 276 (1982).

[144] A. C. Boquete, G. Baio, G. Robb, G.-L. Oppo, P. Griffin, and T. Ackemann, *Spontaneous atomic crystallization via diffractive dephasing in optical cavities,* J. Phys.: Conf. Ser. **1919**, 012014 (2021).

[145] V. Caullet, N. Marsal, D. Wolfersberger, and M. Sciamanna, *Pattern formation using optical vortices in a photorefractive single feedback system,* Opt. Lett. **36**, 2815 (2011).

[146] C. Cleff, B. Gütlich, and C. Denz, *Gradient induced motion control of drifting solitary structures in a nonlinear optical single feedback experiment,* Phys. Rev. Lett. **100**, 233902 (2008).

[147] G. Baio, G. R. M. Robb, A. M. Yao, and G.-L. Oppo, *Optomechanical transport of cold atoms induced by structured light,* Phys. Rev. Res. **2**, 023126 (2020).

[148] L. A. Lugiato, *Transverse nonlinear optics: Introduction and review,* Chaos, Solitons & Fractals **4**, 1251 (1994).

[149] R. W. Boyd, *Nonlinear optics* (Academic press, Burlington MA, 2008).

[150] F. Arecchi and R. Bonifacio, *Theory of optical maser amplifiers,* IEEE J. Quant. Electr. **1**, 169 (1965).

[151] B. McNeil, *Due credit for Maxwell–Bloch equations,* Nat. Phot. **9**, 207 (2015).

[152] L. A. Lugiato and C. Oldano, *Stationary spatial patterns in passive optical systems: two-level atoms,* Phys. Rev. A **37**, 3896 (1988).

[153] P. Meystre, *On the use of the mean-field theory in optical bistability,* Opt. Comm. **26**, 277 (1978).

[154] L. A. Lugiato, *II Theory of optical bistability,* Progr. Opt. **21**, 69 (1984).

[155] Y. K. Chembo, D. Gomila, M. Tlidi, and C. R. Menyuk, *Theory and applications of the Lugiato-Lefever equation,* Eur. Phys. J. D **71** (2017).

[156] P. Del'Haye, A. Schliesser, O. Arcizet, T. Wilken, R. Holzwarth, and T. J. Kippenberg, *Optical frequency comb generation from a monolithic microresonator,* Nature **450**, 1214 (2007).

[157] L. A. Lugiato and F. Castelli, *Quantum noise reduction in a spatial dissipative structure,* Phys. Rev. Lett. **68**, 3284 (1992).

[158] A. Dutt, K. Luke, S. Manipatruni, A. L. Gaeta, P. Nussenzveig, and M. Lipson, *On-chip optical squeezing,* Phys. Rev. Applied **3**, 044005 (2015).

[159] W. J. Firth and A. J. Scroggie, *Spontaneous pattern formation in an absorptive system,* Europhys. Lett. **26**, 521 (1994).

[160] J. E. Bjorkholm, R. R. Freeman, A. Ashkin, and D. B. Pearson, *Observation of focusing of neutral atoms by the dipole forces of resonance-radiation pressure,* Phys. Rev. Lett. **41**, 1361 (1978).

[161] Y. L. Klimontovich and S. N. Luzgin, *Possibility of combined self-focusing of atomic and light beams,* JETP Lett. **30** (1979).

[162] T. G. Walker, D. W. Sesko, and C. E. Wieman, *Collective behavior of optically trapped neutral atoms,* Phys. Rev. Lett. **64**, 408 (1990).

[163] D. W. Sesko, T. G. Walker, and C. E. Wieman, *Behavior of neutral atoms in a spontaneous force trap,* J. Opt. Soc. Am. B **8**, 946 (1991).

[164] M. Saffman, *Self-induced dipole force and filamentation instability of a matter wave,* Phys. Rev. Lett. **81**, 65 (1998).

[165] M. Saffman and Y. Wang, *Collective focusing and modulational instability of light and cold atoms,* Lect. Notes Phys. **751**, 361 (2008).

[166] Y. Wang and M. Saffman, *Experimental study of nonlinear focusing in a magneto-optical trap using a z-scan technique,* Phys. Rev. A **70**, 013801 (2004).

[167] E. Tesio, *Theory of self-organization in cold atoms* (Ph.D. Thesis @ University of Strathclyde, 2014).

[168] J. A. C. Weideman and B. M. Herbst, *Split-step methods for the solution of the nonlinear Schrödinger equation,* SIAM J. Numer. Anal. **23**, 485 (1986).

[169] J. J. Rasmussen and K. Rypdal, *Blow-up in nonlinear Schroedinger equations-I a general review,* Phys. Scr. **33**, 481 (1986).

[170] W. J. Firth and A. Lord, *Two-dimensional solitons in a Kerr cavity,* J. Mod. Opt. **43**, 1071 (1996).

[171] W. J. Firth, G. K. Harkness, A. Lord, J. M. McSloy, D. Gomila, and P. Colet, *Dynamical properties of two-dimensional Kerr cavity solitons,* J. Opt. Soc. Am. B **19**, 747 (2002).

[172] M. Eslami, R. Kheradmand, D. McArthur, and G.-L. Oppo, *Complex structures in media displaying electromagnetically induced transparency: pattern multistability and competition,* Phys. Rev. A **90**, 023840 (2014).

[173] K. Huang, *Statistical mechanics, 2nd ed.* (Wiley, New York, 1991).

[174] G. R. M. Robb, N. Piovella, A. Ferraro, R. Bonifacio, P. W. Courteille, and C. Zimmermann, *Collective atomic recoil lasing including friction and diffusion effects,* Phys. Rev. A **69**, 041403 (2004).

[175] C. F. Barenghi, L. Skrbek, and K. R. Sreenivasan, *Introduction to quantum turbulence,* Proc. Natl. Acad. Sci. **111**, 4647 (2014).

[176] M. C. Tsatsos, P. E. Tavares, A. Cidrim, A. R. Fritsch, M. A. Caracanhas, F. E. A. dos Santos, C. F. Barenghi, and V. S. Bagnato, *Quantum turbulence in trapped atomic bose–einstein condensates,* Phys. Rep. **622**, 1 (2016).

[177] G. Baio, G. R. M. Robb, A. M. Yao, G. L. Oppo, and T. Ackemann, *Multiple self-organized phases and spatial solitons in cold atoms mediated by optical feedback,* Phys. Rev. Lett. **126**, 203201 (2021).

[178] G. Giusfredi, J. F. Valley, R. Pon, G. Khitrova, and H. M. Gibbs, *Optical instabilities in sodium vapor,* J. Opt. Soc. Am. B **5**, 1181 (1988).

[179] R. Macdonald and H. J. Eichler, *Spontaneous optical pattern formation in a nematic liquid crystal with feedback mirror,* Opt. Comm. **89**, 289 (1992).

[180] C. Denz, M. Schwab, and C. Weilnau, *Transverse-pattern formation in photorefractive optics* (Springer Science & Business Media, New York, 2003).

[181] T. Ackemann and W. Lange, *Optical pattern formation in alkali metal vapors: Mechanisms, phenomena and use,* App. Phys. B **72**, 21 (2001).

[182] W. J. Firth, I. Krešić, G. Labeyrie, A. Camara, and T. Ackemann, *Thick-medium model of transverse pattern formation in optically excited cold two-level atoms with a feedback mirror,* Phys. Rev. A **96**, 053806 (2017).

[183] J. B. Geddes, R. A. Indik, J. V. Moloney, and W. J. Firth, *Hexagons and squares in a passive nonlinear optical system,* Phys. Rev. A **50**, 3471 (1994).

[184] M. Tamburrini, M. Bonavita, S. Wabnitz, and E. Santamato, *Hexagonally patterned beam filamentation in a thin liquid-crystal film with a single feedback mirror,* Opt. lett. **18**, 855 (1993).

[185] E. Ciaramella, M. Tamburrini, and E. Santamato, *Talbot assisted hexagonal beam patterning in a thin liquid crystal film with a single feedback mirror at negative distance,* Appl. Phys. Lett. **63**, 1604 (1993).

[186] A. J. Scroggie and W. J. Firth, *Pattern formation in an alkali-metal vapor with a feedback mirror,* Phys. Rev. A **53**, 2752 (1996).

[187] A. Aumann, T. Ackemann, E. G. Westhoff, and W. Lange, *Eightfold quasipatterns in an optical pattern-forming system,* Phys. Rev. E **66**, 046220 (2002).

[188] D. Leduc, M. Le Berre, E. Ressayre, and A. Tallet, *Quasipatterns in a polarization instability,* Phys. Rev. A **53**, 1072 (1996).

[189] G. K. Harkness, W. J. Firth, G.-L. Oppo, and J. M. McSloy, *Computationally determined existence and stability of transverse structures. I. Periodic optical patterns,* Phys. Rev. E **66**, 046605 (2002).

[190] R. A. Cowley, *Structural phase transitions I. Landau theory,* Adv. Phys. **29**, 1 (1980).

[191] Y. C. Zhang, V. Walther, and T. Pohl, *Long-Range Interactions and Symmetry Breaking in Quantum Gases through Optical Feedback,* Phys. Rev. Lett. **121**, 73604 (2018).

[192] P. Manneville, *Dissipative Structures and Weak Turbulence* (Academic Press, San Diego, 1990).

[193] S. A. Brazovskii, I. E. Dzyaloshinskii, and A. R. Muratov, *Theory of weak crystallization,* Zh. Eksp. Teor. Fiz. **93**, 1110 (1987).

[194] E. I. Kats, V. V. Lebedev, and A. R. Muratov, *Weak crystallization theory,* Phys. Rep. **228**, 1 (1993).

[195] Y. C. Zhang, F. Maucher, and T. Pohl, *Supersolidity around a Critical Point in Dipolar Bose-Einstein Condensates,* Phys. Rev. Lett. **123**, 15301 (2019).

[196] F. H. Busse, *Non-linear properties of thermal convection,* Rep. Prog. Phys. **41**, 1929 (1978).

[197] A. Aumann, E. Büthe, Y. A. Logvin, T. Ackemann, and W. Lange, *Polarized patterns in sodium vapor with single mirror feedback,* Phys. Rev. A **56**, R1709 (1997).

[198] M. Tlidi, M. Georgiou, and P. Mandel, *Transverse patterns in nascent optical bistability,* Phys. Rev. A **48**, 4605 (1993).

[199] M. Tlidi, P. Mandel, and R. Lefever, *Localized structures and localized patterns in optical bistability,* Phys. Rev. Lett. **73**, 640 (1994).

[200] R. Neubecker, G.-L. Oppo, B. Thuering, and T. Tschudi, *Pattern formation in a liquid-crystal light valve with feedback, including polarization, saturation, and internal threshold effects,* Phys. Rev. A **52**, 791 (1995).

[201] Y. S. Kivshar and D. E. Pelinovsky, *Self-focusing and transverse instabilities of solitary waves,* Phys. Rep. **331**, 117 (2000).

[202] Y. Wang, *Nonlinear self-focusing in cold Cesium atoms* (Ph.D. Thesis @ University of Wisconsin-Madison, 2005).

[203] Y. V. Kartashov, V. A. Vysloukh, and L. Torner, *Stable ring-profile vortex solitons in Bessel optical lattices,* Phys. Rev. Lett. **94**, 043902 (2005).

[204] B. B. Baizakov, B. A. Malomed, and M. Salerno, *Matter-wave solitons in radially periodic potentials,* Phys. Rev. E **74**, 066615 (2006).

[205] Y. V. Kartashov and D. A. Zezyulin, *Stable multiring and rotating solitons in two-dimensional spin-orbit-coupled Bose-Einstein condensates with a radially periodic potential,* Phys. Rev. Lett. **122**, 123201 (2019).

[206] Y. V. Kartashov, V. A. Vysloukh, and L. Torner, *Rotary solitons in Bessel optical lattices,* Phys. Rev. Lett. **93**, 093904 (2004).

[207] X. Wang, Z. Chen, and P. G. Kevrekidis, *Observation of discrete solitons and soliton rotation in optically induced periodic ring lattices,* Phys. Rev. Lett. **96**, 083904 (2006).

[208] S. P. Obukhov, *Self-organized criticality: Goldstone modes and their interactions,* Phys. Rev. Lett. **65**, 1395 (1990).

[209] B. Schäpers, M. Feldmann, T. Ackemann, and W. Lange, *Interaction of localized structures in an optical pattern-forming system,* Phys. Rev. Lett. **85**, 748 (2000).

[210] P. Parra-Rivas, D. Gomila, P. Colet, and L. Gelens, *Interaction of solitons and the formation of bound states in the generalized lugiato-lefever equation,* Eur. Phys. J. D **71**, 1 (2017).

[211] S. L. Sobolev, *Some applications of functional analysis in Mathematical Physics*, Vol. 90 (American Mathematical Society, 2008).

[212] A. J. Scroggie, J. M. McSloy, and W. J. Firth, *Self-propelled cavity solitons in semiconductor microcavities,* Phys. Rev. E **66**, 036607 (2002).

[213] F. Prati, G. Tissoni, L. A. Lugiato, K. M. Aghdami, and M. Brambilla, *Spontaneously moving solitons in a cavity soliton laser with circular section,* Eur. Phys. J. D **59**, 73 (2010).

[214] F. Prati, L. A. Lugiato, G. Tissoni, and M. Brambilla, *Cavity soliton billiards,* Phys. Rev. A **84**, 053852 (2011).

[215] G. Tissoni, K. M. Aghdami, M. Brambilla, and F. Prati, *Self–propelled soliton collisions in a semiconductor cavity soliton laser,* Eur. Phys. J. Special Topics **203**, 193 (2012).

[216] A. Kumar, R. Dubessy, T. Badr, C. De Rossi, M. de Herve de Goër, L. Longchambon, and H. Perrin, *Producing superfluid circulation states using phase imprinting,* Phys. Rev. A **97**, 043615 (2018).

[217] S. Moulder, S. Beattie, R. P. Smith, N. Tammuz, and Z. Hadzibabic, *Quantized supercurrent decay in an annular Bose-Einstein condensate,* Phys. Rev. A **86**, 013629 (2012).

[218] S. Burger, K. Bongs, S. Dettmer, W. Ertmer, K. Sengstock, A. Sanpera, G. V. Shlyapnikov, and M. Lewenstein, *Dark solitons in Bose-Einstein condensates,* Phys. Rev. Lett. **83**, 5198 (1999).

[219] J. Denschlag, J. E. Simsarian, D. L. Feder, C. W. Clark, L. A. Collins, J. Cubizolles, L. Deng, E. W. Hagley, K. Helmerson, W. P. Reinhardt, *et al.*, *Generating solitons by phase engineering of a Bose-Einstein condensate,* Science **287**, 97 (2000).

[220] J. Hertkorn, J.-N. Schmidt, M. Guo, F. Böttcher, K. S. H. Ng, S. D. Graham, P. Uerlings, T. Langen, M. Zwierlein, and T. Pfau, *Pattern formation in quantum ferrofluids: From supersolids to superglasses,* Phys. Rev. Res. **3**, 033125 (2021).

[221] I. Ferrier-Barbut, H. Kadau, M. Schmitt, M. Wenzel, and T. Pfau, *Observation of quantum droplets in a strongly dipolar Bose Gas,* Phys. Rev. Lett. **116**, 215301 (2016).

[222] G. Semeghini, G. Ferioli, L. Masi, C. Mazzinghi, L. Wolswijk, F. Minardi, M. Modugno, G. Modugno, M. Inguscio, and M. Fattori, *Self-bound quantum droplets of atomic mixtures in free space,* Phys. Rev. Lett. **120**, 235301 (2018).

[223] F. Boettcher, J.-N. Schmidt, J. Hertkorn, K. Ng, S. Graham, M. Guo, T. Langen, and T. Pfau, *New states of matter with fine-tuned interactions: quantum droplets and dipolar supersolids,* Rep. Progr. Phys. **84**, 012403 (2020).

[224] Y. C. Zhang, V. Walther, and T. Pohl, *Self-bound droplet clusters in laser-driven bose-einstein condensates,* Phys. Rev. A **103**, 023308 (2021).

[225] S. M. Roccuzzo, A. Gallemí, A. Recati, and S. Stringari, *Rotating a supersolid dipolar gas,* Phys. Rev. Lett. **124**, 045702 (2020).

[226] L. Tanzi, J. G. Maloberti, G. Biagioni, A. Fioretti, C. Gabbanini, and G. Modugno, *Evidence of superfluidity in a dipolar supersolid from nonclassical rotational inertia,* Science **371**, 1162 (2021).

[227] T. Ackemann, G. Labeyrie, A. Costa-Boquete, G. Baio, J. G. M. Walker, R. Kaiser, G. L. Oppo, and G. R. M. Robb, *Coupling of magnetic and optomechanical structuring in cold atoms,* arXiv preprint:2108.12064 (2021).

[228] V. Bobkova, J. Stegemann, R. Droop, E. Otte, and C. Denz, *Optical grinder: sorting of trapped particles by orbital angular momentum,* Opt. Expr. **29**, 12967 (2021).

[229] J. P. Gordon, *Radiation forces and momenta in dielectric media,* Phys. Rev. A **8**, 14 (1973).

[230] R. El-Ganainy, D. N. Christodoulides, C. Rotschild, and M. Segev, *Soliton dynamics and self-induced transparency in nonlinear nanosuspensions,* Opt. Expr. **15**, 10207 (2007).

[231] V. A. Markel, *Introduction to the Maxwell-Garnett approximation: tutorial,* J. Opt. Soc. Am. A **33**, 1244 (2016).

[232] V. Bobkova, A. Goenner, and C. Denz, *European Quantum Electronics Conference* (2021).

[233] M. M. Burns, J.-M. Fournier, and J. A. Golovchenko, *Optical matter: crystallization and binding in intense optical fields,* Science **249**, 749 (1990).

[234] W. Singer, M. Frick, S. Bernet, and M. Ritsch-Marte, *Self-organized array of regularly spaced microbeads in a fiber-optical trap,* J. Opt. Soc. Am. B **20**, 1568 (2003).

[235] P. J. Reece, E. M. Wright, and K. Dholakia, *Experimental observation of modulation instability and optical spatial soliton arrays in soft condensed matter,* Phys. Rev. Lett. **98**, 203902 (2007).

[236] S. A. Tatarkova, A. E. Carruthers, and K. Dholakia, *One-dimensional optically bound arrays of microscopic particles,* Phys. Rev. Lett. **89**, 283901 (2002).

[237] V. Karásek, T. Čižmár, O. Brzobohatỳ, P. Zemánek, V. Garcés-Chávez, and K. Dholakia, *Long-range one-dimensional longitudinal optical binding,* Phys. Rev. Lett. **101**, 143601 (2008).

[238] V. Karásek, O. Brzobohatỳ, and P. Zemánek, *Longitudinal optical binding of several spherical particles studied by the coupled dipole method,* J. Opt. A **11**, 034009 (2009).

[239] K. Dholakia and P. Zemánek, *Colloquium: Gripped by light: Optical binding,* Rev. Mod. Phys. **82**, 1767 (2010).

[240] D. Tong, *Lectures on kinetic theory,* Lecture notes available at http://www. damtp. cam. ac. uk/user/tong/kinetic.html (University of Cambridge, 2012).

[241] H. Goldstein, C. Poole, and J. Safko, *Classical Mechanics* (Addison-Wesley, Reading, MA, 1980).

[242] C. Cercignani, *The Boltzmann Equation and its applications* (Springer Science & Business Media, New York, 1988).

[243] A. Campa, T. Dauxois, D. Fanelli, and S. Ruffo, *Physics of long-range interacting systems* (Oxford University Press, Oxford, 2014).

[244] C. Limbach, *Landau Damping in the Transverse Modulational Dynamics of Co-Propagating Light and Matter Beams,* arXiv preprint:2104.04100 (2021).

[245] A. Newell and J. V. Moloney, *Nonlinear optics* (CRC Press, Boca Raton, 2018).

[246] W. H. Press, H. William, S. A. Teukolsky, A. Saul, W. T. Vetterling, and B. P. Flannery, *Numerical recipes 3rd edition: The art of scientific computing* (Cambridge University Press, Cambridge, 2007).

[247] A. Taflove and S. C. Hagness, *Computational electrodynamics: the finite-difference time-domain method* (Artech house, Boston, 2005).

[248] C. Besse, *A relaxation scheme for the nonlinear Schrödinger equation,* SIAM J. Numer. Anal. **42**, 934 (2004).

[249] D. Tskhakaya, K. Matyash, R. Schneider, and F. Taccogna, *The particle-in-cell method,* Contrib. Plasma Phys. **47**, 563 (2007).

[250] R. W. Hockney and J. W. Eastwood, *Computer simulation using particles* (CRC Press, Boca Raton, 1988).

[251] R. L. Honeycutt, *Stochastic Runge-Kutta algorithms. I. White noise,* Phys. Rev. A **45**, 600 (1992).